ENCODING VISUAL FEATURES BY PARALLEL GANGLION CELL INITIATED PATHWAYS IN THE HEALTHY, DISEASED AND ARTIFICIAL RETINAT

EDITED BY: Béla Völgyi, Garrett T. Kenyon, David W. Marshak and
Botir Sagdullaev

PUBLISHED IN: Frontiers in Cellular Neuroscience

frontiers Research Topics

ISSN 1664-8714
ISBN 978-2-88963-105-6
DOI 10.3389/978-2-88963-105-6

About Frontiers

Frontiers is more than just an open-access publisher of scholarly articles: it is a pioneering approach to the world of academia, radically improving the way scholarly research is managed. The grand vision of Frontiers is a world where all people have an equal opportunity to seek, share and generate knowledge. Frontiers provides immediate and permanent online open access to all its publications, but this alone is not enough to realize our grand goals.

Frontiers Journal Series

The Frontiers Journal Series is a multi-tier and interdisciplinary set of open-access, online journals, promising a paradigm shift from the current review, selection and dissemination processes in academic publishing. All Frontiers journals are driven by researchers for researchers; therefore, they constitute a service to the scholarly community. At the same time, the Frontiers Journal Series operates on a revolutionary invention, the tiered publishing system, initially addressing specific communities of scholars, and gradually climbing up to broader public understanding, thus serving the interests of the lay society, too.

Dedication to Quality

Each Frontiers article is a landmark of the highest quality, thanks to genuinely collaborative interactions between authors and review editors, who include some of the world's best academicians. Research must be certified by peers before entering a stream of knowledge that may eventually reach the public - and shape society; therefore, Frontiers only applies the most rigorous and unbiased reviews.
Frontiers revolutionizes research publishing by freely delivering the most outstanding research, evaluated with no bias from both the academic and social point of view. By applying the most advanced information technologies, Frontiers is catapulting scholarly publishing into a new generation.

What are Frontiers Research Topics?

Frontiers Research Topics are very popular trademarks of the Frontiers Journals Series: they are collections of at least ten articles, all centered on a particular subject. With their unique mix of varied contributions from Original Research to Review Articles, Frontiers Research Topics unify the most influential researchers, the latest key findings and historical advances in a hot research area! Find out more on how to host your own Frontiers Research Topic or contribute to one as an author by contacting the Frontiers Editorial Office: researchtopics@frontiersin.org

ENCODING VISUAL FEATURES BY PARALLEL GANGLION CELL INITIATED PATHWAYS IN THE HEALTHY, DISEASED AND ARTIFICIAL RETINA

Topic Editors:
Béla Völgyi, University of Pécs, Hungary
Garrett T. Kenyon, Los Alamos National Laboratory, United States
David W. Marshak, University of Texas Health Science Center, United States
Botir Sagdullaev, Cornell University, United States

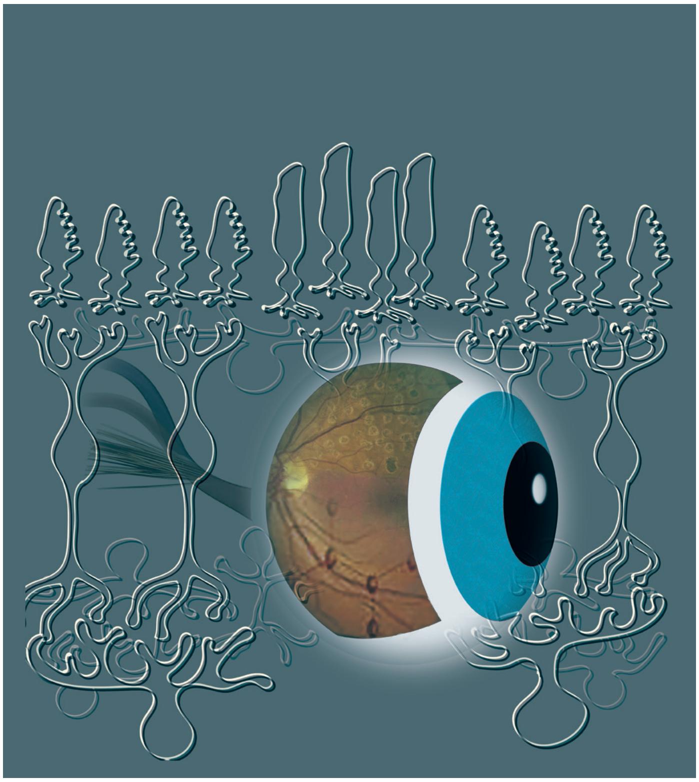

Image by Alma Ganczer and Bela Volgyi

Photons are sensed by retinal photoreceptors whose matrix-like distribution underlies the transformation of illumination patterns of the visual scene into photoreceptor activity patterns in a visuotopic fashion. Activity of neighboring photoreceptors then are compared by secondary bipolar cells to decipher information regarding luminosity- and color-contrast. Bipolar cells achieve this by comparing signals received directly from their center receptive field with those come from spatially offset surrounding receptive field areas mediated by inhibitory, sign-inverting horizontal cells. This information is ultimately sent to retinal ganglion cells, the output neurons of the retina. In addition to the excitatory bipolar cell inputs, spatial and temporal features of ganglion cell activation are robustly modified by inner retinal amacrine cells through inhibitory chemical and/or excitatory electrical synaptic inputs. Ganglion cells sample various bipolar cell subtypes in their dendritic field and utilize collected inputs to generate a spike output code on luminosity-contrast, color-contrast, object motion, background motion, motion direction, changes in background illumination in a subtype specific manner. Ganglion cells in each subtype cover the retinal surface economically, thus collective information across the population provide a feature pattern and through time a feature movie to the brain. Some of these movies are utilized for image perception, whereas others are sent to accessory visual brain centers to control eye-movement, pupil contraction or circadian entrainment. A large body of information has been revealed in the past decade regarding this field, however much of the details still remain unknown or even enigmatic, including: (i) the precise description of neural circuits that serve each ganglion cell subtype to generate a specific feature movie; (ii) the estimation of the number of various ganglion cell subtypes that partake in image forming and non-image forming signaling towards the brain; (iii) the description of changes in the inputs, morphology and signaling of retinal ganglion cells when the tissue is under stress or undergoes disease related degenerative processes; (iv) the comparison of ganglion cell classes with those of the human retina and finally, (v) the practical use of all the above information to establish retina inspired visual algorithms to suit computer, drone and/or robotic vision. Therefore, research articles in this issue were collected to touch upon each of these topics and highlight recent advances of the related field.

Citation: Völgyi, B., Kenyon, G. T., Marshak, D. W., Sagdullaev, B., eds. (2019). Encoding Visual Features by Parallel Ganglion Cell Initiated Pathways in the Healthy, Diseased and Artificial Retina. Lausanne: Frontiers Media. doi: 10.3389/978-2-88963-105-6

Table of Contents

CHAPTER 1

SIGNALING STREAMS IN THE HEALTHY RETINA

CHAPTER 2

SIGNALING IN THE DISEASED RETINA

CHAPTER 3

SIGNALING IN THE ARTIFICIAL RETINA

frontiers
in Cellular Neuroscience

EDITORIAL
published: 24 May 2019
doi: 10.3389/fncel.2019.00229

Editorial: Encoding Visual Features by Parallel Ganglion Cell Initiated Pathways in the Healthy, Diseased and Artificial Retina

Béla Völgyi[1]*, Garrett T. Kenyon[2], David W. Marshak[3] and Botir Sagdullaev[4]

[1] Experimental Zoology and Neurobiology, University of Pécs, Pécs, Hungary, [2] Los Alamos National Laboratory (DOE), Los Alamos, NM, United States, [3] University of Texas Health Science Center at Houston, Houston, TX, United States, [4] Department of Ophthalmology, Burke Neurological Institute, Weill Cornell Medicine, White Plains, NY, United States

Keywords: retina, ganglion cell, parallel signaling, visual coding strategies, retina model

Editorial on the Research Topic

Encoding Visual Features by Parallel Ganglion Cell Initiated Pathways in the Healthy, Diseased and Artificial Retina

Retinal ganglion cells (RGCs) integrate incoming signals transmitted via chemical and electrical synapses from the upstream circuitry. A combination of selective targeting by vertical retinal pathways and subtype specific computation determines the RGC encoding strategy, establishing feature selective signaling to the brain. The collective information from each RGC subtype takes shape as a feature movie (Werblin and Roska, 2007). A collection of such feature movies then are integrated by brain centers to initiate visual perception and visually guided reflexes. A mechanistic understanding of this parallel feature signaling, its pathological alterations as well as its applicability to create artificial vision is crucial on scientific, clinical, and industrial setting. Dendritic integration is one of the most essential tasks RGCs perform, thus mechanisms regulating RGC dendritic development are essential to refine dendritic size and structure. In this topical issue, Elias et al. characterized the dendritic development of JamB RGCs. While the dendritic stratification level was determined in early postnatal days (P8), fine adjustments in dendritic elongation, arbor growth, and reduction in the number of dendritic specializations take place later. Both genetic defects (knocking-out NR1 NMDARs) and suboptimal environmental conditions (light deprivation) impeded healthy maturation of the dendritic arbor indicating a role for NMDA signaling in stimulus dependent wiring in the developing mouse retina. Under optimal conditions developmental wiring results in 30 or more RGC subtypes (Völgyi et al., 2009; Baden et al., 2016), each receiving selective retinal inputs and responding to different attributes of the visual stimulus. An article by Jacoby and Schwartz reviews circuit mechanisms underlying encoding strategies of one distinctive RGC type, the suppressed-by-contrast cells (SbC). These cells decrease their maintained spiking frequency to both contrast increments and decrements, making them potent background illumination detectors. The authors further argue that SbCs form a heterogenous group providing parallel signals of illumination constancy to multiple subcortical target neuron populations.

Animal model studies gain particular importance when results are confirmed using human tissue. In this issue, Kántor et al. described the distribution of gap junction-forming connexin36 (Cx36) plaques in human RGC dendritic arbors. The authors revealed a clear tendency for Cx36 gap junctions to form clusters and to preferentially localize to terminal dendritic segments. It has been shown that certain gap junctions synchronize parasol cell spiking in primates and homologous RGCs in animal models allowing for population coding of visual features (Roy et al., 2017). The findings of Kántor et al. thus support previous descriptions in animal models and further extend

Edited and reviewed by:
Arianna Maffei,
Stony Brook University, United States

***Correspondence:**
Béla Völgyi
volgyibela@gmail.com;
volgyi01@gamma.ttk.pte.hu

Specialty section:
This article was submitted to
Cellular Neurophysiology,
a section of the journal
Frontiers in Cellular Neuroscience

Received: 26 February 2019
Accepted: 07 May 2019
Published: 24 May 2019

Citation:
Völgyi B, Kenyon GT, Marshak DW
and Sagdullaev B (2019) Editorial:
Encoding Visual Features by Parallel
Ganglion Cell Initiated Pathways in the
Healthy, Diseased and Artificial Retina.
Front. Cell. Neurosci. 13:229.
doi: 10.3389/fncel.2019.00229

those with new insights on RGC gap junction coupling. High-throughput approaches are favored methods in modern neuroscience because they yield ample data in each experiment. However, they also require quick and automatized methods to replace the tedious work of manual or half-automated data analysis. High density multi-electrode arrays allow for the examination of thousands of RGCs simultaneously. Jouty et al. presented a non-parametric, automatic scheme that uses only simple stimuli and a "spike train distance measure" as a clustering metric to achieve a quick and efficient physiological classification. By utilizing both synthetic and biological spike trains the authors show that the activity of major mouse RGC subtypes could be readily examined in a single recording session with ∼1,000 cells. Moreover, given its parameter-free nature, the method is broadly applicable for the physiological classification of neurons in other structures, as well.

In retinal degenerations, photoreceptor cell loss has been shown to lead to pathway-specific changes and emergent aberrant activity across numerous RGC classes (Yee et al., 2014). Similarly, RGC morphology and function have been shown to be severely altered in the retinal tissue under stress or during pathological changes. In this issue, Lakk et al. that TRPV1 and TRPV4 expression patterns subdivide RGCs in the mouse retina into four cohorts, including: TRPV1+, TRPV4+ TRPV1/TRPV4 expressing cells and RGCs expressing neither TRP channel. The data predict that RGC subpopulations as well as the feature signals they carry will be differentially sensitive to inflammatory and mechanical stressors. In the work of Li et al. intraocular pressure elevation induced ischemia-reperfusion (IR)-related decline of ABCA1 expression. Induction of ABCA1, a protein recognized as a glaucoma risk factor, reduced RGC apoptosis and promoted anti-inflammatory factor expression, but they reduced microglial activation and pro-inflammatory cytokine expression. The authors also showed a TANK-binding kinase 1 (*TBK1*) dependent regulation of ABCA1 degradation. The results indicated a novel IR mechanism, in which TBK1-dependent ABCA1 ubiquitination leads to retinal inflammation and RGC apoptosis. Targeting the underlying signaling circuit offers a potential treatment strategy to prevent RGC apoptosis in retinal ischemia and glaucoma, two major progressive retinal conditions that eventually cause blindness. The glial S100B protein is thought to be associated with glaucoma-related RGC loss. In this issue, Kuehn et al. introduced a new model for a glaucoma-like degeneration by injecting S100B intraocularly. The injection induced a progressive degradation in RGC optic fibers that was followed by RGC degeneration and, finally, destruction of other retinal neurons. These results proved that S100B intraocular injection provides a potent model to examine the onset and progression of vision loss in glaucoma studies.

Apart from the clinical relevance, the data on parallel visual signaling streams of the retina also serves as a powerful tool in modeling and computational studies (Watkins et al., 2018). Ozimek et al. presented a biologically inspired retino-cortical mapping model that tremendously improves image analysis of Deep Convolutional Neural Nets (DCCNs). The model enables DCCNs to process large images in a single pass by utilizing only a consumer grade graphics processor (GPU), which makes it highly suitable for robot and computer vision applications.

In summary, this topical issue achieved its goal by presenting a collection of work describing mechanisms that contribute to parallel signaling, pinpointing changes that occur in pathological conditions and also showing how the comparison of artificial retinal circuits to their biological counterparts is beneficial for robotics and computer vision.

AUTHOR CONTRIBUTIONS

All authors listed have made a substantial, direct and intellectual contribution to the work, and approved it for publication.

FUNDING

This study was supported by the Hungarian Brain Research Program (KTIA_NAP_13-2-2015-0008) and Hungarian Brain Research Program 2 (2017-1.2.1.-NKP-2017) to BV supported by the European Union and the State of Hungary, co-financed by the European Social Fund in the framework of TAMOP-4.2.4.A/ 2-11/1-2012-0001 National Excellence Program to BV supported by the UNKP-17-3-I-PTE-155 New National Excellence Program of the Ministry of Human Capacities and the National Excellence Program.

REFERENCES

Baden, T., Berens, P., Franke, K., Román Rosón, M., Bethge, M., and Euler, T. (2016). The functional diversity of retinal ganglion cells in the mouse. *Nature* 529, 345–350. doi: 10.1038/nature16468

Roy, K., Kumar, S., and Bloomfield, S. A. (2017). Gap junctional coupling between retinal amacrine and ganglion cells underlies coherent activity integral to global object perception. *Proc. Natl. Acad. Sci. U.S.A.* 114, E10484–E10493. doi: 10.1073/pnas.1708261114

Völgyi, B., Chheda, S., and Bloomfield, S. A. (2009). Tracer coupling patterns of the ganglion cell subtypes in the mouse retina. *J. Comp. Neurol.* 512, 664–6687. doi: 10.1002/cne.21912

Watkins, Y., Thresher, A., MascareAaas, D., and Kenyon, G. T. (2018). "Sparse coding enables the reconstruction of high-fidelity images and video from retinal spike trains," in *Proceedings of the International Conference on Neuromorphic Systems (ICONS)* (Knoxville, TN).

Werblin, F., and Roska, B. (2007). The movies in our eyes. *Sci. Am.* 296, 72–79. doi: 10.1038/scientificamerican0407-72

Yee, C. W., Toychiev, A. H., Ivanova, E., and Sagdullaev, B. T. (2014). Aberrant synaptic input to retinal ganglion cells varies with morphology in a mouse model of retinal degeneration. *J. Comp. Neurol.* 522, 4085–4099. doi: 10.1002/cne.23660

Conflict of Interest Statement: The authors declare that the research was conducted in the absence of any commercial or financial relationships that could be construed as a potential conflict of interest.

frontiers
in Cellular Neuroscience

ORIGINAL RESEARCH
published: 14 August 2018
doi: 10.3389/fncel.2018.00249

Glutamate Activity Regulates and Dendritic Development of J-RGCs

*Eerik Elias[1], Ning Yang[1,2,3], Ping Wang[1,2] and Ning Tian[1,2]**

[1]Department of Ophthalmology and Visual Science, University of Utah School of Medicine, Salt Lake City, UT, United States, [2]VA Salt Lake City Health Care System, Salt Lake City, UT, United States, [3]Eye Center, Renmin Hospital of Wuhan University, Wuhan, China

Retinal ganglion cells (RGCs) have a wide variety of dendritic architectures, which are critical for the formation of their function-specific synaptic circuitry. The developmental regulation of the dendrites of RGCs is thought to be subtype dependent. The purpose of this study is to characterize the dendritic development of a genetically identified RGC subtype, JamB RGCs (J-RGCs), and the roles of glutamate receptor activity on the dendritic development of these cells. We show that the dendrites of J-RGCs are strictly ramified in the outer portion of the inner plexiform layer (IPL) of the retina at the age of postnatal day 8 (P8), mimicking the ramification pattern of adults. However, several other important features of dendrites undergo substantial developmental refinement after P8. From P8 to P13, the dendritic development of J-RGCs is characterized by a dramatic increase of dendritic length and the size of the dendritic field. After eye opening, the dendritic development of J-RGCs is characterized by a tremendous decrease of the number of dendritic protrusions (spine-like structures) and a consolidation of the size of the dendritic field. To determine whether the dendritic development of J-RGCs is regulated by glutamatergic activity, we conditionally knocked out the expression of an obligatory subunit of N-methyl-D-aspartate receptors (NMDARs), NR1 (Grin1), in J-RGCs. We found that J-RGCs with the NMDAR mutation have decreased dendrite outgrowth and dendritic field expansion but increased number of dendritic protrusions before eye opening. To determine if visual experience regulates the development of J-RGC dendrites, we raised the mice in complete darkness after birth. Light deprivation prevented the decrease in the number of dendritic protrusions and the consolidation of the dendritic field of wild type (WT) mice after eye opening. However, light deprivation has no additional effect on the number of dendritic protrusions or the size of the dendritic field of J-RGCs with NMDAR mutation. Together, these results revealed the roles of light stimulation and NMDAR activity on the dendritic development of J-RGCs.

Keywords: glutamate activity, dendritic morphology, development, retinal ganglion cell, activity-dependent plasticity, NMDAR, light deprivation

OPEN ACCESS

Edited by:
Bela Volgyi,
University of Pécs, Hungary

Reviewed by:
Karl Farrow,
Neuroelectronics Research Flanders, Belgium
Patrick William Keeley,
University of California, Santa Barbara, United States

****Correspondence:***
Ning Tian
ning.tian@hsc.utah.edu

Received: *19 April 2018*
Accepted: *23 July 2018*
Published: *14 August 2018*

Citation:
Elias E, Yang N, Wang P and Tian N (2018) Glutamate Activity Regulates and Dendritic Development of J-RGCs. Front. Cell. Neurosci. 12:249. doi: 10.3389/fncel.2018.00249

INTRODUCTION

Neurons are one of the most morphologically diverse cell types due to the large variety of their dendritic patterns, which are specialized structures for synaptic formation (Whitford et al., 2002; Jan and Jan, 2010; Vaney et al., 2012). Retinal ganglion cells (RGCs) also have a wide variety of dendritic patterns, which are critical for specific circuit formation and function

(Masland, 2001; Sun et al., 2002; Badea and Nathans, 2004; Coombs et al., 2007; Berson, 2008; Kim et al., 2008; Völgyi et al., 2009; Kay et al., 2011; Sanes and Masland, 2015). One well-known example is the JamB expressing RGCs (J-RGCs) in mouse retina, which orient their dendrites ventrally to form a polarized dendritic field. This polarized dendritic field is thought to be critical for J-RGCs to preferentially detect the directional movement in the visual field (Kim et al., 2008, 2010), have a color opponent receptive field (Joesch and Meister, 2016) and to have orientation selectivity of J-RGCs (Nath and Schwartz, 2017). In mammals, RGCs were initially classified into subtypes morphologically (Masland, 2001; Sun et al., 2002; Badea and Nathans, 2004; Coombs et al., 2007; Berson, 2008; Kim et al., 2008; Völgyi et al., 2009; Kay et al., 2011), then combined with functional features (Briggman and Euler, 2011; Briggman et al., 2011; Baden et al., 2013). Recently, RGCs are classified into at least 25 subtypes using a combination of morphological, functional and genetic features (Roska and Meister, 2014; Sanes and Masland, 2015). The formation of subtype specific dendritic architecture of RGCs is heterogeneous and dendrites of some subtypes of RGCs undergo dramatic structural refinement during postnatal development as they grow into the inner plexiform layer (IPL), stratify, and form synapses with bipolar and amacrine cells (Tian, 2008; Kim et al., 2010). Conflicting studies, however, disagree as to whether or not RGC dendritic development is activity dependent and increasing evidence suggests that the discrepancy of the activity dependency of the development of RGC dendrites might be the result of the cell subtype specific developmental processes (Bodnarenko and Chalupa, 1993; Tagawa et al., 1999; Guenther et al., 2004; Xu and Tian, 2007; Kerschensteiner et al., 2009; Chang et al., 2010). Therefore, characterizing the developmental profile of the dendrites of each subtype of RGCs and their activity-dependency will directly address this discrepancy.

Glutamate receptors, especially N-methyl-D-aspartate receptors (NMDARs), play important roles in the dendritic development and synaptic formation of the CNS (McAllister, 2000; Cline and Haas, 2008). Impairment of NMDAR function blocks the normal axonal/dendritic morphogenesis of optic tectal neurons, motor neurons and cortical neurons (Inglis et al., 1998; Rajan and Cline, 1998; Datwani et al., 2002; Hebbeler et al., 2002; Lee et al., 2005; Espinosa et al., 2009). NMDARs are expressed by all RGCs (Fletcher et al., 2000; Pourcho et al., 2001; Guenther et al., 2004; Zhang and Diamond, 2009) and NMDAR-mediated mechanisms have been postulated to regulate RGC axonal morphogenesis in zebrafish and *Xenopus* (Ben Fredj et al., 2010; Munz et al., 2014), dendritic morphogenesis and α-amino-3-hydroxy-5-methyl-4-isoxazolepropionic acid receptor (AMPAR) plasticity in RGCs of mice (Xu et al., 2010; Jones et al., 2012). In addition, light stimulation has been shown to regulate the development of RGC dendrites and their synaptic function (Fisher, 1979; Wingate and Thompson, 1994; Sernagor and Grzywacz, 1996; Tian and Copenhagen, 2001, 2003; Xu and Tian, 2007; Tian, 2008; Akimov and Rentería, 2014), as well as the expression and activity of NMDARs on RGCs (Fox et al., 1991; Carmignoto and Vicini, 1992; Xue and Cooper, 2001; Guenther et al., 2004). However, whether and how NMDARs regulate the dendritic morphogenesis of specific subtypes of RGCs has not been reported.

J-RGCs are a unique population of RGCs, which has a unique polarized dendritic architecture corresponding remarkably to their directional selective functionality (Kim et al., 2008, 2010), color opponent receptive field (Joesch and Meister, 2016) and orientation selectivity (Nath and Schwartz, 2017). It has been shown that the dendrites of J-RGCs undergo significant developmental refinement during early postnatal development (Kim et al., 2008, 2010). Therefore, we use this function-specific subtype RGCs as a model to investigate the roles of glutamate receptor-mediated activity in the dendritic development of RGCs. Our results showed that the dendrites of J-RGCs undergo an orderly developmental process during postnatal ages. The ramification of the dendrites of J-RGCs in IPL reaches the adult pattern before postnatal day 8 (P8), while other structural features of dendrites undergo substantial developmental refinement after P8. From P8 to P13, the dendritic development of J-RGCs is characterized by a dramatic increase in the dendritic length and the size of the dendritic field. After eye opening, the dendritic development of J-RGCs is characterized by a complete cease in dendritic growth, a decrease in the number of dendritic protrusions and a consolidation of the size of the dendritic field. Conditional mutation of NMDARs on J-RGCs resulted in decreased dendrite outgrowth and dendritic field expansion but an increased number of dendritic protrusions before eye opening. Light deprivation, on the other hand, prevented the developmental decrease in the number of dendritic protrusions and the consolidation of dendritic field of wild type (WT) mice after eye opening but with little effect on the dendritic structure of J-RGCs with cell-specific mutation of NMDARs. Together, these results have for the first time revealed the roles of light stimulation and NMDAR activity on the dendritic development of a genetically-identified functionally-specific subtype of RGCs.

MATERIALS AND METHODS

Animals

JamB-CreER and Thy1-Stop-YFP (yellow fluorescent protein) mice were obtained from Dr. Joshua Sanes' laboratory at Harvard University (Kim et al., 2008). These mice were generated on a C57BL/6 background and backcrossed with C57BL/6J mice 4–5 generations in our lab. Then the JamB-CreER mice were bred with the Thy1-Stop-YFP mice to create JamB-CreER:Thy1-Stop-YFP double transgenic mice and YFP is expressed specifically in J-RGCs upon intraperitoneal (IP) injection of Tamoxifen. These mice were used as "WT" controls for J-RGC dendritic morphology. B6.129S4-*Grin1*^{tm2Stl}/J mice were obtained from the Jackson Laboratory (Bar Harbor, ME, USA). To generate these mice, the construct was electroporated into 129S4/SvJae derived J1 embryonic stem (ES) cells. Correctly targeted ES cells were injected into C57BL/6 blastocysts. The resulting chimeric animals were crossed to C57BL/6J mice. The colony was then backcrossed to C57BL/6J for eight generations prior to sending to The Jackson Laboratory Repository. Therefore, this mouse strain also has a C57BL background. JamB-CreER:Thy1-Stop-YFP:Grin1$^{flox/flox}$ triple transgenic mice were generated by breeding JamB-CreER:Thy1-Stop-YFP mice with B6.129S4-*Grin1*^{tm2Stl}/J mice. Therefore, both JamB-CreER:Thy1-Stop-YFP double transgenic mice and JamB-CreER:Thy1-Stop-YFP:Grin1$^{flox/flox}$ triple transgenic mice are considered having C57BL/6 background. When the triple transgenic mice are treated with Tamoxifen, J-RGCs in the retina express YFP and stop the expressing of NR1 specifically in J-RGCs (Tsien et al., 1996). All mice were treated with IP injection of Tamoxifen (150 μg) at the ages of P1–3. The control animals were fed and housed under 12:12-h cyclic light/dark conditions. The average light intensity in the animal room during subjective day was 300–400 lux while the light intensity inside the cages during subjective day was 40 lux for control mice. Dark-reared animals were housed in conventional mouse cages, which were placed in a continuously ventilated light-tight box. The temperature and humidity inside the box were continuously monitored and controlled. All the procedures of daily monitoring and routine maintenance of dark-reared mice were conducted under infrared illumination. All animal procedures and care were preformed following protocols approved by the IACUC of the University of Utah in compliance with PHS guidelines and with those prescribed by the Association for Research in Vision and Ophthalmology (ARVO).

Intraocular Injection

The procedure of intraocular injection of GluR antagonists and saline into mouse eyes has been described previously (Xu et al., 2010). Various glutamate receptor antagonists have been used for intraocular injection to pharmacologically manipulate the activity of glutamate receptors. Regardless the types of glutamate receptor analogous and concentration, the procedures of intraocular injection were the same. The actual concentrations of the injected chemicals were prepared so the volume of the solution injected was always 2 μl in order to have the solution evenly distributed inside the eye. For the injection procedure, the mice were anesthetized with Isoflurane (1%–5% Isoflurane mixed with room air delivered in a rate between 0.8–0.9 L/min) through a mouse gas anesthesia head holder (David KOPF Instruments, Tujunga, CA, USA) and local application of 0.5% proparacaine hydrochloride ophthalmic solution on each eye. Glass micropipettes made from borosilicate glass using a Brown-Flaming horizontal puller with very fine tip (about 10–15 μm diameter) were used for injection. The glass needle was mounted on a Nano-injection system, which could precisely control the amount of injected solution at the nl level. The glass needle was aimed to penetrate the eyeball near equator under a dissection microscope and a total of 2 μl solution was slowly injected into each eye. After the procedure, the mice were placed in a clean cage siting on a water blanket. The temperature of the water blanket was set at 33°C. Mice in this cage were continuously monitored until they completely recovered and then they were returned to their original cages. The procedures for anesthesia and intraocular injection fit the procedures described in the University of Utah IACUC Policies.

Primary Antibodies

Rabbit polyclonal antibody against green fluorescent protein (GFP) conjugated with AlexaFluor 488 was purchased from Molecular Probes (Eugene, OR, USA; catalog No. A21311). This antibody was raised against GFP isolated directly from *Aequorea Victoria* and has been characterized by immunocytochemistry in granule cells (Overstreet-Wadiche et al., 2006), olfactory sensory neurons (Lèvai and Strotmann, 2003), and hippocampal neurons that express GFP (Huang et al., 2005). Antibody directed toward choline acetyltransferase (ChAT) was purchased from Millipore (Temecula, CA, USA; catalog No. AB144P). This polyclonal antibody was raised in goat against human placental enzyme and has been characterized by Western blotting, recognizing a band at 68–70 kD.

Preparation of Retinal Whole-Mounts and Retina Sections for Fluorescent Imaging

J-RGC dendritic arbors were imaged on a whole mount retinal preparation while the dendritic ramification of J-RGCs in the IPL was imaged on a retinal slice preparation using confocal microscopy. The procedures for fluorescent immuno-labeling of YFP-expressing RGCs on retinal whole-mount and slide preparations have been described previously in detail (Tian and Copenhagen, 2003; Xu and Tian, 2007; Xu et al., 2010). In brief, mice were euthanized at P8, P13 or P30 with 100% CO_2 followed by either cervical dislocation (for P30 mice) or decapitation (for P8 and P13 mice).

For retinal whole mount preparation, retinas were isolated and fixed in 4% paraformaldehyde (PFA) in 0.01 M phosphate-buffered saline (PBS; pH 7.4) for 30 min at room temperature. Fixed retinas were washed 10 min × 3 in 0.01 M PBS and incubated in blocking solution (10% normal donkey serum) at 4°C for 2 h. Next, retinas were incubated in rabbit polyclonal anti-GFP antibody conjugated with Alexa Fluor488 (1:500) for 7 days at 4°C. Retinas were then washed and flat mounted on Super-Frost slides (Fisher Scientific, Pittsburgh, PA, USA) with Vectashield mounting medium for fluorescence (Vector Laboratories, Burlingame, CA, USA).

For retina section preparation, the whole eyes were removed and fixed in 4% PFA for 2 h. Fixed eyes were washed three times for 10 min each in 0.01 M PBS and incubated in 15% sucrose for 2 h and then 30% sucrose at 4°C overnight. Eyes were than embedded in Tissue-Tek OCT compound (Sakura Finetek USA Inc., Torrance, CA, USA), sectioned vertically at 12–15 μm thickness on a Leica CM-3050-S cryostat microtome (Leica Biosystems, Wetzlar, Germany), and collected on Super-Frost Plus slides. A rabbit polyclonal anti-GFP antibody conjugated with Alexa Fluor488 (1:500) and a goat polyclonal anti-ChAT antibody (1:150) were used to label YFP-expressing J-RGCs and the dendritic plexus of cholinergic amacrine cells, respectively. A rhodamine red-conjugated donkey anti-goat (1:100) secondary antibody was used to reveal the anti-ChAT bindings. The secondary antibody was purchased from Jackson Immuno Research Laboratories (West Grove, PA, USA).

Confocal Laser Scanning Microscopy and Quantitative Image Analysis

Fluorescent images were collected using a dual-channel Zeiss microscope (Carl Zeiss AG, Germany) with the C-Apochromat 40× 1.2 W Korr water immersion lens from retinal section or whole mount preparations. Multiple images of immunolabeled retinal sections were taken at steps of 0.4 μm. Several optical sections were assembled to achieve the final image. The brightness and contrast of the final images were adjusted in Adobe Photoshop CS5 (Adobe Systems Inc., San Jose, CA, USA). The dendritic stratification of each RGC was characterized by the ramification depth (peak dendritic location) and thickness (dendritic width) in the IPL, both of which were calculated by fitting the pixel intensities of the image of retinal cross section into Gaussian distribution using the software Igor (WaveMetrics, Lake Oswego, OR, USA). The IPL was defined as 0%–100% from the border of inner nuclear layer to the border of ganglion cell layer. This approach has been described in details previously (Xu and Tian, 2007). Image stacks of YFP-expressing RGCs in whole-mount retinas were collected at intervals of 0.5 μm. IPLab software (Scanalytics, Inc., Fairfax, VA, USA) was used to align multistacks of images together. The entire dendritic tree of each RGC was traced in the 3D stack using Neurolucida software (Neurolucida 2000, Microbrightfield, Williston, VT, USA). The total dendritic length, the number of dendritic branches, and the number of filopodia were measured by the software based on the tracing using the approach we previously described (Xu et al., 2010). For the measurement of the size of the dendritic field, the image stack of each RGC was maximum projected into a single frame and then the dendritic field was outlined by connecting the tip of terminal dendrites to form a convex enclosure using Neurolucida 2000. The size of the dendritic field was calculated by the software based on the convex enclosure. Because the length of dendrites and the size of the dendritic field of RGCs vary with the eccentricity of the cells in the retina, we only included the RGCs with their soma located ±500 μm around the equator of the eye ball (**Supplementary Figure S1**).

Statistical Analysis

Data are all presented as mean ± SEM in the text and figures. ANOVA, *post hoc* (Bonferroni-Dunn) tests were used to determine the significance of the difference between more than two means. Student t-tests were used to examine the difference between two means. All of the statistical tests were performed with STATVIEW (Abacus Concepts, Berkeley, CA, USA).

RESULTS

The Development of J-RGC Dendrites Undergo an Orderly Process During Postnatal Ages

It has been shown that the dendrites of J-RGCs undergo developmental refinement early in postnatal ages (Kim et al., 2008, 2010). We first quantitatively characterized the developmental profile of the dendritic ramification of J-RGCs at three critical ages: immediately before RGCs receive glutamate synaptic inputs (P8; Bansal et al., 2000; Johnson et al., 2003), around the time of eye opening (P13) and in young adult (P30). The J-RGCs in the JamB-CreER:Thy1-YFP double transgenic mice show strong YFP expression as early as P5 (Kim et al., 2008, 2010), which reveals all details of their dendrites (**Figures 1A,B**). To assess the J-RGC dendritic distribution in the IPL precisely, we measured the pixel intensities of YFP signals of dendrites of individual J-RGCs (**Figure 1C**). The average pixel intensity of a region of interest (white dash line box in **Figure 1C**) was calculated from a z-stack of the confocal image and plotted as a function of the IPL thickness for the estimation of a normalized dendritic density distribution (**Figure 1G**; Xu and Tian, 2007). The IPL was defined as 0%–100% from the border of inner nuclear layer to the border of ganglion cell layer and divided into three regions based on the position of cholinergic amacrine cell dendritic plexus in the IPL. **Figure 1D** shows representative dendritic density distribution curves of three J-RGCs from a P8, a P13 and a P30 retina. Although the dendritic density of these three J-RGCs peak at different locations in the outer portion of the IPL, the average dendritic density distributions of J-RGCs at the three ages substantially overlapped with each other (**Figure 1E**). Quantitatively, the average dendritic distributions of J-RGCs from the three ages in the IPL are not different statistically (**Figure 1F**). These results are consistent with the previous report that the dendrites of J-RGCs reach the adult ramification pattern in the IPL early during postnatal development (Kim et al., 2010).

We then quantitatively analyzed several important dendritic features of J-RGCs during postnatal development. To estimate the dynamics of dendritic growth and branching during postnatal development (Xu et al., 2010; Yang et al., 2010), we quantified the age-dependent changes in the total number of the dendritic protrusions of J-RGCs (**Figure 2B**; Munz et al., 2014), total length of the dendrites (**Figures 2A,C,D**), number of dendritic branches (**Figure 2E**), length of dendritic branches (**Figure 2F**), and size of the dendritic field (**Figure 2C**) of each J-RGC.

Our results showed that the dendrites of J-RGCs undergo significant developmental refinement (**Figure 3A**). Before eye opening (P13), the developmental refinement of dendrites was characterized by active dendritic elongation, a large number of dendritic protrusions and rapid expansion of the dendritic field. From P8 to P13, the total length of dendrites increased by 2.2-fold (from 1332.2 μm ± 97.8 μm at P8–2919.6 μm ± 229.4 μm at P13, $p < 0.0001$; **Figure 3B**), the size of the dendritic field increased by 3.3-fold (from 10391.7 μm^2 ± 267.4 μm^2 at P8–34733.7 μm^2 ± 6489.8 μm^2 at P13, $p < 0.0001$; **Figures 3C,D**), and the number of dendritic protrusions remained at a high level during this period (159.7 ± 11.7 and 145 ± 17.4 for P8 and P13 J-RGCs, respectively; **Figure 3E**). Additional analysis of the dendritic structure of J-RGCs at P8 and P13 showed that the number of dendritic branches increased by 1.4-fold (from 92.3 ± 10.5 at P8 to 124.7 ± 15 at P13, $p = 0.05$;

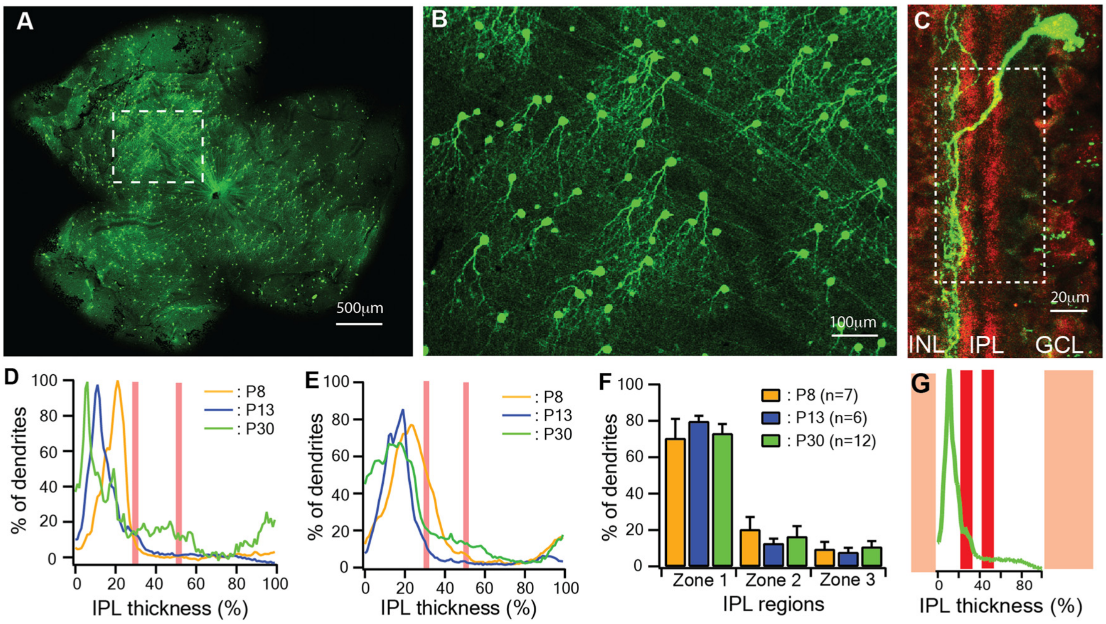

FIGURE 1 | The dendritic ramification of JamB retinal ganglion cells (J-RGCs) reaches adult pattern early during postnatal development. The retinas of JamB-CreER:Thy1-YFP mice were stained with an anti-green fluorescent protein (GFP) antibody and flat mounted for dendritic tree imaging or sectioned for ramification analysis. **(A)** A representative image of a whole mount retina of a JamB-CreER:Thy1-YFP mouse. **(B)** An enlarged view of the retina area indicated by the dashed line box in **(A)** showing YFP expressing J-RGCs. **(C)** Immunolabeling of cholinergic amacrine cell dendritic plexus (red) and the dendritic plexus of a J-RGC (green) of a cross section of a P30 JamBCreER:Thy1-YFP mouse retina. **(D)** Representative dendritic density distribution curves of three J-RGCs from a postnatal day 8 (P8), a P13 and a P30 retina. **(E)** Average dendritic density profile as a function of the inner plexiform layer (IPL) depth measured as the fluorescent intensity of the J-RGCs at three different ages (P8: 2 mice, 7 cells; P13: 2 mice, 6 cells; P30: 3 mice, 12 cells). **(F)** Average dendritic distribution of the J-RGCs in three IPL zones at three ages. **(G)** The fluorescent intensity profile of the dendritic plexus of the J-RGC in **(C)** plotted as a function of the IPL depth (green). The red bands indicate the cholinergic amacrine cell dendritic plexus. The yellow bands indicate the GCL and INL.

Figure 3F), while the length of dendritic branches increased by 1.9-fold (from 116.4 μm ± 7.6 μm at P8 to 219.7 μm ± 15.7 μm at P13, $p < 0.0001$; **Figure 3G**). Therefore, the total dendritic elongation and dendritic field expansion is due to both the elongation of individual dendritic branches and addition of new dendritic branches. Interestingly, the extent of dendritic elongation was most significant for the dendritic branch orders 4–8 (**Figure 3I**) without a proportional increase in the number of dendritic branches in this range (**Figure 3G**), indicating that the developmental changes of the dendritic length and the size of the dendritic field of J-RGCs is unlikely to be the result of developmental retina expansion.

After eye opening, the developmental refinement of J-RGC dendrites was characterized by significant reduction of the number of dendritic protrusions (**Figure 3E**), a complete stop of the dendritic elongation (**Figure 3B**), a significant consolidation of the size of the dendritic field (**Figures 3C,D**), and the pruning of terminal dendritic branches (**Figure 3F**). Specifically, the number of dendritic protrusions decreased by 77% (from 145 ± 17.4 at P13 to 33.3 ± 2.9 at P30, $p < 0.0001$) and the size of the dendritic field decreased by 35% (from 34733.7 μm^2 ± 6489.8 μm^2 at P13 to 22712.3 μm^2 ± 772.3 μm^2 at P30, $p = 0.0133$). However, the total length of dendrites remained at similar levels (2919.6 μm ± 229.4 μm vs. 2607.8 μm ± 94.9 μm for P13 and P30 J-RGCs, respectively; $p = 0.1376$). Further analysis showed that the dendritic field consolidation is associated with a significant decrease in the number of dendritic branches from 124.7 ± 15 at P13 to 85.9 ± 7.5 at P30 ($p = 0.024$; **Figure 3F**), mostly in the higher order of dendritic branches (**Figure 3G**), but very little change in the total length of dendrites (**Figure 3B**) and the average length of dendritic branches was observed (24.5 μm ± 2.5 μm vs. 28.5 μm ± 1.6 μm for P13 and P30 J-RGCs, respectively, $p = 0.2024$; **Figures 3H,I**).

Taken together, the dendrites of J-RGCs undergo an orderly developmental refinement. The dendritic ramification depth of J-RGCs in the IPL reaches the adult level before P8. Then the dendritic growth, branching and dendritic field expansion are completed around the time of eye opening. Finally, the development of dendrites ends by pruning of terminal dendrites and dendritic protrusions, which is associated with a consolidation of the size of the dendritic field before P30. Because the developmental refinement of J-RGC dendrites occurred during the time period in which RGCs start to receive spontaneous glutamatergic synaptic inputs before eye opening (Bansal et al., 2000; Johnson et al., 2003) and light evoked glutamatergic synaptic inputs after eye opening, it opens the possibility that developmental refinement of J-RGC dendrites may be driven by glutamatergic synaptic activity.

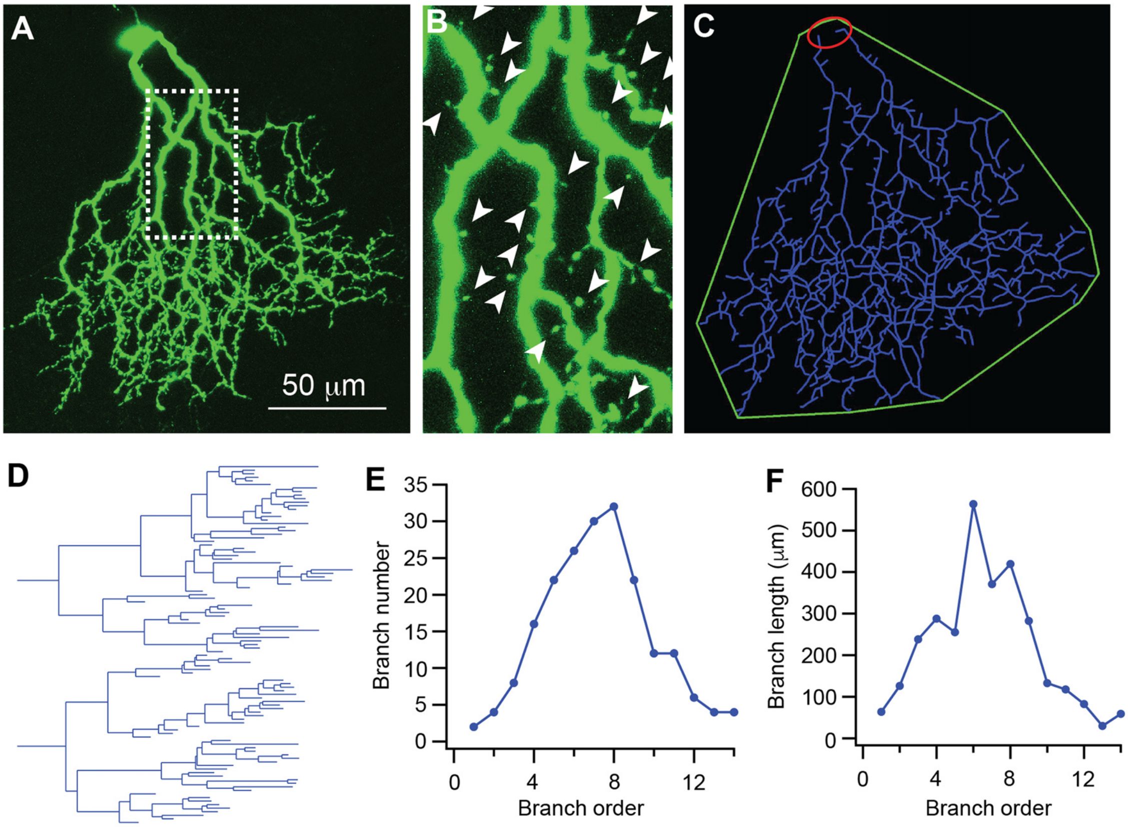

FIGURE 2 | The dendritic pattern of J-RGCs is quantitatively analyzed. The dendritic pattern of J-RGCs was quantitatively analyzed. **(A)** Maximum projection of the confocal image of a J-RGC. **(B)** An enlarged view of the dendrites indicated by the dashed line box of **(A)** showing the dendritic protrusion (arrowheads). **(C)** The tracing result of the J-RGC showing the soma (red), the dendrites (blue), and the dendritic field (green). **(D)** The dendrogram of the tracing result of the J-RGC shown in **(C)**. The total length of dendrites, the number of dendritic branches, and the number of dendritic protrusions were quantified based on this dendrogram. **(E)** The plot of the number of dendritic branches as a function of branch order of the cell in **(A)**. **(F)** The plot of dendritic branch length as a function of branch order of the same cell in **(A)**.

Glutamate Receptor Activity Is Required for the Development of J-RGC Dendrites

Glutamate receptors, especially NMDARs, have been found to play important roles in the development of CNS neurons (Inglis et al., 1998; Rajan and Cline, 1998; Cline and Haas, 2008; McAllister, 2000; Datwani et al., 2002; Hebbeler et al., 2002; Lee et al., 2005; Espinosa et al., 2009) as well as the axonal and dendritic morphogenesis of RGCs (Ben Fredj et al., 2010; Xu et al., 2010; Jones et al., 2012; Munz et al., 2014). To test the possibility that the developmental refinements of J-RGC dendrites during postnatal age is regulated by glutamatergic activity, we blocked glutamatergic synaptic activity with intraocular injections of either the antagonist of AMPARs, CNQX, alone or CNQX with a NMDAR antagonist, AP5, from P8 to P13. Examination of the dendrites of J-RGCs showed that intraocular injection of CNQX+AP5 reduced the developmental elongation of J-RGC dendrites by 27% (2919.6 µm ± 229.4 µm vs. 2139.4 µm ± 103.5 µm for control and CNQX+AP5 treated J-RGCs, $p = 0.01$) while CNQX alone or saline had no significant effect on J-RGC dendritic length ($p = 0.62$ and 0.47, respectively), suggesting that NMDAR might play an important role in dendritic growth of J-RGCs (**Figure 4A**). In addition, the developmental expansion of dendritic field was reduced by 50% in eyes with injection of CNQX+AP5 (34733.7 μm^2 ± 6489.8 μm^2 vs. 17332.1 μm^2 ± 1115.6 μm^2 for control and CNQX+AP5 treated J-RGCs, $p = 0.03$, **Figure 4B**). However, CNQX alone or saline injection also reduced size of the dendritic field by 27% and 43% (34733.7 μm^2 ± 6489.8 μm^2 for control, 25282.6 μm^2 ± 2243.6 μm^2 for CNQX treated J-RGCs, and 19925 μm^2 ± 911.7 μm^2 for saline treated J-RGCs, $p = 0.2$ and 0.06, respectively), suggesting that the procedure of intraocular injection *per se* might have retarded the developmental expansion of the size of the dendritic field of J-RGCs (**Figure 4B**).

To further determine whether NMDARs play critical roles in the developmental refinements of J-RGC dendrites, we generated a triple transgenic mouse line (JamB-CreER:Thy1-YFP:Grin1$^{flox/flox}$), in which the expression of the obligatory subunit of NMDAR, NR1, in J-RGCs is selectively blocked upon the activation of the CreER (Tsien et al., 1996), while the

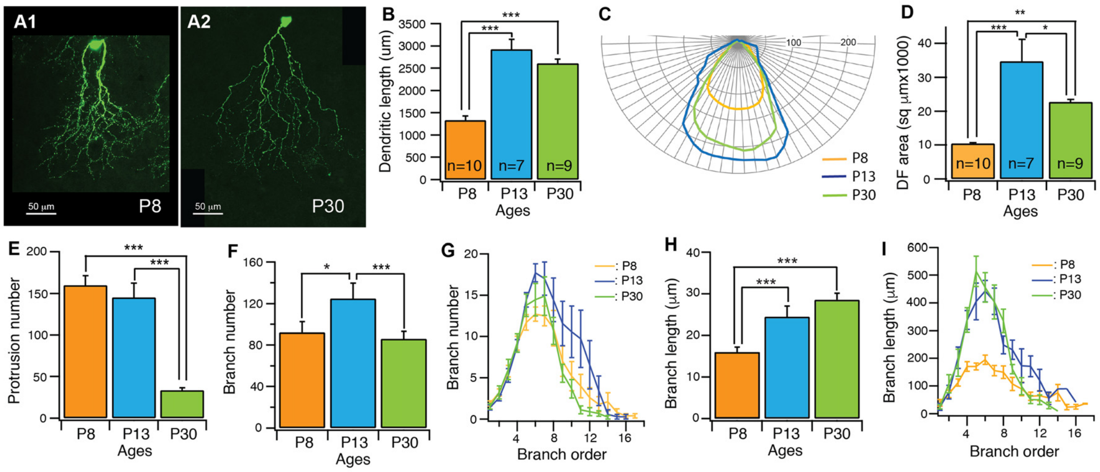

FIGURE 3 | The dendritic pattern of J-RGCs is developmentally refined. The dendritic patterns of J-RGCs were quantitatively analyzed from three groups of JamB-CreER:Thy1-YFP mice at the ages of P8 (3 mice, 10 cells), P13 (2 mice, 7 cells) and P30 (3 mice, 9 cells), respectively. **(A)** Maximum projections of confocal images of J-RGCs from a P8 mouse **(A1)** and a P30 mouse **(A2)**. **(B)** The average total length of dendrites of J-RGCs of the three age groups. **(C)** The average polar plots of the dendritic field (DF) of the J-RGCs of three age groups shown in **(B)**. These average polar plots were calculated by aligning the polar plots of individual J-RGCs based on the soma and the peak of the polar plots. **(D)** The average size of DF of J-RGCs of three age groups shown in **(B)**. **(E)** The average number of dendritic protrusions of J-RGCs of the same three age groups. **(F)** The average number of dendritic branches of the three groups of J-RGCs. **(G)** The plot of the average number of dendritic branch as a function of branch order of the three groups of J-RGCs. **(H)** The average length of dendritic branches of J-RGCs of the three groups. **(I)** The plot of dendritic branch length as a function of branch order of the three groups of J-RGCs. *$P < 0.05$; **$P < 0.01$; and ***$P < 0.001$.

expression of YFP in J-RGCs is selectively activated in the mutant J-RGCs. We activated the NR1 knockout and YFP expression in J-RGCs at the ages of P1–3 and examined the dendrites of J-RGCs at the ages of P13 and P30, respectively.

Our results showed that selective knocking out of NR1 on J-RGCs reduces the expansion of the size of the dendritic field, the dendritic elongation and the number of dendritic protrusions before eye opening (**Figure 5A**). Quantitatively, the size of the dendritic field of Grin1$^{flox/flox}$ J-RGCs at P13 was reduced by 46% in comparison with the age-matched controls (34733.7 $\mu m^2 \pm 6489.83\ \mu m^2$ vs. 18875.2 $\mu m^2 \pm 2229.08\ \mu m^2$, $p = 0.0002$; **Figures 5C,D**). The reduction of the size of the dendritic field is associated with a 17% shorter in the total dendritic length of Grin1$^{flox/flox}$ J-RGCs (2417.3 $\mu m \pm 130.5\ \mu m$ vs. 2919.6 $\mu m \pm 229.4\ \mu m$ for Grin1$^{flox/flox}$ and Grin1+/+ J-RGCs, respectively; $p = 0.0158$; **Figure 5G**) and a 41% increase of the dendritic protrusions (204.6 ± 10.8 vs. 145 ± 17.4 for Grin1$^{flox/flox}$ and Grin1+/+ J-RGCs, respectively, $p = 0.0046$; **Figure 5J**). These results are similar to those seen following the intraocular injection of CNQX+AP5 (**Figure 4**) and our previous study (Xu et al., 2010).

However, the size of the dendritic field of Grin1$^{flox/flox}$ J-RGCs at P30 was not smaller but 27% bigger than that of age-matched controls (28953.9 $\mu m^2 \pm 2088.1\ \mu m^2$ vs. 22712.3 $\mu m^2 \pm 772.3\ \mu m^2$, $p = 0.0167$; **Figures 5B,E,F**) accompanied by a slight increase in the number of dendritic protrusions (24%, **Figure 5J**) without a significant difference in the total dendritic length (**Figure 5G**). On the other hand, the defects in the size of the dendritic field and dendritic elongation of the Grin1$^{flox/flox}$ J-RGCs are not associated with a significant defect of dendritic branching (**Figures 5H,I**). Together these results show that NMDARs are required for the development of J-RGC dendrites, especially before eye opening.

Potential Interplay of Visual Stimulation and NMDAR Activity on the Development of J-RGC Dendrites

Light stimulation has been shown to regulate the dendritic development of RGCs (Fisher, 1979; Wingate and Thompson, 1994; Sernagor and Grzywacz, 1996; Tian and Copenhagen, 2001, 2003; Xu and Tian, 2007; Tian, 2008; Akimov and Rentería, 2014) as well as the expression and activity of NMDARs on RGCs (Fox et al., 1991; Carmignoto and Vicini, 1992; Xue and Cooper, 2001; Guenther et al., 2004). We then investigated the potential interplay between light stimulation and the activity of NMDARs on the development of the dendrites of J-RGCs. We reared JamB-CreER:Thy1-YFP:Grin1$^{flox/flox}$ and JamB-CreER:Thy1-YFP:Grin1+/+ (WT) mice in constant darkness from birth to P30 and examined the dendrites of J-RGCs in these two strains of mice. Our results showed that dark rearing increases the sizes of the dendritic field of Grin1+/+ J-RGCs by 23% in comparison with their age- and genetic-matched controls (22712.3 $\mu m^2 \pm 772.3\ \mu m^2$ vs. 27852 $\mu m^2 \pm 1122.3\ \mu m^2$ for mice raised under cyclic light/dark conditions and constant darkness, $p = 0.0017$; **Figures 6A–C**) but has no effect on the sizes of the dendritic fields of JamB-CreER:Thy1-YFP:Grin1$^{flox/flox}$ mice (28953.9 $\mu m^2 \pm 2088.1\ \mu m^2$ vs. 33055.9 $\mu m^2 \pm 2450.4\ \mu m^2$ for mice raised under cyclic light/dark conditions and constant darkness, $p = 0.2192$; **Figure 6C**). Therefore, mutation of NMDARs alone increases the sizes of the dendritic fields to a similar size of dark reared

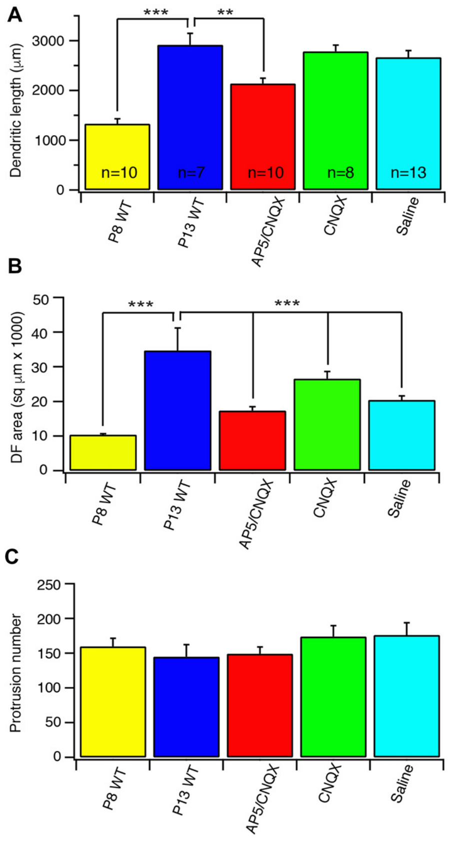

FIGURE 4 | Blockage of glutamate receptor activity retarded the developmental refinement of J-RGC dendrites. The dendritic pattern of J-RGCs was quantitatively analyzed at the age of P13 of JamB-CreER:Thy1-YFP mice with intraocular injection of CNQX or PA5+CNQX for 4 days from P9 to P12. The results were compared with that of JamB-CreER:Thy1-YFP mice at the ages of P8 (P8 wild type (WT): 3 mice, 10 cells) and P13 (P13 WT: 2 mice, 7 cells) without injection and the mice with 4 days intraocular injection of saline. **(A)** The average total dendritic length of J-RGCs at ages of P8 (P8 WT), P13 (P13 WT), P13 mice treated with intraocular injection of CNQX (CNQX: 3 mice, 8 cells), CNQX+AP5 (AP5/CNQX: 3 mice, 10 cells) or saline (Saline: 3 mice, 13 cells). **(B)** The average sizes of DF of J-RGCs of the same five groups of mice as shown in **(A)**. **(C)** The average number of dendritic protrusions of J-RGCs of the same five groups of mice as shown in **(A)**. *$P < 0.05$; **$P < 0.01$; and ***$P < 0.001$.

Grin1+/+ J-RGCs while dark rearing of JamB-CreER:Thy1-YFP:Grin1$^{\text{flox/flox}}$ mice has no additional effect.

In addition, the number of dendritic protrusions has been considered an indication of the activity of dendritic growth and synaptic formation. Additionally, neurons with less guided dendritic growth tends to have more dendritic protrusions (Munz et al., 2014). Consistently, the J-RGCs have large numbers of dendritic protrusions before eye opening (159.7 ± 11.7 and 145 ± 17.4 at P8 and P13, respectively) and the numbers of dendritic protrusions were reduced by 77% after eye opening (33.3 ± 2.9 at P30; **Figure 3E**). Dark reared JamB-CreER:Thy1-YFP:Grin1+/+ mice limited the developmental decrease in the number of dendritic protrusions. Therefore, the number of dendritic protrusions of dark reared Grin1+/+ J-RGCs is 2-fold higher than that of age-match controls raised under cyclic light conditions (33.3 ± 2.9 and 67.4 ± 6.6 for cyclic light and dark reared J-RGCs, respectively; $p < 0.0001$; **Figure 6D**). However, dark rearing has no additional effect on the number of dendritic protrusions of Grin1$^{\text{flox/flox}}$ J-RGCs (**Figure 6D**). Taken together with the observation that mutation of NMDAR on J-RGCs increased the number of dendritic protrusions at P13, these results imply that NMDARs might play different roles in the synaptic formation of J-RGCs before and after eye opening.

Furthermore, light deprivation had no significant effect on the dendritic length and the number of dendritic branches of both Grin1+/+ and Grin1$^{\text{flox/flox}}$ J-RGCs (data not shown). For the dendritic ramification in the IPL, J-RGCs of dark reared mice seem to ramify more dendrites in the outer IPL and reduced the density of dendrites in the inner IPL (**Figures 6E–G**). Overall, light deprivation seems to have specific effects on the developmental refinement of the size of the dendritic field and the number of dendritic protrusions. However, the effects of dark rearing on both of these two structural features are absent in J-RGCs with mutation of NMDARs.

DISCUSSION

In this study, we characterized the developmental profile of the dendrites of a genetically identified subtype of RGC, J-RGCs, and determined the roles of NMDARs and visual experience on the dendritic development of J-RGCs. Our results showed that the dendrites of J-RGCs undergo an orderly developmental process during postnatal ages. The dendritic ramification of J-RGCs in IPL reaches the adult pattern early during postnatal development, while other structural features of dendrites undergo substantial developmental refinement before and after eye opening. Before eye opening, the dendritic development of J-RGCs was characterized by a dramatic increase of dendritic length, the number of dendritic branches and the size of the dendritic field. Following eye opening, the dendritic refinement was characterized by a decrease in the number of dendritic protrusions and a consolidation of the size of the dendritic field. J-RGC specific mutation of NMDARs resulted in decreased dendrite growth, retarded dendritic field expansion and an increased number of dendritic protrusions before eye opening. Light deprivation of WT mice prevented the developmental decrease of the number of dendritic protrusions and the consolidation of dendritic field after eye opening. However, dark rearing of mice with J-RGC specific NMDAR mutation from birth has no effect in the number of dendritic protrusions and the size of the dendritic field. Taken together, these results at the first time revealed the roles of visual experience and NMDAR-mediated activity on the dendritic development of a specific subtype of RGCs.

RGC Dendritic Morphogenesis

Dendrites of neurons are specialized structures to receive and process synaptic inputs from other neurons and thus provide anatomic basis for their specific functions. The size and shape of dendritic arbors of neurons affect the number and type of synaptic inputs, as well as the wiring and

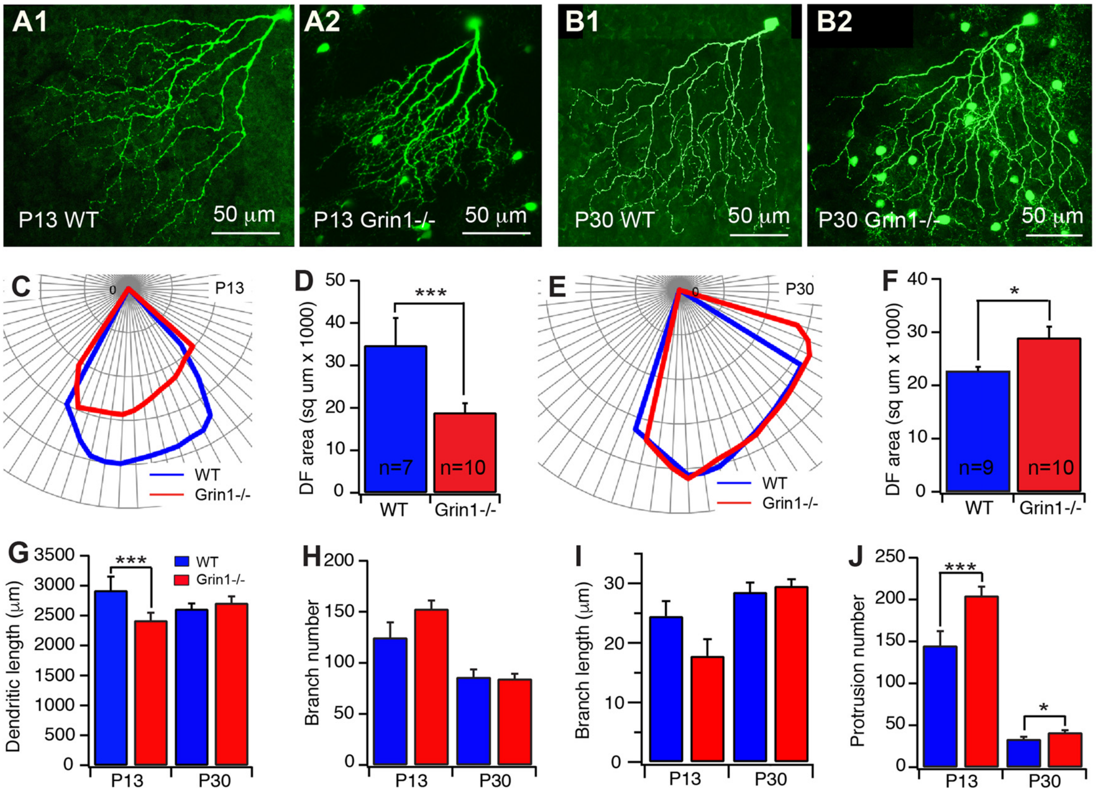

FIGURE 5 | Cell type specific mutation of N-methyl-D-aspartate receptor (NMDAR) retarded the developmental refinement of J-RGC dendrites. The dendritic patterns of J-RGCs were quantitatively analyzed at the ages of P13 and P30 of JamB-CreER:Thy1-YFP mice (WT) and JamB-CreER:Thy1-YFP:Grin1-/- mice (Grin1-/-). **(A)** Representative maximum projections of confocal images of J-RGCs from a P13 JamB-CreER:Thy1-YFP mouse **(A1)** and a P13 JamB-CreER:Thy1-YFP:Grin1-/- mouse **(A2)**. **(B)** Representative maximum projections of confocal images of J-RGCs from a P30 JamB-CreER:Thy1-YFP mouse **(B1)** and a P30 JamB-CreER:Thy1-YFP:Grin1-/- mouse **(B2)**. **(C)** The polar plots of the DFs of the J-RGCs shown in (**A1**; blue) and (**A2**; red). **(D)** The average sizes of DFs of J-RGCs of JamB-CreER:Thy1-YFP mice (2 mice, 7 cells) and JamB-CreER:Thy1-YFP:Grin1-/- mice (3 mice, 10 cells) at P13. **(E)** The polar plots of the DFs of the J-RGCs shown in panels B1 (blue) and B2 (red). **(F)** The average sizes of DFs of J-RGCs of JamB-CreER:Thy1-YFP mice (3 mice, 9 cells) and JamB-CreER:Thy1-YFP:Grin1-/- mice (3 mice, 10 cells) at P30. **(G)** The average total length of dendrites of J-RGCs of JamB-CreER:Thy1-YFP mice and JamB-CreER:Thy1-YFP:Grin1-/- mice at P13 and P30. **(H)** The average number of dendritic branches of J-RGCs of JamB-CreER:Thy1-YFP mice and JamB-CreER:Thy1-YFP:Grin1-/- mice at P13 and P30. **(I)** The average length of dendritic branches of J-RGCs of JamB-CreER:Thy1-YFP mice and JamB-CreER:Thy1-YFP:Grin1-/- mice at P13 and P30. **(J)** The average number of dendritic protrusions of J-RGCs of JamB-CreER:Thy1-YFP mice and JamB-CreER:Thy1-YFP:Grin1-/- mice at P13 and P30. *$P < 0.05$; **$P < 0.01$; and ***$P < 0.001$.

function of the synaptic circuits (Häusser et al., 2000; Parrish et al., 2007; Branco et al., 2010; Branco and Häusser, 2011; Gidon and Segev, 2012; Lavzin et al., 2012). J-RGCs are a unique population of RGCs in which dendritic architecture corresponds remarkably to their function (Kim et al., 2008, 2010). In adults, J-RGCs have a unique polarized dendritic field, which aligns in a dorsal-to-ventral direction across the retina. This polarized dendritic field is thought to be the determinative factor for their direction selective response to upward moving targets in the visual field (Kim et al., 2008, 2010), color opponent center-surround receptive field (Joesch and Meister, 2016) and orientation selectivity (Nath and Schwartz, 2017). However, how this uniquely polarized dendritic field is formed during development has not been fully characterized.

Dendrite morphogenesis is a complex but well-orchestrated process. Although individual neurons have unique developmental patterns of their dendrites, the critical steps in dendritic morphogenesis are similar for most CNS neurons. First, neurons must grow dendrites to form the dendritic field. In this stage, dendritic branches initially appear as filopodia-like dendritic protrusions and then morph into growth cone-like structures and extend to stable branches (Dailey and Smith, 1996). After the dendritic field reaches defined borders, the dendritic growth is restrained and the dendritic arbors are modified via pruning of excessive and inappropriate dendritic branches (Wässle et al., 1981; Gao et al., 1999; Puram and Bonni, 2013).

Developmentally, J-RGCs undergo significant refinement of their dendritic ramification in the IPL postnatally. J-RGCs ramify their dendrites throughout the entire IPL before P5 and then gradually eliminate their dendrites in the inner IPL and expand their dendrites in the outer portion of the IPL. By P12, they acquire adult pattern of dendritic ramification

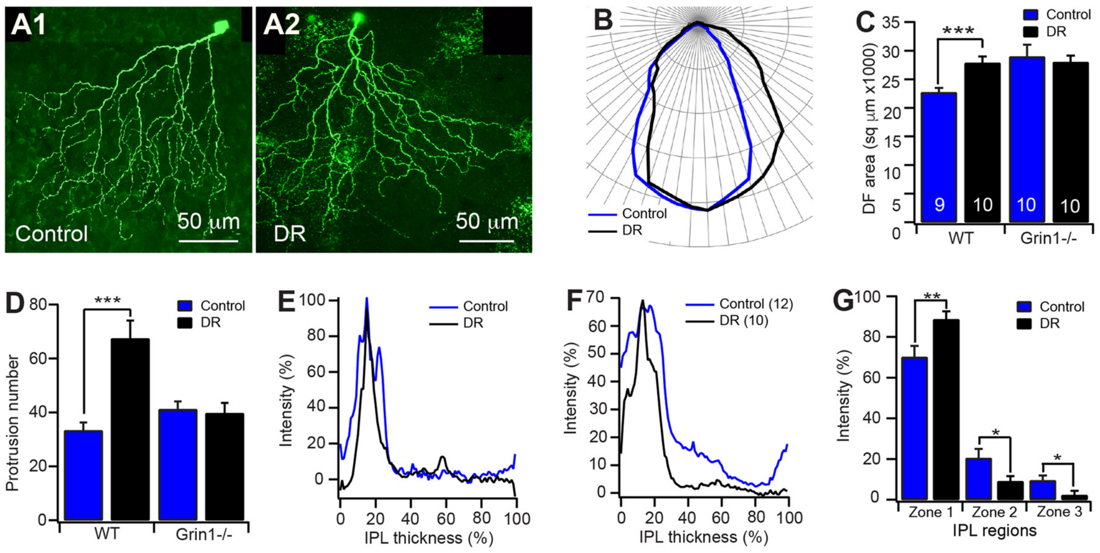

FIGURE 6 | Potential interplay of visual stimulation and NMDAR activity on the development of J-RGC dendrites. The dendritic pattern of J-RGCs of JamB-CreER:Thy1-YFP:Grin1-/- (Grin1-/-) and JamB-CreER:Thy1-YFP (WT) mice raised in constant darkness from birth to P30 was quantitatively analyzed. The results were compared with that of age and genetic background matched mice raised under cyclic light/dark conditions. **(A)** Representative maximum projections of confocal images of J-RGCs of P30 JamB-CreER:Thy1-YFP mice raised under cyclic light/dark conditions **(A1)** and constant darkness from birth **(A2)**. **(B)** The average polar plots of the DFs of the J-RGCs of JamB-CreER:Thy1-YFP mice (3 mice, 9 cells) raised under cyclic light/dark conditions (blue) and constant darkness (black, 3 mice, 10 cells). **(C)** The average sizes of DFs of J-RGCs of JamB-CreER:Thy1-YFP (WT) and JamB-CreER:Thy1-YFP:Grin1-/- (Grin1-/-, 3 mice, 10 cells for both control and DR) mice raised under cyclic light/dark conditions (control) and in constant darkness (DR). **(D)** The average number of dendritic protrusions of J-RGCs of JamB-CreER:Thy1-YFP and JamB-CreER:Thy1-YFP:Grin1-/- mice raised under cyclic light/dark conditions and in constant darkness. **(E)** Representative dendritic density distribution curves as a function of the IPL depth of J-RGCs of JamB-CreER:Thy1-YFP mice raised under cyclic light/dark conditions and in constant darkness. **(F)** Average dendritic density profile as a function of the IPL depth of J-RGCs of JamB-CreER:Thy1-YFP mice raised under cyclic light/dark conditions and in constant darkness. **(G)** The average dendritic density distribution of the J-RGCs in three IPL zones of JamB-CreER:Thy1-YFP mice raised under cyclic light/dark conditions and in constant darkness. $^*P < 0.05$; $^{**}P < 0.01$; and $^{***}P < 0.001$.

in the IPL (Kim et al., 2010). Our results confirmed this developmental refinement of dendritic ramification of J-RGCs in the IPL. However, other structural features of the dendrites of J-RGCs undergo prolonged developmental refinement similar to the common theme of dendritic morphogenesis of CNS neurons (Wässle et al., 1981; Dailey and Smith, 1996; Gao et al., 1999; Puram and Bonni, 2013). The early dendritic elongation, branching and dendritic field expansion occur before eye opening. Consistent with the high dynamic dendritic activity, many filopodia-like dendritic protrusions studded on the dendrites of J-RGCs during this period. After eye opening, J-RGCs completely cease the dendritic growth and branching. In addition, J-RGCs modify their dendritic field by pruning a significant number of terminal dendrites. With the increased visual activity, the number of dendritic protrusions is dramatically reduced after eye opening, consistent with the final step of the common scheme of dendritic morphogenesis (Orner et al., 2014; Puram and Bonni, 2013).

NMDARs and RGC Dendritic Morphogenesis

It is well documented that spontaneous synaptic activity before eye opening is critical for the normal development of RGC dendrites. In early developing vertebrate retinas, RGCs fire periodic bursts of action potentials that are highly correlated and propagate across the RGC layer in a wave-like fashion (Wong, 1999). These spontaneous retina waves are mainly mediated by excitatory neurotransmission with a developmental shift from cholinergic to glutamatergic synaptic transmission (Wong, 1999; Wong et al., 2000). Within the first postnatal week of mice, retinal waves are only mediated by nicotinic acetylcholine receptors (nAChRs). Starting from the middle of the second postnatal week, retinal waves are mediated solely by GluRs (Feller et al., 1996; Bansal et al., 2000; Zhou, 2001; Demas et al., 2003; Feller and Blankenship, 2008). The spontaneous activities mediated by both nAChRs and GluRs are thought to regulate RGC dendritic development (Wong et al., 2000; Wong and Ghosh, 2002). In the retina of turtle hatchlings, chronic blockade of nAChR-mediated retinal waves with curare reduces RGC receptive fields (Sernagor and Grzywacz, 1996). In mice, genetic deletion of β2 subunits of nAChR eliminates the retinal waves mediated by nAChRs during the first postnatal week and disturbs RGC dendritic stratification during early postnatal age (Bansal et al., 2000). However, genetic deletion of ChAT eliminates the retinal waves mediated by AChRs before P5 and reduces the size of the dendritic field of ON arbor of large-field bistratified RGCs at P7–8 but does not significantly affect the OFF arbor and the size of the dendritic filed of large-field monostratified RGCs (Stacy et al., 2005).

The roles of GluR-mediated retinal waves on the development of RGC dendrites are also controversial. It has been shown that intraocular injection of APB during early postnatal ages arrests the developmental stratification and segregation of RGC dendrites in the IPL (Bodnarenko and Chalupa, 1993; Bodnarenko et al., 1995, 1999; Deplano et al., 2004). Pharmacological blockade of GluR activity by intraocular injection of AP5 and NBQX between P10–13 reduces the kinetics of RGC dendritic growth/elimination and increases the dendritic density (Xu et al., 2010). On the other hand, blockade of glutamate release from ON bipolar cells by expressing tetanus toxin (TeNT) in ON bipolar cells has no impact on the dendritic morphology of RGCs at P21, supporting the argument that glutamatergic synaptic activity does not regulate dendritic morphology of RGCs (Kerschensteiner et al., 2009). In addition, genetic deletion of the mGluR6 receptor, which blocks light evoked synaptic activity and depolarizes the membrane potential of ON bipolar cell, fails to impair dendritic stratification of mouse RGCs (Tagawa et al., 1999). There is no consistent interpretation why pharmacological blockade of GluR-mediated activity causes significant dendritic defects of RGCs while genetic inhibition of glutamate release from bipolar cells has no effect on RGC dendrites. Our current study demonstrated that cell specific mutation of NMDAR has significant effects on dendritic morphology of J-RGCs at P13, which is similar to the effects induced by intraocular injection of AP5+CNQX, but much weaker effects on the J-RGCs at P30, indicating an age-dependent mechanism.

In the CNS, synaptic activity mediated by glutamate receptors, particularly NMDARs, of newly established synapses are thought to stabilize the dendritic filopodia and promote them to grow into dendritic branches (Niell et al., 2004). Consistently, pharmacologically or genetically inactivation of NMDARs blocks the elaboration of dendrites of optic tectal neurons (Rajan and Cline, 1998), motor neurons (Inglis et al., 1998; Hebbeler et al., 2002) and barrelette cells (Datwani et al., 2002; Lee et al., 2005), reduces the dendritic pruning of dentate gyrus granule cells (Espinosa et al., 2009) and retards the segregation of whisker afferents (Datwani et al., 2002; Lee et al., 2005), and barrel cortex spiny stellate cells (Espinosa et al., 2009). NMDAR-mediated activity could regulate the dendritic development of RGCs because all RGCs express NMDARs (Guenther et al., 2004) on their dendrites (Fletcher et al., 2000; Pourcho et al., 2001; Zhang and Diamond, 2009) and activation of NMDARs regulates the light responses and AMPAR plasticity of RGCs (Zhang and Diamond, 2009; Jones et al., 2012; Stafford et al., 2014). Similar to the optic tectal neurons, barrelette cells and whisker afferents in mice (Rajan and Cline, 1998; Datwani et al., 2002; Lee et al., 2005), we found that inactivation of NMDARs blocks the developmental dendritic elongation and the expansion of the dendritic field of J-RGCs before eye opening.

The axonal filopodia is an important factor to evaluate the activity of axonal morphogenesis and synaptic formation of neurons. In zebrafish larvae, silenced axons of RGCs form more highly dynamic but short-lived filopodia in NMDAR-dependent manner (Ben Fredj et al., 2010). In the optic tectum of *Xenopus laevis*, RGCs with asynchronized stimulation have more new branches, while RGCs with synchronized stimulation have fewer new but more stable branches in a NMDAR-dependent manner (Munz et al., 2014). Similarly, blockade of the activity of glutamate receptors pharmacologically lead to a significant increase in the density of dendritic protrusions of mouse RGCs (Xu et al., 2010). J-RGCs also show a high number of dendritic protrusions when the cells are in the stage of rapid dendritic growth and dendritic field expansion before eye opening. With the stabilization of dendritic growth after eye opening, the number of dendritic protrusions decreases to a low level, indicating that, similar to axonal filopodia of RGCs, the number of dendritic protrusions is an important factor to evaluate the activity of dendritic morphogenesis. This activity-dependent change of the number of dendritic protrusions is very likely regulated by NMDARs in a cell autonomous manner on J-RGCs because mutation of NMDARs specifically on J-RGCs increases the number of dendritic protrusions during early postnatal development. Because the activity mediated by NMDARs on filopodia is thought to stabilize the newly formed filopodia and promote synaptic formation (Niell et al., 2004; Lohmann et al., 2005), it is important to further investigate whether the synaptic circuit connected to J-RGCs and the synaptic function of J-RGCs is also regulated by the NMDAR-mediated activity. Our recent experimental results provided strong evidence to support the notion that cell-specific mutation of NMDAR on J-RGCs alters the types of bipolar cell inputs to J-RGCs (Young et al., 2018).

Visual Experience and RGC Dendritic Morphogenesis

Visual experience has been shown to regulate the development of both the dendritic architecture and synaptic function of RGCs (Tian, 2008). Light deprivation increases the density of conventional synapses in the IPL (Fisher, 1979), blocks an age-dependent remodeling of dendritic complexity of RGCs (Wingate and Thompson, 1994), retards the developmental dendritic ramification of OFF RGCs in the IPL (Tian and Copenhagen, 2003; Xu and Tian, 2007), enlarges the diameter of the dendritic field and increases the number of dendritic branches of RGCs (Sernagor and Grzywacz, 1996). Functionally, light deprivation slows down a developmental increase of spontaneous synaptic activity of RGCs (Tian and Copenhagen, 2001), retards the functional segregation of ON and OFF inputs to RGCs (Tian and Copenhagen, 2003) as well as the segregation of outputs from RGCs to dLGN neurons (Akerman et al., 2002), and reduces the size of the receptive field of RGCs (Akimov and Rentería, 2014). In addition, light deprivation decreases the levels of NR2A expression in visual cortex and the retina (Nase et al., 1999; Xue and Cooper, 2001), delays an age-dependent decline of NMDAR-mediated response of RGCs (Fox et al., 1991; Carmignoto and Vicini, 1992; Guenther et al., 2004), and prolongs NMDAR-mediated responses in the LGN of ferrets (Ramoa and Prusky, 1997). However, it is still debatable whether visual experience is required for all RGC subtypes to form normal dendritic patterns and sensory maps. A recent report shows that the spacing and the overlap of RGC receptive fields at the time of eye opening were similar to those in adult rats, indicating visual experience has little impact on the development of RGC sensory maps (Anishchenko et al., 2010).

Our results show that dark rearing retards the developmental consolidation of the size of the dendritic field of J-RGCs after eye opening, which is similar to that of the RGCs of turtle retina (Sernagor and Grzywacz, 1996) but opposite to the measurements of the size of the receptive fields of RGCs of mouse retina (Akimov and Rentería, 2014). In addition, J-RGCs of dark reared mice have increased number of dendritic protrusions. Because light deprivation reduces the strength of glutamatergic synaptic activity of RGCs (Tian and Copenhagen, 2001) and pharmacologically blockade of glutamate receptor activity increases the density of dendritic protrusions of mouse RGCs (Xu et al., 2010), the increase of the number of dendritic protrusions on J-RGCs of dark reared mice is likely the results of reduced glutamatergic synaptic activity of J-RGCs. In contrast to previous reports that dark rearing retards the developmental dendritic stratification of OFF RGCs in the outer portion of the IPL (Tian and Copenhagen, 2003; Xu and Tian, 2007), J-RGCs from dark reared mice seem to have narrowly stratified dendrites in the outer IPL. Furthermore, light deprivation has no significant effect on the dendritic length and the number of dendritic branches of J-RGCs, which are also opposite to the effects induced by light deprivation on the RGCs of turtles and hamsters (Wingate and Thompson, 1994; Sernagor and Grzywacz, 1996). All together, these results suggest that visual experience and/or GluR-mediated synaptic activity could be required for the development of the dendritic architecture and sensory maps of RGCs in a subtype specific manner, which is similar to the effects of genetic deletion of ChAT on the dendritic arbors of large-field bistratified and large-field monostratified RGCs (Stacy et al., 2005).

Although both visual experience and NMDAR-mediated activity are required for the dendritic development of RGCs and the strength of glutamatergic synaptic activity of RGCs is regulated by visual stimulation, it is unclear whether visual experience regulates the dendritic development of J-RGCs through NMDAR-mediated activity. In consistent with the idea that visual stimulation promotes the consolidation of the dendritic field of J-RGCs through NMDARs after eye opening, J-RGCs with NMDAR mutation have an increased dendritic field size similar to that of NMDAR-expressing J-RGCs raised in constant darkness while dark rearing of mice with J-RGC specific mutation of NMDARs has no additional effect on the size of dendritic field. In addition, light deprivation significantly increased the number of dendritic protrusions of NMDAR-expressing J-RGCs but not J-RGCs with the NMDAR mutation, further supporting the possibility that light stimulation might regulate the dendritic morphogenesis of J-RGCs through NMDARs as that of RGC axonal morphogenesis (Ben Fredj et al., 2010; Munz et al., 2014). Regardless what are the underlying mechanisms, defects of dendritic structure indicate potential impairments in synaptic connected of J-RGCs. Therefore, the significance of the structural defects of J-RGC dendrites to the physiology of these cells needs to be further investigated.

AUTHOR CONTRIBUTIONS

EE and NY: data collection, data analysis. PW: animal preparation, resource management. NT: experimental design, data analysis, manuscript preparation, research fund management.

FUNDING

This work was supported by the National Eye Institute (R01EY012345, EY014800), Department Veterans Affair (1 I01BX002412-01A2) and Research to Prevent Blindness.

ACKNOWLEDGMENTS

We thank Dr. Joshua Sanes at Harvard University for the contribution to the JamB-CreER and Thy1-Stop-YFP mice for this study. We also like to thank Mr. Brent K. Young for his assistance in the manuscript preparation.

SUPPLEMENTARY MATERIAL

The Supplementary Material for this article can be found online at: https://www.frontiersin.org/articles/10.3389/fncel.2018.00249/full#supplementary-material

FIGURE S1 | The size of the dendritic field of J-RGCs increases with eccentricity. The dendritic field size of each J-RGC was quantified and correlated to the distance of the soma to the optic nerve head. **(A)** A representative image of a maximum projection of confocal image of a flat-mounted whole retina of a P60 JamB-CreER:Thy1-YFP mouse. The circles of white dotted line indicate distance of eccentricity of 500 μm, 1000 μm and 1500 μm from the optic nerve head. **(B)** The scatter plot of the DF size of J-RGCs as a function of the distance of eccentricity of 80 J-RGCs (2 mice, 3 retinas). **(C)** The average DF size of J-RGCs grouped based on their eccentricity distance. $^{*}P < 0.05$; $^{**}P < 0.01$; and $^{***}P < 0.001$.

REFERENCES

Akerman, C. J., Smyth, D., and Thompson, I. D. (2002). Visual experience before eye opening and the development of the retinogeniculate pathway. *Neuron* 36, 869–879. doi: 10.1016/s0896-6273(02)01010-3

Akimov, N. P., and Rentería, R. C. (2014). Dark rearing alters the normal development of spatiotemporal response properties but not of contrast detection threshold in mouse retinal ganglion cells. *Dev. Neurobiol.* 74, 692–706. doi: 10.1002/dneu.22164

Anishchenko, A., Greschner, M., Elstrott, J., Sher, A., Litke, A. M., Feller, M. B., et al. (2010). Receptive field mosaics of retinal ganglion cells are established without visual experience. *J. Neurophysiol.* 103, 1856–1864. doi: 10.1152/jn.00896.2009

Badea, T. C., and Nathans, J. (2004). Quantitative analysis of neuronal morphologies in the mouse retina visualized by using a genetically directed reporter. *J. Comp. Neurol.* 480, 331–351. doi: 10.1002/cne.20304

Baden, T., Berens, P., Bethge, M., and Euler, T. (2013). Spikes in mammalian bipolar cells support temporal layering of the inner retina. *Curr. Biol.* 23, 48–52. doi: 10.1016/j.cub.2012.11.006

Bansal, A., Singer, J. H., Hwang, B. J., Xu, W., Beaudet, A., and Feller, M. B. (2000). Mice lacking specific nicotinic acetylcholine receptor subunits exhibit dramatically altered spontaneous activity patterns and reveal a limited role for retinal waves in forming ON and OFF circuits in the inner retina. *J. Neurosci.* 20, 7672–7681. doi: 10.1523/JNEUROSCI.20-20-07672.2000

Ben Fredj, N., Hammond, S., Otsuna, H., Chien, C. B., Burrone, J., and Meyer, M. P. (2010). Synaptic activity and activity-dependent competition regulates axon arbor maturation, growth arrest and territory in the retinotectal projection. *J. Neurosci.* 30, 10939–10951. doi: 10.1523/JNEUROSCI.1556-10.2010

Berson, D. M. (2008). "Retinal ganglion cell types and their central projections," in *The Senses: A Comprehensive Reference*, (Vol. 1) eds A. I. Basbaum, A. Kaneko, G. M. Shepherd and G. Westheimer (San Diego: Academic Press), 491–520.

Bodnarenko, S. R., and Chalupa, L. M. (1993). Stratification of ON and OFF ganglion cell dendrites depends on glutamate-mediated afferent activity in the developing retina. *Nature* 364, 144–146. doi: 10.1038/364144a0

Bodnarenko, S. R., Jeyarasasingam, G., and Chalupa, L. M. (1995). Development and regulation of dendritic stratification in retinal ganglion cells by glutamate-mediated afferent activity. *J. Neurosci.* 15, 7037–7045. doi: 10.1523/JNEUROSCI.15-11-07037.1995

Bodnarenko, S. R., Yeung, G., Thomas, L., and McCarthy, M. (1999). The development of retinal ganglion cell dendritic stratification in ferrets. *Neuroreport* 10, 2955–2959. doi: 10.1097/00001756-199909290-00015

Branco, T., Clark, B. A., and Häusser, M. (2010). Dendritic discrimination of temporal input sequences in cortical neurons. *Science* 329, 1671–1675. doi: 10.1126/science.1189664

Branco, T., and Häusser, M. (2011). Synaptic integration gradients in single cortical pyramidal cell dendrites. *Neuron* 69, 885–892. doi: 10.1016/j.neuron.2011.02.006

Briggman, K. L., and Euler, T. (2011). Bulk electroporation and population calcium imaging in the adult mammalian retina. *J. Neurophysiol.* 105, 2601–2609. doi: 10.1152/jn.00722.2010

Briggman, K. L., Helmstaedter, M., and Denk, W. (2011). Wiring specificity in the direction-selectivity circuit of the retina. *Nature* 471, 183–188. doi: 10.1038/nature09818

Carmignoto, G., and Vicini, S. (1992). Activity-dependent decrease in NMDA receptor responses during development of the visual cortex. *Science* 258, 1007–1011. doi: 10.1126/science.1279803

Chang, Y. C., Chen, C. Y., and Chiao, C. C. (2010). Visual experience-independent functional expression of NMDA receptors in the developing rabbit retina. *Invest. Ophthalmol. Vis. Sci.* 51, 2744–2754. doi: 10.1167/iovs.09-4217

Cline, H., and Haas, K. (2008). The regulation of dendritic arbor development and plasticity by glutamatergic synaptic input: a review of the synaptotrophic hypothesis. *J. Physiol.* 586, 1509–1517. doi: 10.1113/jphysiol.2007.150029

Coombs, J. L., Van Der List, D., and Chalupa, L. M. (2007). Morphological properties of mouse retinal ganglion cells during postnatal development. *J. Comp. Neurol.* 503, 803–814. doi: 10.1002/cne.21429

Dailey, M. E., and Smith, S. J. (1996). The dynamics of dendritic structure in developing hippocampal slices. *J. Neurosci.* 16, 2983–2994. doi: 10.1523/JNEUROSCI.16-09-02983.1996

Datwani, A., Iwasato, T., Itohara, S., and Erzurumlu, R. S. (2002). NMDA receptor-dependent pattern transfer from afferents to postsynaptic cells and dendritic differentiation in the barrel cortex. *Mol. Cell. Neurosci.* 21, 477–492. doi: 10.1006/mcne.2002.1195

Demas, J., Eglen, S. J., and Wong, R. O. (2003). Developmental loss of synchronous spontaneous activity in the mouse retina is independent of visual experience. *J. Neurosci.* 23, 2851–2860. doi: 10.1523/JNEUROSCI.23-07-02851.2003

Deplano, S., Gargini, C., Maccarone, R., Chalupa, L. M., and Bisti, S. (2004). Long-term treatment of the developing retina with the metabotropic glutamate agonist APB induces long-term changes in the stratification of retinal ganglion cell dendrites. *Dev. Neurosci.* 26, 396–405. doi: 10.1159/000082282

Espinosa, J. S., Wheeler, D. G., Tsien, R. W., and Luo, L. (2009). Uncoupling dendrite growth and patterning: single-cell knockout analysis of NMDA receptor 2B. *Neuron* 62, 205–217. doi: 10.1016/j.neuron.2009.03.006

Feller, M. B., and Blankenship, A. G. (2008). "The function of the retine prior to vision: the phenomenon of retinal waves and retinotopic refinement," in *Eye, Retina, and Visual System of the Mouse*, ed. D. C. Chalupa (Cambridge, MA: MIT Press), 343–351.

Feller, M. B., Wellis, D. P., Stellwagen, D., Werblin, F. S., and Shatz, C. J. (1996). Requirement for cholinergic synaptic transmission in the propagation of spontaneous retinal waves. *Science* 272, 1182–1187. doi: 10.1126/science.272.5265.1182

Fisher, L. J. (1979). Development of retinal synaptic arrays in the inner plexiform layer of dark-reared mice. *J. Embryol. Exp. Morphol.* 54, 219–227.

Fletcher, E. L., Hack, I., Brandstätter, J. H., and Wässle, H. (2000). Synaptic localization of NMDA receptor subunits in the rat retina. *J. Comp. Neurol.* 420, 98–112. doi: 10.1002/(sici)1096-9861(20000424)420:1<98::aid-cne7>3.3.co;2-l

Fox, K., Daw, N., Sato, H., and Czepita, D. (1991). Dark-rearing delays the loss of NMDA-receptor function in kitten visual cortex. *Nature* 350, 342–344. doi: 10.1038/350342a0

Gao, F. B., Brenman, J. E., Jan, L. Y., and Jan, Y. N. (1999). Genes regulating dendritic outgrowth, branching and routing in Drosophila. *Genes Dev.* 13, 2549–2561. doi: 10.1101/gad.13.19.2549

Gidon, A., and Segev, I. (2012). Principles governing the operation of synaptic inhibition in dendrites. *Neuron* 75, 330–341. doi: 10.1016/j.neuron.2012.05.015

Guenther, E., Schmid, S., Wheeler-Schilling, T., Albach, G., Gründer, T., Fauser, S., et al. (2004). Developmental plasticity of NMDA receptor function in the retina and the influence of light. *FASEB J.* 18, 1433–1435. doi: 10.1096/fj.03-0618fje

Häusser, M., Spruston, N., and Stuart, G. J. (2000). Diversity and dynamics of dendritic signaling. *Science* 290, 739–744. doi: 10.1126/science.290.5492.739

Hebbeler, S. L., Verhovshek, T., and Sengelaub, D. R. (2002). N-methyl-D-aspartate receptor blockade inhibits estrogenic support of dendritic growth in a sexually dimorphic rat spinal nucleus. *J. Comp. Neurol.* 451, 142–152. doi: 10.1002/cne.10347

Huang, Z., Zang, K., and Reichardt, L. F. (2005). The origin recognition core complex regulates dendrite and spine development in postmitotic neurons. *J. Cell Biol.* 170, 527–535. doi: 10.1083/jcb.200505075

Inglis, F. M., Furia, F., Zuckerman, K. E., Strittmatter, S. M., and Kalb, R. G. (1998). The role of nitric oxide and NMDA receptors in the development of motor neuron dendrites. *J. Neurosci.* 18, 10493–10501. doi: 10.1523/JNEUROSCI.18-24-10493.1998

Jan, Y. N., and Jan, L. Y. (2010). Branching out: mechanisms of dendritic arborization. *Nat. Rev. Neurosci.* 11, 316–328. doi: 10.1038/nrn2836

Joesch, M., and Meister, M. (2016). A neuronal circuit for colour vision based on rod-cone opponency. *Nature* 532, 236–239. doi: 10.1038/nature17158

Johnson, J., Tian, N., Caywood, M. S., Reimer, R. J., Edwards, R. H., and Copenhagen, D. R. (2003). Vesicular neurotransmitter transporter expression in developing postnatal rodent retina: GABA and glycine precede glutamate. *J. Neurosci.* 23, 518–529. doi: 10.1523/JNEUROSCI.23-02-00518.2003

Jones, R. S., Carroll, R. C., and Nawy, S. (2012). Light-induced plasticity of synaptic AMPA receptor composition in retinal ganglion cells. *Neuron* 75, 467–478. doi: 10.1016/j.neuron.2012.05.030

Kay, J. N., De la Huerta, I., Kim, I. J., Zhang, Y., Yamagata, M., Chu, M. W., et al. (2011). Retinal ganglion cells with distinct directional preferences differ in molecular identity, structure and central projections. *J. Neurosci.* 31, 7753–7762. doi: 10.1523/JNEUROSCI.0907-11.2011

Kerschensteiner, D., Morgan, J. L., Parker, E. D., Lewis, R. M., and Wong, R. O. (2009). Neurotransmission selectively regulates synapse formation in parallel circuits *in vivo*. *Nature* 460, 1016–1020. doi: 10.1038/nature08236

Kim, I. J., Zhang, Y., Meister, M., and Sanes, J. R. (2010). Laminar restriction of retinal ganglion cell dendrites and axons: subtype-specific developmental patterns revealed with transgenic markers. *J. Neurosci.* 30, 1452–1462. doi: 10.1523/JNEUROSCI.4779-09.2010

Kim, I. J., Zhang, Y., Yamagata, M., Meister, M., and Sanes, J. R. (2008). Molecular identification of a retinal cell type that responds to upward motion. *Nature* 452, 478–482. doi: 10.1038/nature06739

Lavzin, M., Rapoport, S., Polsky, A., Garion, L., and Schiller, J. (2012). Nonlinear dendritic processing determines angular tuning of barrel cortex neurons *in vivo*. *Nature* 490, 397–401. doi: 10.1038/nature11451

Lee, L. J., Lo, F. S., and Erzurumlu, R. S. (2005). NMDA receptor-dependent regulation of axonal and dendritic branching. *J. Neurosci.* 25, 2304–2311. doi: 10.1523/JNEUROSCI.4902-04.2005

Lèvai, O., and Strotmann, J. (2003). Projection pattern of nerve fibers from the septal organ: DiI-tracing studies with transgenic OMP mice. *Histochem. Cell Biol.* 120, 483–492. doi: 10.1007/s00418-003-0594-4

Lohmann, C., Finski, A., and Bonhoeffer, T. (2005). Local calcium transients regulate the spontaneous motility of dendritic filopodia. *Nat Neurosci* 8, 305–312. doi: 10.1038/nn1406

Masland, R. H. (2001). The fundamental plan of the retina. *Nat. Neurosci.* 4, 877–886. doi: 10.1038/nn0901-877

McAllister, A. K. (2000). Cellular and molecular mechanisms of dendrite growth. *Cereb. Cortex* 10, 963–973. doi: 10.1093/cercor/10.10.963

Munz, M., Gobert, D., Schohl, A., Poquérusse, J., Podgorski, K., Spratt, P., et al. (2014). Rapid Hebbian axonal remodeling mediated by visual stimulation. *Science* 344, 904–909. doi: 10.1126/science.1251593

Nase, G., Weishaupt, J., Stern, P., Singer, W., and Mpnyer, H. (1999). Genetic and epigenetic regulation of NMDA receptor expression in the rat visual cortex. *Eur. J. Neurosci.* 11, 4320–4326. doi: 10.1046/j.1460-9568.1999.00859.x

Nath, A., and Schwartz, G. W. (2017). Electrical synapses convey orientation selectivity in the mouse retina. *Nat. Commun.* 8:2025. doi: 10.1038/s41467-017-01980-9

Niell, C. M., Meyer, M. P., and Smith, S. J. (2004). *in vivo* imaging of synapse formation on a growing dendritic arbor. *Nat. Neurosci.* 7, 254–260. doi: 10.1038/nn1191

Orner, D. A., Chen, C. C., Orner, D. E., and Brumberg, J. C. (2014). Alterations of dendritic protrusions over the first postnatal year of a mouse: an analysis in layer VI of the barrel cortex. *Brain Struct. Funct.* 219, 1709–1720. doi: 10.1007/s00429-013-0596-5

Overstreet-Wadiche, L. S., Bromberg, D. A., Bensen, A. L., and Westbrook, G. L. (2006). Seizures accelerate functional integration of adult-generated granule cells. *J. Neurosci.* 26, 4095–4103. doi: 10.1523/JNEUROSCI.5508-05.2006

Parrish, J. Z., Emoto, K., Kim, M. D., and Jan, Y. N. (2007). Mechanisms that regulate establishment, maintenance and remodeling of dendritic fields. *Annu. Rev. Neurosci.* 30, 399–423. doi: 10.1146/annurev.neuro.29.051605.112907

Pourcho, R. G., Qin, P., and Goebel, D. J. (2001). Cellular and subcellular distribution of NMDA receptor subunit NR2B in the retina. *J. Comp. Neurol.* 433, 75–85. doi: 10.1002/cne.1126

Puram, S. V., and Bonni, A. (2013). Cell-intrinsic drivers of dendrite morphogenesis. *Development* 140, 4657–4671. doi: 10.1242/dev.087676

Rajan, I., and Cline, H. T. (1998). Glutamate receptor activity is required for normal development of tectal cell dendrites *in vivo*. *J. Neurosci.* 18, 7836–7846. doi: 10.1523/JNEUROSCI.18-19-07836.1998

Ramoa, A. S., and Prusky, G. (1997). Retinal activity regulates developmental switches in functional properties and ifenprodil sensitivity of NMDA receptors in the lateral geniculate nucleus. *Dev. Brain Res.* 101, 165–175. doi: 10.1016/s0165-3806(97)00061-8

Roska, B., and Meister, M. (2014). "The retina dissects the visual scene in distinct features," in *The New Visual Neurosciences*, eds J. S. Werner and L. M. Chalupa (Cambridge, MA: MIT Press), 163–182.

Sanes, J. R., and Masland, R. H. (2015). The types of retinal ganglion cells: current status and implications for neuronal classification. *Annu. Rev. Neurosci.* 38, 221–246. doi: 10.1146/annurev-neuro-071714-034120

Sernagor, E., and Grzywacz, N. M. (1996). Influence of spontaneous activity and visual experience on developing retinal receptive fields. *Curr. Biol.* 6, 1503–1508. doi: 10.1016/s0960-9822(96)00755-5

Stacy, R. C., Demas, J., Burgess, R. W., Sanes, J. R., and Wong, R. O. (2005). Disruption and recovery of patterned retinal activity in the absence of acetylcholine. *J. Neurosci.* 25, 9347–9357. doi: 10.1523/JNEUROSCI.1800-05.2005

Stafford, B. K., Manookin, M. B., Singer, J. H., and Demb, J. B. (2014). NMDA and AMPA receptors contribute similarly to temporal processing in mammalian retinal ganglion cells. *J. Physiol.* 592, 4877–4889. doi: 10.1113/jphysiol.2014.276543

Sun, W., Li, N., and He, S. (2002). Large-scale morphological survey of mouse retinal ganglion cells. *J. Comp. Neurol.* 451, 115–126. doi: 10.1002/cne.10323

Tagawa, Y., Sawai, H., Ueda, Y., Tauchi, M., and Nakanishi, S. (1999). Immunohistological studies of metabotropic glutamate receptor subtype 6-deficient mice show no abnormality of retinal cell organization and ganglion cell maturation. *J. Neurosci.* 19, 2568–2579. doi: 10.1523/JNEUROSCI.19-07-02568.1999

Tian, N. (2008). Synaptic activity, visual experience and the maturation of retinal synaptic circuitry. *J. Physiol.* 586, 4347–4355. doi: 10.1113/jphysiol.2008.159202

Tian, N., and Copenhagen, D. R. (2001). Visual deprivation alters development of synaptic function in inner retina after eye opening. *Neuron* 32, 439–449. doi: 10.1016/s0896-6273(01)00470-6

Tian, N., and Copenhagen, D. R. (2003). Visual stimulation is required for refinement of ON and OFF pathways in postnatal retina. *Neuron* 39, 85–96. doi: 10.1016/s0896-6273(03)00389-1

Tsien, J. Z., Chen, D. F., Gerber, D., Tom, C., Mercer, E. H., Anderson, D. J., et al. (1996). Subregion- and cell type-restricted gene knockout in mouse brain. *Cell* 87, 1317–1326. doi: 10.1016/s0092-8674(00)81826-7

Vaney, D. I., Sivyer, B., and Taylor, W. R. (2012). Direction selectivity in the retina: symmetry and asymmetry in structure and function. *Nat. Rev. Neurosci.* 13, 194–208. doi: 10.1038/nrn3165

Völgyi, B., Chheda, S., and Bloomfield, S. A. (2009). Tracer coupling patterns of the ganglion cell subtypes in the mouse retina. *J. Comp. Neurol.* 512, 664–687. doi: 10.1002/cne.21912

Wässle, H., Peichl, L., and Boycott, B. B. (1981). Dendritic territories of cat retinal ganglion cells. *Nature* 292, 344–345. doi: 10.1038/292344a0

Whitford, K. L., Dijkhuizen, P., Polleux, F., and Ghosh, A. (2002). Molecular control of cortical dendrite development. *Annu. Rev. Neurosci.* 25, 127–149. doi: 10.1146/annurev.neuro.25.112701.142932

Wingate, R. J., and Thompson, I. D. (1994). Targeting and activity-related dendritic modification in mammalian retinal ganglion cells. *J. Neurosci.* 14, 6621–6637. doi: 10.1523/JNEUROSCI.14-11-06621.1994

Wong, R. O. L. (1999). Retinal waves and visual system development. *Annu. Rev. Neurosci.* 22, 29–47. doi: 10.1146/annurev.neuro.22.1.29

Wong, W. T., Faulkner-Jones, B. E., Sanes, J. R., and Wong, R. O. (2000). Rapid dendritic remodeling in the developing retina: dependence on neurotransmission and reciprocal regulation by Rac and Rho. *J. Neurosci.* 20, 5024–5036. doi: 10.1523/JNEUROSCI.20-13-05024.2000

Wong, R. O. L., and Ghosh, A. (2002). Activity-dependent regulation of dendritic growth and patterning. *Nat. Rev. Neurosci.* 3, 803–812. doi: 10.1038/nrn941

Xu, H. P., Chen, H., Ding, Q., Xie, Z. H., Chen, L., Diao, L., et al. (2010). The immune protein CD3ζ is required for normal development of neural circuits in the retina. *Neuron* 65, 503–515. doi: 10.1016/j.neuron.2010.01.035

Xu, H. P., and Tian, N. (2007). Retinal ganglion cell dendrites undergo a visual activity-dependent redistribution after eye opening. *J. Comp. Neurol.* 503, 244–259. doi: 10.1002/cne.21379

Xue, J., and Cooper, N. G. (2001). The modification of NMDA receptors by visual experience in the rat retina is age dependent. *Mol. Brain Res.* 91, 196–203. doi: 10.1016/s0169-328x(01)00141-3

Yang, X., Shi, X., and He, S. (2010). Properties of mouse retinal ganglion cell dendritic growth during postnatal development. *Sci. China Life Sci.* 53, 669–676. doi: 10.1007/s11427-010-4004-6

Young, B. K., Wang, P., Ramakrishnan, C., Deisseroth, K., and Tian, N. (2018). "NMDA receptor activity regulates synaptic connections between retinal ganglion and bipolar cells," in *Annual Meeting of the Association for Research in Vision and Ophthalmology (ARVO) 2018*. Abstract retrieved from Abstracts in ARVO database. (Accession No. 1864–C0168).

Zhang, J., and Diamond, J. S. (2009). Subunit- and pathway-specific localization of NMDA receptors and scaffolding proteins at ganglion cell synapses in rat retina. *J. Neurosci.* 29, 4274–4286. doi: 10.1523/JNEUROSCI.5602-08.2009

Zhou, Z. J. (2001). The function of the cholinergic system in the developing mammalian retina. *Prog. Brain Res.* 131, 599–613. doi: 10.1016/s0079-6123(01)31047-6

Conflict of Interest Statement: The authors declare that the research was conducted in the absence of any commercial or financial relationships that could be construed as a potential conflict of interest.

frontiers
in Cellular Neuroscience

MINI REVIEW
published: 27 August 2018
doi: 10.3389/fncel.2018.00269

Typology and Circuitry of Suppressed-by-Contrast Retinal Ganglion Cells

Jason Jacoby[1] *and Gregory William Schwartz*[1,2,3]*

[1]*Department of Ophthalmology, Feinberg School of Medicine, Northwestern University, Chicago, IL, United States,* [2]*Department of Physiology, Feinberg School of Medicine, Northwestern University, Chicago, IL, United States,* [3]*Department of Neurobiology, Weinberg College of Arts and Sciences, Northwestern University, Chicago, IL, United States*

Retinal ganglion cells (RGCs) relay ∼40 parallel and independent streams of visual information, each encoding a specific feature of a visual scene, to the brain for further processing. The polarity of a visual neuron's response to a change in contrast is generally the first characteristic used for functional classification: ON cells increase their spike rate to positive contrast; OFF cells increase their spike rate for negative contrast; ON-OFF cells increase their spike rate for both contrast polarities. Suppressed-by-Contrast (SbC) neurons represent a less well-known fourth category; they decrease firing below a baseline rate for both positive and negative contrasts. SbC RGCs were discovered over 50 years ago, and SbC visual neurons have now been found in the thalamus and primary visual cortex of several mammalian species, including primates. Recent discoveries of SbC RGCs in mice have provided new opportunities for tracing upstream circuits in the retina responsible for the SbC computation and downstream targets in the brain where this information is used. We review and clarify recent work on the circuit mechanism of the SbC computation in these RGCs. Studies of mechanism rely on precisely defined cell types, and we argue that, like ON, OFF, and ON-OFF RGCs, SbC RGCs consist of more than one type. A new appreciation of the diversity of SbC RGCs will help guide future work on their targets in the brain and their roles in visual perception and behavior.

Keywords: retina, retinal ganglion cells, typology, suppressed-by-contrast, contrast suppression, feature selectivity, encoding visual information

Edited by:
Bela Volgyi,
University of Pécs, Hungary

Reviewed by:
Evelyne Sernagor,
Newcastle University,
United Kingdom
Gautam Awatramani,
University of Victoria, Canada

Correspondence:
Gregory William Schwartz
greg.schwartz@northwestern.edu

Received: *11 June 2018*
Accepted: *02 August 2018*
Published: *27 August 2018*

Citation:
Jacoby J and Schwartz GW (2018) Typology and Circuitry of Suppressed-by-Contrast Retinal Ganglion Cells.
Front. Cell. Neurosci. 12:269.
doi: 10.3389/fncel.2018.00269

INTRODUCTION

Suppressed-by-Contrast (SbC) Retinal ganglion cells (RGCs) were first discovered in 1967 in the cat (Rodieck, 1967) and rabbit retina (Levick, 1967). Since that time, SbC RGCs have been recorded and further characterized by other researchers in the retina of the cat (Mastronarde, 1985; Troy et al., 1989), rabbit (Sivyer et al., 2010, 2011), macaque (de Monasterio, 1978). SbC responses have also been found in visual neurons in the brain, including in the dorsal lateral geniculate nucleus (dLGN) of the macaque (Tailby et al., 2007) as well as both dLGN (Piscopo et al., 2013) and primary visual cortex (Niell and Stryker, 2008) of the mouse. Previous research efforts have postulated that SbC visual neurons in the retina and higher visual centers may play a role in accommodation, contrast gain modulation and saccadic suppression (Rodieck, 1967; Troy et al., 1989; Tien et al., 2015).

SbC RGCs were only recently identified in the mouse retina; in 2015 two research groups presented an RGC that exhibited contrast suppression profiles, and both groups claimed to have found the SbC RGC in the mouse retina (Jacoby et al., 2015; Tien et al., 2015). While both SbC RGCs do share similar properties, a direct comparison reveals distinct differences in morphology, function, synaptic inputs and circuit connectivity.

TYPOLOGY OF SbC RGCs

Identification of neuronal cell types is critical to understanding the brain because they specify a parts list from which circuits are assembled, and one important goal of current brain-mapping initiatives is to map neural connectivity by placing identified cell types into functional circuits (Sanes and Masland, 2015). The retina is a particularly powerful model system for cell typology and circuit mapping because of a rich history of work on typology across several mammalian species. Genetic tools have accelerated the pace of discovery of new retinal cell types and their connections, particularly in the mouse.

With this fast rate of discovery comes a danger that some of the distinctions between similar cell types could be missed. Our principle argument is that two recent articles claiming to have identified the SbC RGC in mouse in fact identified different SbC RGCs. Like ON, OFF, and ON-OFF, SbC is a response polarity class comprising multiple distinct RGC types. At least two different SbC RGCs exist in the mouse retina, and we will review their similarities and differences from the perspectives of genetics, morphology and function. We will argue that one of this types, which we call the transient SbC, is identical to a RGC type that was recently discovered and named the ON delayed RGC (Mani and Schwartz, 2017).

TARGETING SbC RGCs

Transgenic mice have become useful tools for targeting neuronal cell types throughout the central nervous system, but unfortunately, few of the transgenic lines currently available label single cell types (Martersteck et al., 2017). In the preliminary screening of a line that fluorescently labeled three different ganglion cell types (*CCK-cre*), Zhu et al. (2014) observed that one type shared morphological characteristics with an SbC RGC type in rabbit retina, known as the Uniformity Detector RGC. Tien et al. (2015) performed physiological recordings from fluorescently-labeled RGCs in the CCK-cre transgenic line using 2-photon laser-guided targeting, and they confirmed that a subset of labeled cells indeed exhibited a SbC response profile (Tien et al., 2015).

While the CCK-cre is the only transgenic line that contains fluorescently-labeled SbC RGCs that could be directly targeted, other studies non-genetically targeted SbC RGCs strictly by their physiology and morphology in transgenic lines, where SbC RGCs were not fluorescently labeled, but various amacrine cells (ACs) were labeled. In a different study performed concurrently to that of Jacoby et al. (2015) and Tien et al. (2015) physiologically targeted (by stereotyped light response profile and a sustained contrast suppression profile) SbC RGCs in both wild type or the CRH-cre transgenic retina where only CRH-positive ACs were genetically labeled. In two follow-up studies performed in 2016, both Lee et al. (2016) and Tien et al. (2016) targeted SbC RGCs based on their contrast-suppression and/or dendritic morphology in a different transgenic mouse line (*VGluT3-cre*) where an associated AC was labeled but SbC RGCs were not.

MORPHOLOGY

Morphology is a critical component in identifying distinct types of RGCs. This includes characteristics such as size of the dendritic area, diameter of the soma, stratification profile in the inner plexiform layer (IPL) and branch density (Bae et al., 2018). When SbC (Uniformity Detector) RGCs were described in the rabbit retina, one key morphological characteristic was the recursive nature of the cell's dendritic arbor; many of the distal dendrites in the OFF arbor did not terminate there, but instead dove recurrently back to the ON arbor (Sivyer et al., 2010). The presence of recursive dendrites was used to argue that SbC RGCs in mouse are homologous to the rabbit Uniformity Detector RGC (Zhu et al., 2014; Tien et al., 2015). Mani and Schwartz (2017) identified a RGC type they called the ON delayed RGC, and they reported that these RGCs have a greater number and total length of recursive dendrites than the SbC RGC of (Jacoby et al. (2015); their Supplementary Figure S1; Mani and Schwartz, 2017). The full electron-microscopic (EM) reconstruction of all RGCs in a block of mouse retina (Bae et al., 2018) provides a valuable reference for comparing the morphologies of RGCs originating from different publications to determine if they belong to the same or different types. We compared images from our own lab, and an image stack and data graciously provided Nai-Wei Tien and Daniel Kerschensteiner, to the online EM database, focusing on the details of the stratification pattern in the IPL.

The dendrites of the SbC RGC that was identified by Jacoby et al. (2015) stratified proximal to the ON choline acetyl transferase (ChAT) band and distal to the OFF ChAT band (**Figure 1A**). Like other bistratified RGCs, the most of the dendritic length was confined to the ON and OFF strata with 16.4 ± 6.8% between strata for two reconstructed cells. This stratification profile is consistent with type "72" from the EM data set (Bae et al., 2018)[1], which had 13.6 ± 1.2% (mean ± SD, $n = 5$) of its dendritic length between strata. In comparison, the ON delayed RGC (**Figure 1B**) and SbC RGC presented by Tien et al. (2015; **Figure 1C**) both stratify within the ON ChAT band and distal to the OFF ChAT band. The major distinguishing feature of these cells was their high degree of recursive dendrites accounting for a larger proportion of the total dendritic length between strata. OND RGCs had 39 ± 11% of their dendrites between strata, and the image provided to us from the Tien et al. (2015) publication had 38% of its dendrite length between strata. The stratification pattern of both the ON delayed RGC and the SbC RGC of Tien et al. (2015) matched type "73" from the EM data set including the fraction of dendrites between strata (33.5 ± 4.3%, mean ± SD, $n = 6$), and those authors confirmed the identify of type "73" as the ON delayed RGC (Bae et al., 2018).

---

[1] http://museum.eyewire.org

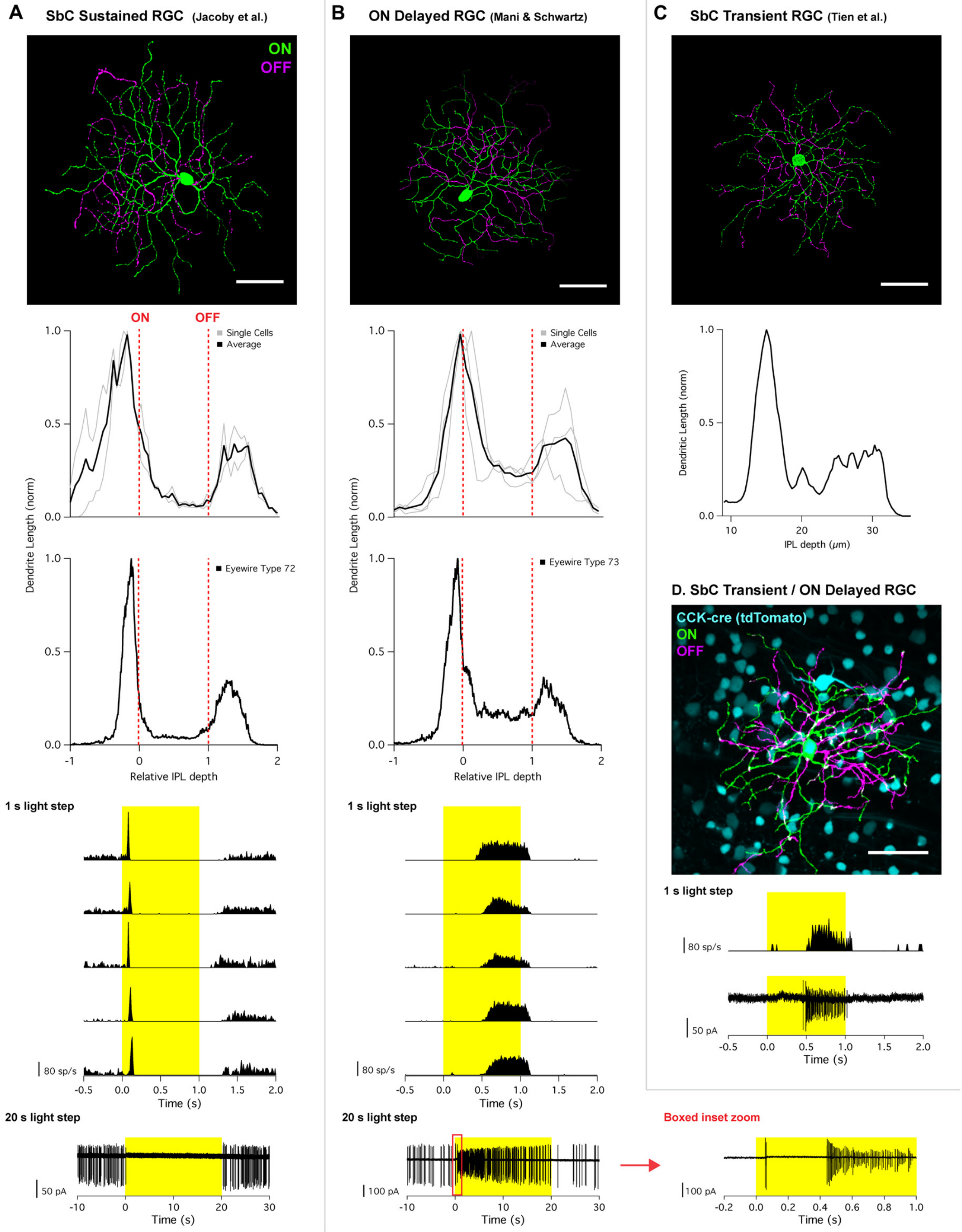

FIGURE 1 | Morphology and physiology of Suppressed-by-Contrast (SbC) retinal neurons. **(A)** SbC sustained retinal ganglion cell (RGC) identified by Jacoby et al. (2015) and **(B)** ON delayed RGC identified by Mani and Schwartz (2017). Top image; representative RGC image showing ON dendrites (green) and OFF dendrites (magenta). Middle section; stratification profiles of several individual cells (gray) overlayed with an average trace (black), followed by stratification profile of corresponding Eyewire cell types. For all stratification profiles, the vertical red dotted lines represent the ON and OFF choline acetyl transferase (ChAT) bands. Bottom traces; peristimulus time histogram (PSTH) of 1 s light step from darkness from five different cells from five different retinas. Bottom traces shows response to 20 s light step in current clamp configuration (SbC sustained RGC) and cell attached mode (ON delayed RGC). For 20 s light step for the ON delayed RGC, a zoomed in trace of the red box inset is plotted to the right. **(C)** SbC transient RGC identified by Tien et al. (2015). Top image; representative image of an SbC transient RGC (ON dendrites = green; OFF dendrites = magenta). Middle section; stratification profile of representative image above using z-axis fluorescent profile. **(D)** ON delayed/SbC transient RGC recorded in CCK transgenic mouse line. Top image; representative image with CCK labeling with tdTomato (cyan), ON dendrites (green), OFF dendrites (magenta). Bottom traces; PSTH and cell attached spikes derived from 1 s light step from darkness recorded from the cell depicted above. All scale bars = 50 μm. Permission from the copyright holders was obtained for use and modification of previously published figures.

FUNCTION

After a RGC is assigned a response polarity, the most common secondary functional parameter used in classification is kinetics: whether the light response profile is transient or sustained. Response kinetics has been important in distinguishing the brisk-transient vs. brisk-sustained RGCs in the rabbit retina (Caldwell and Daw, 1978; Amthor et al., 1989a,b; Devries and Baylor, 1997), parasol vs. midget RGCs in the primate retina (Watanabe and Rodieck, 1989; Dacey, 1994), transient vs. sustained Alpha RGCs in the mouse retina (Pang et al., 2003; Murphy and Rieke, 2006), and the High Definition family (HD1, HD2, UHD) of ON-OFF RGCs in the mouse retina (Jacoby and Schwartz, 2017). We hypothesized that different types of SbC RGCs could also be distinguished based on the kinetics of their stimulus-dependent suppression.

Jacoby et al. (2015) used a 1 s light step from darkness to classify SbC RGCs. The cells in this study were suppressed for the entire duration of this stimulus. Longer timescales were explored, and it was found that suppression for a light step from darkness could extend through the entire duration of a 20 s light step (**Figure 1A**, bottom). When these SbC RGCs were exposed to varying levels of positive/negative contrast spots from mean background illumination, suppression was sustained throughout the entire stimulus time for contrasts exceeding positive or negative 50% (**Figure 2A**).

SbC RGCs reported by Tien et al. (2015) suppressed their firing more transiently (**Figure 2C**). Suppression lasted roughly 0.5 s in duration to positive contrast stimuli that were presented for 2 s (Tien et al., 2015). This transient suppression profile of SbC transient RGCs closely resembles the "spike latency period" of the ON delayed RGC discovered by Mani and Schwartz (2017). In response to a 1 s light step from darkness, ON delayed RGCs were transiently suppressed for ∼0.5 s (**Figure 1B**). For a 20 s light step firing in an ON delayed RGC resumed within 0.5 s (**Figure 1B**, bottom and inset zoom). In the ON delayed RGC, spike suppression was similarly transient for both positive and negative contrasts from a photopic background (**Figure 2B**).

Another group observed significant variability in the kinetics of contrast suppression in the population SbC RGCs they recorded in the mouse retina (Lee et al., 2016). In offering an explanation for this variability, they noted that "…temporal variability may be attributable to subtle differences in recording conditions and/or to an intrinsic cell-to-cell variability, but the existence of different functional subtypes of Uniformity Detector (SbC) RGCs also remains a possibility (Lee et al., 2016)." Indeed, multiple cell types may comprise the data presented in their article and account for the observed response variability; in Figure 3D of their publication the top four traces resemble the response profiles of ON delayed RGC or the transient SbC RGC identified by Tien et al. (2015), and the remainder resemble the more sustained SbC RGCs of Jacoby et al. (2015). Thus, interpretation of the pharmacology and circuit tracing results are complicated by unifying these two different cell types (see below).

To determine if the ON delayed RGC targeted in wild type retina target by Mani and Schwartz (2017) was the same cell type as the SbC transient RGC targeted in the CCK-cre transgenic line described by Tien et al. (2015), the authors of this review obtained the CCK transgenic mouse and recorded from fluorescently labeled RGCs. Despite several ganglion cell types being tagged with the fluorescent marker in this line, both morphological and physiological examination confirmed that ON delayed RGCs are indeed one of the RGC types labeled in CCK-cre mice (**Figure 1D**). The morphology and physiology of these cells recorded in the CCK-cre line were indistinguishable from ON delayed RGCs from wild type retina, but were distinct from the recordings of SbC sustained RGCs (Jacoby et al., 2015). Thus, we conclude that the cells reported by Tien et al. (2015) and in their subsequent article (Tien et al., 2016) are the same type as the ON delayed RGC reported by Mani and Schwartz (2017), and that the SbC sustained RGC type reported by Jacoby et al. (2015) is a different cell type altogether. We will subsequently refer to these cell types as "transient" and "sustained" SbC RGCs respectively, but we acknowledge that there may be additional SbC RGC types and that more precise nomenclature may be required to differentiate them in the future.

CIRCUIT MECHANISMS OF CONTRAST SUPPRESSION

All three groups that published on the SbC RGCs in mouse retina also explored the upstream circuit elements that contributed to the SbC computation. It is important to consider these results in the context of our contention that they stem from two different cell types that may or may not share circuit elements. By identifying specific presynaptic partners of SbC RGCs, these studies inform our understanding of the mechanisms of contrast suppression. We will review both the known and unknown elements of these pathways with emphasis on the mechanistic differences between the transient and sustained SbC circuits.

SYNAPTIC INPUTS

To explore the excitatory and inhibitory synaptic inputs onto SbC RGCs, whole-cell voltage clamp was used to isolate these currents. A common characteristic of the synaptic currents in both SbC types was that inhibition was much larger than excitation (**Figure 2**). This was also true in previous reports of the rabbit Uniformity Detector RGC (Sivyer et al., 2010). Both mouse SbC RGC types had small excitatory currents at light onset, sometimes with separate transient and sustained components (**Figure 2**). Both cell types also showed a small, sustained decrease in tonic excitation at light offset. The lack of increased excitation is notable given that both SbC RGC types had a dendritic stratification in what is known as the OFF layer of the IPL. This constitutes a growing body of evidence that RGCs with dendrites in the outer half of the IPL do not necessarily receive input from OFF bipolar cells (Dumitrescu et al., 2009; Hoshi et al., 2009; Jacoby et al., 2015; Nath and Schwartz, 2016, 2017).

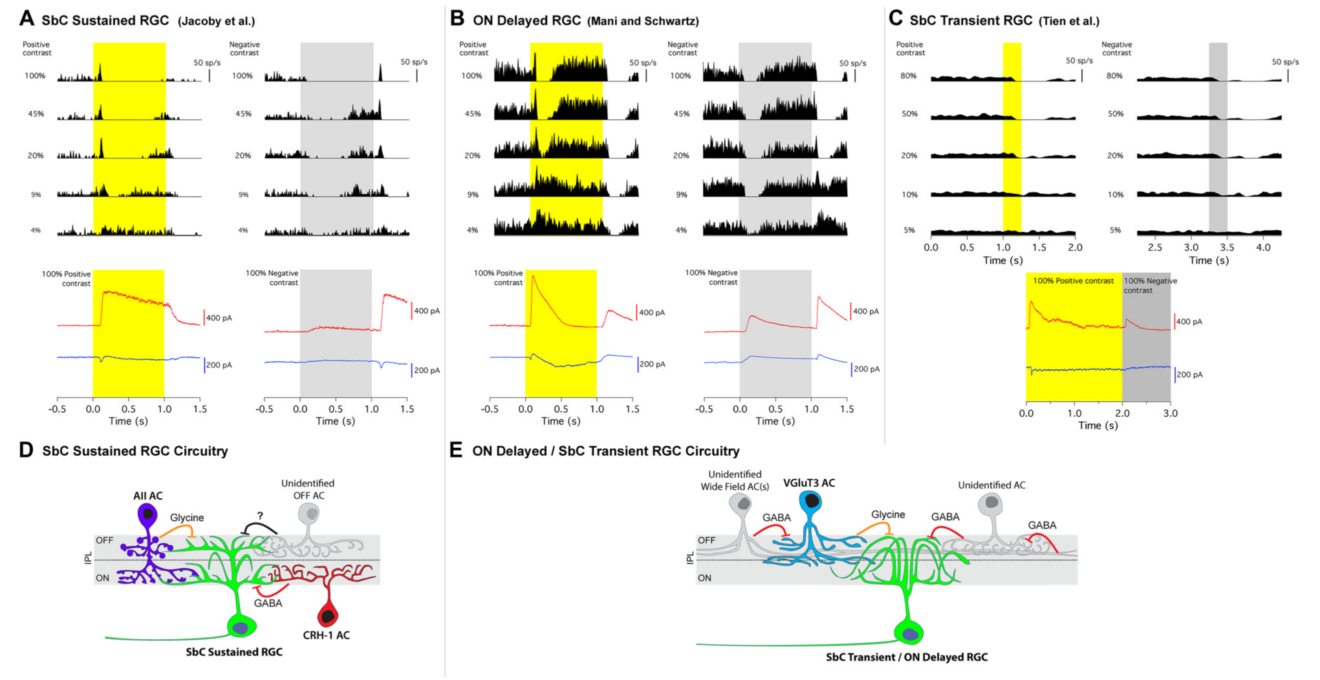

FIGURE 2 | Contrast response profiles, intracellular currents and circuit diagrams of two types of SbC RGCs. **(A)** SbC sustained RGC, **(B)** ON delayed RGC, **(C)** SbC transient RGC. Top traces; cell attached spike responses to varying levels of Weber contrast stimuli to positive (left) and negative (right) contrast from mean illumination. Middle section; excitatory (blue) and inhibitory (red) intracellular currents in response to 100% positive and 100% negative contrast stimuli. Schematic circuit diagrams for the SbC sustained RGC **(D)** and ON delayed/SbC transient RGC **(E)**. Permission from the copyright holders was obtained for use and modification of previously published figures.

In the absence of inhibition, this pattern of excitation (increase for positive contrast and decrease for negative contrast) would yield an ON contrast response profile in the RGC's spiking response, so inhibition must play a critical role in contrast suppression. Both SbC RGC types had a large inhibitory conductance at light onset that dominated the small excitatory conductance to yield a net hyperpolarization and decrease in spiking, but the ON inhibition differed in both kinetics and pharmacology between the two SbC RGC types. SbC sustained RGCs had a sustained inhibitory current that extended throughout the entirety of a 1 s light step (**Figure 2A**), while ON delayed and SbC transient RGCs had a transient inhibitory current at light onset that decayed to baseline within ∼ 500 ms (**Figures 2B,C**), depending on the size of the light stimulus (Mani and Schwartz, 2017).

Inhibition at light onset in the SbC sustained RGC was driven by both GABA_A and/or GABA_C receptors (53%) and glycine receptors (47%; Jacoby et al., 2015). In the transient SbC RGC, the vast majority of inhibition at light onset was from glycine receptors (∼75%) with only a very small GABAergic component remaining after glycine receptor block (∼25%; Tien et al., 2015). However, these results are difficult to interpret because serial inhibition can cause non-additivity of glycine and GABA components (**Figures 2D,E**). Both SbC RGC types also received inhibition at light offset to support the small decrease in excitation in reducing spiking, but the OFF inhibition differed in relative amplitude between the two RGC types. The ratio of ON/OFF inhibition was 6.2 ± 1.4 in SbC sustained RGCs, vs. 2.5 ± 0.9 in SbC transient RGCs.

PRESYNAPTIC AMACRINE CELLS

Not only were synaptic inputs identified, but specific presynaptic AC types were confirmed as sources of inhibition to help shape the contrast suppression profiles of SbC RGCs. Jacoby et al. (2015) identified that GABAergic CRH-1 ACs are direct presynaptic partners to the SbC sustained RGC through paired patch clamp recordings (Jacoby et al., 2015). The highly sustained nature of CRH-1 AC responses to light onset help to drive the sustained suppression of spike activity in SbC sustained RGCs throughout the duration of long visual stimuli (**Figure 1A**, bottom). When CRH-1 ACs surrounding a single SbC sustained RGC were physically ablated from circuit input, suppression to positive contrast was greatly reduced, and the SbC sustained RGC was converted into a stereotypical ON cell with its firing rate increasing to positive contrast (Jacoby et al., 2015). The authors also pharmacologically isolated AII ACs and showed that they supply some of the glycinergic input to sustained SbC RGCs at light onset. Conclusions from this study were that: (1) CRH-1 ACs are a necessary component of contrast suppression in SbC sustained RGCs; and (2) that AII ACs support suppression at light onset. The authors speculated that a different AC type or types provide the smaller inhibitory drive at light offset.

Both Tien et al. (2016) and Lee et al. (2016) confirmed that VGluT3 ACs release glycine onto transient SbC RGCs through optogenetics (both studies) and paired recordings. As noted above, Lee et al. (2016), likely combined both sustained and transient version of SbC RGC types in their study. When VGluT3 ACs were genetically ablated using diphtheria toxin, OFF (but not ON) inhibition was reduced in a size selective manner (for small but not large spots) and the time of spike suppression was reduced (Tien et al., 2016). The authors concluded that VGluT3 ACs play a role in contrast suppression at light offset for small stimuli in SbC transient RGCs, but that different ACs are involved in suppression at light onset and for large OFF stimuli. Schematics summarizing the inhibitory circuit elements identified upstream of both SbC RGC types are shown in (**Figures 2D,E**).

CONCLUSION

SbC RGCs respond to increases and decreases in illumination by decreasing their baseline firing rate, and like the traditional ON, OFF, and ON-OFF response polarity classes, functional distinctions within the SbC class depend on characteristics like response kinetics. Along with the rapid identification of these two SbC cell types in mouse retina, the three groups working on these cells also revealed some of the ACs responsible for the SbC computation.

We provided evidence that this SbC cell class is comprised of at least two distinct cell types. A highly-sustained SbC RGC type was identified in wild type mice by Jacoby et al. (2015) and has distinct morphological, functional, synaptic inputs and circuit connectivity when compared to the SbC transient RGC identified by Tien et al. (2015) and the ON delayed RGC identified by Mani and Schwartz (2017). We show several lines of evidence that the ON delayed and SbC transient RGCs are the same cell type.

It is possible that other types of SbC RGCs exist in the mouse retina. Just as has been shown in the ON, OFF, and ON-OFF polarity classes, SbC RGCs may each fill a specific niche in kinetics and perhaps other parameters such as stimulus size, motion speed and color.

AUTHOR CONTRIBUTIONS

JJ and GS conceived this manuscript idea, wrote the manuscript and created the figures.

FUNDING

This work was supported by Ruth L. Kirschstein National Research Service Award (NRSA) Postdoctoral Fellowship 1F32EY025930-01, NIH DP2-DEY026770A and the Research to Prevent Blindness Career Development Award.

ACKNOWLEDGMENTS

Many thanks to Adam Mani for sharing data and figures from his ON delayed RGC published manuscript. Thank you to Daniel Kerschensteiner and Nai-Wen Tien for sharing their data and figures from their SbC transient RGC published manuscript. Additionally, many thanks to Devon Greer for her assistance and creativity in creating the illustrated circuit diagrams. Many thanks to Sebastian Seung for sharing with us the Eyewire stratification profiles for both cell types addressed in this review.

REFERENCES

Amthor, F. R., Takahashi, E. S., and Oyster, C. W. (1989a). Morphologies of rabbit retinal ganglion cells with complex receptive fields. *J. Comp. Neurol.* 280, 97–121. doi: 10.1002/cne.902800108

Amthor, F. R., Takahashi, E. S., and Oyster, C. W. (1989b). Morphologies of rabbit retinal ganglion cells with concentric receptive fields. *J. Comp. Neurol.* 280, 72–96. doi: 10.1002/cne.902800107

Bae, J. A., Mu, S., Kim, J. S., Turner, N. L., Tartavull, I., Kemnitz, N., et al. (2018). Digital museum of retinal ganglion cells with dense anatomy and physiology. *Cell* 173, 1293–1306.e19. doi: 10.1016/j.cell.2018.04.040

Caldwell, J. H., and Daw, N. W. (1978). New properties of rabbit retinal ganglion cells. *J. Physiol.* 276, 257–276. doi: 10.1113/jphysiol.1978.sp012232

Dacey, D. M. (1994). Physiology, morphology and spatial densities of identified ganglion cell types in primate retina. *Ciba Found. Symp.* 184, 12–28; discussion 28–34, 63–70.

de Monasterio, F. M. (1978). Properties of ganglion cells with atypical receptive-field organization in retina of macaques. *J. Neurophysiol.* 41, 1435–1449. doi: 10.1152/jn.1978.41.6.1435

Devries, S. H., and Baylor, D. A. (1997). Mosaic arrangement of ganglion cell receptive fields in rabbit retina. *J. Neurophysiol.* 78, 2048–2060. doi: 10.1152/jn.1997.78.4.2048

Dumitrescu, O. N., Pucci, F. G., Wong, K. Y., and Berson, D. M. (2009). Ectopic retinal ON bipolar cell synapses in the OFF inner plexiform layer: contacts with dopaminergic amacrine cells and melanopsin ganglion cells. *J. Comp. Neurol.* 517, 226–244. doi: 10.1002/cne.22158

Hoshi, H., Liu, W.-L., Massey, S. C., and Mills, S. L. (2009). ON inputs to the OFF layer: bipolar cells that break the stratification rules of the retina. *J. Neurosci.* 29, 8875–8883. doi: 10.1523/JNEUROSCI.0912-09.2009

Jacoby, J., and Schwartz, G. W. (2017). Three small-receptive-field ganglion cells in the mouse retina are distinctly tuned to size, speed and object motion. *J. Neurosci.* 37, 610–625. doi: 10.1523/JNEUROSCI.2804-16.2016

Jacoby, J., Zhu, Y., DeVries, S. H., and Schwartz, G. W. (2015). An amacrine cell circuit for signaling steady illumination in the retina. *Cell Rep.* 13, 2663–2670. doi: 10.1016/j.celrep.2015.11.062

Lee, S., Zhang, Y., Chen, M., and Zhou, Z. J. (2016). Segregated Glycine-glutamate co-transmission from vGluT3 amacrine cells to contrast-suppressed and contrast-enhanced retinal circuits. *Neuron* 90, 27–34. doi: 10.1016/j.neuron.2016.02.023

Levick, W. R. (1967). Receptive fields and trigger features of ganglion cells in the visual streak of the rabbits retina. *J. Physiol.* 188, 285–307. doi: 10.1113/jphysiol.1967.sp008140

Mani, A., and Schwartz, G. W. (2017). Circuit mechanisms of a retinal ganglion cell with stimulus-dependent response latency and activation beyond its dendrites. *Curr. Biol.* 27, 471–482. doi: 10.1016/j.cub.2016.12.033

Martersteck, E. M., Hirokawa, K. E., Evarts, M., Bernard, A., Duan, X., Li, Y., et al. (2017). Diverse central projection patterns of retinal ganglion cells. *Cell Rep.* 18, 2058–2072. doi: 10.1016/j.celrep.2017.01.075

Mastronarde, D. N. (1985). Two types of cat retinal ganglion cells that are suppressed by contrast. *Vis. Res.* 25, 1195–1196. doi: 10.1016/0042-6989(85)90033-1

Murphy, G. J., and Rieke, F. (2006). Network variability limits stimulus-evoked spike timing precision in retinal ganglion cells. *Neuron* 52, 511–524. doi: 10.1016/j.neuron.2006.09.014

Nath, A., and Schwartz, G. W. (2016). Cardinal orientation selectivity is represented by two distinct ganglion cell types in mouse retina. *J. Neurosci.* 36, 3208–3221. doi: 10.1523/JNEUROSCI.4554-15.2016

Nath, A., and Schwartz, G. W. (2017). Electrical synapses convey orientation selectivity in the mouse retina. *Nat. Commun.* 8:2025. doi: 10.1038/s41467-017-01980-9

Niell, C. M., and Stryker, M. P. (2008). Highly selective receptive fields in mouse visual cortex. *J. Neurosci.* 28, 7520–7536. doi: 10.1523/JNEUROSCI.0623-08.2008

Pang, J. J., Gao, F., and Wu, S. M. (2003). Light-evoked excitatory and inhibitory synaptic inputs to ON and OFF alpha ganglion cells in the mouse retina. *J. Neurosci.* 23, 6063–6073. doi: 10.1523/jneurosci.23-14-06063.2003

Piscopo, D. M., El-Danaf, R. N., Huberman, A. D., and Niell, C. M. (2013). Diverse visual features encoded in mouse lateral geniculate nucleus. *J. Neurosci.* 33, 4642–4656. doi: 10.1523/JNEUROSCI.5187-12.2013

Rodieck, R. W. (1967). Receptive fields in the cat retina: a new type. *Science* 157, 90–92. doi: 10.1126/science.157.3784.90

Sanes, J. R., and Masland, R. H. (2015). The types of retinal ganglion cells: current status and implications for neuronal classification. *Annu. Rev. Neurosci.* 38, 221–246. doi: 10.1146/annurev-neuro-071714-034120

Sivyer, B., Taylor, W. R., and Vaney, D. I. (2010). Uniformity detector retinal ganglion cells fire complex spikes and receive only light-evoked inhibition. *Proc. Natl. Acad. Sci. U S A* 107, 5628–5633. doi: 10.1073/pnas.0909621107

Sivyer, B., Venkataramani, S., Taylor, W. R., and Vaney, D. I. (2011). A novel type of complex ganglion cell in rabbit retina. *J. Comp. Neurol.* 519, 3128–3138. doi: 10.1002/cne.22720

Tailby, C., Solomon, S. G., Peirce, J. W., and Metha, A. B. (2007). Two expressions of "surround suppression" in V1 that arise independent of cortical mechanisms of suppression. *Vis. Neurosci.* 24, 99–109. doi: 10.1017/S0952523807070022

Tien, N.-W., Kim, T., and Kerschensteiner, D. (2016). Target-specific glycinergic transmission from VGluT3-expressing amacrine cells shapes suppressive contrast responses in the retina. *Cell Rep.* 15, 1369–1375. doi: 10.1016/j.celrep.2016.04.025

Tien, N.-W., Pearson, J. T., Heller, C. R., Demas, J., and Kerschensteiner, D. (2015). Genetically identified suppressed-by-contrast retinal ganglion cells reliably signal self-generated visual stimuli. *J. Neurosci.* 35, 10815–10820. doi: 10.1523/JNEUROSCI.1521-15.2015

Troy, J. B., Einstein, G., Schuurmans, R. P., Robson, J. G., and Enroth-Cugell, C. (1989). Responses to sinusoidal gratings of two types of very nonlinear retinal ganglion cells of cat. *Vis. Neurosci.* 3, 213–223. doi: 10.1017/s0952523800009974

Watanabe, M., and Rodieck, R. W. (1989). Parasol and midget ganglion cells of the primate retina. *J. Comp. Neurol.* 289, 434–454. doi: 10.1002/cne.902890308

Zhu, Y., Xu, J., Hauswirth, W. W., and Devries, S. H. (2014). Genetically targeted binary labeling of retinal neurons. *J. Neurosci.* 34, 7845–7861. doi: 10.1523/JNEUROSCI.2960-13.2014

Conflict of Interest Statement: The authors declare that the research was conducted in the absence of any commercial or financial relationships that could be construed as a potential conflict of interest.

frontiers
in Cellular Neuroscience

ORIGINAL RESEARCH
published: 22 November 2018
doi: 10.3389/fncel.2018.00409

Strategic Positioning of Connexin36 Gap Junctions Across Human Retinal Ganglion Cell Dendritic Arbors

Orsolya Kántor[1,2,3†], Gergely Szarka[2,4,5,6†], Zsigmond Benkő[7], Zoltán Somogyvári[7], Emese Pálfi[3], Gábor Baksa[3], Gergely Rácz[8], Roland Nitschke[9,10], Gábor Debertin[2,4,5,6] and Béla Völgyi[2,4,5,6*]

[1] Department of Neuroanatomy, Faculty of Medicine, Institute for Anatomy and Cell Biology, Albert-Ludwigs-University Freiburg, Freiburg, Germany, [2] MTA-PTE NAP 2 Retinal Electrical Synapses Research Group, Pécs, Hungary, [3] Department of Anatomy, Histology and Embryology, Semmelweis University, Budapest, Hungary, [4] Department of Experimental Zoology and Neurobiology, University of Pécs, Pécs, Hungary, [5] Center for Neuroscience, University of Pécs, Pécs, Hungary, [6] János Szentágothai Research Center, University of Pécs, Pécs, Hungary, [7] Complex Systems and Computational Neuroscience Group, Wigner Research Center for Physics, Hungarian Academy of Sciences, Budapest, Hungary, [8] Department of Pathology and Experimental Cancer Research, Semmelweis University, Budapest, Hungary, [9] Life Imaging Center, Center for Biological Systems Analysis, Albert-Ludwigs University, Freiburg, Germany, [10] BIOSS Center for Biological Signaling Studies, Albert-Ludwigs-University Freiburg, Freiburg, Germany

Edited by:
Davide Cervia,
Università degli Studi della Tuscia, Italy

Reviewed by:
Sen Lin,
Army Medical University, China
Karin Dedek,
University of Oldenburg, Germany

***Correspondence:**
Béla Völgyi
volgyi01@gamma.ttk.pte.hu;
volgyibela@gmail.com

† These authors have contributed equally to this work

Received: *27 July 2018*
Accepted: *22 October 2018*
Published: *22 November 2018*

Citation:
Kántor O, Szarka G, Benkő Z, Somogyvári Z, Pálfi E, Baksa G, Rácz G, Nitschke R, Debertin G and Völgyi B (2018) Strategic Positioning of Connexin36 Gap Junctions Across Human Retinal Ganglion Cell Dendritic Arbors. Front. Cell. Neurosci. 12:409.
doi: 10.3389/fncel.2018.00409

Connexin36 (Cx36) subunits form gap junctions (GJ) between neurons throughout the central nervous system. Such GJs of the mammalian retina serve the transmission, averaging and correlation of signals prior to conveying visual information to the brain. Retinal GJs have been exhaustively studied in various animal species, however, there is still a perplexing paucity of information regarding the presence and function of human retinal GJs. Particularly little is known about GJ formation of human retinal ganglion cells (hRGCs) due to the limited number of suitable experimental approaches. Compared to the neuronal coupling studies in animal models, where GJ permeable tracer injection is the gold standard method, the post-mortem nature of scarcely available human retinal samples leaves immunohistochemistry as a sole approach to obtain information on hRGC GJs. In this study Lucifer Yellow (LY) dye injections and Cx36 immunohistochemistry were performed in fixed short-post-mortem samples to stain hRGCs with complete dendritic arbors and locate dendritic Cx36 GJs. Subsequent neuronal reconstructions and morphometric analyses revealed that Cx36 plaques had a clear tendency to form clusters and particularly favored terminal dendritic segments.

Keywords: gap junction, electrical synapse, ganglion cell, inner plexiform layer, ganglion cell layer, human retina

INTRODUCTION

Various connexin (Cx) gene sequences emerged throughout vertebrate evolution and their products comprise a populous protein family with over 20 members (Güldenagel et al., 2000; Cruciani and Mikalsen, 2006; Söhl and Willecke, 2003). Cx subunits are widely expressed in both non-neuronal and neuronal tissues, where they form gap junctions (GJ) between connecting cells. GJs connect neurons throughout the central nervous system in all examined mammals, where they allow the passage of signals between neurons (Furshpan and Potter, 1957; Watanabe, 1958). The mammalian retina has been a popular model of GJ studies as a number of Cx subunits are expressed by various retinal neurons, including Cx30.2, Cx36, Cx45, Cx50, and Cx57 (Güldenagel et al., 2001; Lee et al., 2003; Massey et al., 2003; Hombach et al., 2004; Maxeiner et al., 2005; Müller et al., 2010; Han and Massey, 2005). It has been shown, that similar to other mammalian species the human retina expresses Cx36 and Cx45 both in the IPL and OPL (Söhl et al., 2010) and the expression patterns resemble those of other mammalian species, including the mouse, rabbit, and rat (Feigenspan et al., 2001; Mills et al., 2001; Deans et al., 2002; Kihara et al., 2006, 2010; O'Brien et al., 2012; Kovács-Öller et al., 2014, 2017; Kántor et al., 2016a, 2017). Cx36 comprising retinal GJs have been shown to play a number of roles in signal processing, including the transmission-, averaging- and synchronization of signals (Mastronarde, 1983; Brivanlou et al., 1998; DeVries, 1999; Bloomfield and Völgyi, 2009; Völgyi et al., 2013a,b; Roy et al., 2017). Evidence for retinal ganglion cell (RGC) GJs have been found in most RGC types of the examined animal species, (Hidaka et al., 2004; Schubert et al., 2005a,b; Völgyi et al., 2005, 2009, 2013a,b; Pan et al., 2010) indicating that GJs are integrated into most RGC microcircuits and thus they play essential roles in RGC signaling. However, it is unknown whether hRGCs possess similar electrical synaptic connections or they fundamentally differ in this respect from those of their non-human counterparts.

In this study we combined the intracellular injection of Lucifer yellow (LY), Cx36 immunohistochemistry and 3D reconstruction based morphometric analysis to study the Cx36 plaque distribution across the dendritic branches of hRGCs. We found that Cx36 plaque numbers, densities and distribution over dendritic arbors varied considerably in our heterogeneous sample. Despite this heterogeneity of the examined neurons, we also encountered population wide general features including the relative higher density of plaques in terminal dendrite segments and a tendency for plaques to occur in pairs (or triplets). Possible functional aspects regarding these two general phenomena are discussed in this work as well.

MATERIALS AND METHODS

Histological Preparation

Human donor tissue from patients without reported history of eye disease was collected in accordance with the tenets of Declaration of Helsinki or from cadavers from the 1st Department of Pathology and Cancer Research and from Department of Anatomy, Histology and Embryology, Semmelweis University, Budapest, Hungary. Retinas from 3 patients were investigated in the present study (2 females, 1 male, age: 59–85 years, 3–7 h post-mortem time). All personal identifiers were removed and samples were coded before histological processing. All experimental protocols were approved by the local ethics committee (TUKEB58/2014). To comply with institutional ethics regulations all necessary written consents to utilize human tissue for scientific purposes of this study were obtained from either the donors, or their eligible relatives. After the removal of corneas, posterior eyecups were fixed in 4% buffered paraformaldehyde (PFA) for 2 h at +4°C. Samples were cut into six radial pieces then rinsed several times in 0.1 M phosphate buffered saline (PBS, pH 7.4). Isolated retinal whole mounts (pigment epithelium was carefully removed) were cut in small pieces.

Intracellular Lucifer Yellow Injections

Borosilicate glass pipettes were filled with 4% Lucifer Yellow die (LY, Sigma-Aldrich, Budapest, Hungary, resistance: 150–500 MΩ). Human RGCs from mid-peripheral (3–6 mm centrality) to peripheral (6–9 mm centrality) locations were injected with LY using a Zeiss Axioscope microscope, 40x water immersion lens, Zeiss micromanipulator (Carl Zeiss Inc., Jena, Germany) and Digitimer iontophoretic dye marker (Digitimer Ltd., Welwyn Garden City, UK; current: −4.5 nA, duration: 10–15 min). Afterwards, retinal pieces were postfixed in 4% PFA with 0.5% glutaraldehyde (Sigma-Aldrich, Budapest, Hungary) for 45 min and rinsed extensively in 0.1 M phosphate buffered saline (PBS, pH 7,4). After the LY injection, each further step was carried out under protection from light. To enhance penetration in whole mounts, tissue was soaked in 30% sucrose and freeze-thawed three times. To remove glutaraldehyde from the tissue, retinas were treated with 1% sodium-borohydride for 30 min (Sigma-Aldrich, Budapest, Hungary).

Fluorescent Immunohistochemistry

Fluorescent Cx36 immunohistochemical reactions on the specimens with LY filled neurons were carried out according to standard protocols (Kántor et al., 2016a). Briefly, tissues were washed several times with PBS (25 mM with 0.2% Triton-X, PBS-TX). Non-specific background staining was blocked in 10% donkey serum diluted in PBS-TX. Specimens were then incubated in the anti-Cx36 primary antibody (mouse anti-connexin 35/36 1:1,000; Merck Ltd, cat# MAB3045, clone 8F6.2) at +4°C (72 h). After extensive rinsing, specimens were incubated overnight at 4°C with the anti-mouse IgG secondary antibody conjugated with Alexa 647 (1:500, Life Technologies, Hungary) diluted in PBS-TX and 3% normal donkey serum. After several rinsing steps, whole mounts were mounted on gelatin coated slides and all specimens were coverslipped using AquaPolymount (Polysciences Europe GmbH, Eppelheim, Germany) as mounting medium. Slides were kept at +4°C until imaging. On a separate set of specimens from peripheral retinal locations multiple fluorescent immunohistochemical reactions were carried out to label hRGCs (and other retinal neurons) with neurochemical marker Ca^{++}-binding proteins by using the same staining protocol as specified above for the LY labeled retinal tissue. Appropriate mixtures of the following primary and secondary antibodies were used: mouse anti-connexin 35/36 1:1,000 (Merck Ltd, cat# MAB3045, clone 8F6.2), goat anti-calretinin 1:1,000, rabbit anti-calbindinDK28 1:1,000, goat anti-parvalbumin 1:1,000 (all from SWANT, Marly, Switzerland), donkey anti-mouse IgG conjugated with Alexa 488, donkey anti-goat IgG conjugated with Alexa 555 and donkey anti-rabbit IgG conjugated with DyLight 649 (all Alexa-conjugated antibodies were purchased from Life Technologies, Budapest, Hungary; Dy-Light conjugated antibody was Jackson Immuno Research, Europe, Suffolk, UK).

Imaging, Image Processing

Images were captured on a confocal microscope (Zeiss LSM 780 with upright microscope Axio Imager Z1, Carl Zeiss Inc., Jena, Germany) using the ZEN 2012 software (Carl Zeiss Inc., Jena, Germany) and 40x Plan-Apochromat oil-immersion lens (NA: 1.4). Final images were constructed using Adobe Photoshop 7.0 (San Diego, CA, USA). Only minor adjustments of brightness and contrast were applied, which in no case altered the original appearance of the images.

Neurolucida Reconstruction and Statistical Analysis

Datasets were obtained from Z-stacks of flat-mount human retinal samples. Cell bodies and dendritic branches of 47 RGCs were manually traced using Neurolucida (Version 9, MBF Bioscience Europe, Magdeburg, Germany). Colocalizing Cx36 plaques were marked along the dendritic tree. Data of colocalizing Cx36 plaques were primarily obtained from NeuroLucida reconstructions and utilized for further analysis of this study. For further visualization of hRGCs we traced the dendrites using Fiji's (Schindelin et al., 2012) simple neurite tracer plugin (Longair et al., 2011). In order to obtain the correct dendrite length, the brightness and contrast were adjusted and after completion of the traces, using the fill-out option, we created new image stacks for the reconstruction. With the help of the 3D viewer plugin (Schmid et al., 2010) we created an stl (ASCII) file from the surfaces. The final videos that can be seen in our supplemental 3D material were created using Blender (Blender—a 3D modeling and rendering package, Blender institute, Amsterdam, 2018) from the surface reconstructions.

Analyses, graphical representations and statistical tests (Mann–Whitney *U*-test, Wilcoxon signed-rank test, Kolmogorov-Smirnov test, Kruskal–Wallis H test) of the results were performed by using OriginPro 2018 (Microcal Origin, Northampton, USA). Results of statistical tests were considered significant when $p < 0.05$ occurred.

We also estimated the probability density function ($P(x)$) of the Cx36 plaque number density with a weighted sum of log-normal components:

$$P(x) = \sum_{k=1}^{K} \pi_k \cdot p_k(x)$$

where K is the number of components and π_k is the mixing coefficient of the k-th component. The coefficients are normalized, that is:

$$\sum_{k=1}^{K} \pi_k = 1$$

$p_k(x)$ are the log-normal components which are given by:

$$p(x) = \frac{1}{x\sigma_k\sqrt{2\pi}} \cdot e^{-\frac{(\ln(x)-\mu_k)^2}{2\sigma_k^2}}$$

where μ and σ are the location and the shape parameters of the distribution, respectively. Assuming independent and identically distributed data we fitted the model through maximization of the likelihood given the model using an iterative procedure called the Expectation Maximization (EM) algorithm by utilizing the python scikit-learn package (Pedregosa et al., 2011). The likelihood is the probability of the data set given the parameters:

$$L = P(Data|\pi, \mu, \sigma) = \prod_{n=1}^{N} P(x_n)$$

The data set is the co-occurrence of observed data points (x_n) so the probability of the data set is the product of the N individual data-point probabilities, given independent identically distributed sample. We initialized the parameters randomly and then waited 100 iteration steps, this procedure was repeated 300 times and the solution with maximal likelihood was accepted. We performed the above procedure for a different number of components (from 1 to 6). The optimal number of components (K^*) was chosen according to the Bayesian Information Criterion (BIC). BIC shows the optimality of a model by introducing a tradeoff between the likelihood and model complexity:

$$BIC(K) = -2 \cdot ln(L) + (3K - 1) \cdot ln(N)$$

The first term on the right hand side is the negative logarithm of the likelihood, which is a monotonically decreasing function of K. In the second term is the number of free fitted parameters, namely the log-scale, the shape and the mixing coefficient for each component and minus one due to the normalization restriction for mixing coefficients. This latter term is a monotonically increasing function of K, acting as a penalty for the number of parameters, which is a simple estimate of model complexity. The optimal model has the smallest BIC value.

RESULTS

Following fixation of retinal tissues hRGC somata ($n = 47$) were visualized under DIC in the whole-mount preparation and injected (see Methods) by utilizing LY as a tracer. LY diffused to all dendritic segments, thus allowed for the visualization of the entire arbor of each injected hRGC. All specimens were counterstained with an a-Cx36 serum to detect gap junction sites formed by Cx36 subunits. The LY/Cx36 dual stained materials were processed for NeuroLucida reconstruction (see section Materials and Methods) of both LY labeled hRGCs and the overlapping Cx36 plaques and used to determine colocalizations of the two labels (**Figure 1**). NeuroLucida reconstructions provided 3D views of the injected hRGCs and also allowed for rotation via three angles to localize Cx36 plaques precisely along the labeled dendritic branches. All colocalizing Cx36 plaques for every hRGC of this study were picked manually. This process, though tedious, allowed for the exclusion of background-, blood vessels, LY leakage and other staining that potentially introduce noise into our data. To further minimize false positive colocalizations due to the spatial resolution limit

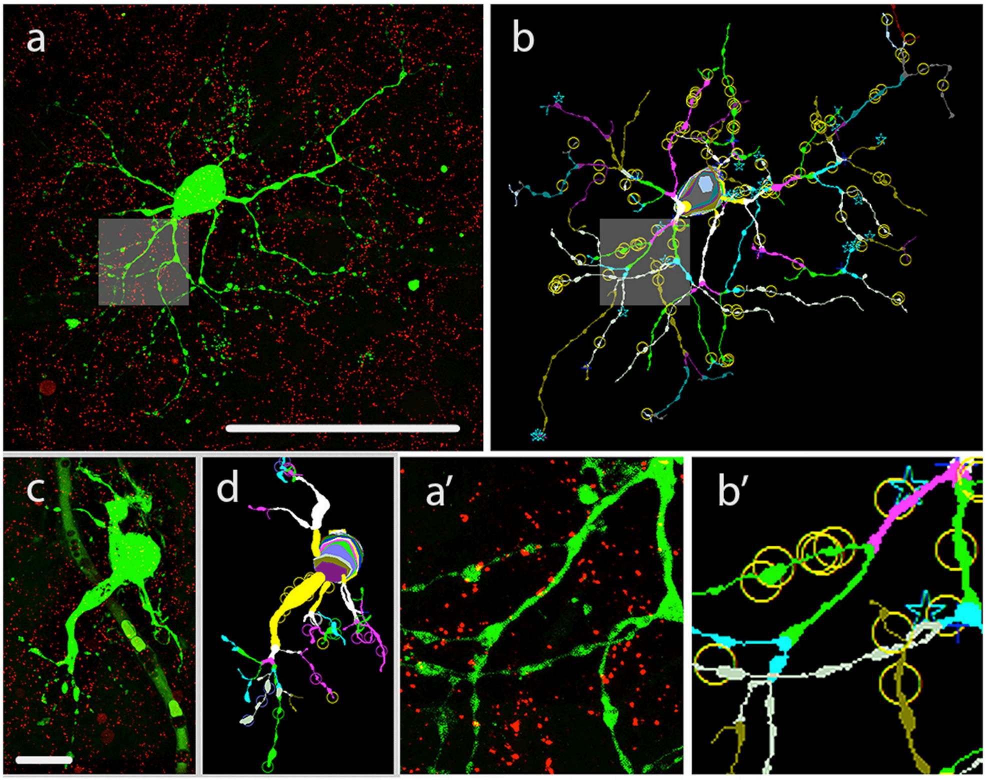

FIGURE 1 | LY injection, visualization and morphometric analysis of hRGCs**. (a)** Dual stained specimen in the human retina, displays a LY injected hRGC (green) with M cell-like soma-dendritic morphology and Cx36 plaque counter labels (red). Shadings in this image and also in **(b)** mark areas enlarged in insets **(a′,b′)**. **(b)** The NeuroLucida reconstruction of the cell in panel *a* depicts the dendritic structure by marking same order dendritic segments with uniform colors. This reconstruction also points out the locations of Cx36 plaques (circles,stars over the dendrites) that were found in colocalization with a dendritic segment of the LY labeled hRGC. **(a′,b′)** Insets display enlarged area of the LY labeled cell in **(a′,b′)**. **(c,d)** LY injected small hRGC with P cell-like morphology **(c)** and the Neurolucida reconstruction of the same cell **(d)**. Scale bar: 100 µm.

along the z-axis only Cx36 plaques whose labeling intensity maximums overlapped with those of the LY injected processes were considered. This latter process also minimized false positives due to the thicker appearance of dye filled fluorescent processes. We also rejected plaque-like structures (likely noise) that were represented by $<2 \times 2$ pixels and/or appeared only in one optical section. Resultant morphometric data were then selected to describe the numbers, somatic proximity, dendritic distribution of Cx36 plaques as well as their tendency to aggregate across hRGC dendritic branches.

Cx36 Plaque Expression by Human Retinal Ganglion Cells

GJ mediated signals from multiple sources may exert a greater effect on hRGC activity when they are efficiently summated, thus the number of functional GJ sites likely correlate with the efficacy by which GJ mediated signals contribute to the hRGC output. To examine the numerosity of such potential current sources over hRGC dendritic trees a morphometric analysis was performed to determine the total number of Cx36 plaques for each hRGC of this study. We found that all reconstructed cells displayed some Cx36 plaques over their dendritic processes. The numbers of these colocalizing plaques were rather high for most but a few cells (mean = 110.85, *SD* = ±115.63) and varied in a rather wide range (5–487; see also **Figure 2A** and **Supplemental Table 1**). This was not surprising as the sample contained hRGCs with various dendritic arbor sizes and morphologies, indicative of the heterogeneity of examined neurons. It was beyond the scope of this study to perform a thorough morphological characterization of hRGCs in the sample. However, based on the available morphological descriptions of human retinal cells (Dacey and Petersen, 1992; Kolb et al., 1992), we found parasol like (P-like) hRGCs with small soma and short, relatively simple dendritic arbors (**Figures 1c,d**). Dendrites of these latter cells maintained relative low number of colocalizing Cx36 plaques (**Supplemental Figure 1**), indicating that the observed variation in plaque counts is subtype specific.

In addition to heterogeneity, hRGCs of the same subtype with slightly different eccentricity can differ in dendritic arbor size and thus to contribute to the variation in Cx36 plaque numbers. Thus, in order to minimize these effects, the density of Cx36 plaques (densCx36) were calculated for each hRGC by dividing total Cx36 counts by the corresponding volume of the dendritic tree. The average plaque density was 0.048 plaque/μm^3 (*SD* = ±0.037) and the actual densCx36 values covered a wide range of 0.007–0.14 plaque/μm^3 (**Figure 2B**). P-like cells were among those

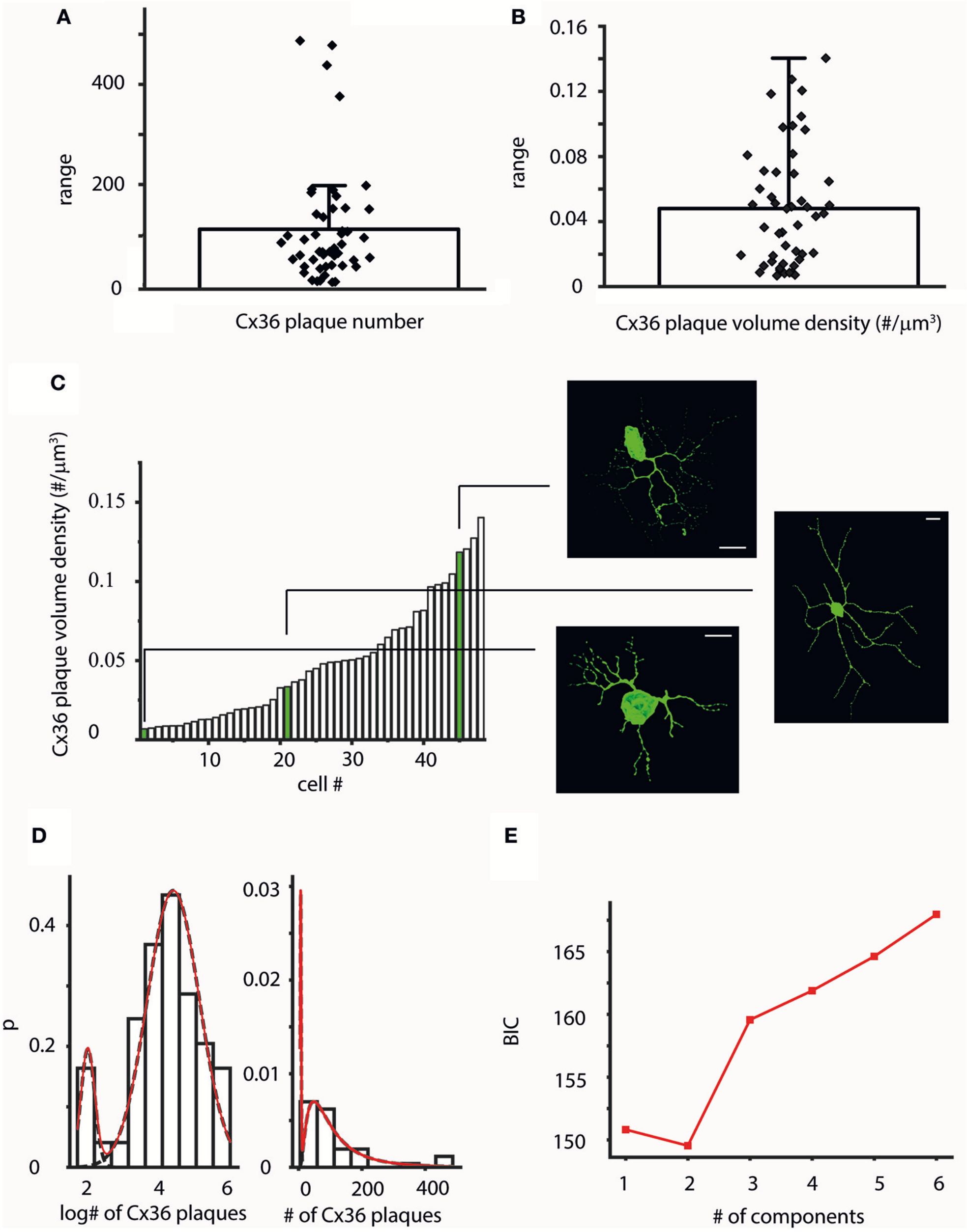

FIGURE 2 | Variations in Cx36 plaque number across the hRGC population. **(A,B)** Bar-overlap charts and scatterplot showing the average values **(A)** and density **(B)** of plaque numbers colocalized with LY labeled hRGC dendrites. Overlapping scatterplot (diamonds) represents individual number **(A)** and density **(B)** values for each examined cell. The wide range of plaque counts and densities are resulted by the heterogeneous nature of the sample. **(C)** After sorting volume density values (# of plaques/μm^3) in an ascending order the resultant histogram displays local plateaus, suggesting that several subgroups of cells with similar plaque densities exist in our dataset (see also **Supplemental Figure 2** for length and surface density values). Snapshots of 3D reconstructed hRGCs corresponding to each of the subgroups are shown on the right (relevant density values are highlighted in green). **(D,E)** Forty-seven cells were clustered into two groups based on CX36 plaque numbers on dendritic surfaces. The two clusters were modeled with lognormal distributions (note the logarithmic scale), with mean plaque numbers 6.824 and 88.481; BIC minimum was determined as 2 components. Approximately 90% of the cells belonged to the cluster with the higher mean Cx36 plaque number. Scale bars: 25 mm.

displaying the lowest plaque densities (**Supplemental Figure 1**). However, when densCx36 values were plotted in an ascending order the histogram displayed multiple plateaus. This finding suggested that our sample contained several subpopulations that differed (besides the absolute numbers of Cx36 plaques) in the overall plaque density over their corresponding dendritic arbors (**Figure 2C**). Note, that calculations to obtain length and surface density of Cx36 plaques for the entire hRGC population were carried out as well and those provided similar results (**Supplemental Figure 2**).

In an attempt to separate ganglion cell subpopulations, probability density distributions of Cx36 numbers were also calculated (see methods for relevant equations). The probability density distribution showed a sign of bimodality and the subsequent mathematical model resulted in a minimum Bayesian Information Criterion (BIC) value at 2 components (**Figures 2D,E**). Thus, this, supporting our above morphometric analysis, further suggested the separation of cells in our sample into two populations based on the numbers of colocalizing Cx36 plaques, one with only a few plaques (mean = 6.82) and another more populous group (~90% of the cells in the sample) with considerably higher number of Cx36 plaques (mean = 88.49).

Cx36 Plaque Proximity to Human Ganglion Cell Somata

Signal efficacy might also be determined by the distance that GJ mediated currents must travel from their origin (GJ site) to the cell body where incoming information is integrated to generate the spike output toward the brain. Therefore, a second set of analyses was carried out to determine the average distance of Cx36 plaques to the soma for all hRGCs. The values covered a wide range of 35–205.1 μm, and the total average was 92.2 μm (SD ±39.1; **Figure 3A**; **Supplementary Table 1**). Due to this wide range it is unlikely that distance is a determining factor in the Cx36 plaque distribution over hRGC dendritic arbors.

To further examine this issue soma-plaque distances were plotted in an ascending order for hRGCs. Cx36 plaque distance values appeared to display even distributions for most examined cells (**Figure 3B**). This finding was supported also by our analysis showing that hRGCs with relative large arbors ($n = 6$) had just as many plaques in distant dendrites as in proximal ones (**Figures 3B,C**; Wilcoxon signed-rank test, $p = 0.22$). Overall, the above findings indicated that distal dendritic locations were just as populous as proximal ones, thus the soma-plaque distance most likely is not a principal factor in determining Cx36 plaque locations.

To gain more insight into Cx36 plaque distribution we performed an analysis that rendered Cx36 plaque numbers to the order of their corresponding dendrites (**Figures 3D–F**). The orderly distribution of plaques varied considerably as shown by the diversity of the obtained distribution histograms and no obvious general features were seen. The great variety in this analysis was not surprising as our heterogeneous sample contained dendritic arbors with branches of 4–19th orders. This indicated that Cx36 plaque distribution was largely independent of dendritic order.

Next, both a "Sholl" and a "Tortuous distance" analyses with 10 μm step-size were carried out in all cells of the sample. The obtained histograms varied considerably in both cases. The plaque distribution pattern seemed random for many cells, showed near Gaussian distribution for others or appeared linearly descending (**Figures 4A–C**). However, results of this analysis were highly affected by the number of processes falling into each step-window. This was especially true for hRGCs where the middle area of the arbor comprised significantly higher number of processes than the proximal or the distalmost areas, in which cases both the "Sholl" and "Tortuous distance" analyses resulted in a near Gaussian distribution. To correct for this the analyses were repeated by calculating the number of Cx36 plaques over a unit length (μm) of the dendritic arbor. These repeated analyses changed the appearance of histograms into more uniform and most cells now showed a near linear plaque distribution over the dendritic arbor with no Gaussian like histograms. However, the most dramatic finding was that numerous cells ($n = 28$) displayed the highest relative plaque numbers in their corresponding highest bins. This suggested that the dendritic endings or terminal branches tend to maintain a more numerous Cx36 plaque population than other dendritic areas (**Figure 4D**).

Cx36 Plaque Distribution Across Dendritic Arbors of Human Ganglion Cells

It appeared in the previous analyses that terminal dendritic branches maintained a relative high number of Cx36 plaques for most cells in our sample. In order to gain a deeper insight in this issue first we examined all hRGCs in our sample ($n = 47$), to see if Cx36 plaques at the very end of dendrite terminals were in higher numbers relative to those with higher plaque-to-end distances. We found that the Cx36 number was considerably higher at <1 μm distance from terminal endings than more proximal terminal segment areas and this difference was significant (**Figure 5A**; Wilcoxon signed-rank test, $p < 0.01$).

To examine this issue further, we next obtained dendrograms for all hRGCs, and Cx36 plaque numbers for both terminal dendrites and entire dendritic arbors were collected. Next, we performed a "Terminal segment analysis" by which the "terminal segment plaques/total plaque number" and the "terminal segment length/total dendrite length" ratios were utilized to determine "terminal segment density/total dendritic density" rates for all hRGCs (**Figure 5B**, **Supplemental Figure 3**). We found that density rates of most hRGCs ($n = 42$ out of 47; ~89%) were >1 indicating higher plaque density over terminal branches (**Figure 5B**); **Supplemental Figures 3A,B**). Moreover, the density rate was >2 for almost a quarter of cells ($n = 11$ out of 47; ~23%) suggesting that Cx36 plaques were twice as numerous at terminal dendrites of these cells than over the rest of their arbors, and for some cells ($n = 4$ out of 47; ~8%) the density rate was 3–7 times higher. These numbers clearly showed that the terminal dendritic branches of hRGCs are preferred sites to form gap junctions with other inner retinal neurons **Figure 5E**.

The dendritic distribution and location of Cx36 plaques were further examined by obtaining information on the position of Cx36 plaques in each dendritic segment with regard to the vicinity of dendritic branches. Calculating the Cx36 plaque distance along branch as a fraction of the total segment length allowed the observation and comparison of plaque positions on their respective segments. In this analysis, plaques with relative low and high values were located in the vicinity to proximal (closer to the soma) and distal (farther from the soma) ends of the segments, respectively. In contrast, the rest of the plaques were located in the midst of their corresponding segments. The frequencies of these distance fractions per cell were plotted.

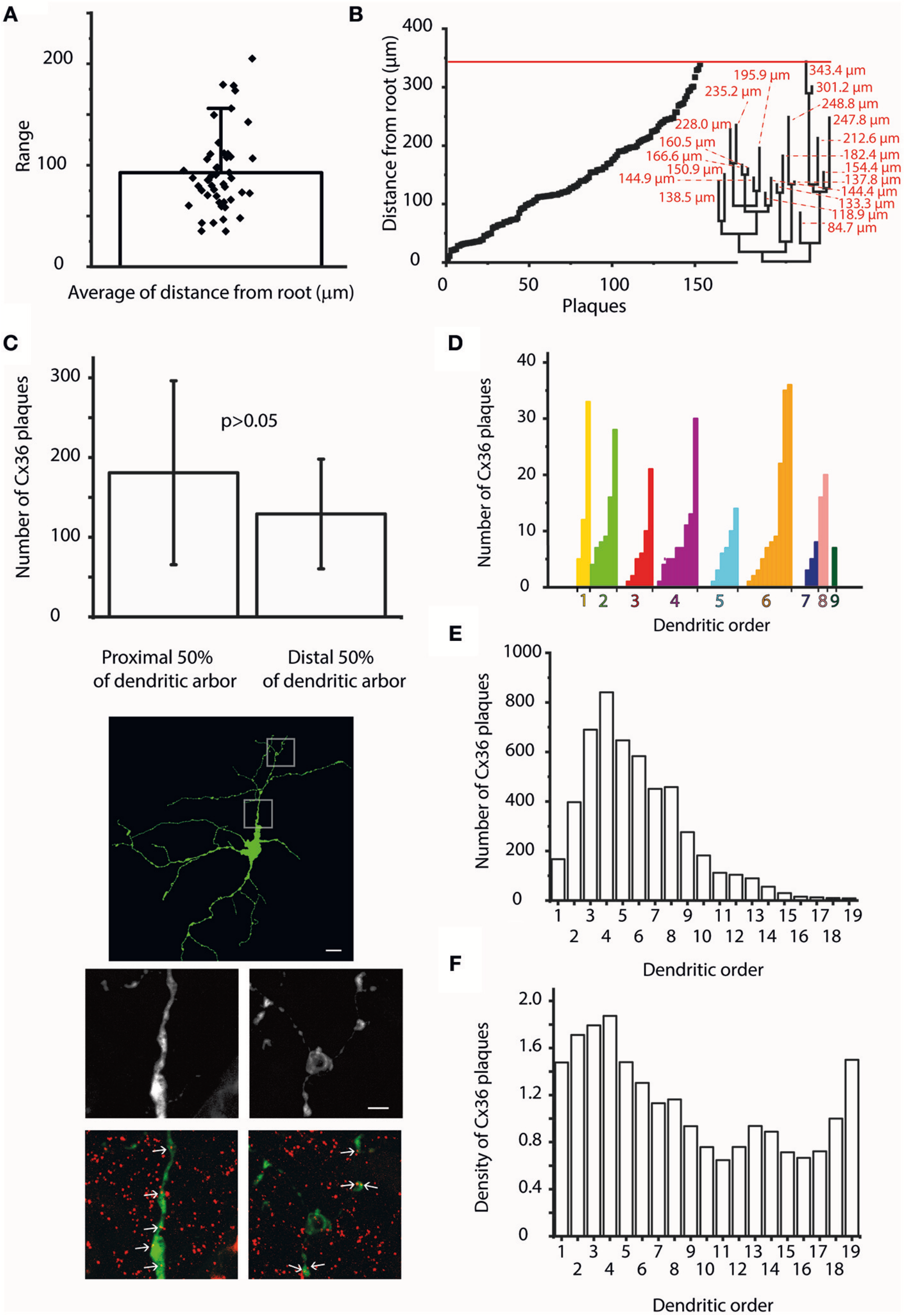

FIGURE 3 | The distance from the soma and dendritic order do not influence Cx36 plaque locations. **(A)** Bar-overlap chart and scatterplot showing the average soma-plaque distance for the 47 hRGCs as well as the average distances for the individual hRGCs. It appears that the actual position of the Cx36 GJs along the dendritic arbor display a relatively even distribution and also a rather wide range. **(B)** Soma-plaque distances were plotted in an ascending order for a representative hRGC. It appears that values display an overall even distribution. Note, that neighboring values do not necessarily correspond to nearby plaques on the same segment or even on the same dendritic branch. Dendrogram on the right shows the structure of the entire arbor with soma-tip distances (red). Red line on the top delineates the distance of the distalmost terminal ending. This combined image shows that distal dendritic locations are just as populous as proximal ones, thus the soma-plaque distance most likely is not a principal factor in determining Cx36 plaque locations. **(C)** Bargraph compares the average Cx36 plaque numbers within the proximal and distal half arbors for six randomly selected hRGCs with large dendritic trees (bars over the columns represent SDs). Clearly, the amount of Cx36 are not significantly different between the proximal and distal halves of dendritic arbors (Wilcoxon signed-rank test, $p = 0.22$). Photomicrographs show a representative hRGC with large dendritic field (top). High magnification images show details of the proximal (middle left) and the distal (middle right) dendrites; images on the bottom show corresponding LY/Cx36 double labeled versions of the same dendritic areas. Largely the same number of Cx36 colocalizations (arrows) could be recognized in both

(Continued)

FIGURE 3 | proximal and distal dendritic arbors. **(D)** Histogram displays the number of colocalizing Cx36 plaques for each dendritic segment of a representative hRGC. Dendritic segments are grouped based on their orders and then sorted into an ascending order of the colocalizing Cx36 numbers. This analysis showed no obvious sign of order related preference for the location of plaques as segments with both low and high Cx36 numbers were found for most branch types.
(E) Histogram displays the Cx36 plaque numbers for all segments of all examined cells of this study as a function of the segmental dendritic order. This analysis resulted a lognormal distribution of the colocalizing plaques with the highest values in 4th order dendrites. **(F)** In order to account for the difference in numbers of segments within a certain dendritic order, the plaque density was calculated and plotted against the dendritic order for all segments of all examined cells. The highest amount still found in the 4th order dendrites, but with a more homogenous distribution. In addition, this analysis revealed a second peak of the histogram for the highest order processes suggesting that terminal dendritic segments are preferred locations for Cx36 plaques. Scale bars: 25 and 5 μm in the low- and high magnification panels, respectively.

Counting the number of plaques within the first and last 10% of each segment, gave an indication whether the preferred plaque position was closer to either ends of the segments. These analyses were performed for every cell and no general pattern could be defined suggesting that the vicinity of dendritic branches is not a general plaque location determining factor (**Figures 5C,D**).

Tendency of Cx36 Plaques to Form Clusters

Having obtained the aforementioned dendrogram for each cell, a "plaque distribution on segment" analysis was also performed and plaque distances measured from the beginning of each segment were recorded ("distance along branch"). These measurements provided data on distances between plaques allowing for the generation of "distance frequency" histograms for each hRGC. This analysis showed that a high percentage of plaque intervals (1866 out of 3390) were 5 μm or less (**Figure 6A**). To support this observation, ratios of nearby (<5 μm) and total plaque numbers on each dendritic segments were calculated. This analysis showed that 33 out of 47 cells had ratios >0.5 meaning that more than half of the examined plaques were closer than 5 μm to their nearest neighbor (**Figure 6B and C**). This indicated that a significant portion of plaques formed clusters (at least pairs) for most examined hRGCs. Furthermore, we counted 2.95 times as many plaques as plaque bearing segments suggesting that many segments had more than one (∼3) plaque on their surfaces ($n = 3{,}227$ out of 3,990 segments in all of the cells; 80.9%).

In order to analyse the distribution of Cx36 plaques on unique segments, we performed Kolmogorov-Smirnov test on each Cx36 bearing segment with at least 10 samples against uniform density of plaques and also against exponentional density of plaque distance intervals. No significant ($p < 0.01$) deviation from uniform density or exponential density were detected (Bonferroni correction was applied). We also performed a pooled analysis of Cx36 plaque densities over all segments to shed light on Cx36 density inhomogeneities. We calculated plaque densities up to 140 μm distance along segments with 20 μm bin resolution for each segment, and treated the calculated density values as separate populations per bin. We compared the population means (Kruskal-Wallis H test) and found that the mean densities over bins significantly deviated from uniform density ($p < 0.01$). This analysis showed that Cx36 plaque density was not uniform over segment length, however the small number of Cx36 plaques per unique segments prevented drawing straightforward conclusions about the spatial distribution-pattern of plaques.

DISCUSSION

Methodological Considerations

Due to the obvious difficulty obtaining human material for experimental purposes, the quantity of our specimen was limited in terms of the utilized samples ($n = 3$ individuals; see Materials and Methods). In addition, only a fraction of the eyes was available for us to inject and counter label hRGCs. Another limiting factor was the challenging nature of the successful intracellular injection of cells in the fixed post-mortem retinas. However, we still successfully injected hRGCs with a rather high success rate (∼60–70%) in such material by adopting and refining a previously existing method (Kántor et al. 2016b). The pool of injected cells contained over 80 hRGCs but only 47 cells with fully labeled arbor and good quality Cx36 counterlabels were used in this work. Our goal was to label hRGCs with various soma sizes to obtain data for several (preferentially all) hRGC subtypes in the human retina. However, certain cell types were easier to encounter and inject thus they are likely overrepresented in our sample. Some of the well-represented hRGCs resemble P or M cells based on their morphological characteristics (Kolb et al., 1992), whereas others may have only a few (or none) representatives in our sample. One hRGC type, with very large cuboid soma were targeted several times but failed to fill fully with the LY dye. We suspect that this cell corresponds to the G23 (monster) cell in Kolb's dataset. This was supported by the fact that we lacked a cell in our sample that shared the characteristic morphological features of G23 cells including the largest somata in the human retina (Kolb et al., 1992). Another limitation of our dataset was that all utilized tissues originated from peripheral areas, which prevented us to examine possible area specific variations in the plaque distribution of hRGCs. However, such area specific comparison is out of the focus of this study and the limited area specific sampling also lowers the number of variables that can affect the dendritic distribution of Cx36 plaques. Contrary to all the above listed limitations this study provides the first overall view on the dendritic distribution of Cx36 plaques over hRGC arbors. Such description allows us to further assess the degree of similarity (or dissimilarity) of hRGCs and those of model animals in order to infer and use results of animal studies for clinical purposes.

Cx36 Plaque Labels of hRGCs

We reported previously that certain Ca^{++}-binding proteins including calretinin (CaR), parvalbumin (PV) and calbindin (CaB) are expressed (exclusively or in combination) in specific subsets of hRGCs (Kántor et al., 2016b). Although, we found

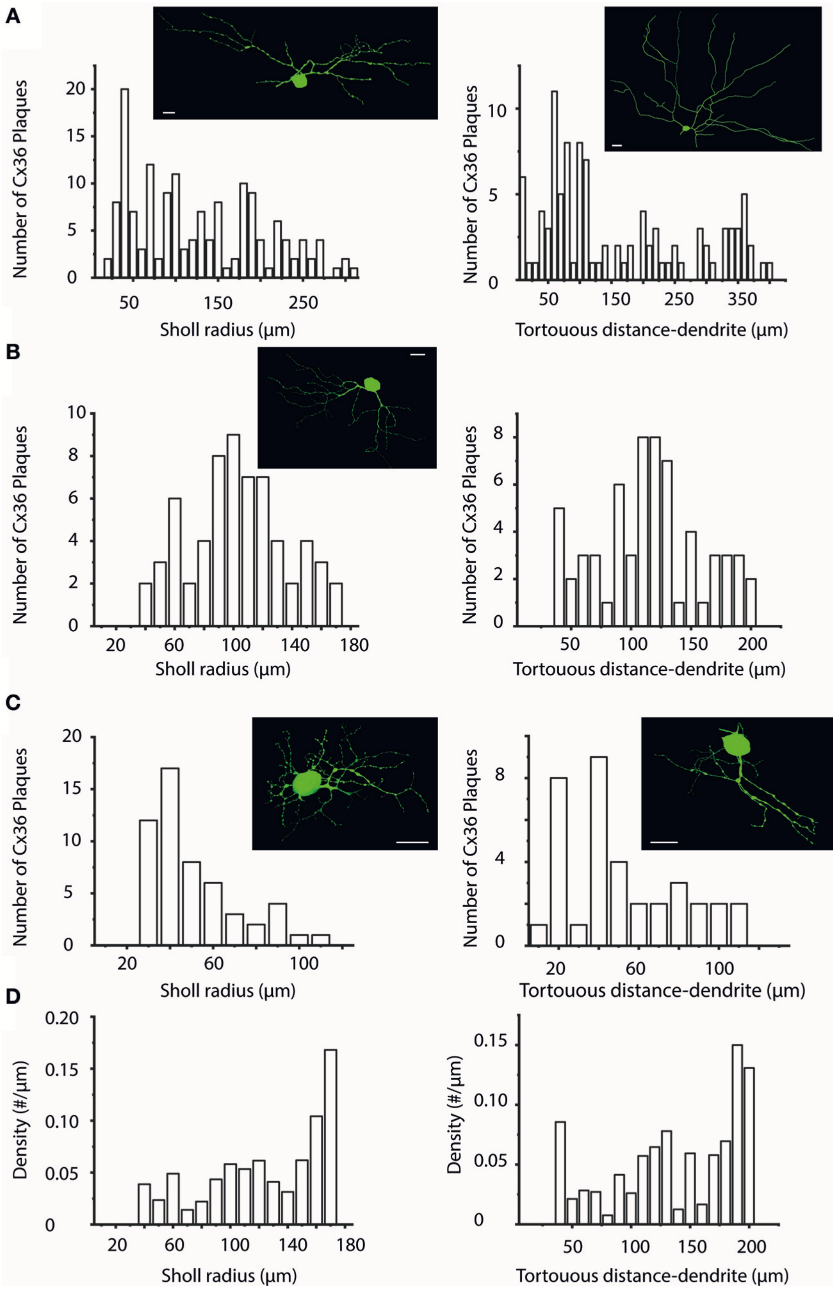

FIGURE 4 | Sholl- and Tortuous Distance Analyses of Cx36 plaques over hRGC dendritic arbors. **(A–C)** Sholl (left panels) and Tortuous Distance (right panels) analyses shown for representative hRGCs (top, middle, and bottom) to visualize the Cx36 plaque distribution as a function of distance (10 μm bins) to the soma. As our sample contained many different hRGC subtypes we found plaque distributions with very different patterns including those appeared random (**A,C** right), showing near Gaussian shape **(B)**, descending (**C** left). These analyses thus did not seem to reveal preferred dendritic locations for Cx36 plaques that are general features for the entire examine hRGC population. Images on the top of each panel display a representative hRGC. Note, that both left and right panels in b display histograms of the same hRGC. **(D)** Due to the fact that actual dendritic segment numbers and lengths may differ considerably in each step window, the plaque density was also plotted against both the Sholl (left) and the Tortuous Distance (right) radii. The two panels in **(D)** shown here were generated on the dataset for the hRGC shown in **(B)**. These graphs clearly show in both the Sholl and the Tortuous Distance Analyses that the distalmost bins display the highest plaque density, suggesting that dendritic terminal endings bear a special importance. Scale bars: 25 μm.

colocalizations of Cx36 plaques with these hRGC markers (**Supplemental Figure 4**) these markers were not selective but labeled multiple cell types and many of those were non-hRGCs. Therefore, multiple label immunohistochemistry was not an adequate method to collect data for this present study. In contrast intracellular LY injections in the fixed human sample appeared to provide hRGC labels in sufficient quality that allowed us to collect data.

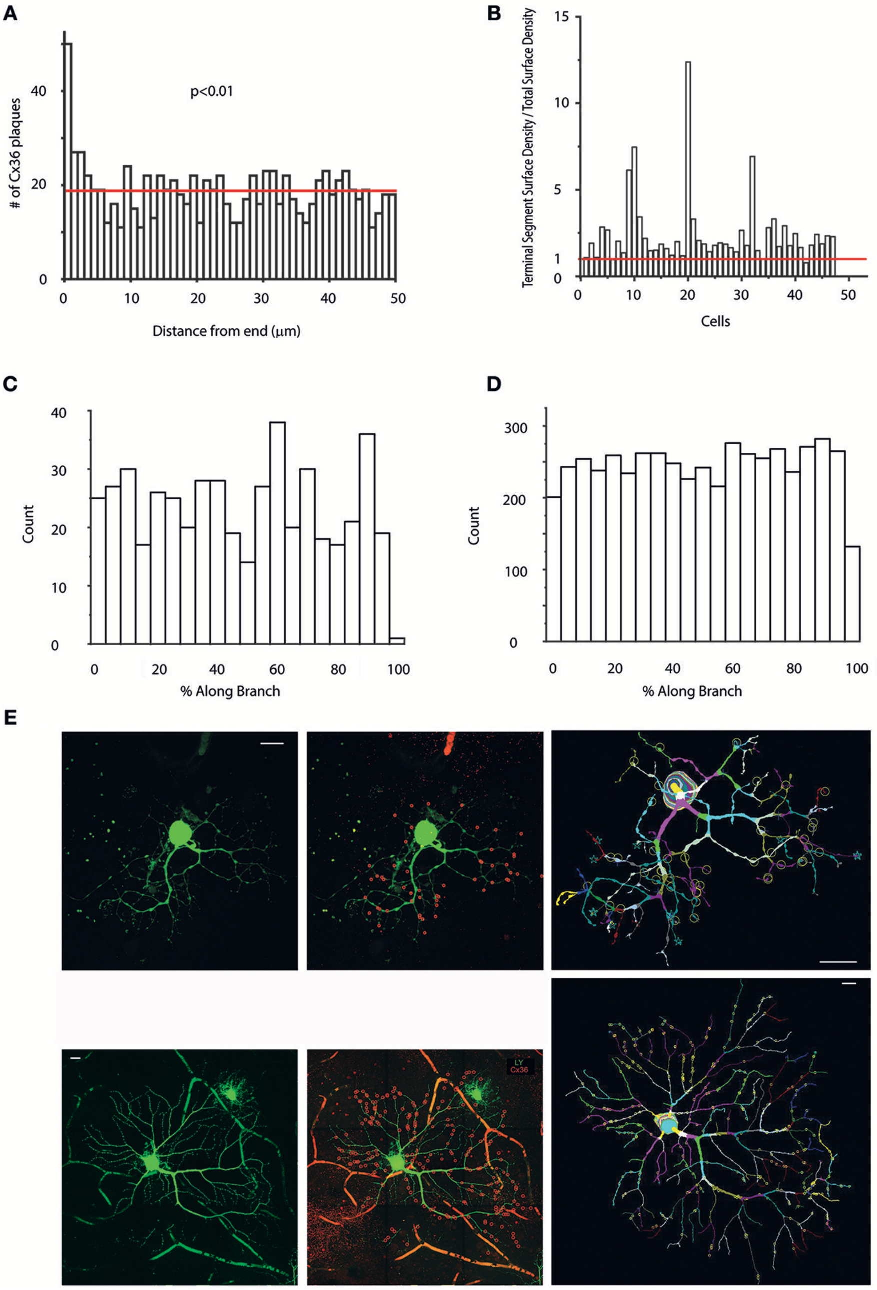

FIGURE 5 | Preferred Cx36 plaque locations in hRGC dendritic arbors. **(A)** Histogram showing the numbers of Cx36 plaques located at only terminal segments as a function of the distance from the ending. Note, that only terminal segments with lengths $>50\,\mu$m (shorter segments would skew the analysis toward the lower values) were selected for this analysis (the red line marks the mean). Clearly Cx36 plaques located at terminal dendritic segments prefer sites that are close to the very endings (Wilcoxon signed-rank test). **(B)** Histogram shows the "Terminal Segment Surface Density/Total Surface Density" ratio for cells in this study (x axis) to reveal if terminal endings are preferred sites for Cx36 plaques. It can clearly be seen that the terminal segment density is higher than the overall density (red line) in case of most (44 out of 47) cells (see also length and volume density charts in **Supplemental Figure 3**). **(C,D)** Graphs display Cx36 plaque counts as a function of the percentage of total length (distance from proximal branch-point/total segment length *100) of their respective dendritic segment for one representative hRGC **(C)** and all cells in the sample **(D)**. Note, that these analyses contain only non-terminal segments, whereas previous analyses in **(B)** examined only terminal segments. Cx36 plaques with lower values are located in the vicinity of proximal end of the segment (end closer to the soma) whereas Cx36 plaques with high values are close to distal branch points (end farther from the soma). We found that both individual histograms and the combined histogram displays no sign of any favored segment locations for Cx36 plaques. **(E)** Two representative hRGCs (left panels) maintaining many Cx36 plaques (red circles in the middle panels and letter marks in the right panel; red circles mark only colocalized Cx36 plaques that were confirmed in Neurolucida reconstructions) over their dendritic arbor. Many colocalizing Cx36 plaques were located near to the terminal endings as shown in both the photograph (middle) and the corresponding Neurolucida reconstruction (right) for both neurons. The cell on the bottom displays a soma-dendritic morphology reminiscent of parasol (M) hRGCs based on previous descriptions by Kolb et al. (1992) Scale bars: $25\,\mu$m.

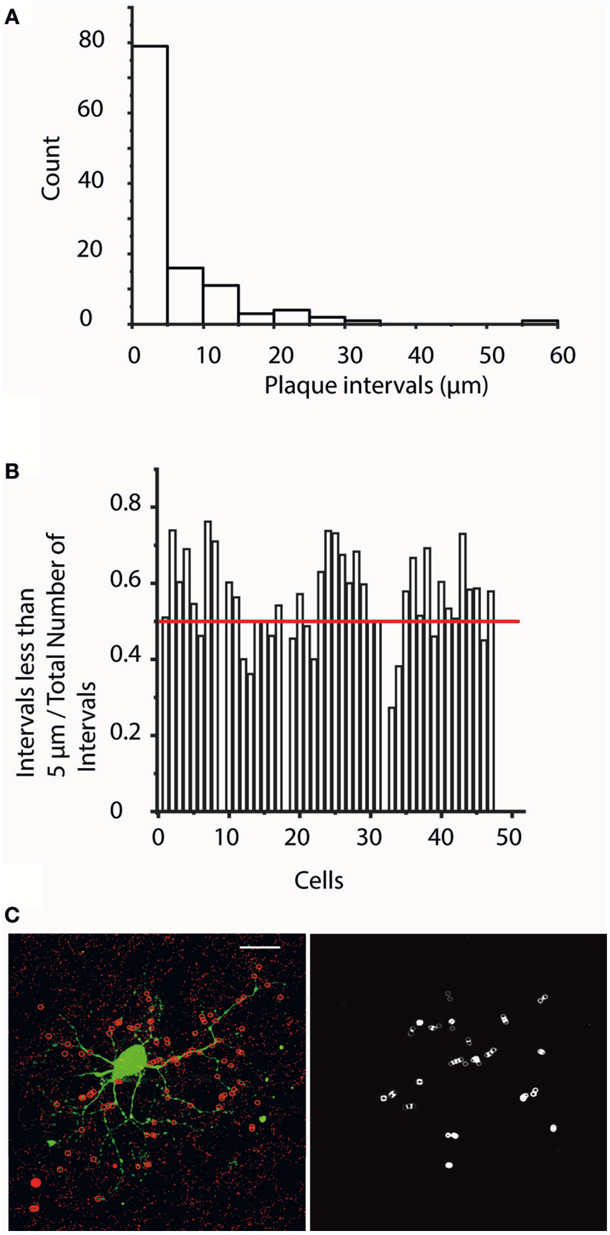

FIGURE 6 | Cx36 plaques tend to form clusters. **(A)** Bar histogram shows the results of "plaque interval" measurements (bin size 5 μm) for one representative hRGC. This analysis provides distance values measured between each plaque and its direct proximal neighbor. It is clear that plaque distances </= 5 μm occur most often indicating that Cx36 plaques of this neuron have a tendency to cluster into doublets or perhaps even triplets. **(B)** This histogram displays the ratio of the number of <5 μm intervals and the total number of intervals for all hRGCs of this study. This analysis indicates that 33 cells display ratios >0.5, suggesting that the majority of the plaques for these 33 cells form pairs/clusters. Note, that very small cells with only one plaque per segment have no plaque intervals, hence on this chart they show up with a value of 0. **(C)** Image on the left displays a representative hRGC and Cx36 labels. Colocalizing plaques were marked with red circles overlaid on dendrites for better visibility (red circles mark only colocalized Cx36 plaques that were confirmed in Neurolucida reconstructions). Note that this hRGC is the same as the one shown in **Figure 1**. The image to the right display circles that mark direct neighbor Cx36 plaques in <5 mm apart. Scale bars: 25 μm.

RGCs of many animal models maintain GJs with neighbor cells and most of these contacts are Cx36 dependent (Hidaka et al., 2004; Schubert et al., 2005a; Völgyi et al., 2005, 2009; Pan et al., 2010). Therefore, it is not surprising that dendritic branches of many cells in our sample colocalized with Cx36 plaques in the counterstained specimen. Although, each potentially colocalizing plaque was thoroughly tested it is inevitable that few colocalizations are only virtual and added noise to our dataset. It is possible to estimate the signal to noise ratio by examining Cx36 colocalizations of hRGCs for cells that have been confirmed uncoupled and thus do not maintain GJs. However, no reports have been published on hRGC GJ coupling and Cx36 expression yet. On the other hand, non-human primate P-cells (parvocellular ganglion cells) have been shown uncoupled when GJ permeable tracer was injected into their soma, whereas M cells maintained extensive tracer couplings (Dacey and Brace, 1992). Assuming that non-human primate and human retinas are similar in this respect, Cx36 colocalizations with human P-cells only happen by chance and not due to the existence of P cell GJ sites. We did not perform a RGC classification in this work but performed a raw sorting based on soma/dendritic dimensions and morphology of hRGCs, which resulted in P-like and non-P-like group of cells. We found in fact that cells in the P-like group associated with low number and density of colocalizing plaques. Both the plaque numbers and density values were significantly lower for P-like cells than those of non-P-like cells even though the latter group was still a heterogeneous neuron population of coupled and uncoupled cells (**Supplemental Figure 1**, Mann–Whitney U test; plaque number: $p = 1.24 \times 10^{-4}$, plaque SA Density: $p = 0.023$). This observation thus suggests that both non-human and human P cells are uncoupled and also indicates that our dataset contains a low level of noise in regard of LY/Cx36 colocalizations. Assuming the same noise level for all examined cells (P-like and non-P-like) we conclude that the signal-to-noise ratio (S/N) in this study was high enough to observe colocalizations associated with real hRGC GJ sites and draw conclusions based on collected data. In addition, apparent colocalizations of Cx36 plaques and putative uncoupled P-like hRGCs also sets the limit for false positive labels. **Supplemental Figure 1** shows that only a small set of non-P cells display Cx36 numbers as low as those of P-like hRGCs. This indicates that the noise due to false positive labels of this study is rather low. It also suggests that similar to the Cx36 expression of RGCs other mammalian species (Völgyi et al., 2009; Pan et al., 2010) most hRGCs maintain Cx36 GJs to contact neighbor RGCs and/or amacrine cells.

Strategic Positioning of Cx36 Plaques Across hRGC Dendritic Arbors

One of our main aims throughout this study was to identify particular locations on hRGC dendritic trees that are preferred sites for Cx36 GJs. We failed to reveal favored Cx36 plaque distance to soma, favored dendritic segment order or the preference for the vicinity to dendritic branching points. On the other hand, we have to point out that our sample is comprised by a heterogeneous neuron population thus our analyses only allowed us to reveal general features shared by the majority of the examined hRGC population. Besides these general features it is possible that certain hRGC subtypes possess preferred Cx36 GJ distance to soma, dendritic order or GJ location along dendritic segments. In fact, we expect that a larger pool of hRGCs could be subdivided based on morphological features. Such a collection of data will allow for recognizing potential cell type specific variations of GJ sites. Contrary to the heterogeneity of the dataset we found a few marked general features of Cx36 GJ locations over hRGC dendrites. These included the tendency of Cx36 plaques to position frequently on terminal dendritic branches. Moreover, we found evidence that many of these GJ sites are $>5\,\mu$m from the very end of their corresponding terminals. This finding suggests that certain intercellular contacts favor the periphery of hRGC dendritic arbor areas. It has been shown that alpha RGCs in the rat retina maintain tip-to-tip GJ contacts with their immediate neighbors that allows them to form electrically coupled arrays (Hidaka et al., 2004). The existence of similar homologous RGC-to-RGC electrical and tracer coupling has been shown for many other mammalian species as well-including rabbits, mice and non-human primates (Dacey and Brace, 1992; DeVries, 1999; Schubert et al., 2005a,b; Völgyi et al., 2005, 2009, 2013a,b). Such pan-mammalian feature of RGCs is then very likely shared by at least a few subsets of hRGCs as well. Therefore, we think that the observed Cx36 plaques found in the dendritic terminals reflect sites of hRGC-to-hRGC homologous GJs. The tip-to-tip configuration is a necessary arrangement, according to which RGCs obey to territorial rules to avoid significant dendritic overlaps with same subtype neighbors thereby reducing redundant sampling and at the same time they still maintain minimal dendritic overlap that allows nearby RGC to form direct GJ contacts. Besides homologous GJs, model animal RGCs electrically couple to nearby amacrine cells as well (Kenyon and Marshak, 1998; Hu and Bloomfield, 2003; Schubert et al., 2005a; Völgyi et al., 2005, 2009, 2013a,b; Bloomfield and Völgyi, 2009; Hu et al., 2010; Pan et al., 2010; Roy et al., 2017). This latter set of GJs serve as an indirect contact between RGCs in an extended (several hundreds of μm-s) retinal surface area (Bloomfield and Völgyi, 2009; Hu et al., 2010). The fact, that amacrine cells which are involved in these heterologous GJs are typically wide-field and polyaxonal amacrine cells (Schubert et al., 2005a; Völgyi et al., 2005, 2009; Roy et al., 2017), means that their processes run several hundreds of μm-s and that they do not share the territorial avoidance rule with the contacting RGCs. Consequently, the RGC-to-amacrine cell GJs are not necessarily located on RGC terminals, but they can be formed on any RGC dendritic segment. Following this logic, the number of non-terminal Cx36 GJ sites must exceed those of terminal dendrite Cx36 GJs, because model animal RGC-to-amacrine cell GJs are maintained by most RGC subtypes, whereas RGC-to-RGC direct contacts are established by only a handful of RGC populations (Völgyi et al., 2009, 2013b; Pan et al., 2010). These observations are now supported by our finding in the human retina that the overall number of Cx36 plaques was rather high for most but a few cells in our sample with higher density values in terminal dendrites. This suggests that hRGCs, similar to their model animal counterparts, form both heterologous hRGC-to-amacrine and homologous hRGC-to-hRGC contacts. These two types of RGC coupling patterns have been shown to serve various forms of action potential synchronizations in model animals (Mastronarde, 1983; Brivanlou et al., 1998; DeVries, 1999; Hu and Bloomfield, 2003; Bloomfield and Völgyi, 2009; Völgyi et al., 2013a,b), therefore we posit that they fulfill similar spike synchronization roles for hRGCs as well. In addition, it has been shown that Golgi interneurons in the cerebellum maintain distal dendritic GJs in high densities to counteract sublinear dendritic integration and enable distal excitatory synapses to drive network activity more effectively (Vervaeke et al., 2012). Similarly, a higher density of Cx36 GJ plaques was found in hRGCs of this study suggesting that besides spike synchronization hRGC GJs at terminal endings may serve to counteract sublinear integration of chemical synaptic inputs due to passive dendrite cable properties.

Tendency of Cx36 Plaques to Form Clusters

A second general feature of this Cx36 plaque distribution survey was the finding that plaques along dendritic segments have a tendency to cluster together. This clustering of Cx36 plaques, to the best of our knowledge, has not been shown before even in model animal experiments. Our dual staining methodology does not allow the visualization and identification of the synaptic partners of hRGCs that partake in GJ contacts, therefore we can only speculate about the function of such plaque cluster formation. If clustered GJs are formed by the same synaptic partner than it is possible that two or three contacts are formed nearby to strengthen the efficacy of the electrical synaptic connection between the contacting neurons. On the other hand, if nearby GJ sites are established with dendritic processes of two (or more) synaptic partners, then there is a possibility for the integration of their inputs. In this scheme, depending on the timing of the incoming signals and/or refractory period inputs, they can enhance or abolish each other functioning as AND, OR, or XIR logical gates, respectively. Besides the possibility of parallel inputs to hRGCs through nearby GJs, it is also possible that GJ site doublets also serve as outputs from hRGCs to multiple synaptic partners, likely amacrine cells. In this latter scenario, hRGCs (and likely RGCs of mammalian models as well) besides sending information toward visual brain centers would also serve with intraretinal output signals for the retinal hypercircuit as well. Through such information loops certain RGC subtypes may affect the functioning of other retinal RGC subtypes. However, the present dataset is very limited and thus future experiments are necessary to prove any of the above hypotheses.

AUTHOR CONTRIBUTIONS

OK performed most experiments and helped out with the experimental design, GD performed some experiments, GS did most of the analysis and some of the manuscript writing, ZB and ZS performed some of the analysis, EP, GR, and RN helped out with the experiments, GB obtained tissues for the experiments

and BV designed the experiments, did some of the analysis and wrote the manuscript.

FUNDING

Supported by the Hungarian Brain Research Program (KTIA_NAP_13-2-2015-0008) and Hungarian Brain Research Program 2 (2017-1.2.1.-NKP-2017) to BV. This research was supported by the European Union and the State of Hungary, co-financed by the European Social Fund in the framework of TÁMOP-4.2.4.A/ 2-11/1-2012-0001 National Excellence Program to BV as well as by the UNKP-17-3-I-PTE-155 New National Excellence Program of the Ministry of Human Capacities. This work was also funded by the European Social Fund in the framework of EFOP-3.6.2-16-2017-00008 The role of neuro-inflammation in neurodegeneration: from molecules to clinics to the Centre for Neuroscience, University of Pécs.

ACKNOWLEDGMENTS

Supported by the Hungarian Brain Research Program (KTIA_NAP_13-2-2015-0008; 2017-1.2.1-NKP-2017-00002) to BV by the European Union and the State of Hungary, co-financed by the European Social Fund in the framework of TÁMOP- 4.2.4.A/2-11/1-2012-0001 National Excellence Program to BV and by the European Union and the Sate of Hungary, co-financed by the European Social Fund (EFOP-3.6.1.-16-2016-00004). The authors thank Zsuzsanna Vidra and Brigitta Fadgyas for their technical or organizational assistance.

SUPPLEMENTARY MATERIAL

The Supplementary Material for this article can be found online at: https://www.frontiersin.org/articles/10.3389/fncel.2018.00409/full#supplementary-material

Supplemental Figure 1 | Number (top) and plaque density (bottom) differences between P-like and non-P-like hRGCs. Statistical analyses reveal that P-like cells display considerably less Cx36 plaque colocalizations than non-P-like cells (Wilcoxon signed-rank test $P < 0.05$). The somata and dendritic arbors of representative P-like and non-P-like hRGCs are shown above the corresponding bars. Scale bars: 25 μm.

Supplemental Figure 2 | Number **(A)**, plaque length density **(B)** and plaque surface density **(C)** histograms for all examined hRGCs display non-homogenously increasing values with several plateaus. This indicates that cells in these analyses form subgroups.

Supplemental Figure 3 | (A,B) Terminal segment length density / total length density **(A)** as well as terminal segment volume density/total segment volume density **(B)** ratios are presented. Should a cell have value >1, that means plaques of that certain cell are most frequent in their terminal segments. Both charts display that for most cells (length density: 42 out of 47 cells, volume density: 34 out of 47) the ratios are > 1.

Supplemental Figure 4 | (A–F) Images display multiple immunolabels of PV, CaR, CaB, and Cx36. Colocalizing Cx36 plaques can be detected on CaR+ **(A,B)**, on CaB+ **(C,D)**, on PV+ **(E)** and on CaB/PV dually stained **(F)** hRGC dendritic processes. It has been shown that PV/CaB dual labeled hRGCs display OFF parasol cell morphology (Kántor et al., 2016b). Scale bars: 20 μm.

Supplemental Table 1 | Table shows measured parameters for all examined hRGCs of this study (left column), the total dendritic lengths (second column, number of all colocalizing Cx36 plaques (third column), the number of Cx36 plaques colocalizing with terminal dendrites, number of all plaque intervals for each cell (fourth column) and the number of plaque intervals < 5 micrometer.

REFERENCES

Bloomfield, S. A., and Völgyi, B. (2009). The diverse functional roles and regulation of neuronal gap junctions in the retina. *Nat. Rev. Neurosci.* 10, 495–506. doi: 10.1038/nrn2636

Brivanlou, I. H., Warland, D. K., and Meister, M. (1998). Mechanisms of concerted firing among retinal ganglion cells. *Neuron* 20, 527–539. doi: 10.1016/S0896-6273(00)80992-7

Cruciani, V., and Mikalsen, S. O. (2006). The vertebrate connexin family. *Cell. Mol. Life Sci.* 63, 1125–1140. doi: 10.1007/s00018-005-5571-8

Dacey, D. M., and Brace, S. (1992). A coupled network for parasol but not midget ganglion cells in the primate retina. *Vis. Neurosci.* 9, 279–290.

Dacey, D. M., and Petersen, M. R. (1992). Dendritic field size and morphology of midget and parasol ganglion cells of the human retina. *Proc. Natl. Acad. Sci. U.S.A.* 89, 9666–9670. doi: 10.1073/pnas.89.20.9666

Deans, M. R., Völgyi, B., Goodenough, D. A., Bloomfield, S. A., and Paul, D. L. (2002). Connexin36 is essential for transmission of rod-mediated visual signals in the mammalian retina. *Neuron* 36, 703–712. doi: 10.1016/S0896-6273(02)01046-2

DeVries, S. H. (1999). Correlated firing in rabbit retinal ganglion cells. *J. Neurophysiol.* 81, 908–920. doi: 10.1152/jn.1999.81.2.908

Feigenspan, A., Teubner, B., Willecke, K., and Weiler, R. (2001). Expression of neuronal connexin36 in AII amacrine cells of the mammalian retina. *J. Neurosci.* 21, 230–239. doi: 10.1523/JNEUROSCI.21-01-00230.2001

Furshpan, E. J., and Potter, D. D. (1957). Mechanism of nerve-impulse transmission at a crayfish synapse. *Nature* 180, 342–343. doi: 10.1038/180342a0

Güldenagel, M., Ammermüller, J., Feigenspan, A., Teubner, B., Degen, J., Söhl, G., et al. (2001). Visual transmission deficits in mice with targeted disruption of the gap junction gene connexin36. *J. Neurosci.* 21, 6036–6044. doi: 10.1523/JNEUROSCI.21-16-06036.2001

Güldenagel, M., Söhl, G., Plum, A., Traub, O., Teubner, B., Weiler, R., et al. (2000). Expression patterns of connexin genes in mouse retina. *J. Comp. Neurol.* 425, 193–201. doi: 10.1002/1096-9861(20000918)425:2<193::AID-CNE3>3.0.CO;2-N

Han, Y., and Massey, S. C. (2005). Electrical synapses in retinal ON cone bipolar cells, subtype-specific expression of connexins. *Proc. Natl. Acad. Sci. U.S.A.* 102, 13313–13318. doi: 10.1073/pnas.0505067102

Hidaka, S., Akahori, Y., and Kurosawa, Y. (2004). Dendrodendritic electrical synapses between mammalian retinal ganglion cells. *J. Neurosci.* 24, 10553–10567. doi: 10.1523/JNEUROSCI.3319-04.2004

Hombach, S., Janssen-Bienhold, U., Söhl, G., Schubert, T., Büssow, H., Ott, T., et al. (2004). Functional expression of connexin57 in horizontal cells of the mouse retina. *Eur. J. Neurosci.* 19, 2633- 2640. doi: 10.1111/j.0953-816X.2004.03360.x

Hu, E. H., and Bloomfield, S. A. (2003). Gap junctional coupling underlies the short-latency spike synchrony of retinal alpha ganglion cells. *J. Neurosci.* 23, 6768–6777. doi: 10.1523/JNEUROSCI.23-17-06768.2003

Hu, E. H., Pan, F., Völgyi, B., and Bloomfield, S. A. (2010). Light increases the gap junctional coupling of retinal ganglion cells. *J. Physiol.* 588(Pt 21), 4145–4163. doi: 10.1113/jphysiol.2010.193268

Kántor, O., Benk˝, Z., Énzsöly, A., Dávid, C., Naumann, A., Nitschke, R., et al. (2016a). Characterization of connexin36 gap junctions in the human outer retina. *Brain Struct. Funct.* 221, 2963–2984. doi: 10.1007/s00429-015-1082-z

Kántor, O., Mezey, S., Adeghate, J., Naumann, A., Nitschke, R., Énzsöly, A., et al. (2016b). Calcium buffer proteins are specific markers of human retinal neurons. *Cell Tissue Res.* 365, 29–50. doi: 10.1007/s00441-016-2376-z

Kántor, O., Varga, A., Nitschke, R., Naumann, A., Énzsöly, A., Lukáts, Á., et al. (2017). Bipolar cell gap junctions serve major signaling pathways in the human retina. *Brain Struct. Funct.* 222, 2603–2624. doi: 10.1007/s00429-016-1360-4

Kenyon, G. T., and Marshak, D. W. (1998). Gap junctions with amacrine cells provide a feedback pathway for ganglion cells within the retina. *Proc. Biol. Sci.* 265, 919–925.

Kihara, A. H., Mantovani de Castro, L., Belmonte, M. A., Yan, C. Y., Moriscot, A. S., and Hamassaki, D. E. (2006). Expression of connexins 36, 43, and 45 during postnatal development of the mouse retina. *J. Neurobiol.* 66, 1397–1410. doi: 10.1002/neu.20299

Kihara, A. H., Santos, T. O., Osuna-Melo, E. J., Paschon, V., Vidal, K. S., Akamine, P. S., et al. (2010). Connexin-mediated communication controls cell proliferation and is essential in retinal histogenesis. *Int. J. Dev. Neurosci.* 28, 39–52. doi: 10.1016/j.ijdevneu.2009.09.006

Kolb, H., Linberg, K. A., and Fischer, S. K. (1992). Neurons of the human retina: a golgi study. *J. Comp. Neurol*. 318, 147–187. doi: 10.1002/cne.903180204

Kovács-Öller, T., Debertin, G., Balogh, M., Ganczer, A., Orbán, J., Nyitrai, M., et al. (2017). Connexin36 Expression in the mammalian retina: a multiple-species comparison. *Front. Cell. Neurosci*. 11:65. doi: 10.3389/fncel.2017.00065

Kovács-Öller, T., Raics, K., Orbán, J., Nyitrai, M., and Völgyi, B. (2014). Developmental changes in the expression level of connexin36 in the rat retina. *Cell Tissue Res*. 358, 289–302. doi: 10.1007/s00441-014-1967-9

Lee, E. J., Han, J. W., Kim, H. J., Kim, I. B., Lee, M. Y., Oh, S. J., et al. (2003). The immunocytochemical localization of connexin 36 at rod and cone gap junctions in the guinea pig retina. *Eur. J. Neurosci.* 18, 2925–2934. doi: 10.1046/j.1460-9568.2003.03049.x

Longair, M. H., Baker, D. A., and Armstrong, J. D. (2011). Simple neurite tracer: open source software for reconstruction, visualization and analysis of neuronal processes. *Bioinformatics* 27, 2453–2454. doi: 10.1093/bioinformatics/btr390

Massey, S. C., O'Brien, J. J., Trexler, E. B., Li, W., Keung, J. W., Mills, S. L., et al. (2003). Multiple neuronal connexins in the mammalian retina. *Cell Commun. Adhes.* 10, 425–430. doi: 10.1080/cac.10.4-6.425.430

Mastronarde, D. N. (1983). Interactions between ganglion cells in cat retina. *J. Neurophysiol*. 49, 350–365. doi: 10.1152/jn.1983.49.2.350

Maxeiner, S., Dedek, K., Janssen-Bienhold, U., Ammermüller, J., Brune, H., Kirsch, T., et al. (2005). Deletion of connexin45 in mouse retinal neurons disrupts the rod/cone signaling pathway between AII amacrine and ON cone bipolar cells and leads to impaired visual transmission. *J. Neurosci.* 25, 566–576. doi: 10.1523/JNEUROSCI.3232-04.2005

Mills, S. L., O'Brien, J. J., Li, W., O'Brien, J., and Massey, S. C. (2001). Rod pathways in the mammalian retina use connexin36. *J. Comp. Neurol.* 436, 336–350. doi: 10.1002/cne.1071

Müller, L. P., Dedek, K., Janssen-Bienhold, U., Meyer, A., Kreuzberg, M. M., Lorenz, S., et al. (2010). Expression and modulation of connexin 30.2, a novel gap junction protein in the mouse retina. *Vis. Neurosci.* 27, 91–101. doi: 10.1017/S0952523810000131

O'Brien, J. J., Chen, X., Macleish, P. R., O'Brien, J., and Massey, S. C. (2012). Photoreceptor coupling mediated by connexin36 in the primate retina. *J. Neurosci*. 32, 4675–4687. doi: 10.1523/JNEUROSCI.4749-11.2012

Pan, F., Paul, D. L., Bloomfield, S. A., and Völgyi, B. (2010). Connexin36 is required for gap junctional coupling of most ganglion cell subtypes in the mouse retina. *J. Comp. Neurol.* 518, 911–927. doi: 10.1002/cne.22254

Pedregosa, P., Varoquaux, G., Gramfort, A., Michel, V., Thirion, B., Grisel, O., et al. (2011). Scikit-learn: machine learning in python. *J. Mach. Learn. Res.* 12, 2825–2830. *arXiv:1201.0490v4* [Preprint].

Roy, K., Kumar, S., and Bloomfield, S. A. (2017). Gap junctional coupling between retinal amacrine and ganglion cells underlies coherent activity integral to global object perception. *Proc. Natl. Acad. Sci. U.S.A.* 114, E10484–E10493. doi: 10.1073/pnas.1708261114

Schindelin, J., Arganda-Carreras, I., Frise, E., Kaynig, V., Longair, M., Pietzsch, T., et al. (2012). Fiji: an open-source platform for biological-image analysis. *Nat. Methods* 9, 676–682. doi: 10.1038/nmeth.2019

Schmid, B., Schindelin, J., Cardona, A., Longair, M., and Heisenberg, M. (2010). A high-level 3D visualization API for Java and ImageJ. *BMC. Bioinformatics* 11, 274. doi: 10.1186/1471-2105-11-274

Schubert, T., Degen, J., Willecke, K., Hormuzdi, S. G., Monyer, H., and Weiler, R. (2005a). Connexin36 mediates gap junctional coupling of alpha-ganglion cells in mouse retina. *J. Comp. Neurol.* 485, 191–201. doi: 10.1002/cne.20510

Schubert, T., Maxeiner, S., Krüger, O., Willecke, K., and Weiler, R. (2005b). Connexin45 mediates gap junctional coupling of bistratified ganglion cells in the mouse retina. *J. Comp. Neurol.* 490, 29–39. doi: 10.1002/cne.20621

Söhl, G., Joussen, A., Kociok, N., and Willecke, K. (2010). Expression of connexin genes in the human retina. *BMC Ophthalmol.* 10:27. doi: 10.1186/1471-2415-10-27

Söhl, G., and Willecke, K. (2003). An update on connexin genes and their nomenclature in mouse and man. *Cell Commun. Adhes.* 10, 173–180. doi: 10.1080/cac.10.4-6.173.180

Vervaeke, K., Lorincz, A., Nusser, Z., and Silver, R. A. (2012). Gap junctions compensate for sublinear dendritic integration in an inhibitory network. *Science* 335, 1624–1628. doi: 10.1126/science.1215101

Völgyi, B., Abrams, J., Paul, D. L., and Bloomfield, S. A. (2005). Morphology and tracer coupling pattern of alpha ganglion cells in the mouse retina. *J. Comp. Neurol.* 492, 66–77. doi: 10.1002/cne.20700

Völgyi, B., Chheda, S., and Bloomfield, S. A. (2009). Tracer coupling patterns of the ganglion cell subtypes in the mouse retina. *J. Comp. Neurol*. 512, 664–687. doi: 10.1002/cne.21912

Völgyi, B., Kovács-Oller, T., Atlasz, T., Wilhelm, M., and Gábriel, R. (2013a). Gap junctional coupling in the vertebrate retina, variations on one theme? *Prog. Retin. Eye Res*. 34, 1–18. doi: 10.1016/j.preteyeres.2012.12.002

Völgyi, B., Pan, F., Paul, D. L., Wang, J. T., Huberman, A. D., and Bloomfield, S. A. (2013b). Gap junctions are essential for generating the correlated spike activity of neighboring retinal ganglion cells. *PLoS ONE* 8:e69426. doi: 10.1371/journal.pone.0069426

Watanabe, A. (1958). The interaction of electrical activity among neurons of lobster cardiac ganglion. *Jpn. J. Physiol*. 8, 305–318. doi: 10.2170/jjphysiol.8.305

Conflict of Interest Statement: The authors declare that the research was conducted in the absence of any commercial or financial relationships that could be construed as a potential conflict of interest.

frontiers
in Cellular Neuroscience

METHODS
published: 07 December 2018
doi: 10.3389/fncel.2018.00481

Non-parametric Physiological Classification of Retinal Ganglion Cells in the Mouse Retina

Jonathan Jouty[1], *Gerrit Hilgen*[2], *Evelyne Sernagor*[2] *and Matthias H. Hennig*[1]*

[1] *Institute for Adaptive and Neural Computation, School of Informatics, University of Edinburgh, Edinburgh, United Kingdom,*
[2] *Institute of Neuroscience, Newcastle University, Newcastle, United Kingdom*

Retinal ganglion cells, the sole output neurons of the retina, exhibit surprising diversity. A recent study reported over 30 distinct types in the mouse retina, indicating that the processing of visual information is highly parallelised in the brain. The advent of high density multi-electrode arrays now enables recording from many hundreds to thousands of neurons from a single retina. Here we describe a method for the automatic classification of large-scale retinal recordings using a simple stimulus paradigm and a spike train distance measure as a clustering metric. We evaluate our approach using synthetic spike trains, and demonstrate that major known cell types are identified in high-density recording sessions from the mouse retina with around 1,000 retinal ganglion cells. A comparison across different retinas reveals substantial variability between preparations, suggesting pooling data across retinas should be approached with caution. As a parameter-free method, our approach is broadly applicable for cellular physiological classification in all sensory modalities.

Keywords: retinal ganglion cells, multi-electrode array, light responses, classification, spike distance

Edited by:
Bela Volgyi,
University of Pécs, Hungary

Reviewed by:
Karl Farrow,
Neuroelectronics Research Flanders,
Belgium
Günther Zeck,
Natural and Medical Sciences
Institute, Germany

***Correspondence:**
Matthias H. Hennig
m.hennig@ed.ac.uk

Received: *01 September 2018*
Accepted: *26 November 2018*
Published: *07 December 2018*

Citation:
Jouty J, Hilgen G, Sernagor E and Hennig MH (2018) Non-parametric Physiological Classification of Retinal Ganglion Cells in the Mouse Retina. Front. Cell. Neurosci. 12:481. doi: 10.3389/fncel.2018.00481

INTRODUCTION

It is well established that the retina has multiple, functionally complementary populations of retinal ganglion cells (RGCs), which together transmit visual information to various central visual areas (Roska and Werblin, 2001). Strikingly, the stratification of RGC dendrites in the inner plexiform layer predicts response polarity and kinetics extremely well. In addition, the retinotopic organization of RGCs is such that each type independently covers the visual space through receptive field tiling as regular mosaics. The retina is among the first neural systems where a clear correspondence between morphology, physiology and function of different cell types has been established (Wässle et al., 1981; Rockhill et al., 2000; Sun et al., 2002; Badea and Nathans, 2004; Kong et al., 2005; Völgyi et al., 2009; Masland, 2012; Jones et al., 2015; Sterling and Laughlin, 2015), an organizing principle that likely exists in other neural systems as well. The actual classification of RGCs typically requires a combination of measures of their cellular physiology, light responses, morphology and, more recently, their gene expression patterns and connectome (Helmstaedter et al., 2013; Macosko et al., 2015; Sanes and Masland, 2015; Krieger et al., 2017; Rheaume et al., 2018).

Despite such well defined principles, in practice classification of RGC types has been challenging because it is difficult to implement all criteria in a single experiment. Classification is particularly challenging when attempted solely based on light responses. In previous studies, features were extracted from responses to a set of stimuli designed to reveal the main spatial and temporal receptive field properties, as well as specific properties such as direction selectivity (DS). Using this approach, Farrow and Masland (2011) found 12 distinct types, which mirrors a similar number of morphological types identified through unsupervised clustering (Kong et al., 2005). Moreover, consistent patterns in spike trains have been shown to allow distinction between major RGC types (Zeck and Masland, 2007). Numerous, more detailed studies have since refined and extended this picture, but without reaching a clear consensus. Recently (Baden et al., 2016), combining clustering, dimensionality reduction of peri-stimulus time histograms (PSTH) and other response criteria and morphological information, reported at least 39 distinct RGC types.

Previous studies thus appear to suggest that light responses alone do not contain sufficient information for reliable RGC classification unless a careful stimulus ensemble is designed to evoke optimal responses, in particular for specialized RGCs such as DS cells. Yet, if different RGC types have distinct cellular physiological properties, light responses, and systematic differences in their presynaptic input neurons, it may be possible to use a sufficiently rich stimulus to evoke responses to unmask their distinctive functional features. Here we propose that it is not necessary to use stimuli that optimally excite the receptive field of each RGC type. Instead, we expect that these cellular differences cause perhaps subtle, but detectable differences in the light responses even to non-optimal stimuli. The actual identity of each RGC type, including specific properties such as DS, can then be confirmed *post-hoc* using more specific stimuli.

A main caveat in previous studies was that RGC recordings from multiple preparations were pooled together to obtain a data set of sufficient size. Large scale, high density microelectrode arrays (MEAs) now make it possible to record large populations comprising thousands of cells from a single retina (Maccione et al., 2014; Portelli et al., 2016; Hilgen et al., 2017a,b). This reduces contaminating effects of variability between animals and experimental conditions, and allows precise control of stimulation for all recorded neurons.

Extending an idea first presented by Zeck and Masland (2007), here we present a method for clustering RGCs based on spike distance measures, which is particularly suited for high density recordings. Its main advantage is that it is a parameter-free distance measure for clustering. We first validate the method using synthetically generated RGC spike trains. The results show that the methods using the parameter-free spike distances compare favorably to clusterings based on feature vectors, especially in the presence of low to medium levels of noise. On recorded RGC data, the method is able to distinguish many distinct RGC types, as confirmed by assessing response properties during stimulation that was not part of the data used for clustering. A comparison between different retinas shows that similar types can be identified, but that heterogeneity between preparations prevents the use of pooled data. Together our work suggests a new strategy for consistent identification of RGC types, and potentially of neurons in other sensory systems where appropriate stimulation paradigms can be designed.

METHODS

All code to reproduce the experimental data analysis presented in this paper, and an example data set is available at https://github.com/mhhennig/rgc-classification. This repository contains additional analysis, and hopefully provides a starting point for refinement and extension of the methods presented in this paper. We therefore encourage the reader to explore this resource, and to contribute to its improvement.

Spike Train Distance Based Clustering

ISI Distance

This measure is sensitive to dissimilarity in the inter-spike intervals (ISI) of two spike trains (Kreuz et al., 2007). The instantaneous ISI distance is the ratio between the ISIs, adjusted so that the distance is symmetric:

$$D_{\mathrm{ISI}}(t) = \begin{cases} \nu^x_{\mathrm{ISI}}(t)/\nu^y_{\mathrm{ISI}}(t) - 1, & \text{if } \nu^x_{\mathrm{ISI}}(t) \le \nu^y_{\mathrm{ISI}}(t) \\ -(\nu^y_{\mathrm{ISI}}(t)/\nu^x_{\mathrm{ISI}}(t) - 1), & \text{otherwise} \end{cases} \quad (1)$$

where $\nu^x_{\mathrm{ISI}}(t)$ and $\nu^y_{\mathrm{ISI}}(t)$ are the instantaneous inter-spike interval values for spike trains x and y, respectively.

SPIKE Distance

The SPIKE distance compares the distances between the preceding and following spikes of the two spike trains (Kreuz et al., 2011, 2013). First, the interval between the previous and following spike pairs are computed as

$$\begin{cases} \Delta t_P(t) = t^{(1)}_P(t) - t^{(2)}_P(t) \\ \Delta t_F(t) = t^{(1)}_F(t) - t^{(2)}_F(t), \end{cases} \quad (2)$$

where 1 and 2 indicate the first and second spike train, and P denotes the spike pair before or at time t, and F the pair at or following t. Then a weighted average is computed as

$$D_{\mathrm{S}}(t) = \frac{||\Delta t_P(t)|| < x^{(n)}_F(t) >_n + ||\Delta t_F(t)|| < x^{(n)}_P(t) >_n}{< x^{(n)}_{\mathrm{ISI}}(t) >^2_n}, \quad (3)$$

where $< x^{(n)}_T(t) >$ is the average of the intervals $x^{(n)}_T(t) = t - t^{(n)}_T(t)$, such that spikes closer together in time dominate the measure.

The ISI and SPIKE measures yield a quasi-instantaneous distance profile, which is averaged to obtain a single distance measure for each pair. These distances were computed using the open source package PySpike (Mulansky and Kreuz, 2016, version 0.5.3). Specifically, the pairwise distances between two units were determined by computing the pairwise distances of all trials of the same stimulus. The resulting distance matrix was then clustered with the hierarchical clustering algorithm as implemented in the Scipy library (Jones et al., 2001, version 1.0.1), using the Ward variance minimization algorithm, as this gave the best results on ground truth data.

Synthetic RGC Responses

Model

To evaluate the clustering quality, synthetic RGC spike trains emulating eight known base types, were generated using a linear-nonlinear-Poisson (LNP) model. The stimulus $s(t)$ was similar to the chirp stimulus used in the MEA experiments (see below) (**Figure 1**): 1.5 s darkness, followed by 2 s full intensity and 2 s darkness; midpoint luminance "gray" value for 2 s; frequency modulation $s_{\text{chirp: freq.}}(t_f) = \sin(\pi t_f^2)$ for 5 s; 2 s midpoint luminance; amplitude modulation $s_{\text{chirp: ampl.}}(t_a) = 0.2t \sin(3\pi t_a)$ for 5 s; 2 s midpoint luminance.

We generated symmetric ON and OFF RGC types, with fast/slow and transient/sustained temporal characteristics, using Gabor functions with two parameters (Dayan and Abbott, 2001):

$$k(t) = p\mathcal{N}\left(t, 0, \frac{l}{2}\right) \sin\left(2\pi \left(\frac{t}{l}\right)^{v}\right) \tag{4}$$

where $\mathcal{N}$ is the Gaussian probability density function, and p the response polarity. This response is normalized in the range $[-1, 1]$.

Here l is the "length" of the temporal receptive field, and modulates over how much the time the RF integrates the stimuli, and v is the "speed" that affects how quickly the cell responds to changes in the stimuli intensity. A "long" RF thus averages out high frequency stimuli, whereas a "short" one is sensitive to high frequency stimuli, consistent with the main known distinguishing characteristics of RGC receptive fields (Sanes and Masland, 2015; Sterling and Laughlin, 2015). Note that these simulated RFs do not have a spatial component, instead its effect during homogeneous illumination can be considered as parameterized by the temporal component. Importantly, the integral $\int_0^\infty k(t)dt$ is constant for a fixed v, hence RFs with a different "length" but the same "speed" will have identical maximum linear response magnitudes, which allows testing the effect of response kinetics independent of response magnitude.

The cell's RF filter $\vec{k}$ is convolved with the time-varying stimulus $s(t)$ to yield the cell's linear response. To simulate spikes, this response is passed through a non-linear function $r(x)$ which transforms the linear response into an instantaneous spike rate. We used a logistic

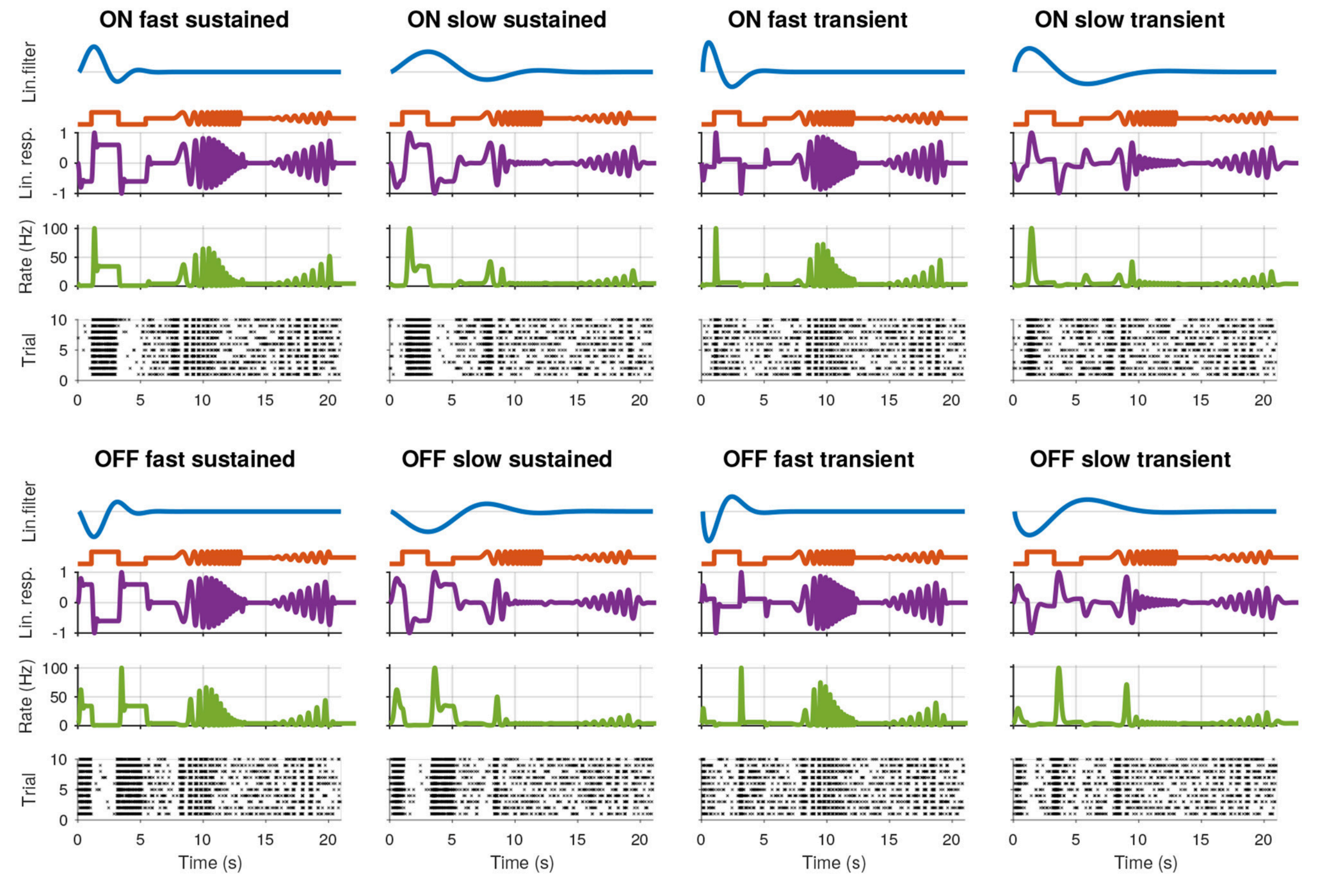

FIGURE 1 | Synthetic retinal ganglion cell response models. For each of the eight cell types, rows from top to bottom: (i) the linear receptive field (RF) of the cell; (ii) the stimulus; (iii) the linear response of the cell, computed by convolving the RF with the stimulus; (iv) the spike rate obtained by passing the linear response through a non-linear function; and (v) the spike raster generated using a Poisson process.

sigmoid function:

$$r(x) = \frac{2r_{\max} - r_{\min}}{1 + e^{-c(x-1)}} + r_{\min} \tag{5}$$

To match observations made in the recorded RGC spike trains, $r_{\min}$ was set to 0.5, and $r_{\max}$ to 100. By changing c and observing the effect on the different cell types, a value of 4.0 was found to result in the most balanced spike rate response across all types.

Finally, Poisson spike trains were generated in discrete time bins (dt) of 1 ms based on the instantaneous rate $P(\text{spike}|r) = r(t) \times dt$.

Model Parameter Selection

We modeled eight cell types by combining the following parameters: "On" and "Off": $p = 1$ and $p = -1$; "Fast" and "slow": $l = 0.4$ and $l = 1.0$; "Transient:" and "sustained:": $\nu = 0.65$ and $\nu = 1.2$. The resulting spike trains for the simulated cells, consisting of eight types, are shown in **Figure 1** together with each cell's RF, the stimulus, linear response to the stimulus, and instantaneous spike rate.

RF Parameter Variation

To simulate cellular variability, each of the baseline RF parameters was varied by sampling from a Gaussian distribution centered around the baseline value, and constrained to positive values. The standard deviation was varied as a percentage proportion of the baseline value, using 5, 10, 15, 20, and 30% of each of the baseline parameters.

Imbalanced Populations

To take into account that different RGC types are found in unequal numbers, imbalanced data sets were created. As representative examples, cell type frequencies were manipulated based on %-ON and %-fast, %-ON and %-transient, and %-fast and %-transient, in steps of 10%: %-ON from 30 to 70%, %-fast from 10 to 90%, and %-transient fixed at 50%; %-ON from 30 to 70%, %-transient from 10 to 90%, and %-fast fixed at 50%; %-transient from 30 to 70%, %-fast from 10 to 90%, and %-ON fixed at 50%. This yielded 120 distinct data sets.

Recording Noise

As perfect spike detection and sorting cannot be fully guaranteed in MEA recordings, the LNP model was augmented to include three sources of experimental noise:

1. Poisson process with a fixed rate throughout the stimulus time, either with a rate of $\beta = 2s^{-}1$, or with a rate randomly chosen uniform between 5 and 30 Hz. This simulates noise contamination of otherwise well isolated units.
2. Randomly removing 70% of the unit's spikes across all trials, simulating false negatives during detection and/or spike sorting.
3. Merging two spike trains from different RFs, to simulate failed single unit isolation.

To generate datasets contaminated with a known amount of noisy units, a random subset of the population was picked and replaced with one of the four noise models. The number of noisy units was evenly distributed between each of the four types. The percentage of noisy units as a percentage of the total population was varied from 10 to 90%, in increments of 10%, and a dataset was generated for each.

Experimental Data

MEA Recording

All experimental procedures were approved by the ethics committee at Newcastle University and carried out in accordance with the guidelines of the UK Home Office, under control of the Animals (Scientific Procedures) Act 1986. In this study, recordings from six C57bl/6 mice aged 59-101 days postnatal, housed under a 12 h light-dark cycle, were used. All experimental procedures are described in detail in Hilgen et al. (2017b). Pan-retinal recordings were performed on the BioCam4096 platform with BioChips 4096S+ (3Brain GmbH, Lanquart, Switzerland), integrating 4,096 square microelectrodes (21 by 21 µm, pitch 42 µm) on an active area of 2.67 by 2.67 mm. The platform records at a sampling rate of 7.1 kHz/electrode when using the full 4096 channel array and recordings were stored at 12 bits resolution per channel with a 8 kHz low-pass filter/0.8 kHz high-pass filter using 3Brain's BrainWave software. Light stimuli were projected onto the retina as described previously (Hilgen et al., 2017b) and attenuated using neutral density filters to high mesopic light levels (mean luminance 11 cd/m^2).

Spike Sorting

Spikes were detected and sorted using the algorithms described in Muthmann et al. (2015) and Hilgen et al. (2017a), using the HS2 software (https://github.com/mhhennig/HS2). Briefly, spikes were first detected as threshold crossings individually on each channel, and then merged into unique events based on spatial and temporal proximity. For each detected spike, a location was estimated based on the signal center of mass. Spike sorting was performed by clustering all events using a feature vector consisting of the locations and the first two principal components of the largest waveform.

Analysis of Light Responses

The bias index (Carcieri et al., 2003) was computed from full field responses as

$$\text{OOi} = \frac{\langle r_{ON} \rangle_t - \langle r_{OFF} \rangle_t}{\langle r_{ON} \rangle_t + \langle r_{OFF} \rangle_t}, \tag{6}$$

where $\langle r_{ON} \rangle_t$ and $\langle r_{OFF} \rangle_t$ are the spike count during the bright and dark part of the stimulus, respectively.

DS was assessed by first recording the maximum spike count for each of 12 directions of a moving bar stimulus, and dividing this by the average across all stimuli and mean spike count of a neuron relative to its minimum spike rate for each of the moving bar stimuli:

$$r_{\min\max} = r_{\max} - r_{\min} \tag{7}$$

where $r_{\max}$ is the maximum and $r_{\min}$ is the minimum spike rate, calculated by counting the number of binned spikes, in this case using 200 ms wide bins. Taking the relative rate was required as it was found that the mean firing rate of the units drifted across the different moving bar stimuli, regardless of their actual peak response. The relative maximum rate was transformed into a vector representing the direction of the stimuli, and the first two normalized eigenvalues were used to compute the DSi:

$$\mathrm{DSi} = 1 - \frac{\lambda_1}{\lambda_2} \tag{8}$$

This value is bounded $[0, 1]$, with a higher value signifying stronger DS.

The linear receptive field was computed as the spike triggered average (STA) stimulus, obtained during white noise stimulation. To increase the spatial resolution, the stimulus squares were shifted randomly with each presentation, as described by Hilgen et al. (2017a). A bivariate Gaussian was fitted to each STA at the time of the first peak, and its average width taken as the receptive field size.

Unit Selection

To avoid false negatives during detection, a low detection threshold was used (threshold 10, see Muthmann et al., 2015 for definition), which led to an excessive high number of putative units. To isolate well-sorted neurons from this set, several heuristic criteria were applied: First, to be included, the eccentricity of the ellipse defined by a bivariate Gaussian fit to the spatial spike locations of each unit was thresholded to <0.85, and the average of the two axes thresholded to below $<17\%$ of the channel separation (7.14 μm). This removed units with poorly localized, and therefore potentially poorly sorted units. Units recorded from the two outer channel rows were removed as this impaired spike sorting. Next, only units with at least 10 spikes in each trial of the chirp stimulus were retained. Here we used six retinas, with a final count of 1,026, 1,849, 1,234, 634, 1,131, and 575 units.

RESULTS

Our procedure to obtain functional RGC clusters consists of two steps. First a spike distance matrix is computed for all single unit pairs in the recording, which is then clustered using agglomerative clustering. This requires a distance measure with the metric properties of non-negativity, zero distance for identity, symmetry and subadditivity (the sum of two distances has to be greater than or equal than the individual distances). These conditions are fulfilled by a number of metrics (Victor, 2005; Kreuz et al., 2007, 2013), of which we evaluated the non-parametric ISI and SPIKE distance measures. Then hierarchical clustering is used to construct a dendrogram based on the distance matrix. In the following, we will first validate this method with synthetic data, and then show its application to a high density MEA recording from the mouse retina.

Evaluation With Synthetic Data

We first evaluate the method with a synthetic ground-truth data set, which contains eight different RGC types (see Methods). Spike trains were generated using LNP models, and the spike distance matrix was computed, followed by hierarchical agglomerative clustering using Ward's linkage. This procedure yields a dendrogram, which was cut such that eight flat clusters were obtained. We note that the last step is not feasible for recorded spike trains, where the number of RGC types is not known. We address this issue below when analyzing an experimental data set.

First we combine all 140 datasets created using the LNP model. In addition to the spike distance-based methods, the ISI and SPIKE distances, we also used the raw PSTH, and the PCA and sparse PCA of the PSTH for comparison (see Baden et al., 2016 for an application of sparse PCA). To assess the quality of the clustering, the median score of the following four measures was used: the adjusted Rand index, which summarizes the fraction of correct clustering choices based on true/false negatives/positives (Murphy, 2012); the adjusted mutual information, which quantifies information gain over random clustering (Vinh et al., 2010); the Fowlkes-Mallows score, the geometric mean of precision and recall; and the completeness score measuring if all true cluster members are in the same cluster. Across almost all conditions, the scores of each individual quality index were very similar. The distribution of the median scores across all conditions for each method is shown in **Figure 2**.

This comparison shows that the different feature sets yield a similar performance. However, it should be noted that the methods using PSTHs, either alone or through a form of dimensionality reduction, require selecting and optimizing the PSTH bin size. Secondly, PCA requires selecting the dimensionality, and sparse PCA has an additional L1 penalty parameter. An exploration of the ground truth data showed that all these parameters strongly affect clustering quality. For the results shown in **Figure 2**, the parameters were optimized through an extensive grid search.

For the PSTH-based clustering, a bin size of 200 ms resulted in the best overall performance, which also proved to be the

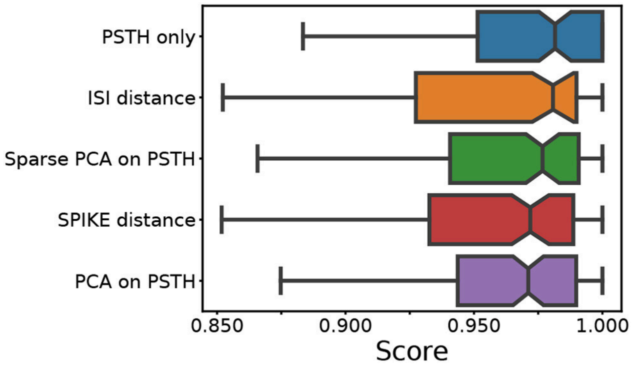

FIGURE 2 | Median score across all conditions. For each of the five feature sets, four external clustering quality scores (adjusted Rand index, adjusted mutual information score, V-measure, and the Fowlkes-Mallows score) were computed for each dataset. The median of the four scores is calculated for each dataset. Finally, the medians for the various datasets (140) are presented in the form of a box plot, one for each method. A higher score implies a better clustering result. Each colored box plot shows the median and interquartile range (IQR). The error bars extend 0.8 times past the IQR in each direction. The methods are ordered from the highest median value (of median scores) to the lowest, from top to bottom.

best bin size for PCA and sparse PCA. Note that this large bin size was likely required due to the high variability introduced by the Poisson spike generation process. In real data, more precise spiking will require a smaller bin size. For PCA, using eight PCs worked best, whereas for sparse PCA, a penalty of 50 with 12 components provided the best scores.

In contrast, the ISI and SPIKE distance based clustering required no such parameter search. The fact that both methods have comparable or better performance demonstrates that they are suitable for the clustering of RGC types based on their physiological response. This is particularly important in the context of real data, where parameter optimisation can only be done heuristically.

Synthetic Data With Biological Variability

Comparing the methods as a function of cell number and RF variation, we find that the performance degraded rapidly as the RF variation increased beyond 15% (**Figure 3**). In particular, the spike distance based measures performed slightly worse than the others as RF variation increased. In all cases, the worst performance is observed when the RF variation is at 30%, and the total number of units is high (800 units). Each of the methods performs consistently with regard to its relative overall performance (the order shown in **Figure 2**). This trend is consistent across all conditions of the synthetic dataset: permitting for minor local variations, there was no single direction in which any of the methods described performed characteristically better or worse.

Synthetic Data With Experimental Noise

To evaluate the effect of experimental noise, we systematically varied the proportion of noisy units (see Methods). For the three methods requiring parameter selection, the values that gave the best results on the non-noisy synthetic data were used. Here, only the labels of the "good," noise-free, units were compared between the clustering results and the original labels. Therefore, the comparison does not assess the methods for their ability to separate the "bad" noisy units from the "good" ones. Instead, the emphasis is purely on being able to separate the different types of RGCs from each other, even if noisy units belong to these clusters. The rationale for this choice is that if an RGC recording has been properly pre-processed and filtered, the proportion of bad units should be relatively low, and, therefore, the mean response of an RGC cluster should not be affected. Moreover, the noise model introduces new "types" of cells, hence constraining the results to eight flat clusters could force erroneous clustering results. Therefore, the results were evaluated against a range of numbers of flat clusters, representing different cutoff points within the hierarchy.

The median score across methods obtained for a clustering result of eight flat clusters show a significant degradation in reconstruction quality as the number of noisy units increases (**Figure 4**). The ISI and SPIKE distance measures in particular appear to deteriorate immediately upon the introduction of bad units, despite a comparable baseline. Closer inspection of the scores shows that the completeness score in particular reveals an interesting result. This score places emphasis on classes being grouped together, and will result in a score of 1.0 even if all classes

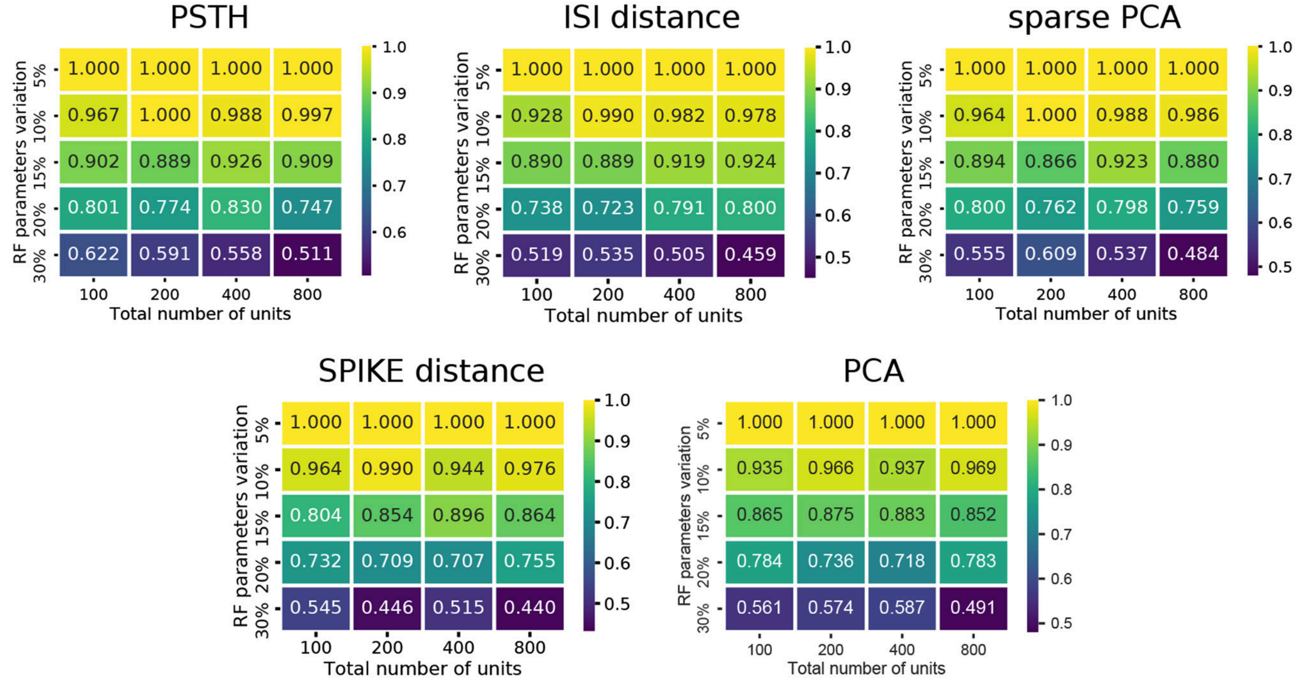

FIGURE 3 | Cluster quality measures as a function of RF variation and total number of units. For each of the five feature sets, the median of four clustering quality scores (adjusted Rand index, adjusted mutual information score, V-measure, and the Fowlkes-Mallows score) are shown for each dataset (140 in total).

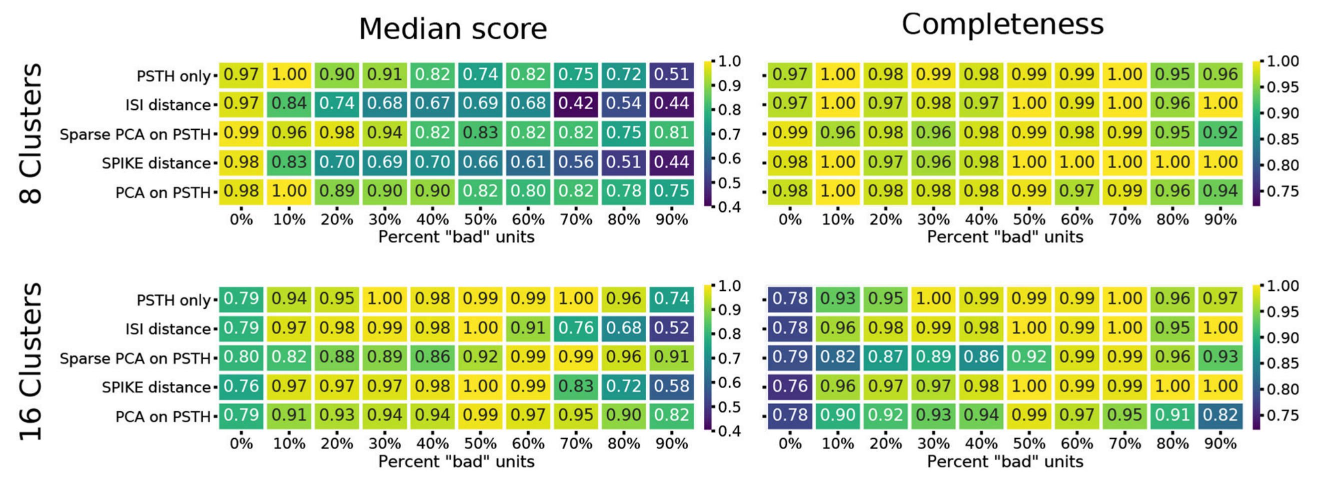

FIGURE 4 | Clustering quality scores on noisy data. For each of the five methods, the median of four external clustering quality scores (adjusted Rand index, adjusted mutual information score, V-measure, and the Fowlkes-Mallows score) are shown in the left panels. Right panels show the completeness score. The top row show the results for 8, and the bottom row for 16 flat clusters.

are part of a single cluster. The high completeness scores for the spike distance measures, in particular the SPIKE distance, for a high fraction of noisy units shows they correctly group RGC types with remarkable accuracy (**Figure 4**). This indicates that the SPIKE distance clustering separates the noisy units into their own clusters, and, as a result of the cutoff point in the hierarchy, a flat clustering of 8 groups is insufficient to capture all types. This leads to lower scores on the other measures, but would allow recovering a correct clustering when more flat clusters are allowed.

This is indeed the case when creating 16 flat clusters (**Figure 4**). While the median score of all the external clustering quality measures improves, the median quality score for the baseline case (0% bad units) is now, as expected, lower for all methods. However, the ISI and SPIKE distance methods improve dramatically for low to medium levels of noise (10–60%), with SPIKE distance surpassing all others over this range. Yet, both spike distance methods continue to fare poorly when the population is dominated by noisy units (70–90%). The completeness scores agree with these observations, but they go further by demonstrating that the reason for the poor performance in the high noise range does not affect its ability to continue to correctly group RGC types in highly contaminated data.

In sum, these results show that spike distance measures can be used to classify RGC responses. In comparison with other methods, the procedure does not depend on any parameters, which would have to be chosen heuristically and can significantly affect the clustering results. In addition, the SPIKE distance in particular is robust to experimental noise, which is hard to avoid in large scale, high-density recordings where manual data curation is infeasible. High completeness scores indicate that clusters are not wrongly mixed in this case, but instead noisy units form separate clusters that can be identified manually.

Clustering Experimental Data

Next we used the spike distance measures to cluster RGC types from one mouse retina high-density MEA recording. Following quality control (see Methods), a set of 1,026 well isolated RGCs was included in this analysis. Light-evoked activity used to compute the distance matrices was obtained during stimulation with either full field flashes, or a stimulus that included a full field contrast step, green and blue full field flashes and a chirp sequence (see Methods).

Hierarchical agglomerative clustering constructs a dendrogram, starting with each single unit as its own cluster, and iteratively merging units and resulting clusters with a minimum variance constraint. As we have shown for synthetic data, the spike distance measures are very robust to variability and noise. However, to ensure noisy units are indeed placed into their own clusters while preventing over-clustering, an appropriate dendrogram cut-off point has to be determined. We evaluated two common metrics: The first was the gap statistic, which compares the compactness of each cluster to a random surrogate (Tibshirani et al., 2001). Using the shuffled distance matrix as surrogate, this metric indicates the data contains between 17 and 18 clusters, depending on the stimulus and metric (**Figure 5A**). These numbers are similar to those reported by Farrow and Masland (2011), but fall short of the higher numbers given by Baden et al. (2016). However, we found that the gap statistic generally favors larger clusters in data with higher variability, as small clusters naturally yield squared distances closer to the random surrogate. Hence the gap statistic may be a measure too conservative to reliably assess data with potentially highly imbalanced clusters.

To see whether the data may contain more valid clusters, we turned to a consensus method. To this end, we compare the results obtained with the ISI and SPIKE distance for the two stimuli, using adjusted mutual information (Vinh et al., 2010). This peaked at 17 clusters for the full field stimulus, and 28

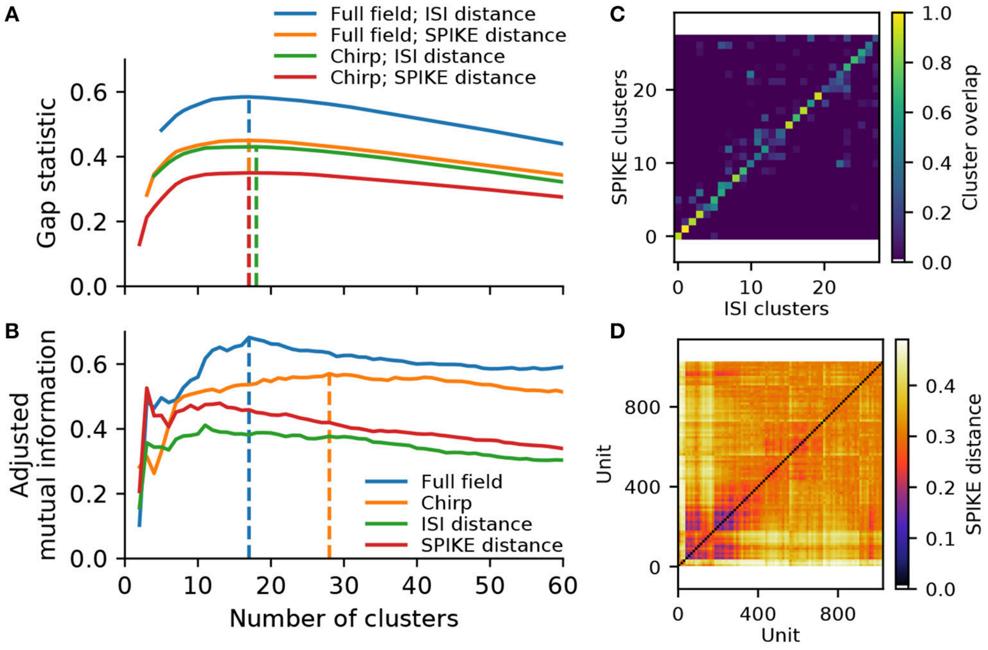

FIGURE 5 | Cluster metrics for a recording from 1,026 retinal ganglion cells. **(A)** The Gap statistic for the two spike distance metrics, computed for the full field and chirp stimulus, as a function of the number of flat clusters. Vertical lines indicate the peak of each curve. **(B)** Paired comparison of different clustering outcomes, quantified using adjusted mutual information. Two pairings were performed: between the ISI and SPIKE distance metrics for full field (blue) and chirp (orange), and between the two stimuli (full field and chirp) for either ISI (green) or SPIKE (red) distance. Vertical lines indicate the peak values for the comparison between spike distances. **(C)** Overlap between clusters obtained with the ISI and SPIKE metric, for 31 flat clusters. **(D)** The SPIKE distance matrix for all units, ordered by linkage.

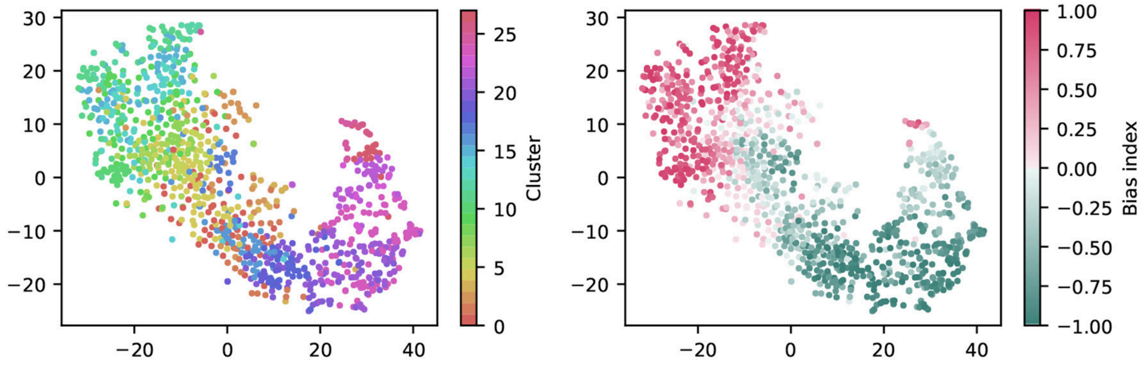

FIGURE 6 | Visualization of the clustering with t-SNE embeddings of the chirp responses. A t-SNE embedding was generated from chirp PSTHs (bin size 50 ms; perplexity 30). Each unit is colored either by cluster membership **(left)** or by bias index **(right)**. Note that similar colors in the cluster plot are perceptually hard to distinguish, colors were chosen such that a similar hue indicates proximity in the cluster dendrogram. The color coding is the same as in **Figure 7**.

clusters for the chirp stimulus (**Figure 5B**). Investigating this metric and the corresponding confusion matrices (see **Figure 5C** for the case of 28 clusters), it is evident that consensus is high for solutions with 15 or more clusters for both stimuli. In addition, the SPIKE distance consistently scored higher for a comparison between full field and chirp stimulus. Therefore, in the following we chose the SPIKE distance, using the peak consensus value of 28 clusters.

To get a first impression of the clustering result, we used t-distributed Stochastic Neighbor Embedding (t-SNE) to create a two-dimensional, non-linear embedding of the chirp PSTHs for visualization (**Figure 6**). In this plot, each dot represents a single cell, and spatial proximity indicates high similarity. Note however that the overall spatial arrangement is arbitrary and that distance does not imply similarity.

Coloring each dot by cluster membership reveals that the area covered by each cluster is limited (**Figure 6, left**). This suggests the clustering captures relevant structure in the data. Moreover, coloring the same plot by the bias index shows that it is a major contributor to similarity (**Figure 6, right**), a feature well captured by the clustering (note that this information was not included explicitly in the clustering process). It is noteworthy that the same analysis for the full field response yields a less structured picture, indicating that the richer chirp stimulus is more informative about specific RGC types (not illustrated).

Finally, a summary of the resulting 28 clusters is shown in **Figure 7**. The dendrogram, which is colored to indicate the average bias index on each branch (green = Off; red = On; gray = no preference) is organized into three main branches. The first contains many On cells and a sub-branch with mixed preference. The second branch contains exclusively Off cells. The third branch has again mixed preferences, with an average bias index close to zero. Common to RGCs in the last branch appears to be transient On or Off responses with a stronger sustained component.

While it is not the aim of this work to exhaustively characterize the RGC types found in this particular dataset, here we discuss a few interesting cases. First, the PSTHs exhibit clear differences in the kinetics of their temporal responses and contrast sensitivity between clusters. In some cases, these differences are rather subtle, for instance clusters 7 and 8 appear superficially similar, and both could be classified as the highly abundant Off alpha cells with transient responses and large RFs. Yet cluster 7 has a slightly higher sustained response and a higher frequency and contrast sensitivity. Cluster 8 may therefore correspond to the "OFF mini alpha transient," while 7 may be the "Off alpha transient" type as described by Baden et al. (2016). To fully confirm their identify, a more detailed analysis would be required.

Figure 7 also shows spatial distribution, DS, RF size estimated from STAs, and the temporal STA profile for each cluster. Direction selectivity and RF size generally show broad distributions, but with consistent differences between types. For instance, the characteristics cells with larger than average RFs match types with known large RFs, such as Off-alpha like cells (clusters 7, 8, 10, and 12), and a putative On alpha type in cluster 17 (Krieger et al., 2017). On the other hand, several clusters have very weak (2, 14, 15, 21–26) or even no well defined (cluster 9) STA, adding variability in the RF fits.

Direction selectivity was measured with a single bar moving in 12 different directions, a paradigm we found to be relatively susceptible to noise. It is therefore unclear if the high variability in many clusters is due to experimental noise, or due to incomplete separation of DS types. Two observations however stand out. First, all cells grouped together into the third mixed supercluster (clusters 1–6) have a very low DS, lower than any other cluster. Second, cluster 9 has a very strong DS. None of the RGCs in this cluster had a measurable STA, suggesting it may correspond to the "ON–OFF DS 2" type (Baden et al., 2016).

Finally, cluster 26 does not appear to have a discernible light response. Closer inspection revealed that it consists of noisy units with highly inconsistent firing patterns. Hence these cluster are not likely to contain reliable RGC activity, but one or several poorly detected neurons. It is encouraging that, as for the synthetic data, these noisy units are sorted into separate clusters, which allows easy removal from further analysis.

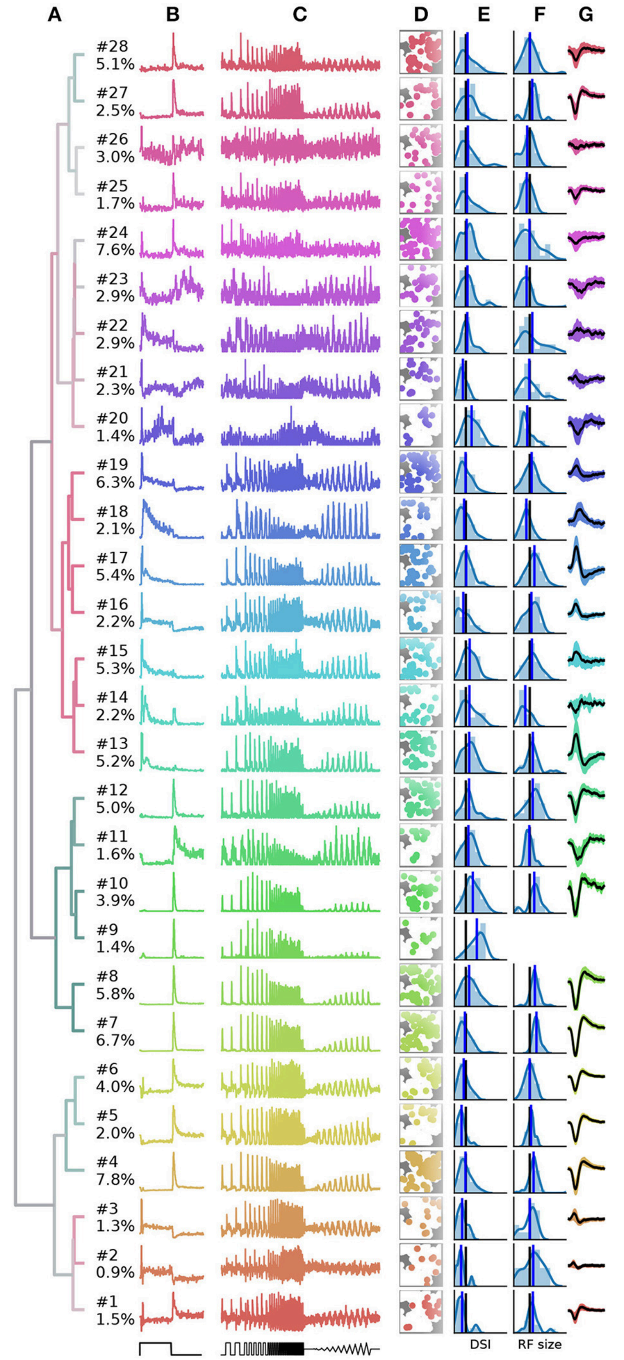

FIGURE 7 | Summary of the RGC types found in a recording from 1,026 retinal ganglion cells (RGCs). **(A)**, Dendrogram, with lines colored according to the average bias index of all units with lower distance (green = –1/Off, red = +1/On, gray = Zero). Percentages at the leafs give the relative abundance of each RGC type. **(B–G)**, Each row shows properties of one cluster: **(B)**, full field PSTH (2 sec bright, 2 sec dark); **(C)**, chirp PSTH; **(D)**, spatial distribution of each cluster, recorded area is indicated in white; **(E)**, histogram of direction selectivity index (DSi); **(F)**, histogram of receptive field sizes; **(G)**, temporal spike triggered average (STA) obtained at the pixel with the largest STA magnitude, shaded area indicates one standard deviation around the mean (black, where missing no receptive field could be fit). In E and F, the black vertical lines are retina averages and blue lines the cluster averages.

Heterogeneity Between Retinas

To assess the consistency of RGC classification across recordings from different retinas, we performed pairwise comparisons between six retinas. These had 1,026, 1,849, 1,234, 634, 1,131, and 575 units, respectively (retina 1 is the same as shown in **Figure 7**). Both the gap statistics and the adjusted mutual information show a similar dependence on the cluster number as shown above for one retina, but vary in their peak values, indicating differences in overall separability in each preparation (not illustrated). Each retina was clustered separately, and a PCA model was fit using the combined, peak-normalized chirp PSTHs from all retinas. Matching clusters between each pair of retinas were found based on the smallest cosine distance between the eight first components. The cosine distance, which is best suited to compute distances in a vector space, ranges from zero to one, where zero indicates identity and two opposing vectors. As expected, averaged distances decrease as the number of clusters is increased, but remains high even for 70 clusters (**Figure 8A**). In addition, we found considerable variability in distances between retinas, indicating that responses from the same RGC type can be variable across retinas.

This effect can also be seen when visualizing the principal components directly for each retina. **Figure 8B** illustrates this for the first three components for three retinas. While some regions in PCA space are shared, each retina occupies distinct areas. As a result, SPIKE distance-based clustering of spike trains pooled from different retinas yields results that primarily separate units by retina, and not by functional type. This is illustrated in **Figure 8C**, where a mixed data set was generated by randomly sampling 500 neurons from retinas 1 and 2. Many of the resulting clusters contain neurons from only one of the two retinas.

The variability between preparations complicates finding matching clusters across all retinas, which we attempted using a greedy search procedure. However, for pairs of retinas this was feasible to some extent, as distances were similarly biased for the corresponding cluster pairs. To find matching pairs, kernel PCA using radial basis functions was fit with 20 components to peak-normalized chirp PSTHs, and cosine distances were computed between all neurons for each pair of clusters and averaged. This procedure was carried out using two retinas, clustered into 34 types each instead of the 28 clusters used above. We chose this number as the synthetic data experiments showed that noisy neurons are assigned their own clusters, while the main types are still preserved. Hence over-clustering is not expected to happen unless this number is increased drastically.

When pairing these clusters by shortest average distance, we found 27 clusters with well matched bias indices, and with correlated direction selectivity (**Figure 9A**). Well matched clusters tended to have small distances, while they were larger for mismatched clusters. The distances increased sharply after 24 clusters (**Figure 9B**), indicating that at least 10 clusters could not be matched well. **Figure 9C** illustrates a direct comparison of these 24 clusters.

For six of these clusters, we could identify corresponding counterparts in the taxonomy developed by Baden et al. (2016): Off DS type without clear STA (group number 2 in Baden et al.,

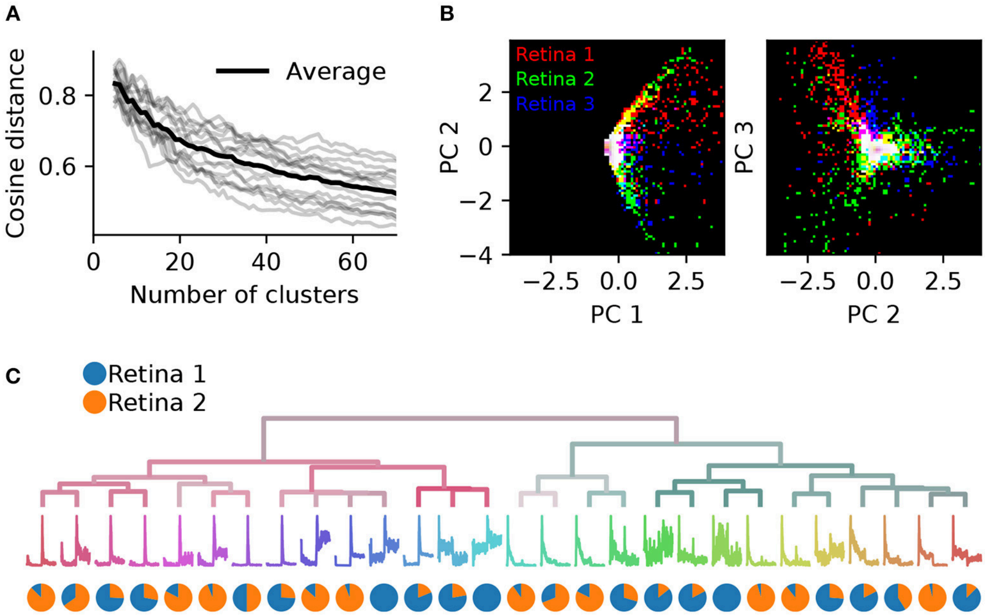

FIGURE 8 | Systematic differences in RGC activity between individual retinas prevents data pooling. **(A)**, Gray lines show, for each pair of six retinas, the average cosine distances between the top eight PCA projections of the best matching chirp PSTHs (explaining 78% variance), as a function of the number of clusters generated. The black line is the average across all data sets. Individual retinas show high variability even for a large number of clusters, indicating considerable differences between preparations. **(B)**, The first and second (left) and second and third PCA projections plotted against each other for three retinas (indicated by color). Each retina occupies a different region in PCA space.**(C)**, Dendrogram obtained by clustering a data set generated from randomly selecting 500 neurons from two retinas. The pie charts show the relative proportion of neurons from each retina in each cluster. Most clusters exhibit a strong bias toward one of the two retinas.

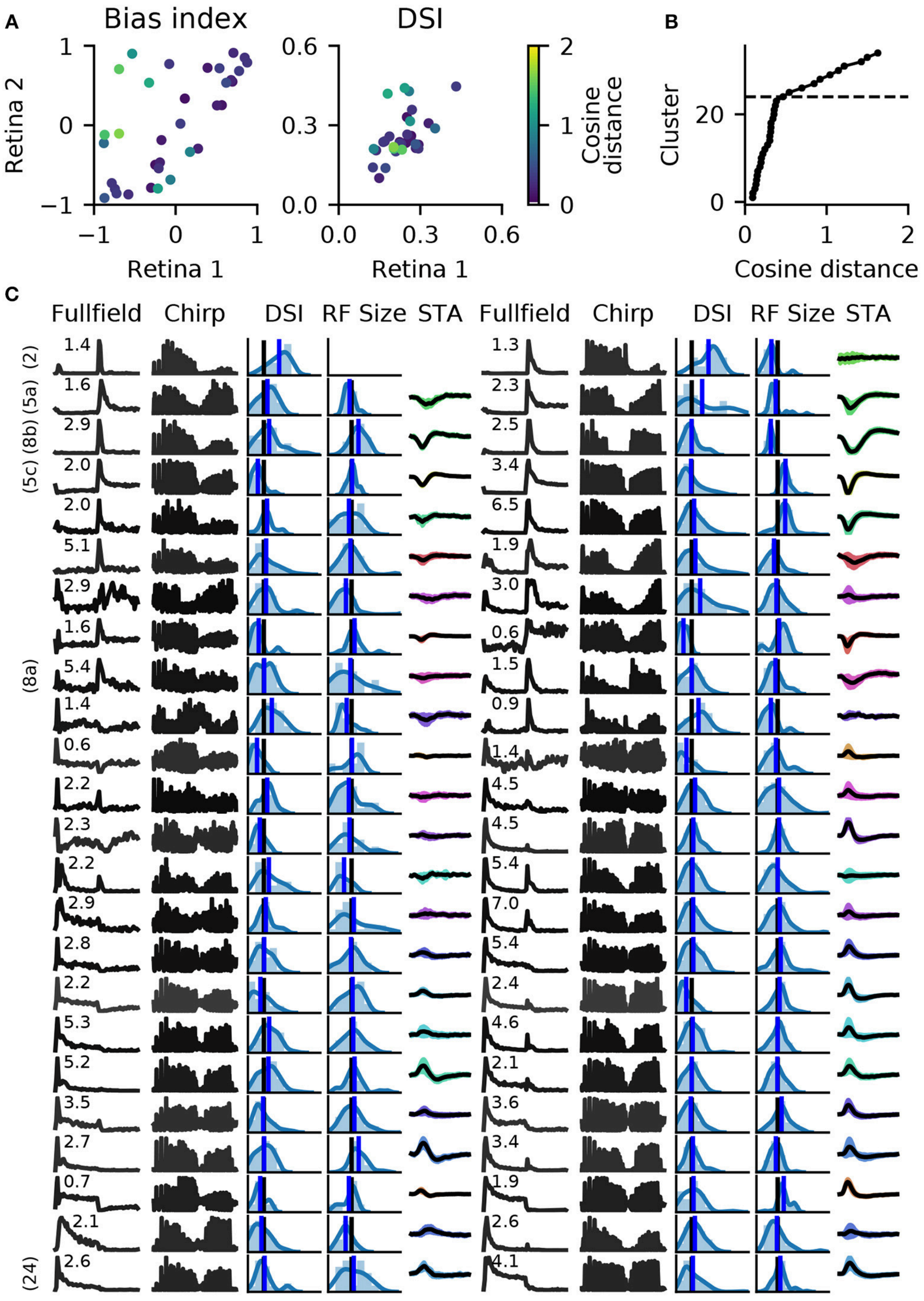

FIGURE 9 | Matching RGC types in two retinas. Spike trains from two retinas (retinas 1 and 2 in **Figure 8**) were independently clustered into 34 types, and matching pairs found using the cosine distance between vectors of length 20, obtained with RBF kernel PCA. **(A)**, A comparison of average bias indices (left) and direction selectivity (right) for each pair of RGC types. Color indicates the distance measure for each pair. **(B)**, Cumulative histogram of average pair distances. Beyond 24 clusters, a sharp increase in distance is observed. **(C)**, Main features of the 24 most similar RGC types for both retinas. Data is presented as in **Figure 7**, with full field and chirp PSTHs, histograms of direction selectivity index (DSi) and receptive field size (black vertical lines are retina averages, blue line is the cluster average), and the STA (shaded area: 1 standard deviation; missing STA could not be fit). Numbers above the full field PSTHs are the percentage abundance of each RGC type. PSTHs are colored by cosine distance, with black indicating zero and gray higher values. On the left, clearly identified RGC types according to the taxonomy by Baden et al. (2016) are given.

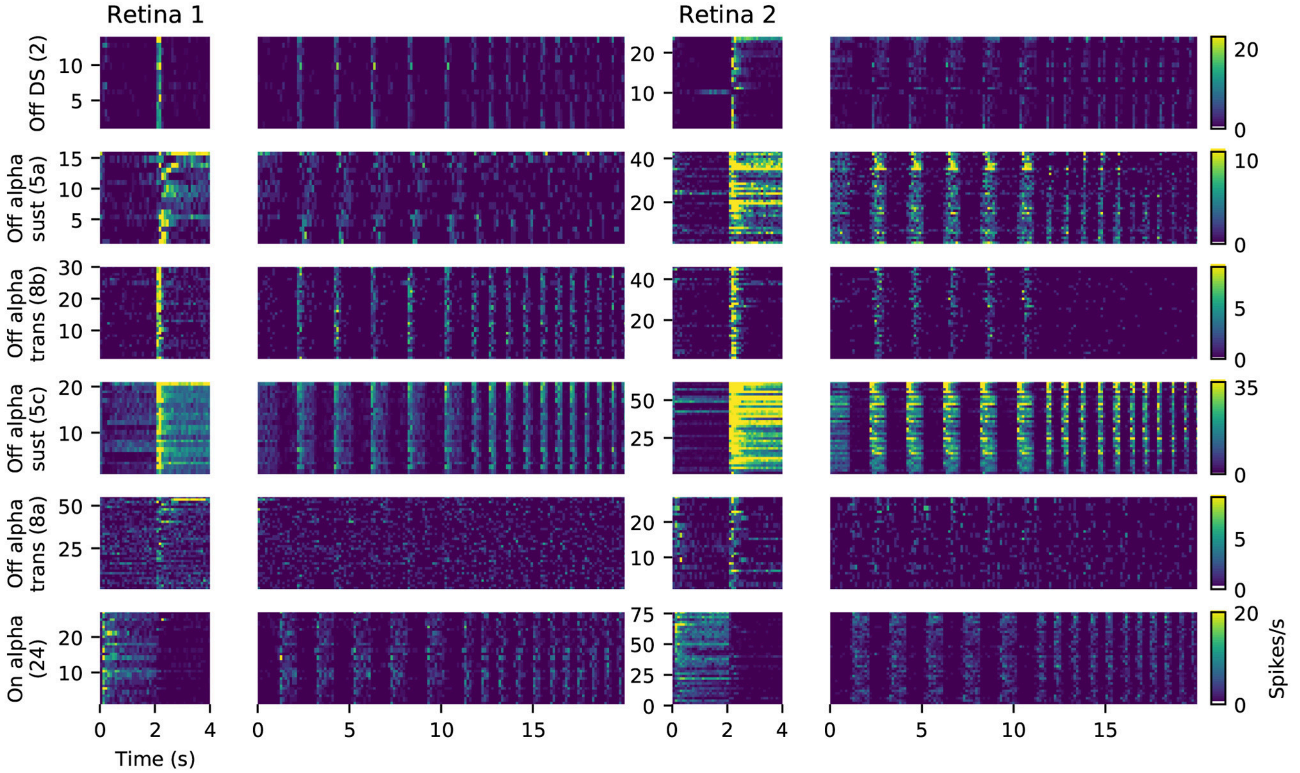

FIGURE 10 | Examples of matched cell types in two retinas. Each panel shows the PSTHs during full field stimulation (small, left) and the frequency-modulated part of the chirp stimulus (right), for all neurons clustered together as the same type. Data is the same as shown in **Figure 9**. The color gradient indicating firing rates is peak-scaled to the largest response across all neurons in retina 1 for the chirp stimulus, separately for each type.

2016), Off alpha sustained (5a and 5c), Off alpha transient (8a, 8b) and On alpha (24) (annotated on the left in **Figure 9C**). However, a direct comparison to other classification studies is difficult because of the nature of the different acquisition conditions. To illustrate the variability within each retina, and between retinas, PSTHs of all neurons for each of these annotated clusters are shown in **Figure 10**. While overall consistent, there are clear differences in firing rates between retinas, and for the same type within the same retina. The origin of this variability is unclear, possible factors include experimental limitations (coupling of the retina to the MEA, variability in spike detection and sorting), differences between the retinal eccentricities and recording locations, and biological neuronal heterogeneity.

DISCUSSION

This work introduces a method for classification of RGC responses based solely on spatially uniform light stimulation, using spike train distances as a metric for hierarchical clustering. The analysis of synthetically generated ground truth data shows that this method performs well. For noisy data, our method outperforms other approaches, which typically perform clustering in a low-dimensional Euclidean feature space obtained through dimensionality reduction (Carcieri et al., 2003; Segev et al., 2006; Farrow and Masland, 2011; Jones et al., 2015; Ravi et al., 2018). Most importantly however, our method is entirely non-parametric, thus does not require searching for optimal hyperparameters, such as the dimensionality of the feature representation (Baden et al., 2016), or the definition or estimation of salient response properties.

Our approach extends the idea by Zeck and Masland (2007) to use salient spike train features directly for clustering. This approach requires all neurons to be stimulated simultaneously with the same stimulus, to ensure the spike distance measure only captures physiological variations. This is a very effective way to probe many RGCs simultaneously with high density MEAs, since a small number of trials of a short, but sufficiently rich stimulus are sufficient. While only modulating contrast and temporal aspects of the RFs, the chirp stimulus appears well suited as it allows to rapidly probe a range of relevant response properties. Some clusters showed distinct receptive field sizes, high direction selectivity or no clearly defined STA, indicating that their responses to this homogeneous stimulus are sufficiently distinct to isolate sub-types also with non-optimal stimuli (Zeck and Masland, 2007).

The output of our method is a dendrogram indicating similarity between units and groups of units. To obtain a flat clustering into distinct RGC types, an appropriate cut-off point has to be determined. This can be done either by computing a consensus score for two or more distance measures, or by manual inspection. Consistent with our simulations, we found that clusters with noisy, unreliable activity were split first when the number of clusters was increased, while well-identified RGC types remained in the same clusters. This allows the identification of frequent types, such as, for instance, Off-alpha cells or On mono- and bi-phasic RGCs. Noisy, invalid units, on the other hand, can be removed by first clustering a full, contaminated data set, then removing clusters with inconsistent responses, followed by re-clustering.

A further method to assess the number of RGC types is consensus clustering of recordings from different retinas. However, perhaps unsurprisingly, we found significant variability between retinas when comparing different recordings. This prevents the joint clustering of pooled data, as spike distance measures are highly sensitive to these systematic differences. As a result, the clusters obtained for pooled data frequently group neurons from the same retina. An alternative approach we explored here is to cluster the recordings individually, followed by computing pairwise distances between all recordings.

As pointed out before, light responses alone are certainly insufficient to conclusively distinguish between individual RGC types (Baden et al., 2016). A very reliable criterion is neural morphology, in particular dendritic stratification in the inner plexiform layer. While this is impossible to obtain for all neurons recorded with large scale MEAs, the registration of sparsely labeled neurons with spike sorted data is feasible (Hilgen et al., 2017a), a method that could be used to augment the clustering obtained with our method. A further criterion to assess the validity of clustered types is regular spatial tiling of each type (Segev et al., 2006; Marre et al., 2012), although there are exceptions to this rule (Bleckert et al., 2014). Indeed our analysis suggests some cell types may be preferentially found in certain regions of the retina (cf. **Figure 7D**), a finding that however has to be substantiated by comparing recordings from the same area in multiple retinas.

Taken together, here we show that spike train distances can be successfully used to classify RGCs in the mouse retina. We expect this approach can be used in other sensory systems where an appropriate homogeneous stimulus can be delivered. A potential shortcoming is that cell types with a continuous variation of selectivity, such as auditory neurons with different frequency tuning, will be wrongly placed into different groups. We also expect our method to be suitable for analysis of spike trains inferred from calcium imaging recordings. The analysis of synthetic data shows that the method is robust even for highly variable Poisson spike trains, as long as key response features are well preserved. As also pointed out by Zeck and Masland (2007), transient, well-timed responses are particularly important for spike-based measures, which we expect can be inferred well from clean imaging data. On the other hand, given the results discussed above, it seems unlikely our method will perform well for data pooled across multiple preparations.

DATA AVAILABILITY

The datasets and analysis code for this study can be found in the https://github.com/mhhennig/rgc-classification

AUTHOR CONTRIBUTIONS

JJ and MH wrote analysis code, GH and ES collected experimental data. JJ and MH wrote the manuscript. All authors contributed conception and design of the study and contributed to manuscript revision, read and approved the submitted version.

FUNDING

Funding was provided by the Engineering and Physical Sciences Research Council grant EP/L027208/1 (MH), and the Leverhulme Trust grant RPG-2016-315 (ES).

REFERENCES

Badea, T. C., and Nathans, J. (2004). Quantitative analysis of neuronal morphologies in the mouse retina visualized by using a genetically directed reporter. *J. Comp. Neurol.* 480, 331–351. doi: 10.1002/cne.20304

Baden, T., Berens, P., Franke, K., Román Rosón, M., Bethge, M., and Euler, T. (2016). The functional diversity of retinal ganglion cells in the mouse. *Nature* 529, 345–350. doi: 10.1038/nature16468

Bleckert, A., Schwartz, G. W., Turner, M. H., Rieke, F., and Wong, R. O. (2014). Visual space is represented by nonmatching topographies of distinct mouse retinal ganglion cell types. *Curr. Biol.* 24, 310–315. doi: 10.1016/j.cub.2013.12.020

Carcieri, S. M., Jacobs, A. L., and Nirenberg, S. (2003). Classification of retinal ganglion cells: a statistical approach. *J. Neurophysiol.* 90, 1704–1713. doi: 10.1152/jn.00127.2003

Dayan, P., and Abbott, L. F. (2001). *Theoretical Neuroscience: Computational and Mathematical Modeling of Neural Systems*. Cambridge, MA: Computational Neuroscience. MIT Press.

Farrow, K., and Masland, R. H. (2011). Physiological clustering of visual channels in the mouse retina. *J. Neurophysiol.* 105, 1516–1530. doi: 10.1152/jn.00331.2010

Helmstaedter, M., Briggman, K. L., Turaga, S. C., Jain, V., Seung, H. S., and Denk, W. (2013). Connectomic reconstruction of the inner plexiform layer in the mouse retina. *Nature* 500, 168. doi: 10.1038/nature12346

Hilgen, G., Pirmoradian, S., Pamplona, D., Kornprobst, P., Cessac, B., Hennig, M. H., et al. (2017a). Pan-retinal Characterisation of light responses from ganglion cells in the developing mouse retina. *Sci. Rep.* 7:42330. doi: 10.1038/srep42330

Hilgen, G., Sorbaro, M., Zanacchi, F. C., Sernagor, E., Hennig, M. H., Pirmoradian, S., et al. (2017b). Unsupervised spike sorting for large-scale, high-density multielectrode arrays. *Cell Rep.* 18, 2521–2532. doi: 10.1016/j.celrep.2017.02.038

Jones, E., Oliphant, T., and Peterson, P. (2001). *SciPy: Open Source Scientific Tools for Python*.

Jones, I. L., Russell, T. L., Farrow, K., Fiscella, M., Franke, F., Müller, J., et al. (2015). A method for electrophysiological characterization of hamster retinal ganglion cells using a high-density cmos microelectrode array. *Front. Neurosci.* 9:360. doi: 10.3389/fnins.2015.00360

Kong, J.-H., Fish, D. R., Rockhill, R. L., and Masland, R. H. (2005). Diversity of ganglion cells in the mouse retina: unsupervised morphological classification and its limits. *J. Comp. Neurol.* 489, 293–310. doi: 10.1002/cne.20631

Kreuz, T., Chicharro, D., Greschner, M., and Andrzejak, R. G. (2011). Time-resolved and time-scale adaptive measures of spike train synchrony. *J. Neurosci. Methods* 195, 92–106. doi: 10.1016/j.jneumeth.2010.11.020

Kreuz, T., Chicharro, D., Houghton, C., Andrzejak, R. G., and Mormann, F. (2013). Monitoring spike train synchrony. *J. Neurophysiol.* 109, 1457–1472. doi: 10.1152/jn.00873.2012

Kreuz, T., Haas, J. S., Morelli, A., Abarbanel, H. D., and Politi, A. (2007). Measuring spike train synchrony. *J. Neurosci. Methods* 165, 151–161. doi: 10.1016/j.jneumeth.2007.05.031

Krieger, B., Qiao, M., Rousso, D. L., Sanes, J. R., and Meister, M. (2017). Four alpha ganglion cell types in mouse retina: function, structure, and molecular signatures. *PLoS ONE* 12:e0180091. doi: 10.1371/journal.pone.0180091

Maccione, A., Hennig, M. H., Gandolfo, M., Muthmann, O., van Coppenhagen, J., Eglen, S. J., et al. (2014). Following the ontogeny of retinal waves: pan-retinal recordings of population dynamics in the neonatal mouse. *J. Physiol.* 592, 1545–1563. doi: 10.1113/jphysiol.2013.262840

Macosko, E. Z., Basu, A., Satija, R., Nemesh, J., Shekhar, K., Goldman, M., et al. (2015). Highly parallel genome-wide expression profiling of individual cells using nanoliter droplets. *Cell* 161, 1202–1214. doi: 10.1016/j.cell.2015.05.002

Marre, O., Amodei, D., Deshmukh, N., Sadeghi, K., Soo, F., Holy, T. E., et al. (2012). Mapping a complete neural population in the retina. *J. Neurosci.* 32, 14859–14873. doi: 10.1523/JNEUROSCI.0723-12.2012

Masland, R. H. (2012). The Neuronal Organization of the Retina. *Neuron* 76, 266–280. doi: 10.1016/j.neuron.2012.10.002

Mulansky, M., and Kreuz, T. (2016). PySpike—A Python library for analyzing spike train synchrony. *SoftwareX* 5:183–189. doi: 10.1016/j.softx.2016.07.006

Murphy, K. P. (2012). *Machine Learning: A Probabilistic Perspective. Adaptive Computation and Machine Learning*. Cambridge, MA: MIT Press.

Muthmann, J.-O., Amin, H., Sernagor, E., Maccione, A., Panas, D., Berdondini, L., et al. (2015). Spike detection for large neural populations using high density multielectrode arrays. *Front. Neuroinformatics* 9:28. doi: 10.3389/fninf.2015.00028

Portelli, G., Barrett, J. M., Hilgen, G., Masquelier, T., Maccione, A., Di Marco, S., et al. (2016). Rank order coding: a retinal information decoding strategy revealed by large-scale multielectrode array retinal recordings. *Eneuro* 3:ENEURO.0134-15.2016. doi: 10.1523/ENEURO.0134-15.2016

Ravi, S., Ahn, D., Greschner, M., Chichilnisky, E., and Field, G. D. (2018). Pathway-specific asymmetries between on and off visual signals. *J. Neurosci.* 38, 9728–9740. doi: 10.1523/JNEUROSCI.2008-18.2018

Rheaume, B. A., Jereen, A., Bolisetty, M., Sajid, M. S., Yang, Y., Renna, K., et al. (2018). Single cell transcriptome profiling of retinal ganglion cells identifies cellular subtypes. *Nat. Commun.* 9, 2759. doi: 10.1038/s41467-018-05134-3

Rockhill, R. L., Euler, T., and Masland, R. H. (2000). Spatial order within but not between types of retinal neurons. *Proc. Natl. Acad. Sci. U.S.A.* 97, 2303–2307. doi: 10.1073/pnas.030413497

Roska, B., and Werblin, F. (2001). Vertical interactions across ten parallel, stacked representations in the mammalian retina. *Nature* 410, 583. doi: 10.1038/35069068

Sanes, J. R., and Masland, R. H. (2015). The types of retinal ganglion cells: current status and implications for neuronal classification. *Ann. Rev. Neurosci.* 38, 221–246. doi: 10.1146/annurev-neuro-071714-034120

Segev, R., Puchalla, J., and Berry, M. J. (2006). Functional organization of ganglion cells in the salamander retina. *J. Neurophysiol.* 95, 2277–2292. doi: 10.1152/jn.00928.2005

Sterling, P., and Laughlin, S. (2015). *Principles of Neural Design*. Cambridge, MA: MIT Press.

Sun, W., Li, N., and He, S. (2002). Large-scale morphological survey of mouse retinal ganglion cells. *J. Comp. Neurol.* 451, 115–126. doi: 10.1002/cne.10323

Tibshirani, R., Walther, G., and Hastie, T. (2001). Estimating the number of clusters in a data set via the gap statistic. *J. R. Stat. Soc. B Stat. Methodol.* 63, 411–423. doi: 10.1111/1467-9868.00293

Victor, J. D. (2005). Spike train metrics. *Curr. Opin. Neurobiol.* 15, 585–592. doi: 10.1016/j.conb.2005.08.002

Vinh, N. X., Epps, J., and Bailey, J. (2010). Information theoretic measures for clusterings comparison: variants, properties, normalization and correction for chance. *J. Mach. Learn. Res.* 11, 2837–2854. doi: 10.1145/1553374.1553511

Völgyi, B., Chheda, S., and Bloomfield, S. A. (2009). Tracer coupling patterns of the ganglion cell subtypes in the mouse retina. *J. Comp. Neurol.* 512, 664–687. doi: 10.1002/cne.21912

Wässle, H., Peichl, L., and Boycott, B. (1981). Dendritic territories of cat retinal ganglion cells. *Nature* 292, 344. doi: 10.1038/292344a0

Zeck, G. M., and Masland, R. H. (2007). Spike train signatures of retinal ganglion cell types. *Eur. J. Neurosci.* 26, 367–380. doi: 10.1111/j.1460-9568.2007.05670.x

Conflict of Interest Statement: The authors declare that the research was conducted in the absence of any commercial or financial relationships that could be construed as a potential conflict of interest.

frontiers in Cellular Neuroscience

ORIGINAL RESEARCH
published: 16 October 2018
doi: 10.3389/fncel.2018.00353

Polymodal TRPV1 and TRPV4 Sensors Colocalize but Do Not Functionally Interact in a Subpopulation of Mouse Retinal Ganglion Cells

Monika Lakk[1]*, Derek Young[1], Jackson M. Baumann[1,2], Andrew O. Jo[1], Hongzhen Hu[3] and David Križaj[1,2,4]*

[1] Department of Ophthalmology and Visual Sciences, University of Utah, Salt Lake City, UT, United States, [2] Department of Bioengineering, University of Utah, Salt Lake City, UT, United States, [3] Department of Anesthesiology, Washington University School of Medicine, St. Louis, MO, United States, [4] Department of Neurobiology and Anatomy, University of Utah, Salt Lake City, UT, United States

Edited by:
Bela Volgyi,
University of Pécs, Hungary

Reviewed by:
Ulrike Janssen-Bienhold,
University of Oldenburg, Germany
Sangsu Bang,
Duke University, United States

***Correspondence:**
Monika Lakk
mlakk@gamma.ttk.pte.hu
David Križaj
david.krizaj@hsc.utah.edu

Received: 02 July 2018
Accepted: 20 September 2018
Published: 16 October 2018

Citation:
Lakk M, Young D, Baumann JM, Jo AO, Hu H and Križaj D (2018) Polymodal TRPV1 and TRPV4 Sensors Colocalize but Do Not Functionally Interact in a Subpopulation of Mouse Retinal Ganglion Cells.
Front. Cell. Neurosci. 12:353.
doi: 10.3389/fncel.2018.00353

Retinal ganglion cells (RGCs) are projection neurons that transmit the visual signal from the retina to the brain. Their excitability and survival can be strongly influenced by mechanical stressors, temperature, lipid metabolites, and inflammatory mediators but the transduction mechanisms for these non-synaptic sensory inputs are not well characterized. Here, we investigate the distribution, functional expression, and localization of two polymodal transducers of mechanical, lipid, and inflammatory signals, TRPV1 and TRPV4 cation channels, in mouse RGCs. The most abundant vanilloid mRNA species was *Trpv4*, followed by *Trpv2* and residual expression of *Trpv3* and *Trpv1*. Immunohistochemical and functional analyses showed that TRPV1 and TRPV4 channels are expressed as separate molecular entities, with TRPV1-only (∼10%), TRPV4-only (∼40%), and TRPV1 + TRPV4 (∼10%) expressing RGC subpopulations. The TRPV1 + TRPV4 cohort included SMI-32-immunopositive alpha RGCs, suggesting potential roles for polymodal signal transduction in modulation of fast visual signaling. Arguing against obligatory heteromerization, optical imaging showed that activation and desensitization of TRPV1 and TRPV4 responses evoked by capsaicin and GSK1016790A are independent of each other. Overall, these data predict that RGC subpopulations will be differentially sensitive to mechanical and inflammatory stressors.

Keywords: retina, calcium, TRPV1, TRPV4, endocannabinoids, glaucoma, RGC

INTRODUCTION

Vertebrate vision is based on separating photon input from background thermal energy and extraction of luminance, local contrast, color, orientation, direction of motion, and "looming" information from the visual scene (Lettvin et al., 1959). Feature extraction is conducted in parallel by over 40 types of retinal ganglion cells (RGCs), which project axons from the retina to a wide range of midbrain nuclei (Morin and Studholme, 2014; Baden et al., 2016). RGCs are typically categorized by their light response and serendipitous expression of molecular markers

(Zeng and Sanes, 2017) but this ignores the possibility that RGC might also be classified based on their responsiveness to the local milieu, which continually bombards them with mechanical, cardiovascular and immune signals. We know that non-canonical non-synaptic sensory inputs can dramatically impact the function and survival of RGC subtypes (Muller et al., 2014; Duan et al., 2015; Križaj, 2016; Ou et al., 2016) yet the lack of knowledge about the transduction mechanisms that mediate them hampers physiological insight and treatment in diseases such as glaucoma, diabetic retinopathy, ischemia, and traumatic ocular injury.

Transient receptor potential (TRP) vanilloid channels are polymodal cation channels that function as molecular integrators of many types of sensory input (Clapham, 2003; Nilius and Szallasi, 2014). The 28 isoforms that constitute the TRP superfamily function as transducers of the ambient physico-chemical and inflammatory environment due to their sensitivity for mechanical stressors (strain, pressure, shear flow, swelling), temperature, pH, lipid, and inflammatory metabolites. Because the channels are permeable to Ca^{2+} and can be activated at resting membrane potentials, they are able to modulate neuronal physiology in the absence of synaptic activation (Bradshaw et al., 2013; Redmon et al., 2017). An archetypal example is the dorsal root ganglion (DRG), composed of sensory neuron populations that can be classified by the relative expression of TRPV1 nociceptors, TRPV4 osmosensors, TRPM8 innocuous pain sensors, TRPA1 cold pain sensors, TRPM2 redox sensors, with TRPC1, TRPC6, and TRPV2 channels adding additional layers of complexity (Sousa-Valente et al., 2014; Teichert et al., 2014). Within the vanilloid subfamily, TRPV1-4 (also known as thermoTRPs for their temperature sensitivity) are non-selective cation channels whereas TRPV5 and TRPV6 are predominantly permeable to Ca^{2+} and typically expressed in epithelial and bone cells (Clapham, 2003). The most studied vanilloid isoforms are TRPV1 and TRPV4, with ~50% sequence homology and activation by distinct agonists, temperature ranges, mechanical, osmotic, and inflammatory stressors (Martins et al., 2014; Nilius and Szallasi, 2014). Gene association and clinical studies identified single-nucleotide polymorphisms in the coding/promoter regions of TRPV4 with mutations that cause debilitating sensory and motor neuropathies and musculoskeletal disorders (Nilius and Voets, 2013; Echaniz-Laguna et al., 2014). Inflammatory agents sensitize TRPV1/4 channels by mechanisms that are not fully defined whereas selective inhibition or deletion of TRPV1- and TRPV4-expressing neurons produces burning, freezing, itch, mechanical pain, and thermosensory phenotypes together with loss of osmoregulation and hearing loss (Caterina et al., 1997; Tominaga et al., 1998; Liedtke and Friedman, 2003; Alessandri-Haber et al., 2004).

Vertebrate retinas express many – perhaps most – TRP isoforms (Gilliam and Wensel, 2011; Križaj, 2016) yet studies of TRP signaling are in their infancy and it is unknown whether different isoforms work together to transduce complementary features of the intra-retinal milieu. In contrast to the canonical TRPC1 isoform which is expressed in most retinal cells (Molnar et al., 2012, 2016), the most extensively studied isoform – TRPV1 – was localized to photoreceptors and subsets of RGCs, bipolar, and amacrine cells (Yazulla, 2008; Middleton and Protti, 2011; Ryskamp et al., 2014a; Jo et al., 2017). Its cognate, TRPV4, has been detected in RGCs, Müller glia, and endothelial cells (Ryskamp et al., 2011, 2014b; Jo et al., 2015; Phuong et al., 2017; Taylor et al., 2017) but, unlike TRPV1, appears to be absent from amacrine, bipolar, and photoreceptor cells (Yarishkin et al., 2018). The relative expression of vanilloid isoforms across RGCs is unknown, nor is it clear whether TRPV1 and TRPV4 colocalize and/or can interact. Because heteromultimerization could increase the cells' capacity to sense changes in ambient environment, we studied the relative expression levels of TRPV1 and TRPV4 channels, investigated their functional distribution and integration, and tested the influence of channel activation on cellular calcium homeostasis in mouse RGCs. We identified distinct RGC constellations that include TRPV4-, TRPV1-, and TRPV1 + TRPV4-expressing populations in which TRPV1 and TRPV4 channels are activated independently. These data suggest that sensing of ambient information (temperature, mechanical stress, pH, and endocannabinoids) across physiological and pathological ranges may be differentially distributed across RGC populations.

MATERIALS AND METHODS

Ethical Approval and Animals

Animal handling, anesthetic procedures, and experiments were performed in accordance with the NIH Guide for the Care and Use of Laboratory Animals and the ARVO Statement for the Use of Animals in Ophthalmic and Vision Research. The project was approved by the Institutional Animal Care and Use Committees at the University of Utah. We assessed retinal TRPV1 expression using a knock-in mouse in which *Cre* was inserted into Exon 15 of *Trpv1* (TRPV1Cre; Jackson Laboratory 017769). This line was crossed to B6.Cg-*Gt(ROSA)26Sortm9(CAG-tdTomato)Hze*/J (Ai9; 007909) in which the LoxP-STOP-LoxP TdTomato construct is knocked in at the *Gt(ROSA)26Sor* locus (Madison et al., 2010; Jo et al., 2017). *Trpv4*$^{-/-}$ mice have an excised exon 12-encoding transmembrane pore domains 5 and 6 (Liedtke and Friedman, 2003). C57BL/6J (C57), bacterial artificial chromosome (BAC)-transgenic Tg(TRPV4-EGFP)MT43Gsat mice (referred to as TRPV4^{eGFP}), TRPV1$^{-/-}$, TRPV4$^{-/-}$, *TRPV1Cre:Ai3*, and *Trpv1Cre:Ai9* mice were maintained in a pathogen-free facility with a 12-h light/dark cycle and unrestrained access to food and water. Data were gathered from male and female mice with no noted gender differences.

Reagents

The TRPV4 agonist GSK1016790A (GSK101) and antagonist HC-067047 (HC-06) were purchased from Sigma. The TRPV1 agonist capsaicin (CAP; 8-methyl-*N*-vanillyl-6-nonenamide) and the TRPV1 antagonist capsazepine (CPZ; *N*-[2-(4-Chlorophenyl)ethyl]-1,3,4,5-tetrahydro-7,8-dihydroxy-2*H*-2-benzazepine-2-carbothioamide) and the endogenous agonist of CB1 receptors 2-arachidonoylglycerol (2-AG)

TABLE 1 | Primer sequences used for PCR and semiquantitative real-time PCR analysis.

Name	Forward primer	Reverse primer	Product size (bp)
Trpv1	AGGGTGGATGAGGTGAACTGGACT	GCTGGGTGCTATGCCTATCTCG	199
Trpv2	GTTGGCCTACGTCCTCCTCACCTA	TGCACCACCAGTAACCATTCTCC	158
Trpv3	CTCACCTTCGTCCTCCTCCTCAAC	CAGCCGGAAGTCCTCATCTGCTA	201
Trpv4	TCCTGAGGCCGAGAAGTACA	TCCCCCTCAAACAGATTGGC	166
Gapdh	GGTTGTCTCCTGCGACTTCA	TAGGGCCTCTCTTCCTCAGT	220
Actb	CCACCATGTACCCAGGCATT	AGGGTGTAAAACGCAGCTCA	253

were obtained from Cayman Chemicals. BDNF and CNTF used to culture RGCs were obtained from GenWay Biotech. Other salts and reagents were purchased from Sigma, VWR, Across Organics, or Thermo Fisher. GSK101 (1 mM), HC-06 (10 mM), CAP (10 mM), and CPZ (20 mM) stocks in DMSO were diluted in extracellular saline before use and placed into reservoirs connected to gravity-fed perfusion systems (Warner Instruments).

Magnetic-Activated Cell Sorting (MACS)

The retinas were incubated in an enzyme solution containing 16 U/ml papain (Worthington), 0.2 mg/ml L-cysteine (Sigma), and 50 U/ml DNase I recombinant (Roche) for 45 min at 37°C with gentle agitation and triturated with D-PBS solution containing 1.5 mg/ml BSA, 1.5 mg/ml Trypsin inhibitor, pH: 7.4, to yield a single cell suspension that was passed through a 30 μm pre-separation filter and centrifuged. The cell pellet was re-suspended and incubated in 0.5% BSA solution containing CD90.1 MicroBeads (1:10; Miltenyi Biotech) for 15 min at 4°C. After additional washing and centrifugation, cells were separated using MACS LS columns and incubated in serum-free neurobasal medium (Gibco/ThermoFisher) with 1% penicillin/streptomycin (Sciencell), transferrin (0.1 mg/ml), putrescine (16 ng/ml), insulin (5 μg/ml), 3,5,3-triiodothyronine T3 (100 nM), progesterone (20 nM), 2% B27, N-acetyl cysteine (5 ng/ml), sodium pyruvate (1 mM), L-glutamine (2 mM), brain-derived neurotrophic factor (BDNF, 50 ng/ml), ciliary neurotrophic factor (CNTF, 10 ng/ml), and forskolin (5 μM). The growth medium was changed every 2–3 days.

Semiquantitative Real-Time PCR

Total RNA was isolated using the Arcturus PicoPure RNA Isolation Kit (Applied Biosystems) as described (Phuong et al., 2017). One microgram of total RNA was used for reverse transcription. First-strand cDNA synthesis and PCR amplification of cDNA were performed using qScript^{TM} XLT cDNA SuperMix cDNA synthesis kit (Quanta Biosciences). The PCR products were run on 2% agarose gels and visualized by ethidium bromide staining, along with 100-bp DNA ladder (ThermoFisher). SYBR Green-based real-time PCR was performed using Apex qPCR Master Mix (Genesee Scientific). The results were performed in triplicate of at least four separate experiments. The comparative C_T method ($\Delta\Delta C_T$) was used to measure relative gene expression where the fold enrichment was calculated as: $2^{-[\Delta CT(\text{sample})-\Delta CT(\text{calibrator})]}$ after normalization. To normalize fluorescence signals, GAPDH and β-actin were utilized as endogenous controls. The primer sequences and expected product sizes are given in **Table 1**.

Retinal Dissociation and Optical Imaging

The animals were euthanized by isoflurane inhalation. The retinas were isolated in ice-cold Leibovitz 15 (L15) medium containing 11 mg/ml L15 powder, with (in mM) 20 D-glucose, 10 Na-HEPES, 2 sodium pyruvate, 0.3 sodium ascorbate, and 1 glutathione. Incubation in L15 containing papain (7 U/ml; Worthington) digested the extracellular matrix, and was terminated by rinsing with cold L15 solution; 500 μm pieces of retina were mechanically dissociated and cells were plated onto concanavalin A (0.2–0.5 mg/ml) coated coverslips. Calcium imaging followed established protocols (Ryskamp et al., 2011; Jo et al., 2016; Lakk et al., 2017), with the cells loaded with the Fura-2 AM (5–10 μM, Life Technologies) indicator dye for 45–60 min. Extracellular saline contained: (in mM) 133 NaCl, 10 HEPES hemisodium salt, 10 glucose, 2.5 KCl, 2 $CaCl_2$, 1.5 $MgCl_2$, 1.25 NaH_2PO_4, 1 pyruvic acid, 1 lactic acid, and 0.5 glutathione. Epifluorescence images were acquired using an inverted Nikon microscope with a 40x (1.3 NA oil) objective. Subsets of cells were stimulated with agonists and antagonists of TRPV1/4 channels. 340 and 380 nm excitation was delivered from an Xe lamp (Lambda DG-4, Sutter Instruments). Emissions were collected at 510 nm with 14-bit CoolSNAPHQ2 or Delta Evolve cameras and analyzed using NIS-Elements. $\Delta R/R$ (peak $F340/F380$ ratio – baseline/baseline) was used to quantify the amplitude of Ca^{2+} signals.

Immunofluorescence

The immunolabeling protocol for vertical sections followed the procedures described in Molnar et al. (2016) and Jo et al. (2017). The retinas were fixed for 1 h in 4% paraformaldehyde, rinsed with PBS, dehydrated, and embedded in OCT compound mounting medium (Electron Microscopy Sciences); 12 μm thick cryosections were incubated in a blocking buffer (5% FBS and 0.3% Triton X-100 in 1X PBS) for 20 min. Primary antibodies (rabbit anti-TRPV4, 1:1000, LifeSpan Biosciences; rabbit anti-RBPMS, 1:500, PhosphoSolutions; mouse anti-Thy1.1, Sigma, 1:500; mouse SMI-32, 1:100, Covance; mouse anti-GFP, 1:500, Santa Cruz) were diluted in the diluent (2% BSA and 0.2% Triton X-100 in 1X PBS) and applied overnight at 4°C, followed by incubation in fluorophore-conjugated secondary antibodies (1:500; goat anti-mouse AlexaFluor 405, 488, or 647, goat anti-rabbit AlexaFuor 488 or 594, Life Technologies) for 1 h at

RT. Images were acquired on an Olympus CV1200 confocal microscope using 20x (NA water) and 40x (0.9 NA water) objectives.

Statistical Analysis

Data are presented as means $\pm$ SEM. Statistical comparisons were made with one-way ANOVA test followed by *post hoc* Tukey's multiple comparison of means (Origin 8.0, Origin Lab Corporation). A difference of $P \leq 0.05$ (*), $P \leq 0.01$ (**), $P \leq 0.001$ (***), and $P \leq 0.0001$ (****) were considered statistically significant.

RESULTS

Mammalian RGCs Express Multiple Vanilloid TRP Isoforms

Vanilloid TRP channels are osmo- and thermosensitive non-selective cation channels with critical functions in neuronal neural plasticity, synaptic transmission, synapse formation, neurogenesis, apoptosis, and survival (Sousa-Valente et al., 2014; Ramírez-Barrantes et al., 2016; White et al., 2016). The mouse retina expresses multiple members of the vanilloid subfamily (Gilliam and Wensel, 2011) but their relative expression in RGCs is not known. RNA profiling shows that mouse RGCs express all four thermo*Trp* transcripts (*Trpv1-4*) (**Figure 1A**), with expression dominated by *Trpv4*, followed by *Trpv2*, *Trpv3*, and *Trpv1* mRNAs, respectively (**Figure 1B**). TRPV4$^{-/-}$ RGCs showed a trend toward *Trpv1* upregulation but these changes were not significant (**Figure 1C**). Examination of mRNAs in TRPV4$^{-/-}$ RGCs showed little evidence of cross-isoform plasticity apart from a (non-significant) trend toward *Trpv1* (**Figure 1C**). We conclude that mouse RGCs as a group express all non-epithelial vanilloid *Trp* genes. Lack of compensatory upregulation in KO mice lacking the dominant TRPV4 channel might indicate absence of regulatory interaction at the transcriptional level, or an absence of obligatory heteromerization.

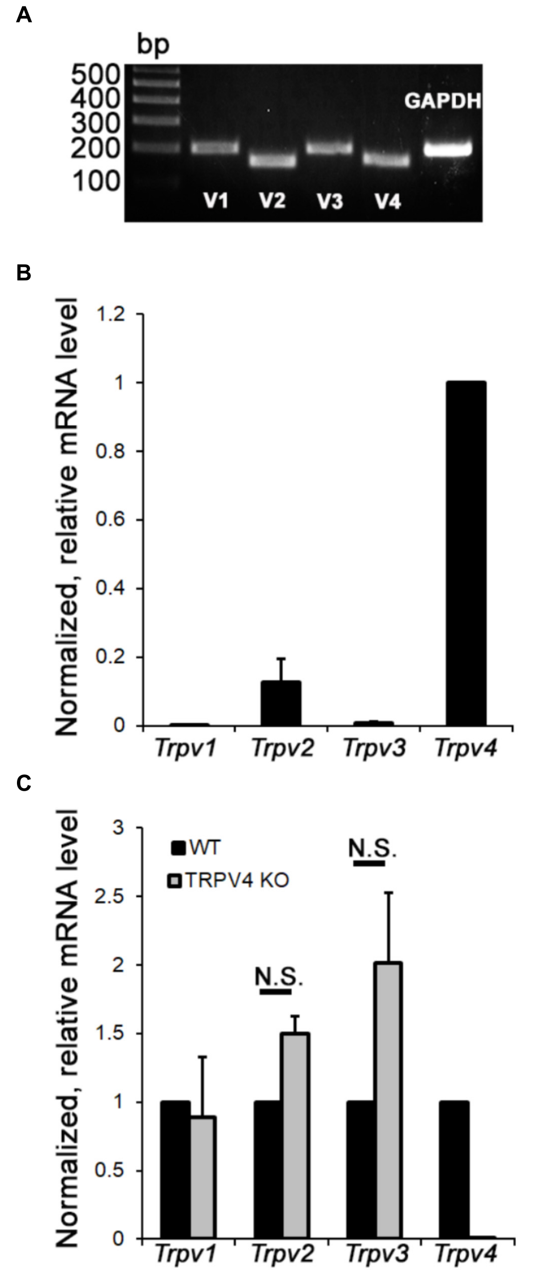

FIGURE 1 | Relative mRNA expression levels of vanilloid thermoTRP channels in primary mouse RGCs. **(A)** End point PCR. RGCs express all four thermo *Trpv* transcripts. *Gapdh* (glyceraldehyde 3-phosphate dehydrogenase) mRNA served as a loading control. **(B)** Semiquantitative RT-PCR. The relative abundance of thermo *Trpv* transcripts normalized with respect to *Trpv4* content ($n = 4$). **(C)** Fold change in mRNA expression in TRPV4$^{-/-}$ RGCs ($n = 4$) was calculated relative to expression in wild type cells.

Pharmacological Activation of TRPV1 and TRPV4 Channels Reveals Functional Overlap in a Subset of RGCs

TRPV1 and TRPV4 channels have been implicated in optic nerve degeneration (Križaj et al., 2014; Sappington et al., 2015) and axonal neuropathies (Echaniz-Laguna et al., 2014), and shown to be sensitive to mechanical stressors (such as changes in cell volume and strain; Sudbury et al., 2010; Ryskamp et al., 2016). To categorize the relative fractions of TRPV1- and TRPV4-expressing RGCs, we used microfluorimetry. Dissociated cells were identified by the size and morphology of the somata, and responsiveness to glutamate (100 μM) and high K$^+$ (35 mM; Ryskamp et al., 2011). After loading with the calcium indicator Fura-2-AM, cells were stimulated with pharmacological activators and inhibitors of TRPV1 and TRPV4 channels. The largest RGC cohort (35.08%) showed intracellular Ca^{2+} ([Ca^{2+}]$_i$) increases in response to the TRPV4 agonist GSK101 (25 nM) and lack of sensitivity to the TRPV1 agonist CAP (10 μM; **Figures 2A,B**). On average, in these cells, GSK101 evoked an increase in the 340/380 ratio of 0.51 ± 0.05 ($n = 87$; $P < 0.001$). As shown previously (Ryskamp et al., 2011, 2014a), the responses to the TRPV4 agonist were characterized by a transient [Ca^{2+}]$_i$

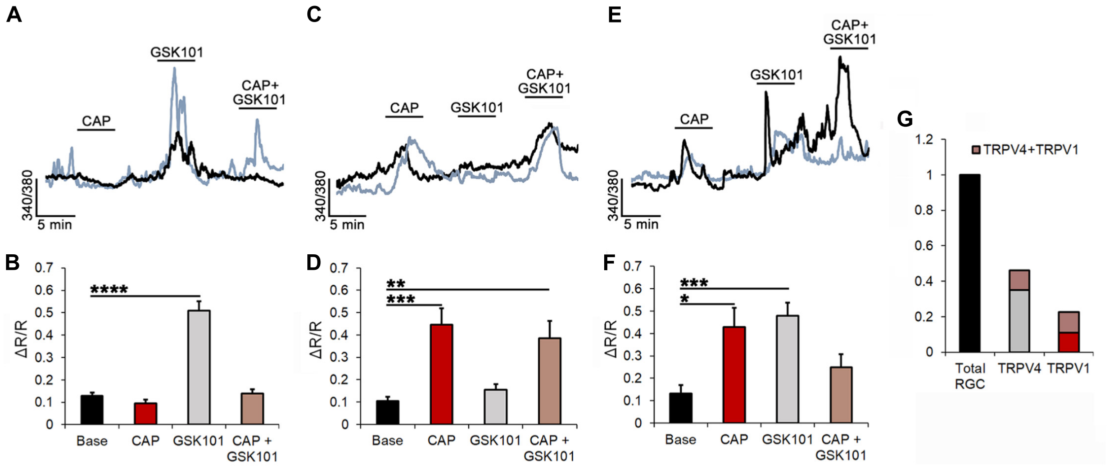

FIGURE 2 | TRPV1 and TRPV4 modulate Ca^{2+} homeostasis in subsets of RGCs. **(A)** Two simultaneously recorded RGCs (denoted by black and blue traces) respond to GSK101 with [Ca^{2+}]$_i$ elevations but are insensitive to CAP. **(B)** Averaged data for the GSK101-responding CAP-insensitive pool of cells (*n* = 87). **(C)** Representative traces of CAP responders that were insensitive to GSK101. **(D)** Averaged data for the CAP-responding GSK101-insensitive cohort (*n* = 29). **(E,F)** Traces and averaged data from GSK101 + CAP responders (*n* = 27). **(G)** Summary of averaged data. ~24% of the TRPV4-expressing RGCs responded to CAP, whereas ~48% of TRPV1-expressing RGCs responded to GSK101. **P* ≤ 0.05, ***P* ≤ 0.01, ****P* ≤ 0.001, *****P* ≤ 0.0001.

peak that inactivated in the continued presence of GSK101. Subsequent co-applications of the drug evinced lower-amplitude or missing Ca^{2+} responses due to tachyphylaxis (continued channel desensitization). Pretreatment with CAP did not affect the amplitude of GSK101-evoked [Ca^{2+}]$_i$ responses in this cohort, suggesting that tachyphylaxis is isoform-specific.

Another population, encompassing 11.69% of RGCs, responded to CAP administration with increased [Ca^{2+}]$_i$ with an average CAP-evoked ratio increase of 0.45 ± 0.07 (*n* = 29; *P* < 0.001; **Figures 2C,D**). These cells were unresponsive to GSK101, and co-application of GSK101 and CAP yielded a ratio increase of 0.39 ± 0.08 that was not significantly different from the exposure to CAP alone. The third functional type (10.89%) responded to both TRPV1 and TRPV4 agonists (0.43 ± 0.09 and 0.48 ± 0.06 ratio increases, respectively; *n* = 27; **Figures 2E,F**). A representative example of a cell classified into the third cohort is shown in **Figure 3**, with vertical lines in **Figure 3A**, corresponding to fluorescence images of free [Ca^{2+}]$_i$ elevations in the RGC cytosol shown in **Figure 3B**. As expected (Ryskamp et al., 2011; Jo et al., 2017), the response to both agonists desensitized in the continued presence of the agonist (**Figures 3Biv,viii**). The dataset in **Figure 2G** shows that ~46% of total glutamate responder RGCs express TRPV4, and ~20% express TRPV1. Another way of parsing the data shows that ~48% of TRPV1 expressing RGCs (22.6% of total glutamate-responding cells) functionally express TRPV4 channels whereas ~24% of TRPV4-expressing cells express TRPV1 as well.

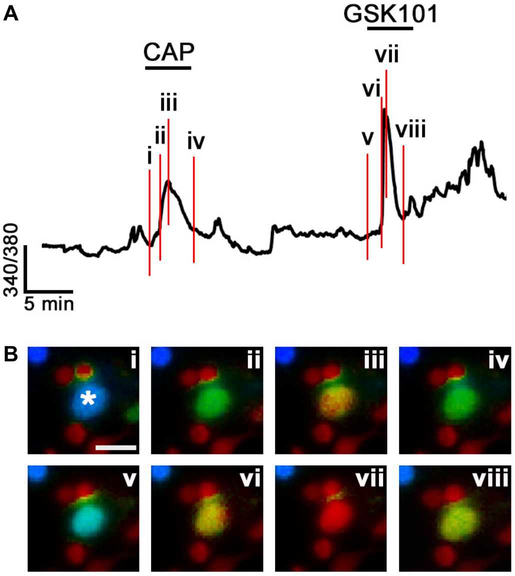

FIGURE 3 | Functional coexpression of TRPV1 and TRPV4 channels in a representative RGC (*asterisk*). **(A)** The time course of the calcium response in a C57 RGC sequentially stimulated with CAP and GSK101. The red vertical lines denote the time points shown in panel **Bi–viii**. **(B)** Ratio images from the RGC (asterisk) shown in **A**. Note that [Ca^{2+}]$_i$ declines in the continued presence of both agonists. The small-diameter somata adjacent to the RGC are rod somata. Scale bar = 10 μm.

TRPV4 Is Coexpressed With TRPV1 in a Subset of RGCs

We next investigated whether the results from functional studies (**Figures 2**, **3**) can be mirrored by proof-of-principle histochemical evidence. TRPV4 channels can be studied with validated antibodies (Ryskamp et al., 2011; Jo et al., 2016) but the specificity of commercial TRPV1 antibodies is questionable (Gilliam and Wensel, 2011; Molnar et al., 2012). We therefore studied TRPV1Cre:Ai9 and TRPV1Cre:Ai3 retinas in which channel expression manifests in the fluorescence

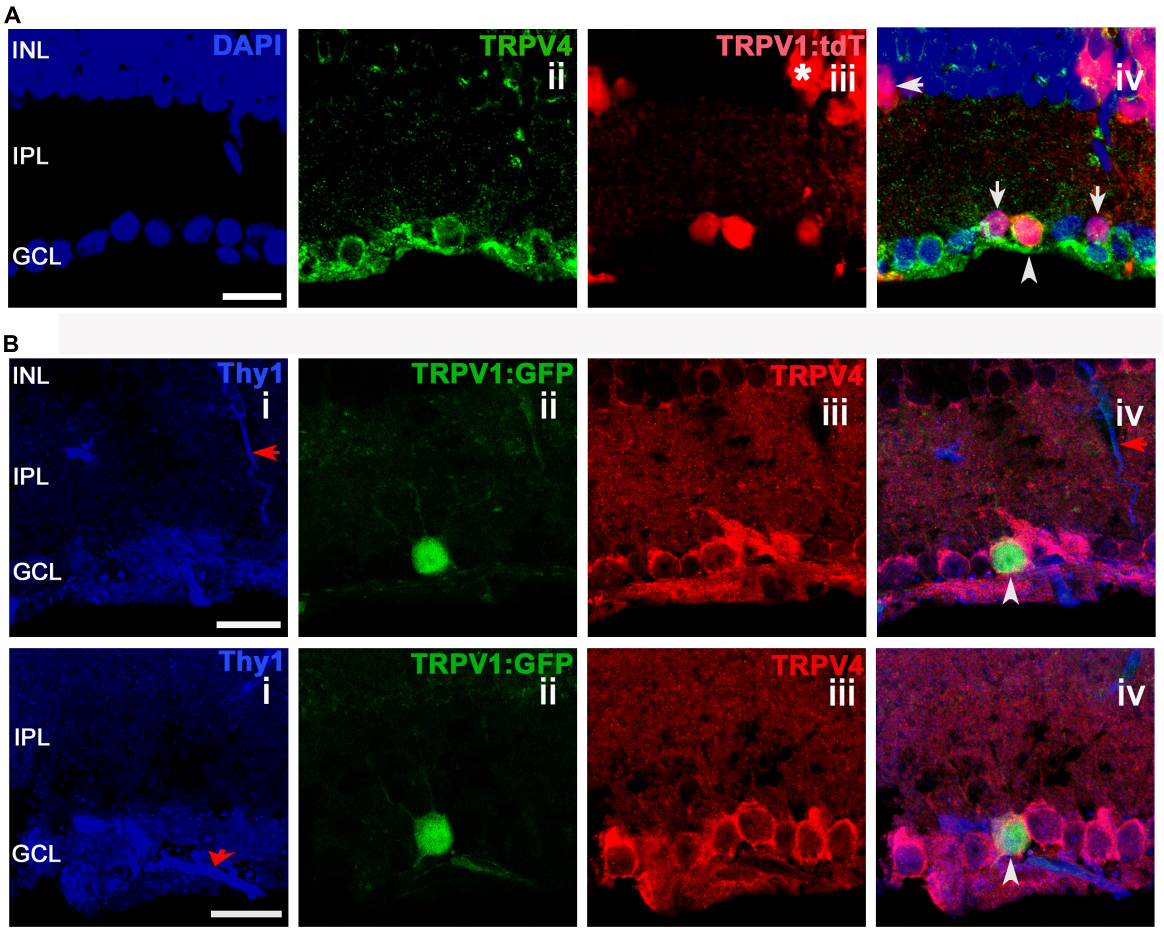

FIGURE 4 | TRPV1 expression in RGCs but not amacrine cells overlaps with TRPV4-ir. Confocal microscopy, vertical sections from the mouse retina. **(A)** TRPV1Cre/Ai9 retina labeled for DAPI, TRPV4, and TRPV1. TRPV1:tdTomato is expressed in cell somata localized in ganglion cell layer (GCL), inner nuclear layer (INL), and in a subset of putative Müller cells (asterisk). RGC that colocalizes TRPV1 and TRPV4 is marked by an arrowhead in panel iv. Arrows mark putative (small-diameter) amacrine cells in RGCL and IPL that are TRPV4$^-$. **(B)** TRPV1Cre/Ai3 section showing a TRPV1$^+$ cell labeled by the GFP reporter. The cell was immunopositive for TRPV4 and Thy1. Red arrows donate blood vessels. Pictures were obtained from two optical sections with a thickness of 1 μm. Scale bars = 20 μm.

patterns of tdTomato and GFP reporters, respectively (Mishra and Hoon, 2010; Jo et al., 2017). Cells were evaluated in vertical sections from the central- to mid-peripheral retina in order to increase the likelihood of hitting on TRPV1-expressing RGCs (e.g., Jo et al., 2017).

We found that TRPV4 is localized to a substantial population of putative RGCs (identified by Thy1 or RBPMS-ir). TRPV1$^+$ cells, identified by tdT$^+$ and GFP$^+$ fluorescence (**Figure 4**), typically colocalized with TRPV4-ir, with rare examples (arrow in **Figure 4A**) that were immunonegative for TRPV4. Two examples of TRPV1^{GFP} cell that colocalized the RGC marker Thy1 (CD90) with TRPV4 are shown in **Figure 4B** (arrowheads). Although Thy1 labels a subset of displaced cholinergic syntaxin$^+$ cells in the RGC layer (Raymond et al., 2008), the presence of TRPV4 (which is absent from amacrines; Ryskamp et al., 2011) indicates that the labeled cell is a RGC.

We investigated whether TRPV1 and 4 channels might be expressed in SMI-32 cells, which label αRGCs, large-diameter monostratified cells that arborize in ON or OFF sublaminae of the inner plexiform layer (Coombs et al., 2006), play a role in contrast sensitivity and are sensitive to ocular hypertension (Della Santina et al., 2013; Schmidt et al., 2014; Ou et al., 2016). All TRPV1-expressing RGCL cells were immunopositive for SMI-32 and TRPV4. **Figures 5A,B** show a TRPV1-expressing (RBPMS$^+$) RGC that strongly expresses SMI-32. Another example, shown in **Figures 5C,D**, showcases a TRPV1-expressing αRGC that also expresses TRPV4 (arrowhead in **Figure 5D**), whereas a TRPV1-expressing putative amacrine cell (arrow in **Figure 5C**) was TRPV4 immunonegative. We conclude that most RBPMS$^+$ TRPV1$^+$ cells are SMI-32$^+$ and can thus be classified as αRGCs. Of SMI-32$^+$ cells, 35.9% were TRPV1$^+$. TRPV1 expression was detected in some Müller cells that were immunopositive for TRPV4 (asterisks in **Figure 4A**). These data suggest that RGCs sense their ambient environment through different combinations of sensory transducers, with TRPV4 channels as dominant non-epithelial vanilloid transducers. Moreover, Müller glia appear to

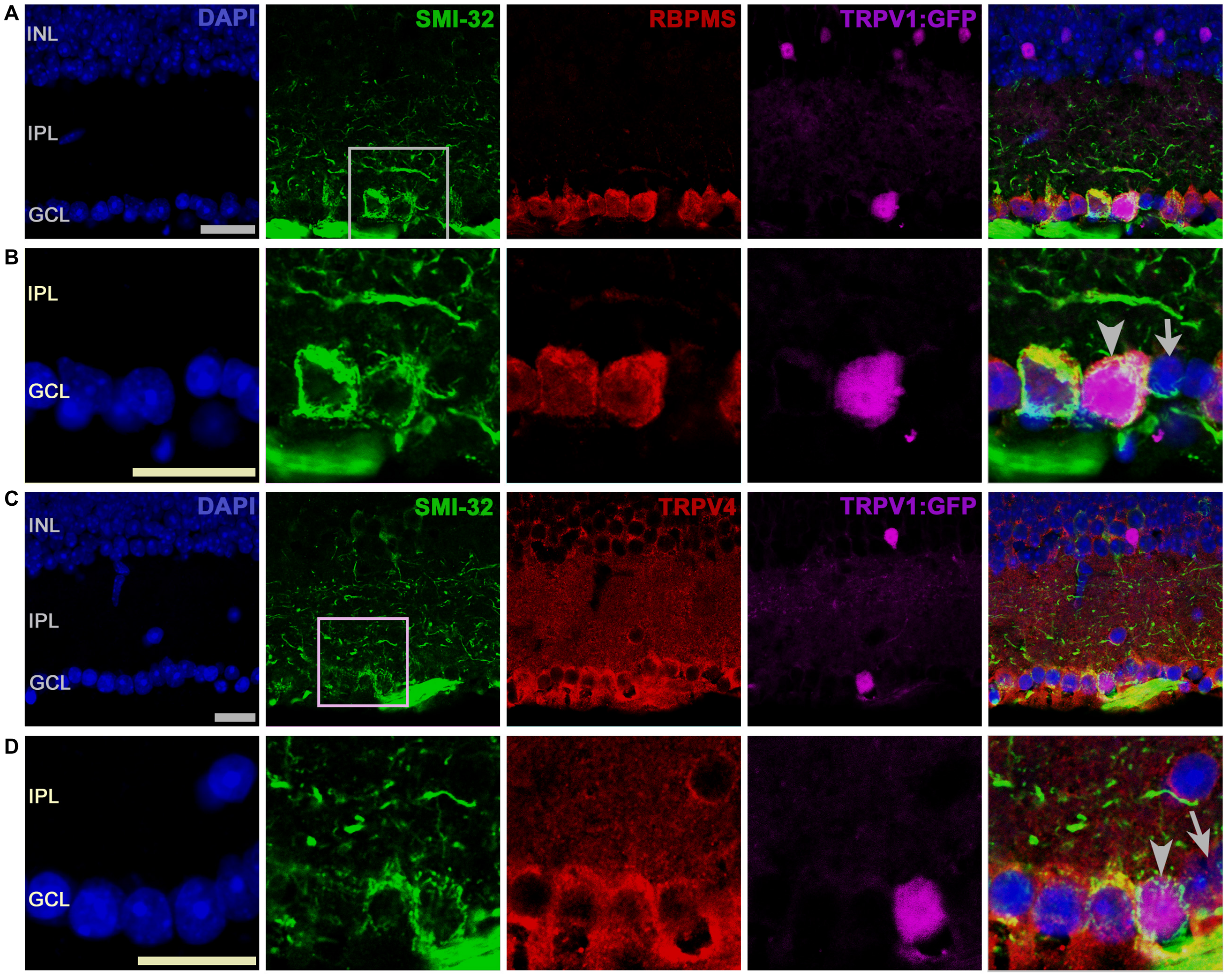

FIGURE 5 | SMI-32$^+$ RGCs coexpress TRPV1 and TRPV4 signals. **(A)** A representative TRPV1-expressing RGC is labeled by the GFP reporter that was immunopositive for SMI-32 and RBPMS. **(B)** Inset from **A**. **(C)** TRPV1-expressing RGCL neuron is labeled by SMI-32 and TRPV4 (**D**, arrowhead) antibodies. The arrow denotes a TRPV4- and SMI-32-immunonegative putative amacrine cell in the proximal INL. Pictures were obtained from one optical section. Scale bars = 20 μm.

express both vanilloid isoforms, which is consistent with their function as regulators in the retinal microenvironment (Ryskamp et al., 2015).

TRPV4 Signaling in TRPV1-Expressing RGCs Does Not Involve Subunit Heteromerization

Vanilloid TRP channels preferentially assemble into homomeric channels (Hellwig et al., 2005); however, formation of macromolecular complexes between TRPV4 and TRPC1 (Ma et al., 2015), TRPP2 (Stewart et al., 2010), and TRPV1 (Sappington et al., 2015) has been reported for endothelial, kidney, and ganglion cells, respectively. We recently reported that pharmacological blockade of TRPV4 has no effect on TRPV1-mediated calcium signals (Jo et al., 2017). Here, we took advantage of transgenic mice to test whether heteromerization with TRPV1 is obligatory for TRPV4 functionality. To test TRPV1–V4 interactions, we assessed the responsiveness to CAP in RGCs expressing a fluorescent reporter (eGFP) under the control of the TRPV4 promoter (Gu et al., 2016). Recordings from CAP responding TRPV4^{eGFP+} RGCs (**Figures 6Ai,ii**) showed an absence of effect of the TRPV1 antagonist CPZ on baseline $[Ca^{2+}]_i$. The amplitude of GSK101-induced $[Ca^{2+}]_i$ elevations in the presence of CPZ was 0.66 ± 0.12 (n = 12, $P < 0.001$; **Figures 6A,B**), not significantly different from GSK101 responses in WT cells (0.51 ± 0.05; **Figure 2D**). These data indicate that TRPV1 in mouse RGCs is not required for TRPV4 function and vice versa, TRPV4-mediated responses are largely unaffected by TRPV1 knockdown.

TRPV1 Channel Does Not Influence TRPV4 Functionality in Subset of RGCs

Expression of cannabinoid receptors in most, if not all, mammalian retinal cells (Ryskamp et al., 2014b; Jo et al., 2017)

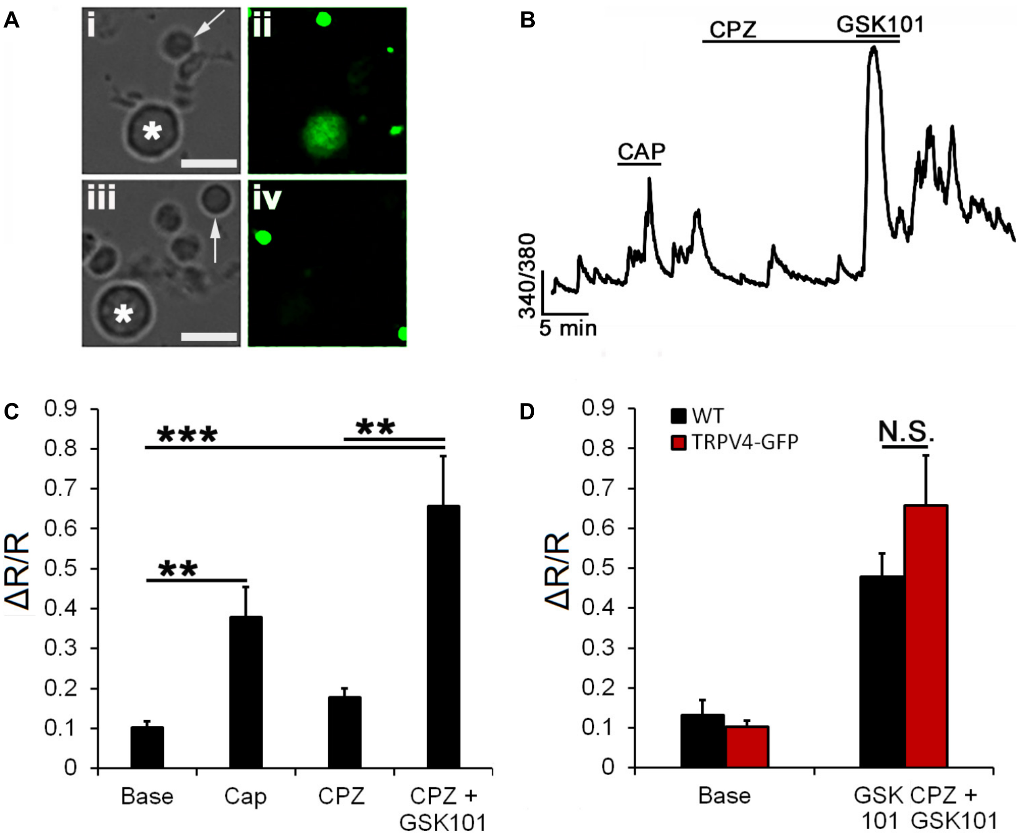

FIGURE 6 | TRPV4 signaling does not require TRPV1. **(A)** Cells dissociated from transgenic TRPV4^{GFP} retinas **(i,ii)** and control retinas **(iii,iv)** show reporter expression in large-diameter neurons (asterisk) but not rod somata (arrow). **(B)** Representative trace from a TRPV4^{GFP+} RGC shows a potential response to CAP superimposed on spontaneous background Ca^{2+} transients. The TRPV1 antagonist CPZ (10 μM) did not affect the $[Ca^{2+}]_i$ baseline or inhibit GSK101-evoked $[Ca^{2+}]_i$ elevations. **(C)** Averaged data for CAP and CPZ responses in TRPV4^{GFP+} RGCs ($n = 12$). **(D)** CPZ had no effect on the amplitude of GSK101-evoked $[Ca^{2+}]_i$ signals ($n = 12$). Scale bar = 10 μm. N.S., $P < 0.05$, $^{**}P \leq 0.01$, $^{***}P \leq 0.001$.

suggests that tonic and/or activity dependent release of endocannabinoids might be important for processing of visual signals. Endocannabinoids regulate TRPV1 directly and through CB1R-dependent intracellular messengers (Zygmunt et al., 1999) but were also suggested to influence TRPV4 activation (Watanabe et al., 2003; Ho et al., 2015). Exposure to the endogenous agonist of CB1 receptor 2-AG suppresses TRPV1 channels in mouse RGC (Jo et al., 2017). To establish whether 2-AG has comparable effects on RGC TRPV4 activation we recorded calcium signals from TRPV4^{eGFP} (**Figures 7A,B**), as well as wild type (black traces, **Figures 7C–E**) and TRPV1$^{-/-}$ RGCs (orange traces, **Figures 7C–E**) in the presence or absence of 2-AG. **Figures 7B,C** show that 2-AG (1 μM) does not affect the $[Ca^{2+}]_{RGC}$ baseline and GSK101-evoked $[Ca^{2+}]_i$ signals in both TRPV4$^+$ (0.63 ± 0.12; $n = 10$) and TRPV1-TRPV4$^+$ (0.56 ± 0.12; $n = 10$) RGCs. Moreover, in TRPV1$^{-/-}$ RGCs (**Figures 7C–E**), GSK101-evoked $[Ca^{2+}]_i$ signals recorded in cells preincubated with 2-AG (0.62 ± 0.05; $n = 24$) were also indistinguishable from control responses (0.59 ± 0.05; $n = 24$). Consistent with the pharmacological experiments (**Figure 6**), we found that ablation of TRPV1 has no effect on GSK101-evoked signals ($n = 8$; **Figure 7A**). These data suggest that, unlike TRPV1 signals, TRPV4 signaling in the mouse retina will resist endocannabinoid modulation.

DISCUSSION

This study provides a number of novel observations that are relevant for the understanding of non-canonical sensory transduction in vertebrate vision. First, we quantified the TRPV isoform expression across RGCs. This is important because it identifies potential targets for mechanical and inflammatory stressors that affect specific subpopulations of these projection neurons. Second, we determined the relative abundance and colocalization of the two most extensively studied vanilloid channel isoforms in mouse RGCs. Third, we provide evidence against obligatory functional heteromerization between TRPV1 and TRPV4 channels. Fourth, we show that a proportion of SMI-32$^+$ αRGCs – cells known to be sensitive to IOP – coexpress TRPV1 and TRPV4 channels. Together, these findings suggest that projection of sensory information to retinorecipient nuclei in the midbrain is differentially distributed across subpopulations of RGCs.

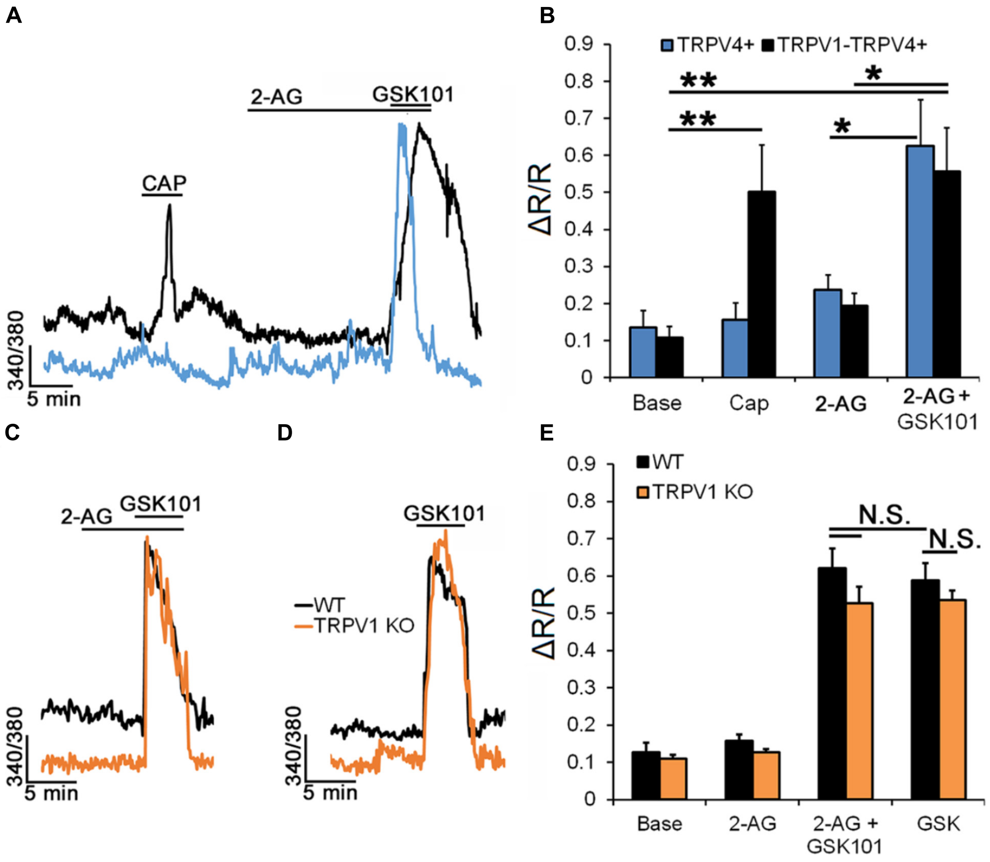

FIGURE 7 | RGC TRPV4 signaling is not modulated by endocannabinoids. Recordings from TRPV4^{eGFP}, wild type (C57), and TRPV1$^{-/-}$ RGCs. **(A)** Representative traces and **(B)** cumulative averaged data for CAP and 2-AG responses in TRPV4^{+} (*n* = 10) and TRPV1-TRPV4^{+} (*n* = 10) RGCs. **(C)** Preincubation with 2-AG has no effect on the amplitude of the GSK101-evoked [Ca^{2+}]$_i$ response (*n* = 24). **(D)** Ablation of the *Trpv1* gene has no effect on the TRPV4 response (*n* = 8). **(E)** Cumulative averaged data from WT (black) and TRPV1 (orange) KO RGCs. Neither exposure to 2-AG nor absence of TRPV1 impact GSK101-evoked [Ca^{2+}]$_i$ signaling. $^{*}P \leq 0.05$, $^{**}P \leq 0.01$.

Transcript analysis in mouse RGCs revealed that the cells express all four non-epithelial vanilloid mRNAs, with *Trpv4* by far the most prevalent transcript, followed by *Trpv2* and residual expression of *Trpv1* and *Trpv3* (**Figures 1A,B**). Our functional data were broadly reflective of the *Trpv* transcriptome, with ∼50% RGCs responding to the TRPV4 agonist, ∼20% responded to the TRPV1 agonist, and ∼10% responsive to agonists specific for both channels. A similar expression pattern emerged from immunohistochemical and electrophysiological analyses in the rat DRG, in which ∼89% neurons were shown to express TRPV4, ∼34% express TRPV1 channels, and 28% express projection of both channels (Cao et al., 2009) whereas TRPV1 and TRPV2 (Lewinter et al., 2004) and TRPV1 and TRPM8 displayed little coexpression (Kobayashi et al., 2005). The percentage of TRPV4-ir RGCs exceeds the size of the GSK101-responding pool, presumably because cell dissociation/separation compromises the activation of these stretch-activated channels (e.g., Ryskamp et al., 2011).

TRPV1 and TRPV4 coexpression in mouse RGCs is in accord with quantifications that had been conducted separately for each isoform (Ryskamp et al., 2011; Jo et al., 2017). Previous work localized TRPV4 to RGC somata, and primary dendrites, but there is little information about subcellular TRPV1 expression due to the lack of specificity of TRPV1 antibodies (Gilliam and Wensel, 2011; Molnar et al., 2012). Coexpression of multiple thermoTRPs isoforms in single RGCs suggests that the cells may be capable of parallel transduction of sensory information that includes osmotic gradients, mechanical strain, acidity, and biolipids such as endocannabinoids and polyunsaturated fatty acids (e.g., arachidonic acid and eicosanoids). The possibility that TRPV4 channels mediate the disproportionate sensitivity of certain neurons to mechanical stressors is supported by the observations that (i) TRPV4 activation augments excitability by stimulating TTX-sensitive currents and voltage-operated calcium channels (Li et al., 2011) and increases the firing of substantia nigra (Guatteo et al., 2005), DRG (Cao et al., 2009), hippocampal neurons (Shibasaki et al., 2007), and RGCs (Ryskamp et al., 2011), (ii) TRPV4 mutations underlie debilitating sensory and motor neuropathies (Nilius and Voets, 2013) whereas (iii) TRPV4$^{-/-}$ mice exhibit impaired mechanical nociception (Liedtke and Friedman, 2003) and (iv) may be protected from mechanical hyperalgesia and glaucomatous neurodegeneration (Alessandri-Haber et al., 2004; Ryskamp et al., 2016). Mice lacking a functional *Trpv4* gene show impaired responses to intense mechanical stimuli but normal responses to low threshold stimulation (Liedtke and Friedman, 2003; Suzuki et al., 2003), suggesting that TRPV4 will preferentially mediate calcium signals in respond to excessive mechanical stress (for example, in hypertensive glaucoma). Consistent with this, elevated calcium levels were reported in glaucomatous RGCs (Niittykoski et al., 2010).

TRPV1 is the most extensively studied retinal vanilloid channel, with reports suggesting pre- and postsynaptic expression across multiple cell types (Yazulla, 2008; Ryskamp et al., 2014b) that include a subpopulation of RGCs (Jo et al., 2017). Although *Trpv1* mRNA levels in RGCS were negligible compared to *Trpv2* and *Trpv4* expression, CAP-responding cells constituted ∼20% of the overall magnetoseparated population. This suggests that low expression of the *Trpv1* gene is sufficient to support TRPV1-mediated Ca^{2+} entry in a substantial mouse RGC cohort. Our findings in the retina mirror previous studies the brain, which was reported to show low *Trpv1* expression (Cavanaugh et al., 2011) even though neurons across multiple brain regions respond to CAP with TRPV1-dependent modulation of synaptic plasticity and vesicle release (Gibson et al., 2008; Wu et al., 2014; Fenwick et al., 2017). While physiological functions of retinal TRPV1 have not been clearly defined, its localization to αRGCs, which respond to modest IOP elevations with dendritic and synaptic remodeling (Ou et al., 2016) potentially links pressure-dependent RGC excitability (Weitlauf et al., 2014) and apoptosis (Sappington et al., 2009) to the early loss of large-diameter RGCs exposed to glaucomatous stressors such as IOP (Glovinsky et al., 1991). Arguing against a direct TRPV1 role in pressure transduction are the limited expression of the channel in RGCs and the reports that TRPV1 ablation augments RGC injury in a mouse model of ocular hypertension (Ward et al., 2014). There is also conflicting evidence about whether TRPV1 is expressed in retinal glia, as the channel was reported in rabbit but not detected in rat Müller cells (Leonelli et al., 2009; Martínez-García et al., 2013). Our analysis of reporter mice shows that TRPV1 is expressed in a subset of Müller glia but it remains unclear whether this was due to non-uniformity of *Trpv1* expression or an artifact resulting from differential expression of the reporter transgene.

This is the first report that a small but significant fraction of RGCs (∼10%) functionally coexpress TRPV1 and TRPV4 isoforms. Interestingly, this cohort included cells that were immunopositive for SMI-32, a marker of αRGCs which form four independent mosaics within the IPL-RGCL (Krieger et al., 2017), include M4 ipRGCs (Schmidt et al., 2014), and constitute one of the fastest pathways for retina–brain information transfer. Whether native TRPV1 and TRPV4 channels are capable of heteromultimerization has been controversial given that subunit interactions predicted by FRET studies (Cheng et al., 2007) and co-immunoprecipitation (Sappington et al., 2015) have not been not substantiated by investigations of TRPV1-4 subunit expression in heterologously expressing cells (Hellwig et al., 2005). $TRPV4^{-/-}$ mice exhibit impaired mechanical nociception but show conserved TRPV1-mediated responses to noxious heat (Liedtke and Friedman, 2003; Suzuki et al., 2003). We expand on these studies to show that heteromerization is not obligatory for the activation of native neuronal TRPV1 or TRPV4 channels as indicated the observation that neither activation nor inhibition of TRPV1 affect the amplitude and kinetics of GSK101-evoked calcium responses. *Vice versa*, pretreatment with TRPV4 agonists/antagonists had no effect on the cells' responsiveness to CAP. We also found that (i) desensitization of one isoform has little effect on the agonist-evoked responsiveness of the other and (ii) CB1 receptor activation which inhibits TRPV1 channels (Jo et al., 2017) has no effect on TRPV4-mediated signals in TRPV1-expressing RGCs; this finding mirrors the analyses in DRG neurons which showed that native TRPV1 and TRPV4 currents can be explained by single channel properties of each channel (Premkumar et al., 2002; Kim et al., 2016). It is possible that interactions between the two channels will emerge under pathological circumstances, as either channel can contribute to mechanical hyperalgesia (Vennekens et al., 2008; Huynh et al., 2014) and both were linked to optic neuropathy (Ryskamp et al., 2011; Weitlauf et al., 2014). Indeed, TRPV1 activation that is not harmful in healthy tissue can be pathological during mechanical hyperalgesia and facilitated by pro-inflammatory molecules that have been implicated in glaucoma such as ATP, prostaglandins, and arachidonic acid metabolites (Nilius and Szallasi, 2014). We hypothesize that TRPV1/4 sensitization ("allodynia") amplifies pressure-induced neuronal damage through eicosanoid products of CYP450, which activate TRPV4 (5′6′-EET, 11′,12′-EET) and TRPV1 (12-(S)-HETE, 20-HETE) (Watanabe et al., 2003; Wen et al., 2012; Ryskamp et al., 2014b) or N-arachidonoyl taurine which activates both channels (Bradshaw et al., 2013). TRPV1/4-dependent mechanical allodynia is a characteristic feature of neurogenic inflammatory and neuropathic pain paradigms in sensory neurons (Alessandri-Haber et al., 2004; Amadesi et al., 2006; Grant et al., 2007). Importantly, hyperalgesia-associated properties of thermoTRPs channels would also augment the susceptibility of retinal neurons and glia to glaucomatous injury (Križaj, 2016). Among inflammatory agents that sensitize TRPV1 and TRPV4 are ATP, bradykinin, prostaglandin E2, and PAR2 agonists which have been linked to cytotoxicity and neurodegeneration (Grant et al., 2007; Nilius and Szallasi, 2014; Lu et al., 2015). However, certain messenger molecules may preferentially stimulate one isoform over the other. For example, TRPV4 signaling in RGCs is unaffected by the long-chain unsaturated acyl-amide 2-AG that potently modulates TRPV1 activation (Bradshaw et al., 2013; Ryskamp et al., 2014b; Jo et al., 2017).

Collectively, these findings extend our understanding of how non-canonical sensory stimuli are transduced in mammalian RGCs. We know that the devastating effects of pressure, strain, swelling, ocular trauma and inflammatory inputs on vision tend to be associated with early effects of mechanical stress on the viability and function of RGCs (Križaj, 2016). It remains to be seen whether synergistic activation of TRPV1 and 4 under pathological conditions unlocks novel models of sensory transduction, as observed for somatosensory afferents, in which combined expression of TRPV1, TRPM3, and TRPA1 is required for the transduction of noxious heat (Vandewauw et al., 2018). A non-mutually exclusive possibility is that the two vanilloid isoforms impart complementary sensory information that could be important for signaling in specific RGC classes such as αRGCs. Because mouse RGC subpopulations tend to be conserved in primates (Chalupa and Williams, 2008), our findings might extend across phylogenetic domains.

AUTHOR CONTRIBUTIONS

ML and DK conceived the project. JB, DY, AJ, and ML performed the experiments. HH contributed transgenic mice. ML and DK analyzed the data and wrote the paper.

FUNDING

This work was supported by the National Institutes of Health (EY022076, EY027920, T32EY024234, and P30EY014800), Willard L. Eccles Foundation, Glaucoma Research Foundation (DK), the University of Utah Undergraduate Research Opportunity Program (DY and AJ), and unrestricted support from Research to Prevent Blindness to the Moran Eye Institute at the University of Utah.

ACKNOWLEDGMENTS

We thank Dr. Maureen McCall (University of Louisville) for the transgenic TRPV1 retinas and Dr. Wolfgang Liedtke (Duke University) for TRPV4$^{-/-}$ mice.

REFERENCES

Alessandri-Haber, N., Dina, O. A., Yeh, J. J., Parada, C. A., Reichling, D. B., and Levine, J. D. (2004). Transient receptor potential vanilloid 4 is essential in chemotherapy-induced neuropathic pain in the rat. *J. Neurosci.* 24, 4444–4452. doi: 10.1523/JNEUROSCI.0242-04.2004

Amadesi, S., Cottrell, G. S., Divino, L., Chapman, K., Grady, E. F., Bautista, F., et al. (2006). Protease-activated receptor 2 sensitizes TRPV1 by protein kinase Cepsilon- and A-dependent mechanisms in rats and mice. *J. Physiol.* 575, 555–571. doi: 10.1113/jphysiol.2006.111534

Baden, T., Berens, P., Franke, K., Román Rosón, M., Bethge, M., and Euler, T. (2016). The functional diversity of retinal ganglion cells in the mouse. *Nature* 529, 345–350. doi: 10.1038/nature16468

Bradshaw, H. B., Raboune, S., and Hollis, J. L. (2013). Opportunistic activation of TRP receptors by endogenous lipids: exploiting lipidomics to. Understand TRP receptor cellular communication. *Life Sci.* 92, 404–409. doi: 10.1016/j.lfs.2012.11.008

Cao, D. S., Yu, S. Q., and Premkumar, L. S. (2009). Modulation of transient receptor potential Vanilloid 4-mediated membrane currents and synaptic transmission by protein kinase C. *Mol. Pain* 5:5. doi: 10.1186/1744-8069-5-5

Caterina, M. J., Schumacher, M. A., Tominaga, M., Rosen, T. A., Levine, J. D., and Julius, D. (1997). The capsaicin receptor: a heat-activated ion channel in the pain pathway. *Nature* 389, 816–824. doi: 10.1038/39807

Cavanaugh, D. J., Chesler, A. T., Jackson, A. C., Sigal, Y. M., Yamanaka, H., Grant, R., et al. (2011). Trpv1 reporter mice reveal highly restricted brain distribution and functional expression in arteriolar smooth muscle cells. *J. Neurosci.* 31, 5067–5077. doi: 10.1523/JNEUROSCI.6451-10.2011

Chalupa, L. M., and Williams, R. W. (2008). *Eye, Retina, and Visual System of the Mouse*. Cambridge, MA: MIT Press.

Cheng, W., Yang, F., Takanishi, C. L., and Zheng, J. (2007). Thermosensitive TRPV channel subunits coassemble into heteromeric channels with intermediate conductance and gating properties. *J. Gen. Physiol.* 129, 191–207. doi: 10.1085/jgp.200709731

Clapham, D. E. (2003). TRP channels as cellular sensors. *Nature* 426, 517–524. doi: 10.1038/nature02196

Coombs, J., van der List, D., Wang, G. Y., and Chalupa, L. M. (2006). Morphological properties of mouse retinal ganglion cells. *Neuroscience* 140, 123–136. doi: 10.1016/j.neuroscience.2006.02.079

Della Santina, L., Inman, D. M., Lupien, C. B., Horner, P. J., and Wong, R. O. (2013). Differential progression of structural and functional alterations in distinct retinal ganglion cell types in a mouse model of glaucoma. *J. Neurosci.* 33, 17444–17457. doi: 10.1523/JNEUROSCI.5461-12.2013

Duan, X., Qiao, M., Bei, F., Kim, I. J., He, Z., and Sanes, J. R. (2015). Subtype-specific regeneration of retinal ganglion cells following axotomy: effects of osteopontin and mTOR signaling. *Neuron* 85, 1244–1256. doi: 10.1016/j.neuron.2015.02.017

Echaniz-Laguna, A., Dubourg, O., Carlier, P., Carlier, R. Y., Sabouraud, P., Péréon, Y., et al. (2014). Phenotypic spectrum and incidence of TRPV4 mutations in patients with inherited axonal neuropathy. *Neurology* 82, 1919–1926. doi: 10.1212/WNL.0000000000000450

Fenwick, A. J., Fowler, D. K., Wu, S. W., Shaffer, F. J., Lindberg, J. E. M., Kinch, D. C., et al. (2017). Direct anandamide activation of TRPV1 produces divergent calcium and current responses. *Front. Mol. Neurosci.* 10:200. doi: 10.3389/fnmol.2017.00200

Gibson, H. E., Edwards, J. G., Page, R. S., Van Hook, M. J., and Kauer, J. A. (2008). TRPV1 channels mediate long-term depression at synapses on hippocampal interneurons. *Neuron* 57, 746–759. doi: 10.1016/j.neuron.2007.12.027

Gilliam, J. C., and Wensel, T. G. (2011). TRP channel gene expression in the mouse retina. *Vision Res.* 51, 2440–2452. doi: 10.1016/j.visres.2011.10.009

Glovinsky, Y., Quigley, H. A., and Dunkelberger, G. R. (1991). Retinal ganglion cell loss is size dependent in experimental glaucoma. *Invest. Ophthalmol. Vis. Sci.* 32, 484–491.

Grant, A. D., Cottrell, G. S., Amadesi, S., Trevisani, M., Nicoletti, P., Materazzi, S., et al. (2007). Protease-activated receptor 2 sensitizes the transient receptor potential vanilloid 4 ion channel to cause mechanical hyperalgesia in mice. *J. Physiol.* 578, 715–733. doi: 10.1113/jphysiol.2006.121111

Gu, Q. D., Moss, C. R. II, Kettelhut, K. L., Gilbert, C. A., and Hu, H. (2016). Activation of TRPV4 regulates respiration through indirect activation of bronchopulmonary sensory neurons. *Front. Physiol.* 7:65. doi: 10.3389/fphys.2016.00065

Guatteo, E., Chung, K. K., Bowala, T. K., Bernardi, G., Mercuri, N. B., and Lipski, J. (2005). Temperature sensitivity of dopaminergic neurons of the substantia nigra pars compacta: involvement of transient receptor potential channels. *J. Neurophysiol.* 94, 3069–3080. doi: 10.1152/jn.00066.2005

Hellwig, N., Albrecht, N., Harteneck, C., Schultz, G., and Schaefer, M. (2005). Homo- and heteromeric assembly of TRPV channel subunits. *J. Cell Sci.* 118, 917–928. doi: 10.1242/jcs.01675

Ho, W. S., Zheng, X., and Zhang, D. X. (2015). Role of endothelial TRPV4 channels in vascular actions of the endocannabinoid, 2-arachidonoylglycerol. *Br. J. Pharmacol.* 172, 5251–5264. doi: 10.1111/bph.13312

Huynh, K. W., Cohen, M. R., Chakrapani, S., Holdaway, H. A., Stewart, P. L., and Moiseenkova-Bell, V. Y. (2014). Structural insight into the assembly of TRPV channels. *Structure* 22, 260–268. doi: 10.1016/j.str.2013.11.008

Jo, A., Ryskamp, D., Phuong, T., Verkman, A., Yarishkin, O., MacAulay, N., et al. (2015). TRPV4 and AQP4 channels synergistically regulate cells volume and calcium homeostasis in retinal Müller glia. *J. Neurosci.* 35, 13525–13537. doi: 10.1523/JNEUROSCI.1987-15.2015

Jo, A. O., Lakk, M., Frye, A. M., Phuong, T. T., Redmon, S. N., Roberts, R., et al. (2016). Differential volume regulation and calcium signaling in two ciliary body cell types is subserved by TRPV4 channels. *Proc. Natl. Acad. Sci. U.S.A.* 113, 3885–3890. doi: 10.1073/pnas.1515895113

Jo, A. O., Noel, J. M., Lakk, M., Yarishkin, O., Ryskamp, D. A., Shibasaki, K., et al. (2017). Mouse retinal ganglion cell signalling is dynamically modulated through parallel anterograde activation of cannabinoid and vanilloid pathways. *J. Physiol.* 595, 6499–6516. doi: 10.1113/JP274562

Kim, S., Barry, D. M., Liu, X. Y., Yin, S., Munanairi, A., Meng, Q. T., et al. (2016). Facilitation of TRPV4 by TRPV1 is required for itch transmission in some sensory neuron populations. *Sci. Signal.* 9:ra71. doi: 10.1126/scisignal.aaf1047

Kobayashi, K., Fukuoka, T., Obata, K., Yamanaka, H., Dai, Y., Tokunaga, A., et al. (2005). Distinct expression of TRPM8, TRPA1, and TRPV1 mRNAs in rat primary afferent neurons with adelta/c-fibers and colocalization with trk receptors. *J. Comp. Neurol.* 493, 596–606. doi: 10.1002/cne.20794

Krieger, B., Qiao, M., Rousso, D. L., Sanes, J. R., and Meister, M. (2017). Four alpha ganglion cell types in mouse retina: function, structure, and molecular signatures. *PLoS One* 12:e0180091. doi: 10.1371/journal.pone.0180091

Križaj, D. (2016). Polymodal sensory integration in retinal ganglion cells. *Adv. Exp. Med. Biol.* 854, 693–698. doi: 10.1007/978-3-319-17121-0_92

Križaj, D., Ryskamp, D. A., Tian, N., Tezel, G., Mitchell, C. H., Slepak, V. Z., et al. (2014). From mechanosensitivity to inflammatory responses: new players in the pathology of glaucoma. *Curr. Eye Res.* 39, 105–119. doi: 10.3109/02713683.2013.836541

Lakk, M., Yarishkin, O., Baumann, J. M., Iuso, A., and Križaj, D. (2017). Cholesterol regulates polymodal sensory transduction in Müller glia. *Glia* 65, 2038–2050. doi: 10.1002/glia.23213

Leonelli, M., Martins, D. O., Kihara, A. H., and Britto, L. R. (2009). Ontogenetic expression of the vanilloid receptors TRPV1 and TRPV2 in the rat retina. *Int. J. Dev. Neurosci.* 27, 709–718. doi: 10.1016/j.ijdevneu.2009.07.003

Lettvin, J. Y., Maturana, H. R., McCulloch, W. S., and Pitts, W. H. (1959). What the frog's eye tells the frog's brain. *Proc. IRE* 47, 1940–1951. doi: 10.1109/JRPROC.1959.287207

Lewinter, R. D., Skinner, K., Julius, D., and Basbaum, A. I. (2004). Immunoreactive TRPV-2 (VRL-1), a capsaicin receptor homolog, in the spinal cord of the rat. *J. Comp. Neurol.* 470, 400–408. doi: 10.1002/cne.20024

Li, L., Liu, C., Chen, L., and Chen, L. (2011). Hypotonicity modulates tetrodotoxin-sensitive sodium current in trigeminal ganglion neurons. *Mol. Pain* 7:27. doi: 10.1186/1744-8069-7-27

Liedtke, W., and Friedman, J. M. (2003). Abnormal osmotic regulation in Trpv4-/- mice. *Proc. Natl. Acad. Sci. U.S.A.* 100, 13698–13703. doi: 10.1073/pnas.1735416100

Lu, W., Hu, H., Sévigny, J., Gabelt, B. T., Kaufman, P. L., Johnson, E. C., et al. (2015). Rat, mouse, and primate models of chronic glaucoma show sustained elevation of extracellular ATP and altered purinergic signaling in the posterior eye. *Invest. Ophthalmol. Vis. Sci.* 56, 3075–3083. doi: 10.1167/iovs.14-15891

Ma, Y., Zhang, P., Li, J., Lu, J., Ge, J., Zhao, Z., et al. (2015). Epoxyeicosatrienoic acids act through TRPV4-TRPC1-KCa1.1 complex to induce smooth muscle membrane hyperpolarization and relaxation in human internal mammary arteries. *Biochim. Biophys. Acta* 1852, 552–559. doi: 10.1016/j.bbadis.2014.12.010

Madison, L., Zwingman, T. A., Sunkin, S. M., Oh, S. W., Zariwala, H. A., Gu, H., et al. (2010). A robust and high-throughput Cre reporting and characterization system for the whole mouse brain. *Nat. Neurosci.* 13, 133–140. doi: 10.1038/nn.2467

Martínez-García, M. C., Martínez, T., Pañeda, C., Gallego, P., Jimenez, A. I., and Merayo, J. (2013). Differential expression and localization of transient receptor potential vanilloid 1 in rabbit and human eyes. *Histol. Histopathol.* 28, 1507–1516. doi: 10.14670/HH-28.1507

Martins, D., Tavares, I., and Morgado, C. (2014). "Hotheaded": the role OF TRPV1 in brain functions. *Neuropharmacology* 85, 151–157. doi: 10.1016/j.neuropharm.2014.05.034

Middleton, T. P., and Protti, D. A. (2011). Cannabinoids modulate spontaneous synaptic activity in retinal ganglion cells. *Vis. Neurosci.* 28, 393–402. doi: 10.1017/S0952523811000198

Mishra, S. K., and Hoon, M. A. (2010). Ablation of TrpV1 neurons reveals their selective role in thermal pain sensation. *Mol. Cell. Neurosci.* 43, 157–163. doi: 10.1016/j.mcn.2009.10.006

Molnar, T., Barabas, P., Birnbaumer, L., Punzo, C., Kefalov, V., and Križaj, D. (2012). Store-operated channels regulate intracellular calcium in mammalian rods. *J. Physiol.* 590, 3465–3481. doi: 10.1113/jphysiol.2012.234641

Molnar, T., Yarishkin, O., Iuso, A., Barabas, P., Jones, B., Marc, R. E., et al. (2016). Store-operated calcium entry in Müller glia is controlled by synergistic activation of TRPC and Orai channels. *J. Neurosci.* 36, 3184–3198. doi: 10.1523/JNEUROSCI.4069-15.2016

Morin, L. P., and Studholme, K. M. (2014). Retinofugal projections in the mouse. *J. Comp. Neurol.* 522, 3733–3753. doi: 10.1002/cne.23635

Muller, L. P. D., Sargoy, A., Rodriguez, A. R., and Brecha, N. C. (2014). Melanopsin ganglion cells are the most resistant retinal ganglion cell type to axonal injury in the rat retina. *PLoS One* 9:e93274. doi: 10.1371/journal.pone.0093274

Niittykoski, M., Kalesnykas, G., Larsson, K. P., Kaarniranta, K., Akerman, K. E., and Uusitalo, H. (2010). Altered calcium signaling in an experimental model of glaucoma. *Invest. Ophthalmol. Vis. Sci.* 51, 6387–6393. doi: 10.1167/iovs.09-3816

Nilius, B., and Szallasi, A. (2014). Transient receptor potential channels as drug targets: from the science of basic research to the art of medicine. *Pharmacol. Rev.* 66, 676–814. doi: 10.1124/pr.113.008268

Nilius, B., and Voets, T. (2013). The puzzle of TRPV4 channelopathies. *EMBO Rep.* 14, 152–163. doi: 10.1038/embor.2012.219

Ou, Y., Jo, R. E., Ullian, E. M., Wong, R. O., and Della Santina, L. (2016). Selective vulnerability of specific retinal ganglion cell types and synapses after transient ocular hypertension. *J. Neurosci.* 36, 9240–9252. doi: 10.1523/JNEUROSCI.0940-16.2016

Phuong, T. T. T., Redmon, S. N., Yarishkin, O., Winter, J. M., Li, D. Y., and Križaj, D. (2017). Calcium influx through TRPV4 channels modulates the adherens contacts between retinal microvascular endothelial cells. *J. Physiol.* 595, 6869–6885. doi: 10.1113/JP275052

Premkumar, L. S., Agarwal, S., and Steffen, D. (2002). Single-channel properties of native and cloned rat vanilloid receptors. *J. Physiol.* 545, 107–117. doi: 10.1113/jphysiol.2002.016352

Ramírez-Barrantes, R., Cordova, C., Poblete, H., Muñoz, P., Marchant, I., Wianny, F., et al. (2016). Perspectives of TRPV1 function on the neurogenesis and neural plasticity. *Neural Plast.* 2016:1568145. doi: 10.1155/2016/1568145

Raymond, I. D., Vila, A., Huynh, U. C., and Brecha, N. C. (2008). Cyan fluorescent protein expression in ganglion and amacrine cells in a Thy1-CFP transgenic mouse retina. *Mol. Vis.* 14, 1559–1574.

Redmon, S. N., Shibasaki, K., and Krizaj, D. (2017). "Transient receptor potential cation channel subfamily V member 4," in *Encyclopedia of Signaling Molecules*, 2nd Edn, ed. S. Choi (Berlin: Springer Verlag).

Ryskamp, D. A., Frye, A. M., Phuong, T. T. T., Yarishkin, O., Jo, A. O., Xu, Y., et al. (2016). TRPV4 regulates calcium homeostasis, cytoskeletal remodeling, conventional outflow and intraocular pressure in the mammalian eye. *Sci. Rep.* 6:30583. doi: 10.1038/srep30583

Ryskamp, D. A., Iuso, A., and Križaj, D. (2015). TRPV4 links inflammatory signaling and neuroglial swelling. *Channels* 9, 70–72. doi: 10.1080/19336950.2015.1017998

Ryskamp, D. A., Jo, A. O., Frye, A. M., Vazquez-Chona, F., MacAulay, N., Thoreson, W. B., et al. (2014a). Swelling and eicosanoid metabolites differentially gate TRPV4 channels in retinal neurons and glia. *J. Neurosci.* 34, 15689–15700. doi: 10.1523/JNEUROSCI.2540-14.2014

Ryskamp, D. A., Redmon, S., Jo, A. O., and Križaj, D. (2014b). TRPV1 and endocannabinoids: emerging molecular signals that modulate mammalian vision. *Cells* 3, 914–938. doi: 10.3390/cells3030914

Ryskamp, D. A., Witkovsky, P., Barabas, P., Huang, W., Koehler, C., Akimov, N. P., et al. (2011). The polymodal ion channel transient receptor potential vanilloid 4 modulates calcium flux, spiking rate, and apoptosis of mouse retinal ganglion cells. *J. Neurosci.* 31, 7089–7101. doi: 10.1523/JNEUROSCI.0359-11.2011

Sappington, R. M., Sidorova, T., Long, D. J., and Calkins, D. J. (2009). TRPV1: contribution to retinal ganglion cell apoptosis and increased intracellular $Ca2^{+}$ with exposure to hydrostatic pressure. *Invest. Ophthalmol. Vis. Sci.* 50, 717–728. doi: 10.1167/iovs.08-2321

Sappington, R. M., Sidorova, T., Ward, N. J., Chakravarthy, R., Ho, K. W., and Calkins, D. J. (2015). Activation of transient receptor potential vanilloid-1 (TRPV1) influences how retinal ganglion cell neurons respond to pressure-related stress. *Channels* 9, 102–113. doi: 10.1080/19336950.2015.1009272

Schmidt, T. M., Alam, N. M., Chen, S., Kofuji, P., Li, W., Prusky, G. T., et al. (2014). A role for melanopsin in alpha retinal ganglion cells and contrast detection. *Neuron* 82, 781–788. doi: 10.1016/j.neuron.2014.03.022

Shibasaki, K., Suzuki, M., Mizuno, A., and Tominaga, M. (2007). Effects of body temperature on neural activity in the hippocampus: regulation of resting membrane potentials by transient receptor potential vanilloid 4. *J. Neurosci.* 27, 1566–1575. doi: 10.1523/JNEUROSCI.4284-06.2007

Sousa-Valente, J., Andreou, A. P., Urban, L., and Nagy, I. (2014). Transient receptor potential ion channels in primary sensory neurons as targets for novel analgesics. *Br. J. Pharmacol.* 171, 2508–2527. doi: 10.1111/bph.12532

Stewart, A. P., Smith, G. D., Sandford, R. N., and Edwardson, J. M. (2010). Atomic force microscopy reveals the alternating subunit arrangement of the TRPP2-TRPV4 heterotetramer. *Biophys. J.* 99, 790–797. doi: 10.1016/j.bpj.2010.05.012

Sudbury, J. R., Ciura, S., Sharif-Naeini, R., and Bourque, C. W. (2010). Osmotic and thermal control of magnocellular neurosecretory neurons-role of an N-terminal variant of TRPV1. *Eur. J. Neurosci.* 32, 2022–2030. doi: 10.1111/j.1460-9568.2010.07512.x

Suzuki, M., Mizuno, A., Kodaira, K., and Imai, M. (2003). Impaired pressure sensation in mice lacking TRPV4. *J. Biol. Chem.* 278, 22664–22668. doi: 10.1074/jbc.M302561200

Taylor, L., Arnér, K., and Ghosh, F. (2017). Specific inhibition of TRPV4 enhances retinal ganglion cell survival in adult porcine retinal explants. *Exp. Eye Res.* 154, 10–21. doi: 10.1016/j.exer.2016.11.002

Teichert, R. W., Memon, T., Aman, J. W., and Olivera, B. M. (2014). Using constellation pharmacology to define comprehensively a somatosensory neuronal subclass. *Proc. Natl. Acad. Sci. U.S.A.* 111, 2319–2324. doi: 10.1073/pnas.1324019111

Tominaga, M., Caterina, M. J., Malmberg, A. B., Rosen, T. A., Gilbert, H., Skinner, K., et al. (1998). The cloned capsaicin receptor integrates multiple pain-producing stimuli. *Neuron* 21, 531–543. doi: 10.1016/S0896-6273(00)80564-4

Vandewauw, I., De Clercq, K., Mulier, M., Held, K., Pinto, S., Van Ranst, N., et al. (2018). A TRP channel trio mediates acute noxious heat sensing. *Nature* 555, 662–666. doi: 10.1038/nature26137

Vennekens, R., Owsianik, G., and Nilius, B. (2008). Vanilloid transient receptor potential cation channels: an overview. *Curr. Pharm. Des.* 14, 18–31. doi: 10.2174/138161208783330763

Ward, N. J., Ho, K. W., Lambert, W. S., Weitlauf, C., and Calkins, D. J. (2014). Absence of transient receptor potential vanilloid-1 accelerates stress-induced axonopathy in the optic projection. *J. Neurosci.* 34, 3161–3170. doi: 10.1523/JNEUROSCI.4089-13.2014

Watanabe, H., Vriens, J., Prenen, J., Droogmans, G., Voets, T., and Nilius, B. (2003). Anandamide and arachidonic acid use epoxyeicosatrienoic acids to activate TRPV4 channels. *Nature* 424, 434–438. doi: 10.1038/nature01807

Weitlauf, C., Ward, N. J., Lambert, W. S., Sidorova, T. N., Ho, K. W., Sappington, R. M., et al. (2014). Short-term increases in transient receptor potential vanilloid-1 mediate stress-induced enhancement of neuronal excitation. *J. Neurosci.* 34, 15369–15381. doi: 10.1523/JNEUROSCI.3424-14.2014

Wen, H., Ostman, J., Bubb, K. J., Panayiotou, C., Priestley, J. V., Baker, M. D., et al. (2012). 20-Hydroxyeicosatetraenoic acid (20-HETE) is a novel activator of transient receptor potential vanilloid 1 (TRPV1) channel. *J. Biol. Chem.* 287, 13868–13876. doi: 10.1074/jbc.M111.334896

White, J. P., Cibelli, M., Urban, L., Nilius, B., McGeown, J. G., and Nagy, I. (2016). TRPV4: molecular conductor of a diverse orchestra. *Physiol. Rev.* 96, 911–973. doi: 10.1152/physrev.00016.2015

Wu, T. T., Peters, A. A., Tan, P. T., Roberts-Thomson, S. J., and Monteith, G. R. (2014). Consequences of activating the calcium-permeable ion channel TRPV1 in breast cancer cells with regulated TRPV1 expression. *Cell Calcium* 56, 59–67. doi: 10.1016/j.ceca.2014.04.006

Yarishkin, O., Phuong, T. T. T., Lakk, M., and Križaj, D. (2018). TRPV4 does not regulate the distal retinal light response. *Adv. Exp. Med. Biol.* 1074, 553–560. doi: 10.1007/978-3-319-75402-4_67

Yazulla, S. (2008). Endocannabinoids in the retina: from marijuana to neuroprotection. *Prog. Retin. Eye Res.* 27, 501–526. doi: 10.1016/j.preteyeres.2008.07.002

Zeng, H., and Sanes, J. R. (2017). Neuronal cell-type classification: challenges, opportunities and the path forward. *Nat. Rev. Neurosci.* 18, 530–546. doi: 10.1038/nrn.2017.85

Zygmunt, P. M., Petersson, J., Andersson, D. A., Chuang, H., Sørgård, M., Di Marzo, V., et al. (1999). Vanilloid receptors on sensory nerves mediate the vasodilator action of anandamide. *Nature* 400, 452–457. doi: 10.1038/22761

Conflict of Interest Statement: The authors declare that the research was conducted in the absence of any commercial or financial relationships that could be construed as a potential conflict of interest.

frontiers
in Cellular Neuroscience

ORIGINAL RESEARCH
published: 11 October 2018
doi: 10.3389/fncel.2018.00347

Reduced Annexin A1 Secretion by ABCA1 Causes Retinal Inflammation and Ganglion Cell Apoptosis in a Murine Glaucoma Model

***Lu Li*[1,2,†], *Lingjuan Xu*[1†], *Wei Chen*[1], *Xing Li*[3,4], *Qian Xia*[3,4], *Lu Zheng*[3,4], *Qiming Duan*[5], *Hong Zhang*[1] and *Yin Zhao*[1*]**

[1] Department of Ophthalmology, Tongji Medical College, Tongji Hospital, Huazhong University of Science and Technology, Wuhan, China, [2] Department of Ophthalmology, The First Affiliated Hospital, Shihezi University School of Medicine, Shihezi, China, [3] Key Laboratory of Neurological Diseases, Department of Neurobiology, Ministry of Education, Tongji Medical College, Huazhong University of Science and Technology, Wuhan, China, [4] The Institute for Brain Research, Collaborative Innovation Center for Brain Science, Huazhong University of Science and Technology, Wuhan, China, [5] Gladstone Institutes, San Francisco, CA, United States

Edited by:
Botir T. Sagdullaev,
Weill Cornell Medicine, Cornell University, United States

Reviewed by:
Bela Volgyi,
University of Pécs, Hungary
Lei Pei,
Huazhong University of Science and Technology, China
Antje Grosche,
Ludwig-Maximilians-Universität München, Germany

***Correspondence:**
Yin Zhao
zhaoyin85@hust.edu.cn

[†]*These authors have contributed equally to this work*

Received: *04 May 2018*
Accepted: *18 September 2018*
Published: *11 October 2018*

Citation:
Li L, Xu L, Chen W, Li X, Xia Q, Zheng L, Duan Q, Zhang H and Zhao Y (2018) Reduced Annexin A1 Secretion by ABCA1 Causes Retinal Inflammation and Ganglion Cell Apoptosis in a Murine Glaucoma Model. Front. Cell. Neurosci. 12:347. doi: 10.3389/fncel.2018.00347

Variants near the ATP-binding cassette transporter A1 (*ABCA1*) gene are associated with elevated intraocular pressure and newly discovered risk factors for glaucoma. Previous studies have shown an association between ABCA1 deficiency and retinal inflammation. Using a mouse model of ischemia-reperfusion (IR) induced by acute intraocular pressure elevation, we found that the retinal expression of ABCA1 protein was decreased. An induction of ABCA1 expression by liver X receptor agonist TO901317 reduced retinal ganglion cell (RGC) apoptosis after IR and promoted membrane translocation and secretion of the anti-inflammatory factor annexin A1 (ANXA1). Moreover, ABCA1 and ANXA1 co-localized in cell membranes, and the interaction domain is amino acid 196 to 274 of ANXA1 fragment. TO901317 also reduced microglia migration and activation and decreased the expression of pro-inflammatory cytokines interleukin (IL)-17A and IL-1β, which could be reversed by the ANXA1 receptor blocker Boc2. Overexpression of TANK-binding kinase 1 (*TBK1*) increased ABCA1 degradation, which was reversed by the proteasome inhibitor carbobenzoxy-L-leucyl-L-leucyl-L-leucinal (MG132). Silencing *Tbk1* with siRNA increased ABCA1 expression and promoted ANXA1 membrane translocation. These results indicate a novel IR mechanism, that leads via TBK1 activation to ABCA1 ubiquitination. This degradation decreases ANXA1 secretion, thus facilitating retinal inflammation and RGC apoptosis. Our findings suggest a potential treatment strategy to prevent RGC apoptosis in retinal ischemia and glaucoma.

Keywords: retina, ischemia/reperfusion injury, retinal ganglion cells (RGCs), ABCA1, annexin A1

INTRODUCTION

Glaucoma is one of the leading causes of irreversible blindness worldwide, affecting nearly 60 million people (Quigley and Broman, 2006). As a neurodegenerative disorder caused by protein misfolding, glaucoma is characterized by retinal ganglion cell (RGC) death and axonal damage of the optic nerve (Levin et al., 2017; Nuzzi and Tridico, 2017). The degeneration of RGCs may be triggered by increased intraocular pressure (IOP), gene defects, high glucose levels, oxidative stress, and aging. IOP provides the best treatment target for glaucoma; however, in some patients, the RGC degeneration is progressive despite a reduction in IOP (Zhang et al., 2012).

Treatment of RGC degeneration in glaucoma is complex and still at a preclinical stage. Ding et al. created a coculture of murine induced pluripotent stem cells (iPSCs) and primary human trabecular meshwork (TM) to produce TM-like cells, which helped in controlling IOP (Ding et al., 2014). However, the restoration of axonal functions in RGCs following treatment with iPSCs was limited in this study. Duplication of TANK-binding kinase 1 (*TBK1*) genes induced by optineurin mutations plays a significant role in glaucoma (Minegishi et al., 2016). In our previous studies, we observed that the TBK1 inhibitor BX795 and *Tbk1* siRNA prevent via p16INK4a inhibition RGC senescence in a mouse model of glaucoma, thus, providing a promising target for a molecular glaucoma therapy (Li et al., 2017).

Several genome-wide association studies found that common variants near the ATP-binding cassette (ABC) transporter A1 (*ABCA1*) gene are associated with glaucoma (Chen Y. et al., 2014; Gharahkhani et al., 2014; Hysi et al., 2014). ABCA1 belongs to a large superfamily of ABC transmembrane transporters that mediate cholesterol efflux to lipid-free apolipoprotein AI and apolipoprotein E (Wang and Smith, 2014). ABCA1 is transcriptionally regulated by the liver X receptor (LXR), a member of the nuclear receptor superfamily, with TO901317 being an LXR agonist. In the ophthalmological research field, Yang et al. reported that an increase of ABCA1 levels with TO901317 reduces ocular inflammation in an experimental model of autoimmune uveitis (Yang et al., 2014). In addition, Zheng et al. found that TO901317 protects against N-Methyl-D-aspartate-induced retinal damage through inhibition of nuclear factor κB and amyloid β formation (Zheng et al., 2015). However, the function of ABCA1 in animal models of glaucoma is still unclear.

Previous studies demonstrated a role for ABCA1 in annexin A1 (ANXA1) externalization (Chapman et al., 2003; Omer et al., 2006). ANXA1 that translocates to the cell membrane interacts with formyl peptide receptors (FPRs) and is involved in inflammation, neuroendocrine system regulation, skeletal muscle differentiation, and cancer progression (Boudhraa et al., 2016). Nuclear translocation of ANXA1 directly regulates the expression of the pro-apoptosis gene *Bid* (Li et al., 2016). Our previous study found that nuclear translocation of ANXA1 is associated with glaucoma-induced apoptosis of RGCs (Zhao et al., 2017). However, in mouse models of glaucoma, it is still unclear whether ABCA1 participates in ANXA1 membrane translocation, and whether and how blocking TBK1 directly protects against RGC apoptosis.

MATERIALS AND METHODS

Animals

Male C57BL/6J mice (3 months, 20–25 g; The Experiment Animal Center of the Tongji Medical College, Huazhong University of Science and Technology, China) were housed in covered cages, fed with a standard rodent diet ad libitum, and kept on a 12 h light/12 h dark cycle. All procedures concerning animals were performed in accordance with the Association for Research in Vision and Ophthalmology (ARVO) statement for the Use of Animals in Ophthalmic and Vision Research and under protocols approved by the Institutional Animal Care and Use Committees at Huazhong University of Science and Technology (2015-K-023).

Reagents and Antibodies

The non-selective LXR agonist TO901317 was obtained from Sigma-Aldrich (T2320; China). MG132 was purchased from Calbiochem (474790, WI, USA). The FPR pan-antagonist N-tert-butoxycarbonyl-L-Phe-D-Leu-L-Phe-D-Leu-L-Phe (Boc2) was obtained from MP Biomedicals (02152760; Solon, OH, USA). Terminal deoxynucleotidyl transferase-mediated nick end labeling (TUNEL) assay kit was provided by Roche (11684817910, Basel, Switzerland).

The primary antibodies used in this study are shown in **Table 1**.

Ischemia-Reperfusion Mouse Model

The mice were anesthetized by intraperitoneal injections of 10 mL/kg of 4% chloral hydrate. The corneas were topically anesthetized with 0.5% tetracaine hydrochloride, and the pupils were dilated with 1% tropicamide. A 30-G needle was inserted into the anterior chamber of the right eye that was connected via flexible tubing to a saline reservoir. By raising the reservoir, the IOP was elevated to 75 mmHg and maintained at this value for 45 min. Retinal ischemia was confirmed by whitening of the iris and the loss of the red reflex. The subsequent reperfusion was evident from the return of this reflex. After 45 min, the needle was withdrawn, and tobramycin was applied to avoid bacterial infection. The left eye served as a control. Mice were sacrificed 48 h after this procedure.

Intravitreal Injections

The experimental eyes were injected with TO901317 (30 μM/2 μL), Boc2 (5 mg/kg, 2 μL), vehicle (DMSO, 2 μL), or *Tbk1* siRNA (2 μL) into the vitreous cavity through a 35-G needle with a 10-μL Hamilton microsyringe (Hamilton, Reno, NV, USA) before the onset of reperfusion. Tobramycin was applied to prevent bacterial infection.

Immunofluorescence

The paraffin-embedded retinal sections (5 μm) were gently washed twice with phosphate-buffered saline (PBS) preheated to 37°C. Afterward, the sections were treated again with 5% bovine serum albumin (BSA) for an additional 60 min to block nonspecific binding, before incubating them with rabbit polyclonal TBK1 antibody, rabbit monoclonal ANXA1 antibody, mouse monoclonal ABCA1 antibody, or mouse monoclonal anti-beta 1 sodium-potassium ATPase in 5% BSA at 4°C overnight (**Table 1**). Retinal sections were then washed and incubated with a conjugated secondary antibody (1:200; Invitrogen) in 5% BSA at 37°C for 1 h. A confocal microscope (Zeiss 510 Meta, Zeiss, Germany) was used to acquire fluorescence images.

TABLE 1 | Antibodies employed in the study.

Antibody	Type	WB	IH	IF	IP	Source
Flag (DYKDDDDK tag)	mAb	1:1000			1:50	Cell signaling (#14793)
IL-17	pAb	1:500	1:100			Santa cruz (sc-7927)
IL-1β	pAb	1:500	1:200			Santa cruz (sc-7884)
Iba1	pAb	1:500	1:200			Abcam (ab5076)
β-actin	mAb	1:1000				Santa cruz (sc-47778)
Anti-beta 1 sodium potassium ATPase	mAb	1:250		1:200		Abcam (ab-2873)
Annexin A1	mAb	1:2000		1:1000		Abcam (ab-214486)
ABCA1	mAb	1:500	1:200	1:200		Abcam (ab-18180)
TBK1	mAb			1:100		Abcam (ab-40676)
GFP	mAb	1:3000			1:200	Abcam (ab6556)
Phospho-(Ser/Thr)	pAb	1:1000				Cell signaling (#9631)

WB, Western blotting; IH, Immunohistochemistry; IF, Immunofluorescence; IP, Immunoprecipitation.

Tunel Assay

Apoptotic cells were visualized using the TUNEL assay of an *in situ* Cell Death Detection Kit according to the manufacturer's instructions. Briefly, paraffin-embedded tissue sections were deparaffinized, rehydrated, and fixed in 4% paraformaldehyde solution. After rinsing with PBS twice, the tissue sections were incubated with 20 μg/mL proteinase K for 10 min and refixed in paraformaldehyde solution for 5 min at 24°C. Afterward, the tissue sections were rinsed with PBS and incubated at 37°C for 60 min in a humidified chamber with the TUNEL reaction mix, in order to allow the end-labeling reactions to occur. The sections were then immersed in saline sodium citrate for 15 min at room temperature to terminate the reaction, which was followed by the immersion in 0.3% hydrogen peroxide in PBS for 5 min at room temperature. In accordance with the manufacturer's instructions, the TUNEL reaction mixture was freshly prepared for each experiment; the tissue sections were incubated with a total volume of 100 μL of the reaction mixture for 1 h at room temperature in the dark. Following this, the sections were rinsed with 0.1 M PBS supplemented with 4′,6-diamidino-2-phenylindole (DAPI) and then observed under a fluorescence microscope. TUNEL-positive cells in the ganglion cell layer were counted in eight viewing fields from retinal sections per condition ($n = 6$ retinas) by two investigators in a blinded manner, and the scores were averaged.

Cell Culture

HEK293 cells and BV2 cells were maintained in Dulbecco's modified Eagle's medium (DMEM) supplemented with 10% fetal bovine serum (Gibco), penicillin (100 U/mL), and streptomycin (100 μg/mL) at 37°C in an incubator equilibrated with 5% CO_2. Confluent cell layers were split two times per week.

Immunopanning and Primary RGCs Cultures

Primary cultured RGCs were purified using a two-step immunopanning method according to a published protocol (Winzeler and Wang, 2013). In short, the retinas were digested with papain (16.5 units/mL) and triturated. The cell suspension was first incubated on a panning plate coated with goat anti-rabbit IgG (Thermo Fisher Scientific, Waltham, MA, USA). The nonadherent cells were incubated on a second panning plate coated with goat anti-mouse IgM and mouse anti-Thy1.1 antibodies. Then, the plate was washed with PBS, and the adherent RGCs were released by treatment with 0.125% trypsin. The isolated RGCs were suspended in the medium as described in the above-mentioned publication. Finally, 96-well culture plates were coated with poly-D-lysine and laminin (Sigma-Aldrich). The RGCs were plated at a density of 5,000 cells/well and cultured for at least 10 days prior to further experimental procedures.

In vitro Migration Assays

For transwell migration assays, the chambers (24-well inserts, 8 μm pore size; BD Bioscience) were placed in DMEM containing 0.1% BSA and incubated at 37°C for 2 h to hydrate and block the membrane. BV2 cells were washed with DMEM and counted. Purified RGCs with RGC-conditioned medium (RCM) were placed in the lower well. For experiments using TO901317 and Boc2, media in the lower chambers (RGCs) were supplemented with 10 μM TO901317, or/and 10 μM Boc2 incubated with BV2 respectively. After 24 h incubation at 37°C and 5% CO_2, all cells that did not migrate through the pores were removed by a cotton swab. Cells on the lower surface of the membrane were fixed with 4% paraformaldehyde and then stained with mouse monoclonal ionized calcium-binding adapter molecule 1 (Iba1) antibody. The migrated cells were investigated using bright field microscopy.

Plasmid Construct and *TBK1* siRNA

DNA fragments corresponding to the full-length *TBK1* were amplified by polymerase chain reaction (PCR), followed by cloning into the pEGFP-N1 vector (Invitrogen). Mouse *Tbk1* siRNA plasmids were purchased from GeneChem (Shanghai, China). HEK293 cells were then transfected using Lipofectamine 3000 reagents (Invitrogen).

The siRNA sequence that targeted the *Tbk1* sequence (GenBank No.NM_019786) was designed as follows: *5′-GTTTAA AGATAAGTCGGAA′-3*.

Reverse Transcriptase PCR (RT-PCR) Analysis

Total RNA was isolated from mouse retinas using TRIzol reagent (Invitrogen). Total RNA (1 μg) of each sample was reverse-transcribed using EasyScript First-Strand cDNA Synthesis SuperMix (TransGen) in a 20-μL volume. According to the manufacturer's instructions, the PCR amplification was carried out in a total volume of 25 μL containing 0.5 μL of each primer, 1 μL of cDNA, 12.5 μL Taq Master Mix, and H_2O to 25 μL. Murine *Gapdh* was amplified as a reference standard. Primers were used as follows: *Gapdh* forward, *5′-GACAAAATGGTGAAGGTCGGT-3′; Gapdh* reverse, *5′-GAGGTCAATGAAGGGGTCG-3′; Abca1* forward, *5′-ATTCAGCTTGGTGATGCGvGA-3′; Abca1* reverse*; 5′-CCAAGCTGTCAAGCAACACT-3′*. The melt curves were analyzed to verify that only a single product per primer was amplified. The gene expression was calculated by the delta-delta Ct method. The results were expressed as fold changes in the target gene normalized to the reference gene *Gapdh*.

Co-immunoprecipitation (Co-IP)

Briefly, cell lysates were generated by sonication in a buffer containing 20 mM 4-(2-hydroxyethyl)-1-piperazineethanesulfonic acid (HEPES), 400 mM KCl, 5% glycerol, 5 mM ethylenediaminetetraacetic acid (EDTA), 0.4% NP-40, and protease inhibitors, and precleared by centrifugation. The cell lysates were then incubated with an anti-ABCA1 antibody overnight at 4°C. The reaction mixture was afterward incubated with protein A/G PLUS-Agarose beads (sc-2003; Santa Cruz) for 2 h at 4°C. The precipitates were washed three times with wash buffer and then eluted from the protein A/G PLUS-Agarose beads by boiling with 1× sodium dodecyl sulfate (SDS) for 5 min at 95°C. The protein samples were resolved by SDS-polyacrylamide gel electrophoresis.

Protein Extraction and Preparation

Protein samples were prepared using the Membrane and Cytosol Protein Extraction Kit (P0033; Beyotime, China) according to the recommended protocol. Briefly, cultured HEK293 cells were washed with ice-cold PBS, harvested using a cell scraper, and centrifuged at 3,000 *g* for 5 min. Cell pellets were then resuspended in a membrane and cytoplasmic extraction reagent containing phosphatase inhibitors Phenylmethanesulfonyl fluoride, and protease inhibitors, and incubated on ice for 30 min. Lysates were then centrifuged at 12,000 *g* at 4°C for 10 min to obtain membrane-bound and cytoplasmic protein fractions for later expression analysis.

Western Blot Analysis

For analysis of protein expression, total protein was isolated and harvested from retina samples, cultured HEK293 cells, or primary RGC cells at defined time-points. Samples were separated using 6, 10, or 12% polyacrylamide gels and transferred to polyvinylidene difluoride (PVDF) membranes. PVDF membranes were blocked with 5% BSA at room temperature for 60-90 min and afterward incubated overnight at 4°C with antigen-specific primary antibodies (**Table 1**). Blots were incubated with species-specific horseradish peroxidase-conjugated secondary antibodies for 60 min at room temperature. Proteins were visualized using a chemiluminescence substrate kit (ECL Plus; PerkinElmer Inc, Covina, CA, USA). Target proteins were quantified using ImageJ (NIH, Bethesda, MD, USA) software. These values were normalized to the expression levels of β-actin or anti-beta 1 sodium-potassium ATPase.

Statistical Analysis

Data are expressed as mean ± standard deviation (S.D.) The statistical analysis was performed with GraphPad Prism software (version 5.0, GraphPad Software Inc.) Data were analyzed by one-way analysis of variance (ANOVA) and Student's *t* test in order to determine statistically significant differences. $P < 0.05$ was considered statistically significant.

RESULTS

ABCA1 Expression Is Decreased in a Mouse Model of Ischemia-Reperfusion

To investigate the change of ABCA1 expression in RGCs after ischemia-reperfusion, we used a mouse model of ischemia induced by acute IOP elevation. This involved an IOP increase to 75 mmHg for 45 min and a reperfusion phase for 48 h. As shown in **Figure 1**, both immunohistochemical and immunofluorescence analyses revealed that expression of ABCA1 was significantly lower in the IR groups than in the control groups (**Figures 1A–D**). IR reduced the expression of ABCA1 specifically in the ganglion cell layer GCL (**Figure 1A**, **Supplementary Figure 1B**). Western blot analysis of retina extracts also confirmed that compared to the control groups the expression of ABCA1 in the IR groups was significantly decreased (**Figures 1E,F**). However, there was no difference in mRNA levels between control and IR groups (**Figure 1G**).

The LXR Agonist TO901317 Decreases the Cell Apoptosis of RGCs After IR

The LXR agonist TO901317 (30 μM) was injected into the vitreous chambers of mice exposed to IR to induce ABCA1 expression. In accordance with previous experiments, we found that compared with IR+vehicle groups, IR+TO901317 groups effectively increased ABCA1 expression (**Figures 2A,B**). Western blot results also confirmed that TO901317 could induce the expression of ABCA1 in the retina extract from mice exposed to IR (**Figures 2C,D**). Cell apoptosis analysis by TUNEL staining revealed that the RGC apoptosis rate was significantly higher in the IR+vehicle group, whereas the LXR agonist decreased this rate after IR induction (**Figures 2E,F**). Hematoxylin-eosin (H&E) stainings of murine retinas revealed that IR+vehicle groups exhibited a decreased cell number in the GCL, whereas TO901317 reversed this cell loss (**Figures 2G,H**). Further, we used an antibody against Brn-3a to detect the number of RGCs in the GCL. We found that IR+vehicle groups displayed an RGC loss in the GCL, while TO901317 reverted this RGC loss in the retina slices (**Figures 2I,J**). These data indicate that TO901317 reduces RGC apoptosis in retinas after IR damage.

The LXR Agonist TO901317 Promotes Membrane Translocation of ANXA1

Previous studies proved that in pituitary folliculostellate cells, the membrane transport of the anti-inflammatory factor ANXA1 is dependent on ABCA1 expression (Chapman et al., 2003; Omer et al., 2006). To observe the effects of ABCA1 on mediating membrane translocation ANXA1 in RGCs, we performed immunofluorescence stainings of retinal slices and extracted cytoplasm and membrane proteins for western blot analyses. Here we used anti-beta 1 sodium-potassium ATPase antibodies to label cell membranes in the GCL. The immunofluorescence analysis indicated that ABCA1 and ANXA1 co-localized on cell membranes in the GCL. However, IR reduced the membrane localization of ANXA1 as well as the co-localization of ABCA1 and ANXA1. Moreover, TO901317 promoted the ABCA1 expression, the ABCA1-ANXA1 co-localization, and the ANXA1 translocation to the cell membrane after IR *in vivo* (**Figures 3A,B**, **Supplementary Figure 1A**). Western blotting analyses demonstrated that TO901317 (3 μM) increased the protein levels of ANXA1 in membrane extracts of lipopolysaccharide (LPS)-stimulated HEK293 cells, while ANXA1 expression in the cytoplasm was reduced (**Figures 3C–F**).

ABCA1 Interacts With ANXA1

Previous data have shown that ANXA1 membrane localization is promoted by ABCA1 (Chapman et al., 2003; Omer et al., 2006), however, how ABCA1 induces membrane transport of ANXA1 is still unclear. To identify where and how ABCA1 interacts with ANXA1, we extracted membrane proteins from whole cell lysates and then used Co-IP to examine the binding between ABCA1 and ANXA1 (**Figure 4A**). Results indicated that EDTA decreased the binding between ABCA1 and ANXA1 (**Figure 4B**). As shown in **Figure 4C**, LPS stimulation blocked the interaction, whereas TO901317 increased ANXA1 and ABCA1 binding. We

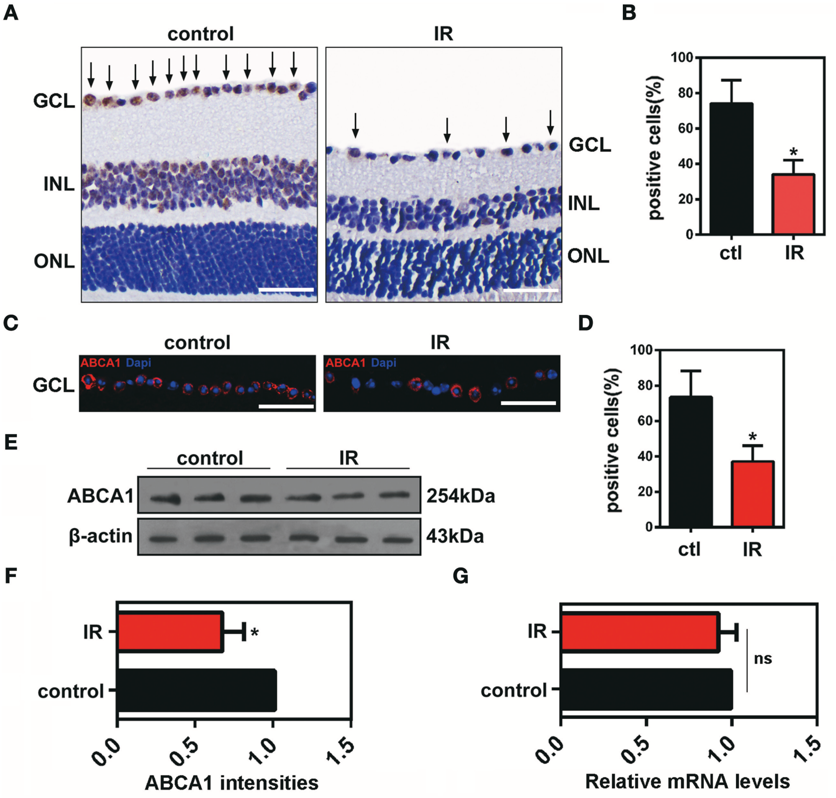

FIGURE 1 | The effects of ischemia-reperfusion on ABCA1 expression *in vivo.* **(A)** Representative immunohistochemistry images of ABCA1 expression in ischemic retina slices. Arrows indicate ABCA1-positive cells. GCL, ganglion cell layer; INL, inner nuclear layer; ONL, outer nuclear layer. Scale bar = 50 μm. **(B)** Statistical analysis of **(A)**. The data are presented as the mean ± S.D. ($n = 6$ retinas per group). $^*P < 0.05$, unpaired Student's t test vs. control. **(C)** Immunofluorescence analysis showing the expression of ABCA1 in a retina after IR. A representative result from three independent experiments is shown. Blue: DAPI; red: ABCA1. Scale bar = 50 μm. **(D)** Statistical analysis of **(C)**.The data are expressed as the means ± S.D. ($n = 6$ retinas per group). $^*P < 0.05$, unpaired Student's t test vs. control. **(E)** Western blot analysis showing the expression of ABCA1 in a retina after IR. These results were obtained in three independent experiments. **(F)** Statistical analysis of **(E)**. The data are expressed as the means ± S.D. ($n = 3$ retinas per group). $^*P < 0.05$, unpaired Student's t test vs. control. **(G)** RT-PCR analysis of *Abca1* gene expression in ischemic retinas 48 h after reperfusion. There was no difference between *Abca1* mRNA levels in the IR and control groups ($n = 3$ retinas per group). $P > 0.05$, unpaired Student's t test.

then constructed full-length and fragmented ANXA1 plasmids to explore the binding domain (**Figure 4D**). Results indicated that the C3 domain of ANXA1 (amino acids 196 to 274) may be responsible for the binding between ANXA1 and ABCA1 (**Figure 4E**). These data indicate that ABCA1 interacts with the C3 domain of ANXA1, that this interaction is calcium-dependent and that LPS inhibits the ABCA1-ANXA1 binding.

TO901317 Decreases Microglia Activation via Regulation of ANXA1 Secretion

To observe the function of ANXA1 in the IR-induced retina damage and microglia activation, co-cultures of primary cultured RGCs and microglia were used in this study. Primary cultured RGCs from murine retinas were isolated by immunopanning using the anti-Thy-1.1 antibody, and then co-cultured with BV2 microglial cells (**Figure 5A**). Enzyme-linked immunosorbent assay (ELISA) results revealed that LPS stimulation reduced ANXA1 secretion, whereas TO901317 led to an increase of ANXA1 secretion in primary cultured RGCs (**Figure 5B**). Since Boc2 is a selective blocker of ANXA1 receptors, we investigated whether the administration of Boc2 can block the IR-induced effects of ANXA1 on microglia activation *in vivo* and *in vitro*. Here, we used Iba1 to label activated microglial cells *in vivo* and *in vitro*. Immunohistochemical analyses indicated that TO901317 suppressed the activation of microglia after IR, whereas Boc2 (10 μM) induced their activation (**Figure 5C**). We collected RCMs from cultures in the

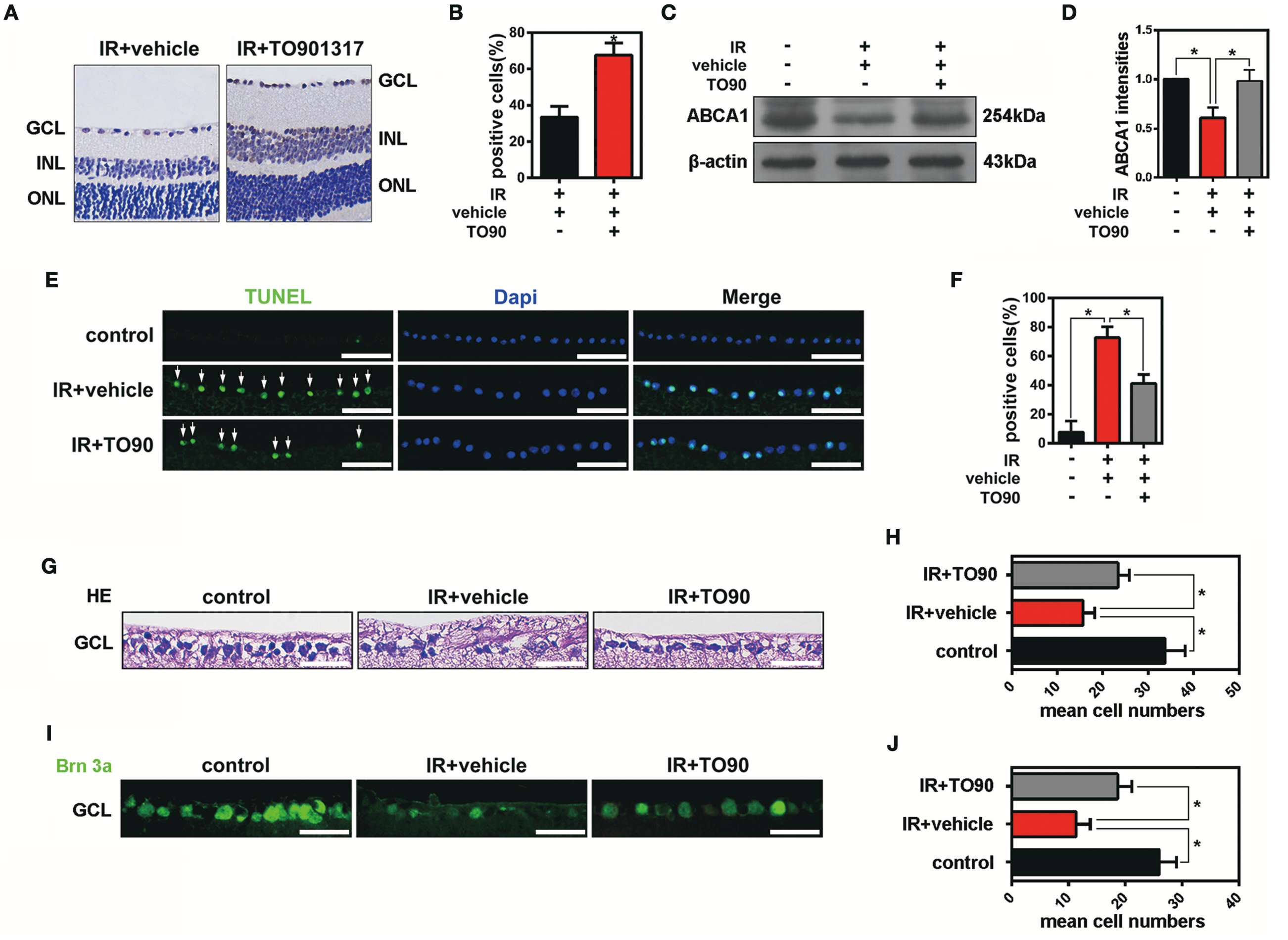

FIGURE 2 | The effects of TO901317 on RGC death after IR *in vivo.* **(A)** Representative immunohistochemical images of ABCA1 expression in the experimental groups IR+vehicle and IR+TO901317 (30 μM). Arrows indicate positive labels. Scale bar = 50 μm. **(B)** Statistical analysis of **(A)**. The data are presented as the mean ± S.D. (*n* = 6 retinas per group). $^*P < 0.05$, unpaired Student's *t* test vs. IR+vehicle. **(C)** Western blot showing the expression of ABCA1 after IR with and without TO901317 pretreatment of the retina. **(D)** Statistical analysis of **(C)**. The data are presented as the mean ± S.D. (*n* = 3 retinas per group). $^*P < 0.05$, one-way ANOVA with Bonferroni *post hoc* test. **(E)** TUNEL staining showing apoptotic cells in the GCL after IR. Please note that TO901317 decreases RGC apoptosis. Arrows indicate positive labels. The statistical analysis is shown in **(F)** (*n* = 6 retinas per group). A one-way ANOVA with Bonferroni *post hoc* test was used. Scale bar = 50 μm. **(G)** Representative HE stainings of retinas show the degeneration of RGCs after IR with and without TO901317 pretreatment. Scale bar = 50 μm. **(H)** Statistical analysis of three independent experiments as shown in **(G)**. The data are expressed as the means ± S.D. (*n* = 6 retinas per group). $^*P < 0.05$, one-way ANOVA with Bonferroni *post hoc* test. **(I)** Representative immunofluorescence images show the Brn-3a staining in the GCL. The statistical analysis of three independent experiments is shown in **(J)** (*n* = 6 retinas per group). $^*P < 0.05$, one-way ANOVA with Bonferroni *post hoc* test. Scale bar = 50 μm.

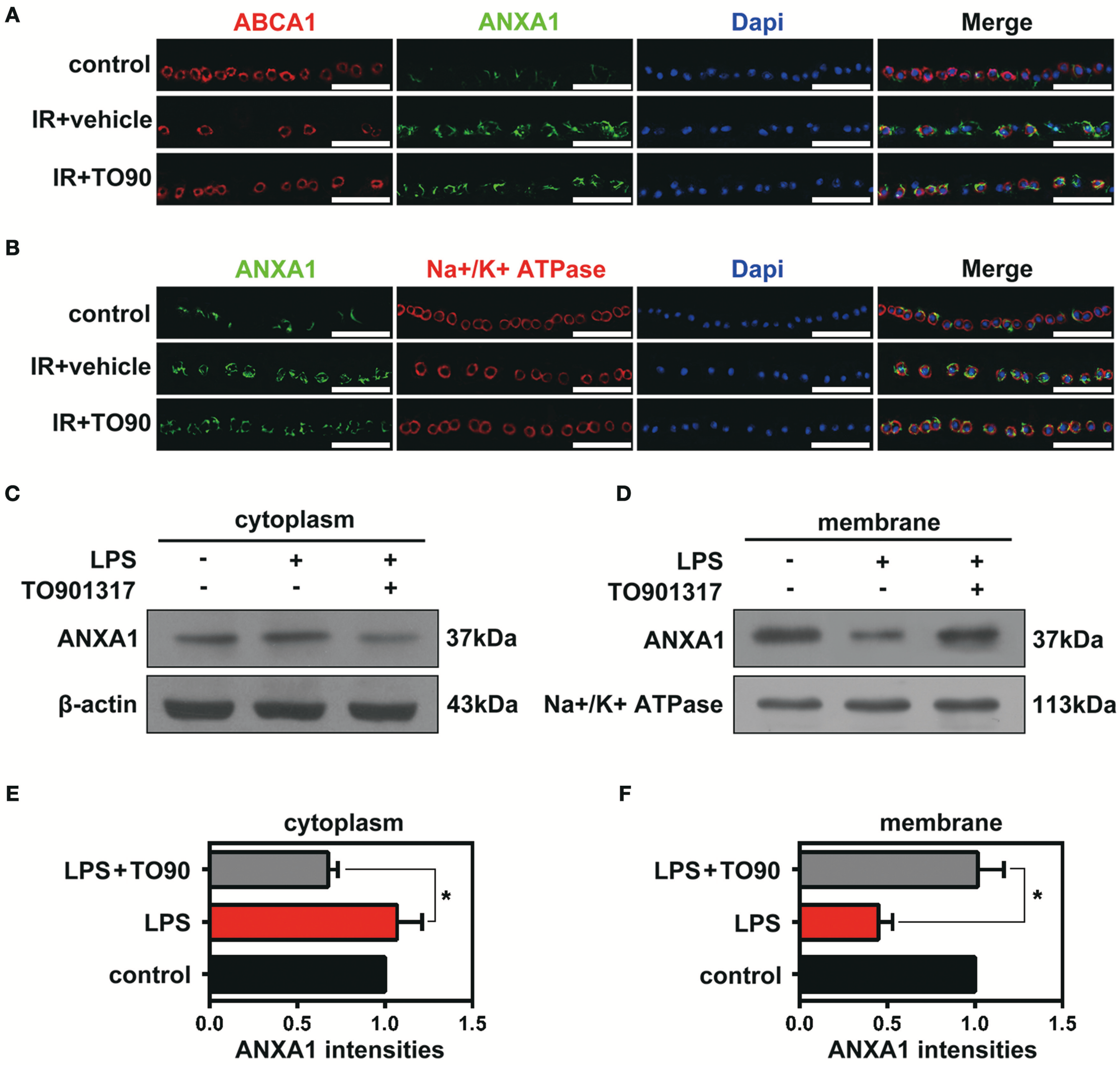

FIGURE 3 | The effects of TO901317 on the ANXA1 translocation to the cell membrane. **(A)** Immunofluorescence results indicate that ABCA1 and ANXA1 can be co-localized on the membrane of cells in the GCL ($n = 6$ retinas per group). Blue: DAPI; red: ABCA1; green: ANXA1. Scale bar = 50 µm. **(B)** TO901317 promotes translocation of ANXA1 to the cell membrane after IR *in vivo* ($n = 6$ retinas per group). Blue: DAPI; red: Na^+/K^+-ATPase; green: ANXA1. Scale bar=50 µm. **(C,D)** Western blots demonstrate that TO901317 (3 µM) increases the protein levels of ANXA1 in the membrane of LPS-stimulated HEK293 cells, while ANXA1 expression in the cytoplasm is reduced. **(E,F)** Statistical analysis of the data shown in **(C,D)**. The data from three independent experiments are expressed as the means ± S.D. $^*P < 0.05$, one-way ANOVA with Bonferroni *post hoc* test.

presence (RCM+TO901317) and absence of TO901317 and used these media to stimulate BV2 cells. Western blotting analysis demonstrated that TO901317 (3 µM) reduced the expression of Iba1 and that this effect could be inhibited by Boc2 (**Figures 5D,E**). RGCs and BV2 were incubated with TO901317 and Boc2 for 6 h respectively in the first step, then replaced with normal medium and co-cultured for 24 h, after that BV2 migration was assessed via Iba1 immunohistochemical staining. We found that TO901317 inhibited microglial migration induced by LPS and that this effect could be reversed by Boc2 (**Figure 5F**). These results indicate that TO901317 downregulates microglial activation via regulation of ANXA1 secretion.

TO901317 Decreases Retina Inflammation via ANXA1

It is well recognized that microglia activated by external stimuli secrete a large number of pro-inflammatory cytokines (e.g., interleukin [IL]-1β) (Ramirez et al., 2017; Song et al., 2017). Here, we collected RCM and TO901317 incubated RGCs mediums (RCM+TO901317) to stimulate BV2 microglia and used Boc2 to block the function of ANXA1 in BV2. ELISA results revealed that stimulation of BV2 cells with RCM increased their IL-1β and IL-17A secretion, which was reduced by TO901317. However, Boc2 reversed this TO901317 effect in BV2 microglia (**Figure 6A,B**). Western blot analyses revealed that the elevated IOP increased the expression of IL-17A and IL-1β in the IR group, which could be reduced by TO901317, whereas this TO901317 effect was reversed by Boc2 administration (**Figures 6C,D**). Similarly, immunohistochemical analyses showed that TO901317 alleviated the IL-1β and IL-17A expression in the GCL, while this effect was reverted by Boc2 (**Figures 6E,F**). These data indicate that TO901317 reduces via ANXA1 the secretion and expression of the pro-inflammatory cytokines IL-1β and IL-17A in IR-induced retina injury.

TBK1 Stimulates ABCA1 Degradation by the Ubiquitin-Proteasome System

Cellular protein homeostasis is maintained by two major degradation pathways, namely the ubiquitin-proteasome system and autophagy. TBK1 has been shown to have a major role in autophagy and mitophagy, chiefly by phosphorylation of autophagy adaptors. However, the function of TBK1 in the ubiquitin-proteasome pathway and in ABCA1 degradation is unclear. To determine the potential relationship between ABCA1 and TBK1, we injected *Tbk1* siRNA (Li et al., 2017) into murine vitreous chambers 10 days before IR and then measured the co-localization of TBK1 with ABCA1 in retinal slices. The results of the immunofluorescence analyses indicated that TBK1 and ABCA1 co-localized and, importantly, that *Tbk1* siRNA increased the expression of ABCA1 in GCL (**Figure 7A**). As shown in **Figures 7B,C**, western blot analyses revealed that the expression of ABCA1 was dose-dependently decreased in HEK293 cells after full-length *TBK1* transfection. Western blot analyses also identified that *Tbk1* siRNA reversed the downregulation of ABCA1 after LPS stimulation (1 μg/mL) to imitate cell injury during IR (**Figures 7D,E**). Western blot results revealed that MG132 (10 μM) could inhibit the decrease in ABCA1 expression induced by *TBK1* overexpression (**Figures 7F,G**). However, RT-PCR results showed that there is no significant difference between control and *TBK1* overexpression groups in *ABCA1* expression on the mRNA level (**Figure 7H**). **Figures 7I,J** revealed that phospho-(Ser/Thr)-linked ubiquitination and binding between ABCA1 and ubiquitin proteasomes were increased following *TBK1* transfection. Finally, we examined the effects of *Tbk1* siRNA on ANXA1 membrane translocation. As shown in **Figures 7K–M**, *Tbk1* siRNA increased ANXA1 expression in the membranes of LPS-stimulated HEK293 cells, while ANXA1 expression in the cytoplasm was decreased. Together, these results suggest a pivotal role for TBK1 in ABCA1 degradation and function.

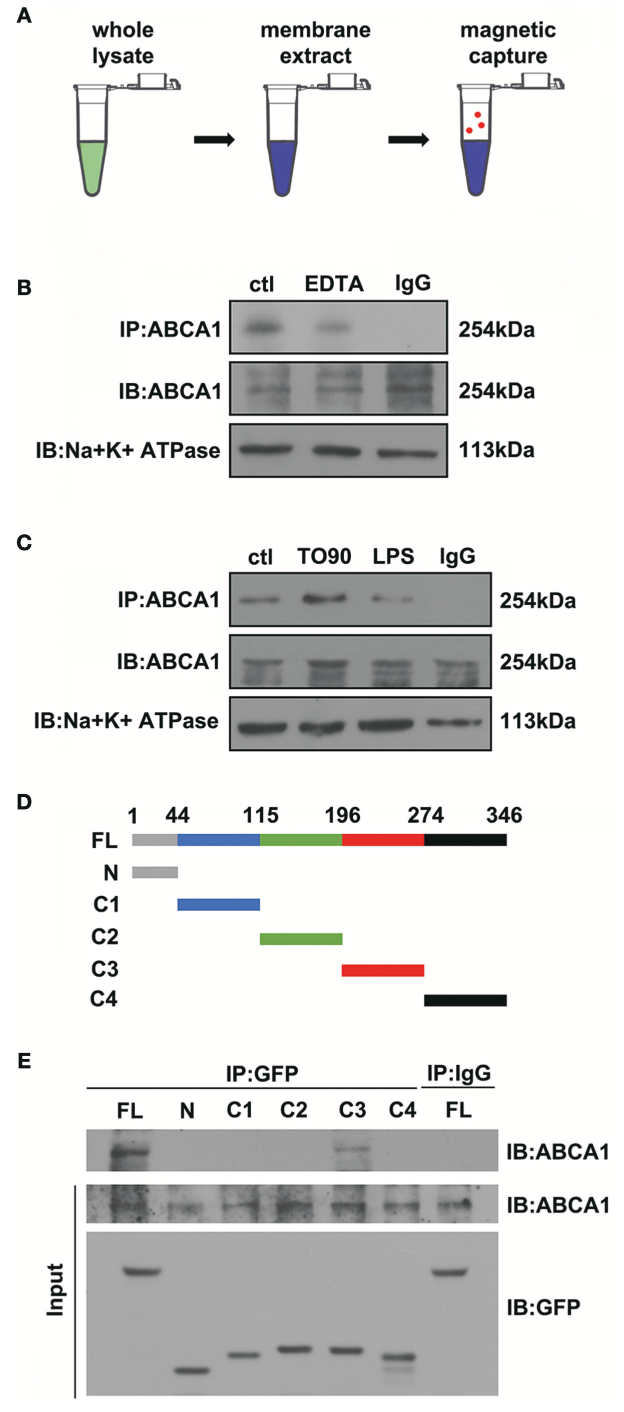

FIGURE 4 | The interaction between ABCA1 and ANXA1. **(A)** Schematic diagram of Co-IP between ABCA1 and ANXA1. **(B)** Western blotting analysis demonstrating that EDTA decreases the interaction between ABCA1 and ANXA1. **(C)** A western blotting analysis indicates that LPS reduces the interaction between ABCA1 and ANXA1, and this effect is inhibited by TO901317. **(D)** Schematic diagram of full-length and fragment ANXA1 plasmids. **(E)** Co-IP results demonstrate that the binding between ANXA1 and ABCA1 involves the C3 domain of ANXA1 (amino acids 196 to 274).

DISCUSSION

Acute glaucoma is a major cause of irreversible blindness and a sight-threatening disease that is characterized by acute retinal ischemic inflammatory injury and the death of RGCs secondary to the elevated IOP. Several studies have reported that ABCA1 participates in the externalization of ANXA1 (Chapman et al., 2003; Omer et al., 2006) and that TO901317

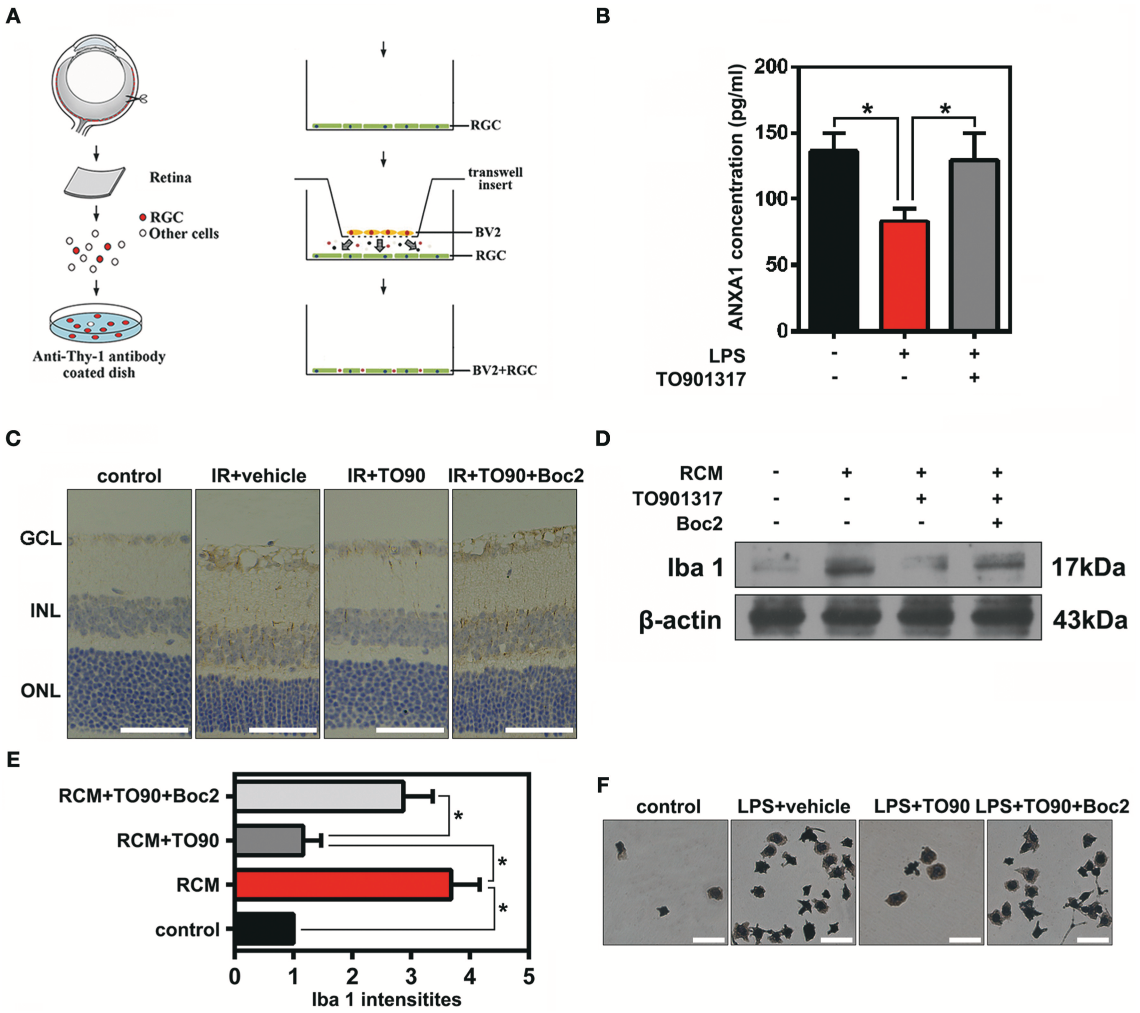

FIGURE 5 | The effects of TO901317 on microglial activation. **(A)** Schematic diagram of immunopanning and transwell migration assays. **(B)** ELISA results reveal that TO901317 leads to an increase of ANXA1 secretion in primary cultured RGCs. A one-way ANOVA with Bonferroni *post hoc* test was used. **(C)** Immunohistochemical results indicate that TO901317 suppresses the activation of microglia after IR *in vivo*, while Boc2 (10 µM) reverses this effect ($n = 6$ retinas per group). Scale bar = 50 µm. **(D)** Western blotting analysis demonstrating that TO901317 reduces the expression of Iba1 in BV2 cells incubated with RCM. This effect is inhibited by Boc2. **(E)** Statistical analysis of the data shown in **(D)**. The data of three independent experiments are expressed as the means ± S.D. $^{*}P < 0.05$, one-way ANOVA with Bonferroni *post hoc* test. **(F)** TO901317 inhibits microglial migration induced by LPS, and this effect is reversed by Boc2 (10 µM). Scale bar = 20 µm.

administration protects the retina and preserves visual functions by suppressing inflammation (Yang et al., 2014). In the present study, we found that the expression of ABCA1 was decreased in a mouse model of IR with no difference in its mRNA levels between the control and IR groups. TO901317 increased the expression of ABCA1 and reversed RGC apoptosis and retinal inflammation *in vivo*. ABCA1 interacted with ANXA1 and induced ANXA1 membrane secretion, which determined the activation of retinal microglia. The IR-induced upregulation of TBK1 might be involved in ABCA1 ubiquitination and degradation.

Previous studies identified that ABCA1 plays a major role in high-density lipoprotein formation (Feingold and Grunfeld, 2000; Rosenson et al., 2016). As high-density lipoproteins were considered to have anti-inflammatory and other beneficial effects (Murphy et al., 2012; Mao et al., 2017), ABCA1 was implicated in macrophage-associated inflammatory diseases. Microglia are specialized resident macrophages in the neural retina, and they are normally located in the nerve fiber layer, ganglion cell layer, inner plexiform layer, and outer plexiform layer (Chinnery et al., 2017). In this study, we found that TO901317 increases the ABCA1 expression and, thus, prevents the expression of the pro-inflammatory cytokines IL-1β and IL-17A as well as the apoptosis of RGCs after ischemia-reperfusion injury.

We also investigated the mechanisms of ABCA1 in retinal inflammation. Previous studies have shown that ANXA1 acts via FPRs as an anti-inflammatory factor in the host defense system and the nervous system (Parente and Solito, 2004; Chen L. et al., 2014). Liu et al. found that *Anxa1* knock

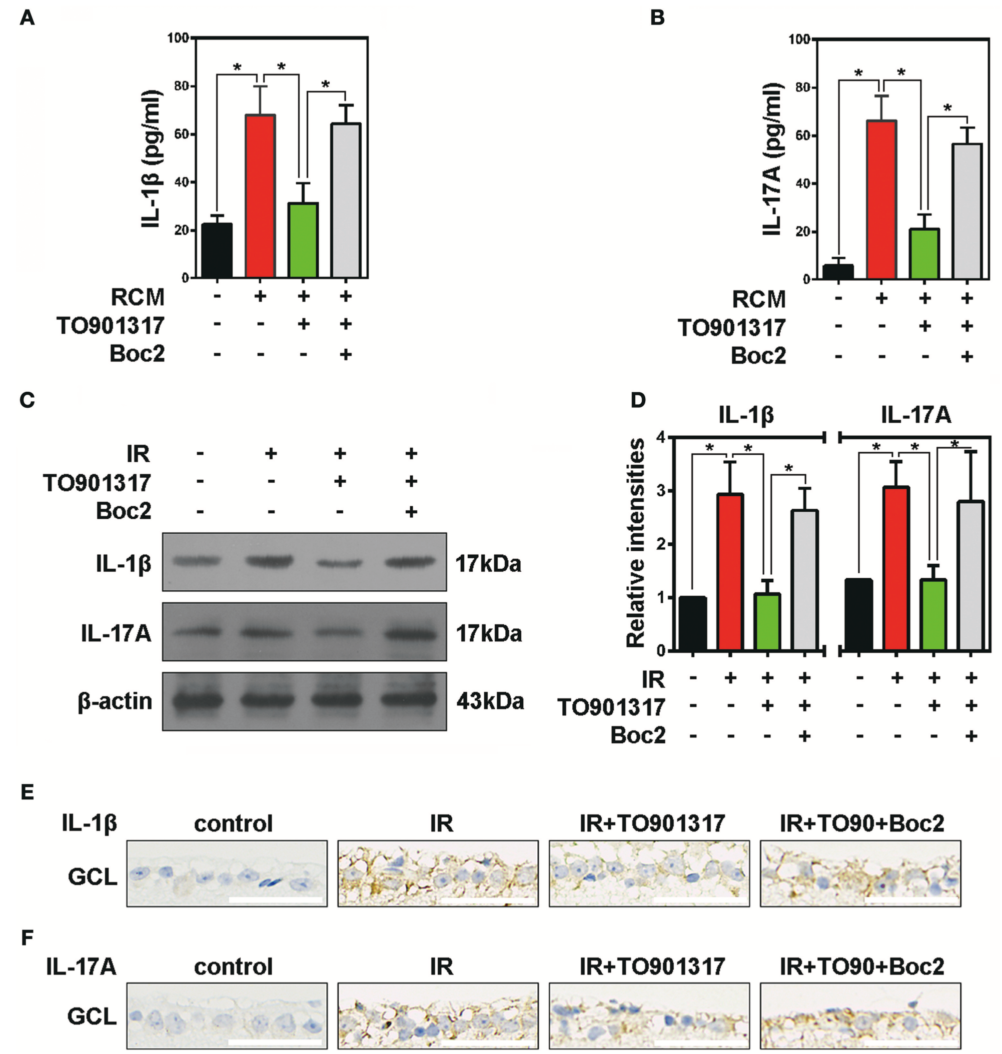

FIGURE 6 | The effects of TO901317 on retinal inflammation. **(A)** ELISA results show the secretion of IL-1β by primary cultured RGCs after RCM or RCM+TO901317 stimulation. The data of three independent experiments are expressed as the means ± S.D. $^{*}P < 0.05$, one-way ANOVA with Bonferroni *post hoc* test. **(B)** Secretion of IL-17A by primary cultured RGCs detected in ELISAs. The data of three independent experiments are expressed as the means ± S.D. $^{*}P < 0.05$, one-way ANOVA with Bonferroni *post hoc* test. **(C)** Western blots showing the effects of TO901317 and TO901317+Boc2 on IL-17A and IL-1β expression in ischemic retinas. **(D)** Statistical analysis of the data shown in **(C)**. The data of three independent experiments are expressed as the means ± S.D. $^{*}P < 0.05$, one-way ANOVA with Bonferroni *post hoc* test. **(E)** Representative immunohistochemical images of IL-1β expression in the GCL. Scale bar = 50 μm. **(F)** Representative immunohistochemical images of IL-17A expression in the GCL. Scale bar = 50 μm.

out increases the expression of the pro-inflammatory cytokines IL-1β, IL-6, and tumor necrosis factor (TNF)-α (Liu et al., 2015). In addition, Luo et al. identified that the FPR antagonist Boc2 downregulates microglia activation (Luo et al., 2014). ABCA1 was known to bind to ANXA1 (Chapman et al., 2003; Omer et al., 2006), but the function and mechanism were not clear. We speculated that ABCA1 might assist in ANXA1 secretion. Co-IP results from membrane extracts revealed that ABCA1 interacts with ANXA1 and that TO901317 increased ABCA1-ANXA1 membrane binding as well as ANXA1 secretion. In addition, we found that pretreatment of primary cultured RGCs with TO901317 decreases the migration of BV2 microglia and reduces their activation and expression of pro-inflammatory factors. All of these effects are reversed by Boc2. These results suggest that ABCA1 plays a role in ANXA1 membrane secretion and in the alleviation of inflammation.

Transcriptional programs operate to mediate the long-term control of ABCA1 (Koldamova et al., 2014). The liver X receptor agonist TO901317 was considered an effective up-regulator of ABCA1 expression. However, the ABCA1 post-translational modifications were unclear, especially as ABCA1 is ubiquitylated and degraded by as yet unknown E3 ligases (Sharpe et al., 2014). Hsieh et al. found that

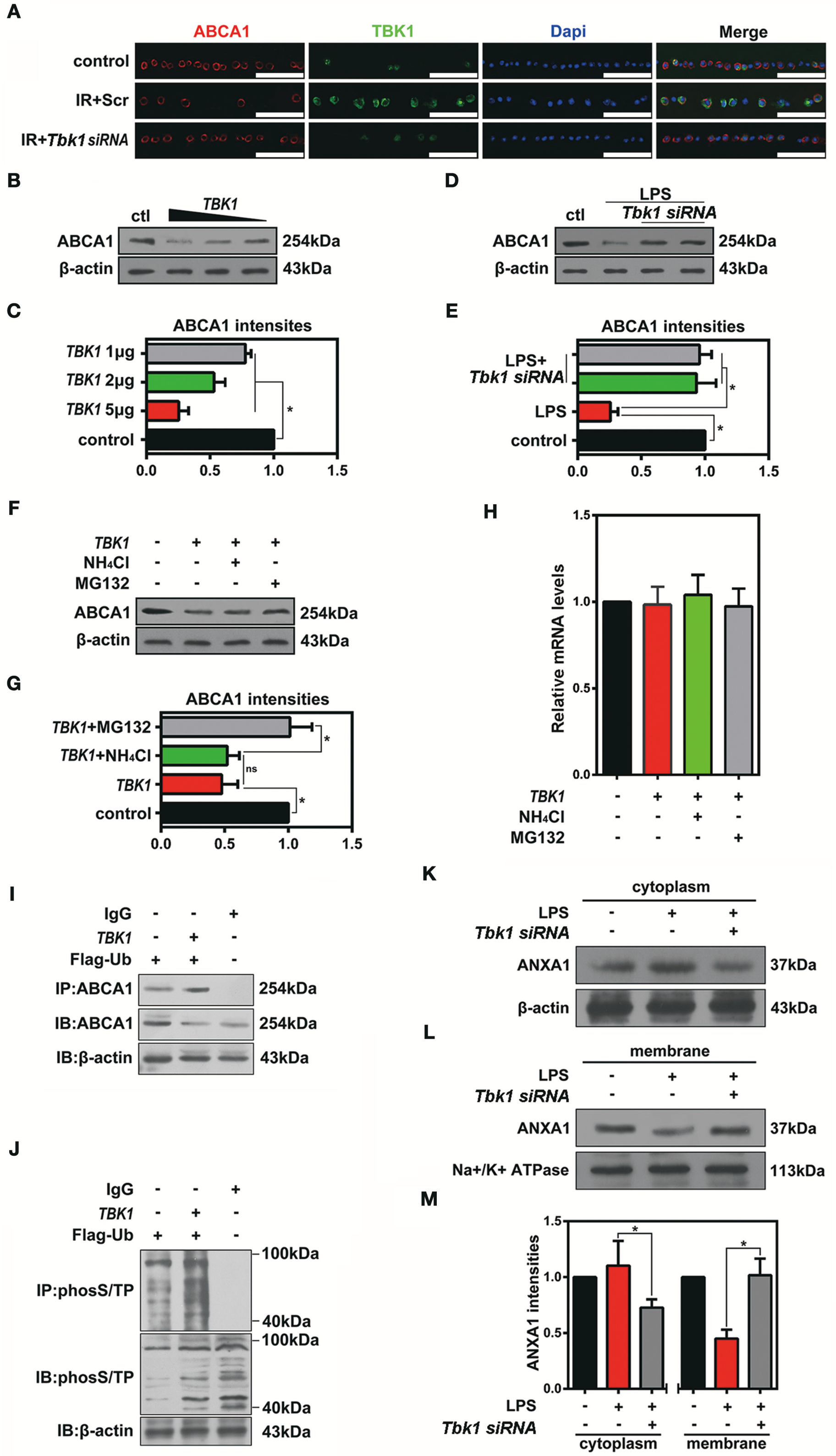

FIGURE 7 | The effects of TBK1 on ABCA1 expression and degradation. **(A)** Immunofluorescence results showing that TBK1 and ABCA1 can be co-localized and that *Tbk1* siRNA knockdown increases the expression of ABCA1 in RGCs ($n = 6$ retinas per group). Blue: DAPI; red: ABCA1; green: TBK1. Scr, Scrambled siRNA. *(Continued)*

FIGURE 7 | Scale bar = 50 µm. **(B)** Western blots showing the dose-dependent decrease in ABCA1 expression in HEK293 cells after *TBK1* overexpression. **(C)** Statistical analysis of the data shown in **(B)**. The data of three independent experiments are expressed as the means ± S.D. *$P < 0.05$, one-way ANOVA with Bonferroni *post hoc* test vs. control. **(D)** Western blot showing *Tbk1* siRNA knockdown reverse the reduction of ABCA1 which stimulated by LPS (1 µg/mL). **(E)** Statistical analysis of the data shown in **(D)**. The data of three independent experiments are expressed as the means ± S.D. *$P < 0.05$, one-way ANOVA with Bonferroni *post hoc* test. **(F)** Western blot showing that Mg132 (10 µM) can prevent in HEK293 a decrease in ABCA1 levels induced by *TBK1* overexpression. **(G)** Statistical analysis of the data shown in **(F)**. The data of three independent experiments are expressed as the means ± S.D. *$P < 0.05$, one-way ANOVA with Bonferroni *post hoc* test. **(H)** RT-PCR results show the expression of *ABCA1*. The data of three independent experiments are expressed as the means ± S.D. $P > 0.05$, one-way ANOVA with Bonferroni *post hoc* test. **(I)** Co-IP results indicate that ABCA1 ubiquitination is increased following *TBK1* overexpression. **(J)** Representative Co-IP results show that phospho-(Ser/Thr)-linked ubiquitination is increased following transfection with *TBK1*. **(K,L)** Western blots reveal that *Tbk1* siRNA increases the ANXA1 expression in the cell membrane after LPS stimulation, while ANXA1 expression in the cytoplasm is decreased. **(M)** Statistical analysis of the data shown in **(K,L)**. The data of three independent experiments are expressed as the means ± S.D. *$P < 0.05$, one-way ANOVA with Bonferroni *post hoc* test.

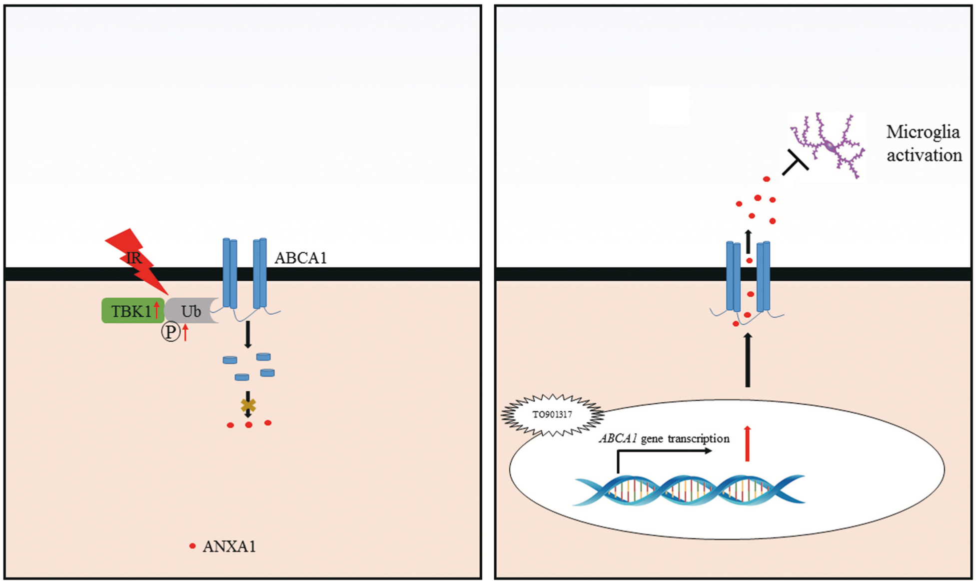

FIGURE 8 | Schematic representation of the cellular events influencing RGC apoptosis in ischemic injury. Ischemia-reperfusion injury induces an increase in TBK1 expression, which promotes ABCA1 ubiquitination and degradation, thus decreasing ANXA1 membrane transport (**Left**). TO901317 administration during ischemia-reperfusion increases the expression of ABCA1. This maintains ANXA1 membrane translocation and secretion, which inhibits microglia activation (**Right**).

the degradation of ABCA1 is completely inhibited by the proteasome inhibitor MG132 (Hsieh et al., 2014). In our study, we found that the expression of ABCA1 was negatively correlated with TBK1. *TBK1* overexpression increased ABCA1-ubiquitin proteasome binding and ubiquitin-proteasome phosphorylation. The proteasome inhibitor MG132 prevented the ABCA1 degradation induced by *TBK1* overexpression. These results suggest that *TBK1*-induced ABCA1 degradation might occur through the promotion of ubiquitin-proteasome phosphorylation.

The determination of the cell fate by ANXA1 was dependent on the subcellular protein localization not only in cancer cells but also in neural cells. Secreted ANXA1 interacts with FPRs and is involved in inflammation, neuroendocrine system regulation, skeletal muscle differentiation and cancer progression (Boudhraa et al., 2016), while nuclear translocation of ANXA1 is implicated in neuronal apoptosis after stroke (Zhao et al., 2015; Li et al., 2016). Omer et al. demonstrated that ABCA1 is co-localized with ANXA1 on the cell membrane of folliculostellate cells and that ABCA1 is involved in ANXA1 transport across the plasma membrane. In our study, ABCA1 and ANXA1 could be co-localized on the cell membranes of RGCs and, more importantly, administration of both *Tbk1* siRNA and TO901317 increased the expression of ANXA1 on the membranes and decreased the expression in the cytoplasm. More significantly, the Co-IP results indicate that the interactions between ABCA1 and ANXA1 occur on the ANXA1 C3 fragment.

Our findings identify a novel mechanism for ABCA1 in glaucoma. Ischemia reperfusion injury decreases ABCA1 expression in the GCL, which causes a decreased ANXA1 translocation to the cell membrane and its secretion. The TBK1 upregulation induced by IR stimulates ABCA1 degradation. TO901317 induces ABCA1 expression, thus, stimulating ANXA1 membrane translocation and secretion, which then prevents microglia activation (**Figure 8**). These findings provide with ABCA1 and TBK1 novel targets for glaucoma therapies.

AUTHOR CONTRIBUTIONS

YZ and HZ conceived and designed the study. LL, XL, LX, WC, and YZ performed the experiments. QD, QX, LZ, and HZ assisted with analyzing the data. LL and YZ drafted the manuscript, which was reviewed by and YZ.

FUNDING

This work was supported by a grant from the National Natural Science Foundation of China (grant numbers 81770921 and 31800868) and a grant from Huazhong University of Science and Technology (HUST grant number 2017KFYXJJ123).

SUPPLEMENTARY MATERIAL

The Supplementary Material for this article can be found online at: https://www.frontiersin.org/articles/10.3389/fncel.2018.00347/full#supplementary-material

Supplementary Figure 1 | The expression of ABCA1/ANXA1 in full retinal slice after IR. **(A)** Representative immunofluorescence images of ANXA1 expression in ischemic retina slices. GCL: ganglion cell layer; INL: inner nuclear layer; ONL: outer nuclear layer. **(B)** Immunofluorescence analysis showing the expression of ABCA1 in a full retina slice after IR.

REFERENCES

Boudhraa, Z., Bouchon, B., Viallard, C., D'Incan, M., and Degoul, F. (2016). Annexin A1 localization and its relevance to cancer. *Clin. Sci.* 130, 205–220. doi: 10.1042/CS20150415

Chapman, L. P., Epton, M. J., Buckingham, J. C., Morris, J. F., and Christian, H. C. (2003). Evidence for a role of the adenosine 5'-triphosphate-binding cassette transporter A1 in the externalization of annexin I from pituitary folliculo-stellate cells. *Endocrinology* 144, 1062–1073. doi: 10.1210/en.2002-220650

Chen, L., Lv, F., and Pei, L. (2014). Annexin 1: a glucocorticoid-inducible protein that modulates inflammatory pain. *Eur. J. Pain* 18, 338–347. doi: 10.1002/j.1532-2149.2013.00373.x

Chen, Y., Lin, Y., Vithana, E. N., Jia, L., Zuo, X., Wong, T. Y., et al. (2014). Common variants near ABCA1 and in PMM2 are associated with primary open-angle glaucoma. *Nat. Genet.* 46, 1115–1119. doi: 10.1038/ng.3078

Chinnery, H. R., McMenamin, P. G., and Dando, S. J. (2017). Macrophage physiology in the eye. *Pflugers Archiv Eur. J. Physiol.* 469, 501–515. doi: 10.1007/s00424-017-1947-5

Ding, Q. J., Zhu, W., Cook, A. C., Anfinson, K. R., Tucker, B. A., and Kuehn, M. H. (2014). Induction of trabecular meshwork cells from induced pluripotent stem cells. *Invest. Ophthalmol. Vis. Sci.* 55, 7065–7072. doi: 10.1167/iovs.14-14800

Feingold, K. R., and Grunfeld, C. (2000). *MDText.com, Inc.* Endotext, eds L. J. De Groot et al.

Gharahkhani, P., Burdon, K. P., Fogarty, R., Sharma, S., Hewitt, A. W., Martin, S., et al. (2014). Common variants near ABCA1, AFAP1 and GMDS confer risk of primary open-angle glaucoma. *Nat. Genet.* 46, 1120–1125. doi: 10.1038/ng.3079

Hsieh, V., Kim, M. J., Gelissen, I. C., Brown, A. J., Sandoval, C., Hallab, J. C., et al. (2014). Cellular cholesterol regulates ubiquitination and degradation of the cholesterol export proteins ABCA1 and ABCG1. *J. Biol. Chem.* 289, 7524–7536. doi: 10.1074/jbc.M113.515890

Hysi, P. G., Cheng, C. Y., Springelkamp, H., Macgregor, S., Bailey, J. N. C., Wojciechowski, R., et al. (2014). Genome-wide analysis of multi-ancestry cohorts identifies new loci influencing intraocular pressure and susceptibility to glaucoma. *Nat. Genet.* 46, 1126–1130. doi: 10.1038/ng.3087

Koldamova, R., Fitz, N. F., and Lefterov, I. (2014). ATP-binding cassette transporter A1: from metabolism to neurodegeneration. *Neurobiol. Dis.* 72(Pt A), 13–21. doi: 10.1016/j.nbd.2014.05.007

Levin, L. A., Crowe, M. E., and Quigley, H. A. (2017). Neuroprotection for glaucoma: requirements for clinical translation. *Exp. Eye Res.* 157, 34–37. doi: 10.1016/j.exer.2016.12.005

Li, L. U., Zhao, Y., and Zhang, H. (2017). P16INK4a upregulation mediated by TBK1 induces retinal ganglion cell senescence in ischemic injury. *Cell Death Dis.* 8:e2752. doi: 10.1038/cddis.2017.169

Li, X., Zhao, Y., Xia, Q., Zheng, L., Liu, L., Zhao, B., et al. (2016). Nuclear translocation of annexin 1 following oxygen-glucose deprivation-reperfusion induces apoptosis by regulating Bid expression via p53 binding. *Cell Death Dis.* 7:e2356. doi: 10.1038/cddis.2016.259

Liu, J. H., Feng, D., Zhang, Y. F., Shang, Y., Wu, Y., Li, X. F., et al. (2015). Chloral hydrate preconditioning protects against ischemic stroke via upregulating annexin A1. *CNS Neurosci. Therapeut.* 21, 718–726. doi: 10.1111/cns.12435

Luo, Z. Z., Gao, Y., Sun, N., Zhao, Y., Wang, J., Tian, B., et al. (2014). Enhancing the interaction between annexin-1 and formyl peptide receptors regulates microglial activation to protect neurons from ischemia-like injury. *J. Neuroimmunol.* 276, 24–36. doi: 10.1016/j.jneuroim.2014.07.013

Mao, J. Y., Sun, J. T., Yang, K., Shen, W. F., Lu, L., Zhang, R. Y., et al. (2017). Serum amyloid A enrichment impairs the anti-inflammatory ability of HDL from diabetic nephropathy patients. *J. Diabetes Complications* 31, 1538–1543. doi: 10.1016/j.jdiacomp.2017.07.005

Minegishi, Y., Nakayama, M., Iejima, D., Kawase, K., and Iwata, T. (2016). Significance of optineurin mutations in glaucoma and other diseases. *Prog. Retinal Eye Res.* 55, 149–181. doi: 10.1016/j.preteyeres.2016.08.002

Murphy, A. J., Westerterp, M., Yvan-Charvet, L., and Tall, A. R. (2012). Anti-atherogenic mechanisms of high density lipoprotein: effects on myeloid cells. *Biochim. Biophys. Acta* 1821, 513–521. doi: 10.1016/j.bbalip.2011.08.003

Nuzzi, R., and Tridico, F. (2017). Glaucoma: biological trabecular and neuroretinal pathology with perspectives of therapy innovation and preventive diagnosis. *Front. Neurosci.* 11:494. doi: 10.3389/fnins.2017.00494

Omer, S., Meredith, D., Morris, J. F., and Christian, H. C. (2006). Evidence for the role of adenosine 5'-triphosphate-binding cassette (ABC)-A1 in the externalization of annexin 1 from pituitary folliculostellate cells and ABCA1-transfected cell models. *Endocrinology* 147, 3219–3227. doi: 10.1210/en.2006-0099

Parente, L., and Solito, E. (2004). Annexin 1: more than an anti-phospholipase protein. *Inflammation Res.* 53, 125–132. doi: 10.1007/s00011-003-1235-z

Quigley, H. A., and Broman, A. T. (2006). The number of people with glaucoma worldwide in 2010 and 2020. *Br. J. Ophthalmol.* 90, 262–267. doi: 10.1136/bjo.2005.081224

Ramirez, A. I., de Hoz, R., Salobrar-Garcia, E., Salazar, J. J., Rojas, B., Ajoy, D., et al. (2017). The role of microglia in retinal neurodegeneration: Alzheimer's disease, Parkinson, and Glaucoma. *Front. Aging Neurosci.* 9:214. doi: 10.3389/fnagi.2017.00214

Rosenson, R. S., Brewer, H. B. Jr, Ansell, B. J., Barter, P., Chapman, M. J., Heinecke, J. W., et al. (2016). Dysfunctional HDL and atherosclerotic cardiovascular disease. *Nat. Rev. Cardiol.* 13, 48–60. doi: 10.1038/nrcardio.2015.124

Sharpe, L. J., Cook, E. C., Zelcer, N., and Brown, A. J. (2014). The UPS and downs of cholesterol homeostasis. *Trends Biochem. Sci.* 39, 527–535. doi: 10.1016/j.tibs.2014.08.008

Song, L., Pei, L., Yao, S., Wu, Y., and Shang, Y. (2017). NLRP3 inflammasome in neurological diseases, from functions to therapies. *Front. Cell. Neurosci.* 11:63. doi: 10.3389/fncel.2017.00063

Wang, S., and Smith, J. D. (2014). ABCA1 and nascent HDL biogenesis. *BioFactors* 40, 547–554. doi: 10.1002/biof.1187

Winzeler, A., and Wang, J. T. (2013). Purification and culture of retinal ganglion cells from rodents. *Cold Spring Harbor Protocols* 2013, 643–652. doi: 10.1101/pdb.prot074906

Yang, H., Zheng, S., Qiu, Y., Yang, Y., Wang, C., Yang, P., et al. (2014). Activation of liver X receptor alleviates ocular inflammation in experimental autoimmune uveitis. *Investig. Ophthalmol. Vis. Sci.* 55, 2795–2804. doi: 10.1167/iovs.13-13323

Zhang, K., Zhang, L., and Weinreb, R. N. (2012). Ophthalmic drug discovery: novel targets and mechanisms for retinal diseases and glaucoma. *Nat. Rev. Drug Discovery* 11, 541–559. doi: 10.1038/nrd3745

Zhao, Y., Li, X., Gong, J., Li, L., Chen, L., Zheng, L., et al. (2017). Annexin A1 nuclear translocation induces retinal ganglion cell apoptosis after ischemia-reperfusion injury through the p65/IL-1beta pathway. *Biochim. Biophys. Acta* 1863, 1350–1358. doi: 10.1016/j.bbadis.2017.04.001

Zhao, Y., Wang, J., Jiang, H., Yu, Z., Li, X., Shi, J., et al. (2015). Following OGD/R, annexin 1 nuclear translocation and subsequent induction of apoptosis in neurons are assisted by myosin IIA in a TRPM7 kinase-dependent manner. *Mol. Neurobiol.* 51, 729–742. doi: 10.1007/s12035-014-8781-y

Zheng, S., Yang, H., Chen, Z., Zheng, C., Lei, C., and Lei, B. (2015). Activation of liver X receptor protects inner retinal damage induced by N-methyl-D-aspartate. *Investig. Ophthalmol. Vis. Sci.* 56, 1168–1180. doi: 10.1167/iovs.14-15612

Conflict of Interest Statement: The authors declare that the research was conducted in the absence of any commercial or financial relationships that could be construed as a potential conflict of interest.

The reviewer LP declared a shared affiliation, with no collaboration, with the authors to the handling Editor.

frontiers
in Cellular Neuroscience

ORIGINAL RESEARCH
published: 26 September 2018
doi: 10.3389/fncel.2018.00312

Intravitreal S100B Injection Leads to Progressive Glaucoma Like Damage in Retina and Optic Nerve

Sandra Kuehn[1]†, Wilhelm Meißner[1]†, Pia Grotegut[1], Carsten Theiss[2], H. Burkhard Dick[1] and Stephanie C. Joachim[1]*

[1] Experimental Eye Research Institute, University Eye Hospital, Ruhr-University Bochum, Bochum, Germany, [2] Department of Cytology, Institute of Anatomy, Ruhr-University Bochum, Bochum, Germany

The glial protein S100B, which belongs to a calcium binding protein family, is up-regulated in neurological diseases, like multiple sclerosis or glaucoma. In previous studies, S100B immunization led to retinal ganglion cell (RGC) loss in an experimental autoimmune glaucoma (EAG) model. Now, the direct degenerative impact of S100B on the retina and optic nerve was evaluated. Therefore, 2 μl of S100B was intravitreally injected in two concentrations (0.2 and 0.5 μg/μl). At day 3, 14 and 21, retinal neurons, such as RGCs, amacrine and bipolar cells, as well as apoptotic mechanisms were analyzed. Furthermore, neurofilaments, myelin fibers and axons of optic nerves were evaluated. In addition, retinal function and immunoglobulin G (IgG) level in the serum were measured. At day 3, RGCs were unaffected in the S100B groups, when compared to the PBS group. Later, at days 14 and 21, the RGC number as well as the β-III tubulin protein level was reduced in the S100B groups. Only at day 14, active apoptotic mechanisms were noted. The number of amacrine cells was first affected at day 21, while the bipolar cell amount remained comparable to the PBS group. Also, the optic nerve neurofilament structure was damaged from day 3 on. At day 14, numerous swollen axons were observed. The intraocular injection of S100B is a new model for a glaucoma like degeneration. Although the application site was the eye, the optic nerve degenerated first, already at day 3. From day 14 on, retinal damage and loss of function was noted. The RGCs in the middle part of the retina were first affected. At day 21, the damage expanded and RGCs had degenerated in all areas of the retina as well as amacrine cells. Furthermore, elevated IgG levels in the serum were measured at day 21, which could be a sign of a late and S100B independet immune response. In summary, S100B had a direct destroying impact on the axons of the optic nerve. The damage of the retinal cell bodies seems to be a consequence of this axon loss.

Keywords: glaucoma, animal model, S100B protein, retinal ganglion cell damage, optic nerve degeneration, electroretinogram

OPEN ACCESS

Edited by:
Bela Volgyi,
University of Pécs, Hungary

Reviewed by:
Tamas Atlasz,
University of Pécs, Hungary
Valery I. Shestopalov,
University of Miami Miller School of Medicine, United States

****Correspondence:***
Stephanie C. Joachim
stephanie.joachim@rub.de

† These authors have contributed equally to this work

Received: *28 June 2018*
Accepted: *28 August 2018*
Published: *26 September 2018*

Citation:
Kuehn S, Meißner W, Grotegut P, Theiss C, Dick HB and Joachim SC (2018) Intravitreal S100B Injection Leads to Progressive Glaucoma Like Damage in Retina and Optic Nerve. Front. Cell. Neurosci. 12:312. doi: 10.3389/fncel.2018.00312

Abbreviations: EAG model, experimental autoimmune glaucoma model; ERG, electroretinogram; GCL, ganglion cell layer; HE, hematoxylin and eosin; IgG, immunoglobulin G; INL, inner nuclear layer; IOP, intraocular pressure; IPL, inner plexiform layer; LFB, luxol fast blue; NFL, nerve fiber layer; NMDA, N-methyl-D-aspartate; ONL, outer nuclear layer; OPL, outer plexiform layer; PARP-1, poly (ADP-ribose) polymerase 1; PB, phosphate buffer; PFA, paraformaldehyde; PKCα, protein kinase Cα; RGC, retinal ganglion cell; SEM, standard error of mean.

INTRODUCTION

The causes of the most retina degenerations are unidentified, this includes glaucoma. Glaucoma is defined by a progressive loss of retinal ganglion cells (RGCs) and degeneration of the optic nerve, which leads to slow continuous loss of the visual field (EGS, 2017). The pathomechanisms of this disease are still unknown. Oxidative stress (Tezel et al., 2010), excitotoxicity (Dreyer et al., 1996) and immunological processes (Grus et al., 2004) might play a role. An approach of the last years was to study of the association of the immune system and autoimmune processes with glaucoma. It could be demonstrated that glaucoma patients have altered autoantibody titers, both up- and down-regulated, against different types of structural molecules and proteins, such as heat shock proteins (Tezel et al., 1998; Joachim et al., 2007), phosphatidylserine (Kremmer et al., 2001), γ-enolase (Maruyama et al., 2000), neuron specific enolase (Ikeda et al., 2002) and glutathione-S-transferase (Yang et al., 2001). Altered antibody pattern were detected not only in serum, but also in aqueous humor or tear fluid of glaucoma patients. An increase of autoreactive antibodies against the S100B protein was detectable in the tears of glaucoma patients (Grus et al., 2010).

S100B is a small calcium binding protein, which is expressed in glia cells (Huttunen et al., 2000). It belongs to the S100 protein family, which currently consists of 25 members (Marenholz et al., 2006; Santamaria-Kisiel et al., 2006), and represents a potential effector of inflammatory reactions and oxidative stress in neurons (Huttunen et al., 2000; Rothermundt et al., 2003). Furthermore, it is also known that increased concentrations of S100B occur in neurodegenerative diseases, like Alzheimer's disease (Goncalves et al., 2000), epilepsy (Rothermundt et al., 2001) and schizophrenia (Griffin et al., 1989). The relevance of the protein S100B in pathophysiology of glaucoma was also investigated in an animal model. In this case, the S100B was applied systemically in rats and induced an immune response against S100B. Due to this damage mechanism, this model is called experimental autoimmune glaucoma model (EAG model). The optic nerve filament degenerated at first (Noristani et al., 2016), while the neurons of the inner retinal layers were affected later in the EAG model (Reinehr et al., 2018). S100B directly influences pathophysiological mechanisms inducing glaucomatous degenerations in retina and optic nerve.

In order to examine the local effects of the S100B protein on retina and optic nerve and to exclude potentially systemically immunological effects, we applied S100B intravitreally in rat eyes. The goal of this study is to investigate, if it is possible to ascertain a RGCs deprivation and optic nerve degeneration after intravitreal application of S100B.

MATERIALS AND METHODS

Animals

Eight week old male Wistar rats from Charles River (176–200 g; Sulzfeld, Germany) were included in this study. All experiments that involved animals were performed in compliance with the ARVO Statement for the Use of Animals in Ophthalmic and Vision Research. Furthermore, the study was approved by the animal care committee of North Rhine-Westphalia in Germany (84-02.04.2013.A442). During the whole experiment, the rats were kept in a room with constant temperature and a 12:12 h dark-light lightening cycle. They were housed under environmentally controlled conditions with free access to food and water *ad libitum* and in the absence of pathogens.

Intraocular S100B Injection

Rats were anesthetized with a mixture of ketamine (50 mg/ml, Ratiopharm) and xylazine (2%, Bayer Health Care). After the application of a topical anesthetic (Conjuncain, 4 mg/ml, Bausch&Lomb), the pupil was dilated with a mydriaticum (Tropicamide, 5 mg/ml, Stulln). The S100B protein was used in two different concentrations. One group was treated with 2 μl of a 0.2 μg/μl S100B solution (S100B I group, Sigma-Aldrich) and the other group was treated with 2 μl of a 0.5 μg/μl S100B solution (S100B II group, Sigma-Aldrich). S100B was injected in the vitreous of one eye with a 32-gauge needle (Hamilton) under a stereomicroscope (Zeiss). The control group received 2 μl PBS (Biochrome), since this was used as a solvent for S100B. The corresponding eyes remained untreated. Therefore, four groups were compared in this study: native, PBS, S100B I and S100B II. After the injection, the eyes were treated with Floxal, an antibiotic ointment (Bausch&Lomb), and examined after 2 h and on the next day. Animals with eye bleeding or cataracts were excluded. In addition, the general behavior and look of the animals was evaluated once a week.

Intraocular Pressure Measurements

The intraocular pressure (IOP) of all groups ($n = 6$ eyes/group) was measured using a rebound tonometer (TonoLab; Icare, Oy, Finland) up to day 21, once a week (Biermann et al., 2012). Means were calculated from 10 single measurements per eye and point in time.

Electroretinogram Analysis

The rats were dark adapted for the electroretinogram (ERG) recording overnight. The measurements were done under dark conditions. A headlamp with red light was needed for the orientation of the investigator. A full-field flash electroretinography (HMsERG system; OcuScience LLC, Rolla, MO, USA) was used to analyze the function of the retina at day 14 (Schmid et al., 2014). Therefore, rats were anesthetized with a ketamine/xylazine mixture (100/4 mg/kg). Eyes were dilated with a mydriaticum and locally anesthetized with conjuncain. During the measurement the body temperature was maintained at 37°C with a temperature controller (TC-1000, CWE Inc., Ardmore, PA, USA). A ground electrode was placed subcutaneously in the back over the tail and reference electrodes were located under the both ears. One drop of methocel (Omni Vision, Puchheim, Germany) was directly applicated on the cornea. Recording electrodes combined with a contact lens were placed in the center of both eyes. The function of the electrodes was tested before the faraday cage was closed over the whole equipment (OcuScience, LLC). Scotopic flash series were recorded with light flash intensity at 0.1, 0.3, 1, 3, 10 and 25 cd/m^2. The ERGView 4.380R software (OcuScience, LLC) was used for the data evaluation. Therefore, a low pass filter (150 Hz) was necessary. All single waves were controlled. The amplitude of the a- and b-wave was exported to excel (Microsoft Corp., Redmond, WA, USA) for further statistical analysis.

IgG ELISA Measurement

The immunoglobulin G (IgG) level was measured in the sera of PBS and S100B I animals at 14 and 21 days. Doublets of undiluted serum sample were analyzed using an IgG ELISA kit (Cloud-Clone Corp.) according to the manufacture's protocol. All measurements were performed on a microplate reader (AESKU Reader with Gen5 ELISA Software, AESKU. DIAGNOSTICS). The IgG level of the S100B I was compared to the level of the PBS group at day 14 and 21 (n = 7/group and point in time).

Immunohistochemistry of Retinal Flatmounts After 3 and 14 Days

Three and 14 days after the intraocular injection of PBS or S100B, eyes were prepared for flatmounts as previously described (Casola et al., 2015; 3 days: n = 3–4/group; 14 days: n = 6–7/group). Briefly, after fixation in 4% paraformaldehyde (PFA; Merck) for 2 h, the eye was opened and the retina was gently dissected. The retina was divided into four sections and then mounted on a black gridded nitrocellulose membrane (Millipore) with the vitreous facing up. For investigation of the RGCs, the retinas were stained with an antibody against Brn-3a (**Table 1**) in a 12-well plate on a shaker. With an Apotom.2 microscope (Zeiss) four images per flatmount arm (one peripheral, two middle and one central photo) were taken. The Brn-3a$^+$ cells were counted in a masked fashion and the percentage of Brn-3a$^+$ cells was calculated by setting the mean count of the native group to 100%.

Preparation of Retina Cross-Section and Optic Nerve Longitudinal Sections

Eyes and optic nerves were examined 3, 14 and 21 days after intraocular injection of PBS and S100B, like previously described (Noristani et al., 2016). Subsequently, eyes (14 and 21 days: 6–7 retinas/group) were fixed with 4% PFA for 1 h and finally treated with 30% sucrose. Thereafter, retinal cross-sections (10 μm) were cut with a microtome (Thermo Scientific, Waltham, MA, USA). Optic nerves were fixed for 2 h in 4% PFA followed by 30% sucrose and cut in 4 μm thick longitudinal sections (3 days: 3–4 optic nerves/group; 14 and 21 days: 6–7 optic nerves/group). The retinal cross-sections as well as optic nerve longitudinal sections were mounted on slices (Histobond). Finally, the tissues on the slices were fixed in ice-cold acetone for 10 min.

Histological Stainings and Analysis

Hematoxylin and eosin (HE, both Merck) staining was used for retinal cross-sections (Horstmann et al., 2013). We microscopically examined (Axio Imager.M1, Zeiss) the HE stained retinal cross-sections and recorded four images per retina (two peripheral and two central).

Luxol fast blue (LFB, RAL Diagnostic) staining of optic nerve sections was performed (Noristani et al., 2016). Microscopy and image acquisition of the LFB stained sections was carried out by recording three pictures per nerve (proximal, middle and distal). The pictures were scored from 0 = intact up to 2 = destroyed, in regard to integrity of the nerve fibers. The LFB scoring focuses on the shorting of myelin fibers and fissure development in the "combed" structure (Horstmann et al., 2013). The statistical evaluation of the LFB score was performed by a comparative analysis of the S100B groups with the native as well as with the PBS treated group.

Immunofluorescence Staining of Specific Cell Types in Retina and Optic Nerve

The staining protocol was performed as previously described (Noristani et al., 2016). Briefly, retinal cross-sections and optic nerve longitudinal sections were blocked with a mixture of a 10%–20% serum, 0.1%–0.2% TritonX-100 (Sigma-Aldrich) and PBS (Santa Cruz). The primary antibodies (**Table 1**) were diluted in the same mixture and incubated at room temperature overnight. Then, sections were incubated with AlexaFluor 555 or AlexaFluor 488 labeled secondary antibodies in the same mixture (**Table 1**). The nuclei were stained with DAPI (0.01 μg, Sera) for 5 min. Finally, sections were covered with Shandon-mount (Thermo Scientific, Waltham, MA, USA). Negative controls of all stainings were performed using secondary antibodies only.

For further evaluations, four images per retina (two peripheral and two central) and three per optic nerve (proximal, middle and distal) were taken with an Axio Imager.M1 microscope (Zeiss) in 400× magnification. The cell quantification of retinas was carried out by counting the positive signals (Brn-3a, calretinin, protein kinase Cα (PKCα)). We used an already established scoring system for the analysis of SMI-32 labeled neurofilaments in optic nerves (Noristani et al., 2016). The SMI-32 scoring respects the shortening of the neurofilaments and the development of retraction bulbs (0 = intact, 2 = destroyed).

Preparation of Optic Nerve Cross-Sections

At day 14, animals (n = 6–7/group) were perfused with 4% PFA solution for 20 min. Thereafter, the optic nerves were fixed in 2.5% glutaraldehyde in 1% phosphate buffer (PB). A detailed description of the embedding procedure is given in Krause et al. (2016). Briefly, after rinsing in PB the optic nerves were placed in Dalton solution (5% potassium dichromate, 3.4% sodium chloride, distilled water and osmium tetra-oxide) and then dehydrated in an ethanol series. The tissue was carefully transferred into epoxy resin and followed by an EPON mixture using a slightly modified protocol first described by Luft (1961).

TABLE 1 | Primary and secondary antibodies used for immune histological and Western blot stainings.

Primary antibodies			**Secondary antibodies**		
Name	**Company**	**Dilution**	**Name**	**Company**	**Dilution**
Retinal flatmounts					
Brn-3a	Santa Cruz	1:100	Donkey anti-goat AlexaFluor 488	Abcam	1:400
Retinal cross-sections					
Brn-3a	Santa Cruz	1:100	Donkey anti-goat AlexaFluor 488	Abcam	1:400
Calretinin	Millipore	1:2,000	Donkey anti-goat AlexaFluor 488	Abcam	1:500
PKCα	Santa Cruz	1:300	Donkey anti-mouse A488	Invitrogen	1:500
Longitudinal optic nerve sections					
SMI-32	Biolegend	1:2,000	Goat anti-mouse A488	Invitrogen	1:400
Western blot					
β-actin	Cell Signaling	1:1,000	Donkey anti-rabbit DyeLight800	Thermo Fisher	1:20,000
β-actin	Sigma-Aldrich	1:6,000	IRDye donkey anti-mouse DL800	LICOR	1:20,000
β-III-tubulin	R&D System	1:15,000	Donkey anti-mouse AlexaFluor 680	Invitrogen	1:5,000
Calretinin	Millipore	1:30,000	Rabbit anti-goat AlexaFluor 680	Invitrogen	1:5,000
Cleaved caspase 3	Sigma-Aldrich	1:300	Donkey anti-rabbit AlexaFluor 680	Invitrogen	1:5,000
PARP	Abcam	1:400	Donkey anti-rabbit AlexaFluor 680	Invitrogen	1:5,000

0.5 μm thick semi-thin slices were cut with a Leica EM TRIM (Leica Microsystems GmbH, Wetzlar, Germany).

Methylene blue stained cross-sections (n = 6/optic nerve) were scored as described by Pang and Clark (2007), which reach from 1 (intact) up to 5 (damage with strong gliosis and axon swelling up to 95% of optic nerve).

Western Blot Analysis

For Western blot analysis we prepared retinas as previously described (Noristani et al., 2016). Initially, proteins had to be isolated from the tissue. Therefore, the retinas were homogenized with mechanical (metal homogenizer, Neolab) and chemical methods (150 μl of the commercial lysis buffer RIPA, Cell Signaling Technology). After the samples were incubated on ice for 50 min, then centrifugation took place and the supernatants were pipetted off. We determined the protein concentration in the samples with a light absorption photometry. For the gel electrophoresis we used 12% Bis-Tris or 4%–12% Bis-Tris gels (NuPAGE, Invitrogen) and loaded 10 μg sample per lane. After performing the blotting with NuPAGE transfer buffer (Invitrogen), the nitrocellulose membranes were blocked with a mixture of 5% milk powder (Applichem) in a PBS/0.05% Tween-20 solution (Santa Cruz, Sigma-Aldrich). For the detection of the different proteins we used specific primary antibodies (**Table 1**). For the detection of the bound primary antibodies fluorochrome labeled compatible secondary antibodies were used (**Table 1**). The visualization and analysis of the protein bands was done by means of the Odyssey infrared imager system 2.1 (LI-COR Biosciences). For the statistical evaluation, the band intensities of the target protein were always normalized with β-actin and then the normalized intensities of the S100B group were evaluated against both normalized controls.

Statistics

The statistical analysis was performed using Statistica software (version 13, Dell). Data are presented as mean ± standard error (SEM). In the course of the statistical analysis, the S100B groups were compared with the respective PBS (*) and native group ($^{\#}$) using one-way ANOVA with *post hoc* Tukey test. Student's t-test was used to compare both groups of the ELISA analysis. A $p < 0.05$ was considered statistically significant.

RESULTS

Unchanged Intraocular Pressure With First Signs of Disrupted Signal Transfer

IOP was measured 1 day before S100B was intravitreally injected and 7, 14 and 21 days after the injection. At all points in time, the IOP of the S100B I group remained comparable to the PBS ($p > 0.05$) and native group ($p > 0.05$, **Figure 1A**).

The a- and b-wave amplitudes of the retina were investigated via ERG. The a-wave amplitude of the S100B I group was slightly reduced at a flash intensity of 1 cd.s/m^2 (67.5 ± 7.1 μV) compared to the PBS (97.5 ± 5.7 μV, $p = 0.049$) and to the native group (111.1 ± 11.1 μV, $p = 0.004$; **Figure 1B**). No differences were noted between all groups at all other flash intensities. The b-wave amplitude of the S100B I group was decreased at 0.1 cd (196.5 ± 15.4 μV), 0.3 cd (209.2 ± 11.0 μV) and 1 cd (41.7 ± 15.8 μV) compared to the native group (0.1 cd: 281.5 ± 27.2 μV, $p = 0.048$; 0.3 cd: 345.1 ± 40.7 μV, $p = 0.01$; 1 cd: 355.1 ± 37.2 μV, $p = 0.02$; **Figure 1C**). In comparison to the PBS group, only the flash intensities at 0.3 (322.5 ± 28.3 μV, $p = 0.035$) and 1 cd (337.0 ± 29.5 μV, $p = 0.04$) were altered.

The IgG level was analyzed in the sera of PBS and S100B I group. At day 14, the PBS group had a mean IgG level of 11.2 ± 1.0 μg/ml. A similar IgG level was noted in S100B I serum samples (11.9 ± 1.2 μg/ml, $p = 0.65$, **Figure 1D**). However, higher IgG level were measured in the S100B I group (11.6 ± 0.7 μg/ml) in comparison to the PBS group (8.4 ± 0.8 μg/ml, $p = 0.014$, **Figure 1E**) at day 21.

Analysis of Retina

Intact Retina Structure Despite Time-Dependent Apoptotic Mechanisms

In order to gain a first impression, we explored the effects of S100B on retinal cross-sections and evaluated the HE stained

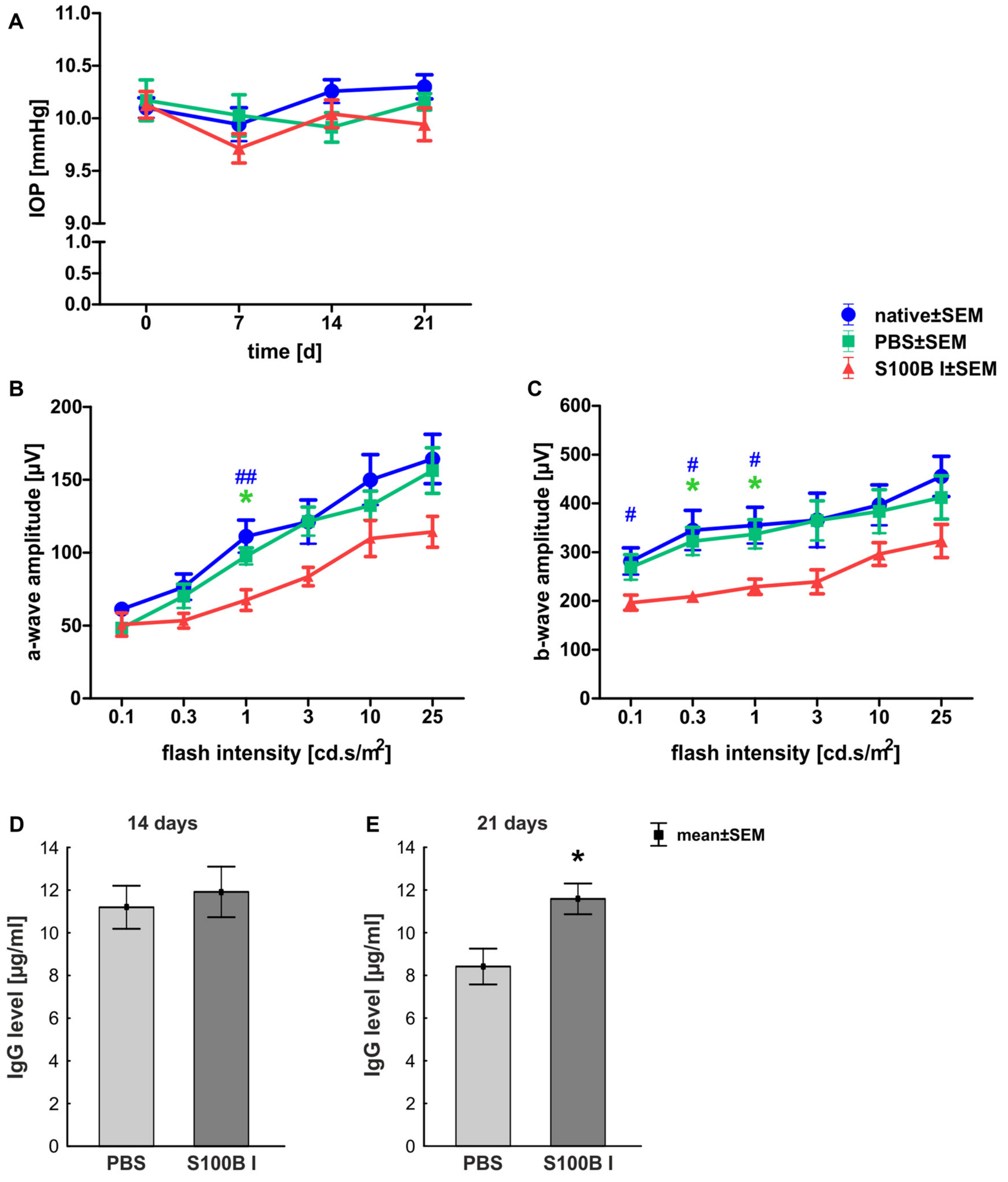

FIGURE 1 | Stable intraocular pressure (IOP) and reduced electroretinogram (ERG) amplitudes. **(A)** The IOP was measured weekly for 21 days. No differences between the groups was noted at all points in time. **(B)** The a-wave amplitude of the ERG measurements was only affected at 1.0 cd.s/m^2 in the S100B I group (PBS: $p = 0.049$, native: $p = 0.004$). **(C)** However, the b-wave amplitude of the S100B I group was reduced compared to the PBS group at 0.3 ($p = 0.035$) and 1.0 cd.s/m^2 ($p = 0.04$) and in comparison to the native group at 0.1 cd ($p = 0.048$), 0.3 cd ($p = 0.01$) and 1.0 cd ($p = 0.02$). **(D)** The immunoglobulin G (IgG) level in the sera of PBS and S100B I group was analyzed via IgG ELISA. No differences between both groups were measured at day 14. **(E)** Later, at day 21, the IgG level in the serum of the S100B I group was higher than that of the PBS group ($p = 0.014$). $^{*}p < 0.05$ (compared to PBS group); $^{\#}p < 0.05$, $^{\#\#}p < 0.01$ (compared to native group).

sections according to morphological aspects at day 14 and 21. The retina layers and structure of all groups remained intact during the course of the study (**Figure 2A**). No signs of retinal inflammation were noted. However, apoptotic mechanisms occurred in the S100B I group. Western blot analysis of cleaved caspase 3 (**Figure 2B**) showed an increased signal intensity in the S100B I group (7.6 ± 0.9 units) compared to the PBS (2.8 ± 0.7 units, $p < 0.001$) and native group (2.4 ± 0.1 units, $p < 0.001$, **Figure 2C**) at day 14. At day 21, Western blot stainings of poly (ADP-ribose) polymerase 1 (PARP-1) were

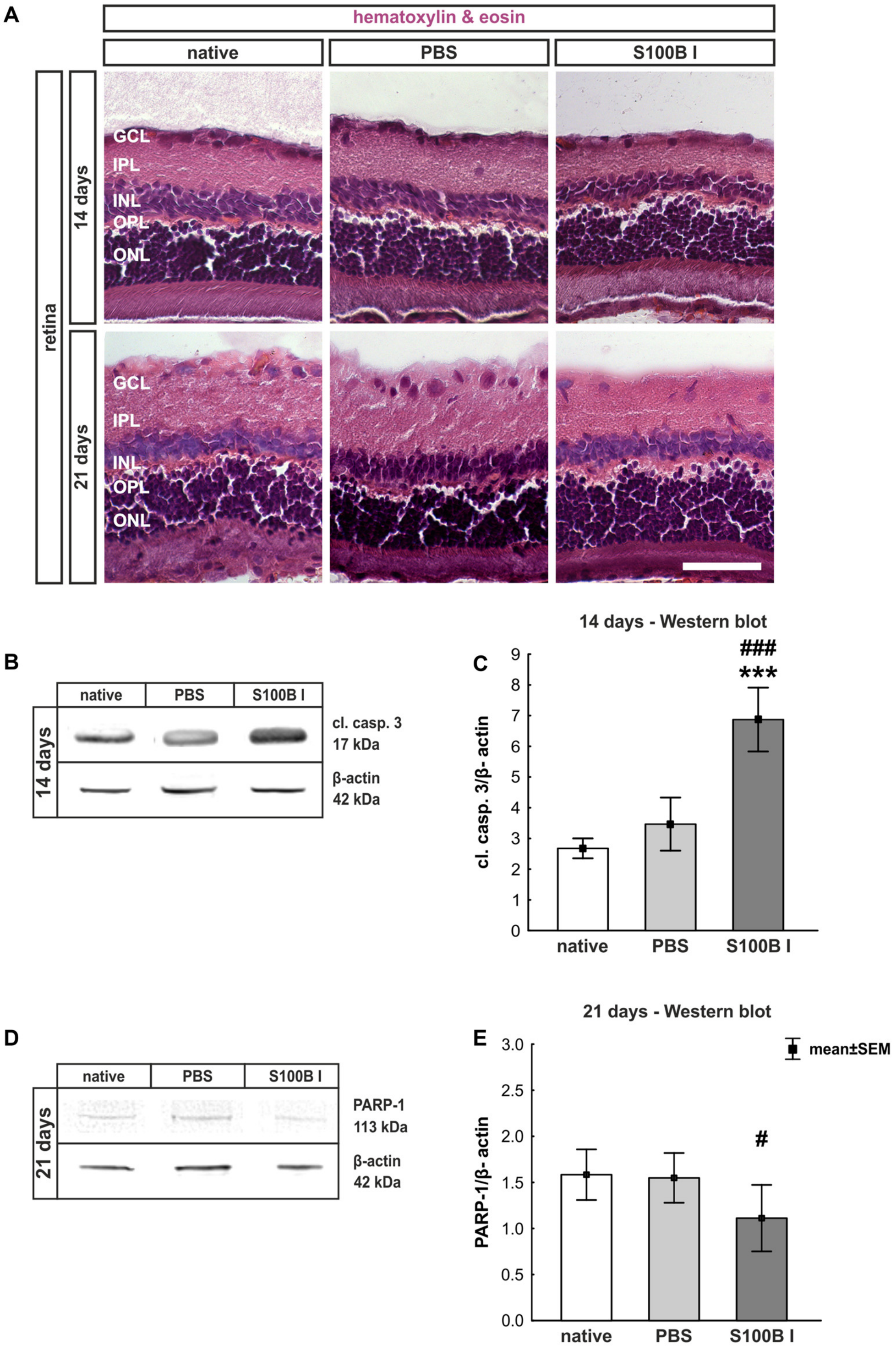

FIGURE 2 | Intact retinal morphology, but peak of apoptosis at day 14. **(A)** Via hematoxylin and eosin staining, we could show that retinas still had an intact structure at 14 and 21 days in all groups. S100B I did not induce cellular infiltrations or damage to retinal layers. **(B)** Western blot analysis of cleaved caspase 3 (17 kDa) was normalized with β-actin (42 kDa) at 14 days. **(C)** At day 14, the protein level of cleaved caspase 3 was increased in the S100B I group compared to PBS and native group (both: $p < 0.001$). **(D)** At day 21, poly (ADP-ribose) polymerase 1 (PARP-1; 113 kDa) was analyzed via Western blot. **(E)** Here, differences between the S100B I and native group were observed ($p = 0.027$) and a decreasing trend in comparison to the PBS group ($p = 0.06$). GCL, ganglion cell layer; IPL, inner plexiform layer; INL, inner nuclear layer; OPL, outer plexiform layer; ONL, outer nuclear layer; scale bar = 50 μm; $^{***}p < 0.001$ (compared to PBS group); $^{\#}p < 0.05$, $^{\#\#\#}p < 0.001$ (compared to native group).

performed (**Figure 2D**). A reduction of PARP-1 at 113 kDa is a sign for apoptosis (Yu et al., 2006). A decreasing trend of PARP-1 level was observed in the S100B I group (0.8 ± 0.3 units) compared to the PBS group (1.8 ± 0.2 units, $p = 0.06$; **Figure 2E**). In comparison to the native group (1.9 ± 0.3 units), a lower protein level was noted in S100B retinas ($p = 0.027$, **Figure 2E**).

Time-Dependent but Concentration Independent Loss of Retinal Ganglion Cells

Three and 14 days after the intraocular application of S100B in two different concentrations retinal flatmounts were stained with anti-Brn-3a (**Figure 3A**). At day 3, the Brn-3a$^+$ cell counts of the native (100.0 ± 8.1% Brn-3a$^+$ cells, $p > 0.9$) and PBS group (99.5 ± 8.7% Brn-3a$^+$ cells) were similar to counts of the S100B I (103.5 ± 3.7%, $p > 0.9$) and S100B II group (103.6 ± 4.8%, $p > 0.9$, **Figure 3B**) in all evaluated areas (**Supplementary Figure S1A**). However, a reduced Brn-3a$^+$ cell number was noted in both S100B groups (S100B I: 82.1 ± 3.8%, S100B II: 81.8 ± 2.8%) compared to the PBS (98.9 ± 3.3%, both $p = 0.01$) and native group (100.0 ± 3.4%, S100B I: $p = 0.008$, S100B II: $p = 0.003$, **Figure 3C**) at day 14. In relation to the PBS group (101.3 ± 3.6%) the degeneration started in the middle part of the retina in both S100B concentrations (S100B I: 83.6 ± 3.5%, $p = 0.009$; S100B II: 80.6 ± 2.6%, $p = 0.002$, **Supplementary Figure S1B**). Similar findings were observed in comparison to the native group (100.0 ± 3.5%; S100B I: $p = 0.02$; S100B II: $p = 0.002$). The loss of RGC was independent of the applied S100B concentration, so subsequent evaluations were done with the lower S100B concentration.

In addition to immunohistochemistry, we investigated the influence of S100B on the neurons via Western blot analysis and detected β-III-tubulin, a specific marker for neurons (**Figures 3D,F**). The evaluation underlined the immune histological results, since the β-III-tubulin intensity was significantly lower in the S100B I group (0.69 ± 0.03 units) in comparison to the PBS (0.89 ± 0.02 units; $p < 0.001$) and native group (0.89 ± 0.03 units; $p < 0.001$, **Figure 3E**) at 14 days. We evaluated the effects of the intraocular application of S100B I at 21 days. Here, a lower β-III-tubulin signal intensity was also measured in the S100B I group (1.08 ± 0.35 units) when compared to the PBS (1.65 ± 0.08 units, $p = 0.02$) or native group (1.61 ± 0.15 units, $p = 0.02$, **Figure 3G**).

To verify the Western blot results at day 21, retinal cross-sections were stained with an anti-Brn-3a antibody (**Figure 3H**). Fewer Brn-3a$^+$ cells were noted in the S100B I (16.53 ± 12.61 cells/mm) than in the PBS (34.29 ± 3.21 cells/mm, $p = 0.006$) and native group (32.36 ± 5.15 cells/mm, $p = 0.02$, **Figure 3I**). We could prove the first degenerations signs of the RGCs at day 14. This was independently of the S100B concentration. The damage aggravated at day 21.

Significant Degeneration of Amacrine Cells After S100B Injection

In order to evaluate the extent of retinal damage after the intraocular application of S100B, the cells of the inner nuclear layer (INL) were analyzed. For this purpose, we performed

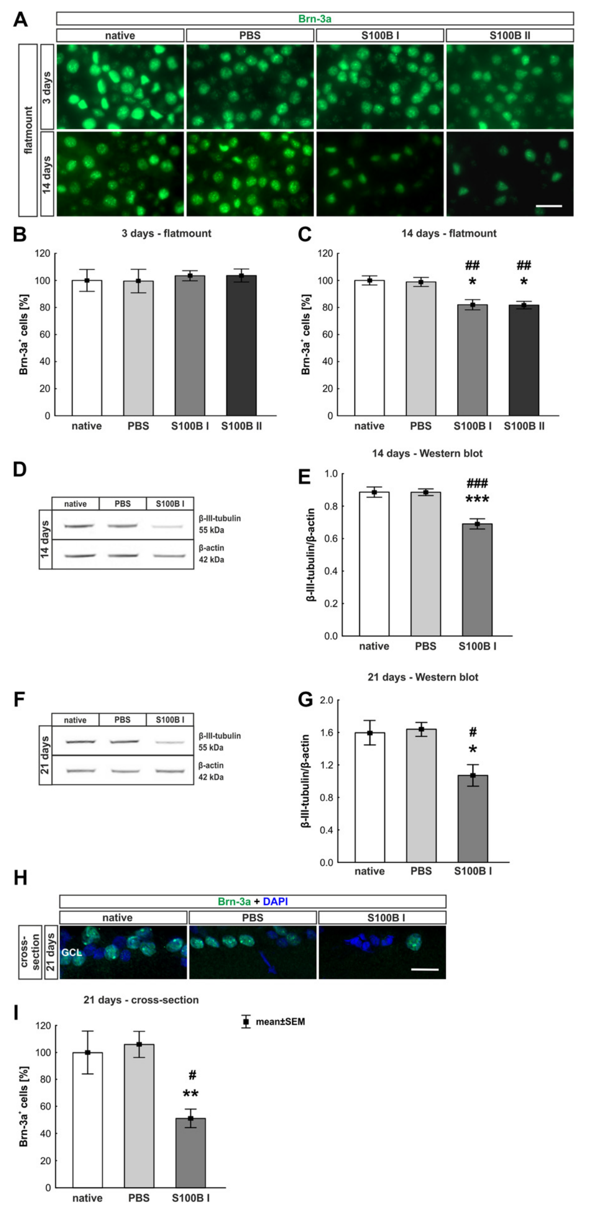

FIGURE 3 | Significant retinal ganglion cell (RGC) loss from day 14 on. **(A)** RGCs were stained on retinal flatmounts with anti-Brn-3a antibody at 3 and 14 days. **(B)** After 3 days, RGC density in the S100B I and II group was comparable to the PBS and native group. **(C)** However, after 14 days, a significant reduction of RGC density was noticed in both S100B groups compared to the PBS (both: $p = 0.01$) and native group (S100B I: $p = 0.008$, S100B II: $p = 0.003$). **(D)** Western blots of β-III-tubulin (55 kDa) were analyzed using β-actin (42 kDa) for normalization at day 14. **(E)** A significant reduction of β-III-tubulin signal intensity was noted in the S100B I group compared to both controls (both: $p < 0.001$). **(F)** Also, at day 21, the β-III-tubulin protein level was analyzed with Western blot. **(G)** Here, a significant reduction of the signal intensity in the S100B I group could be seen in comparison to PBS and native group (both: $p = 0.02$). **(H)** RGCs were stained with Brn-3a on retinal cross-section at day 21. **(I)** A degeneration of RGCs was seen in the S100B I group compared to the PBS ($p = 0.006$) and native group ($p = 0.02$). GCL, ganglion cell layer; scale bar = 20 μm, $^*p < 0.05$, $^{**}p < 0.01$, $^{***}p < 0.001$ (compared to PBS group); $^{\#}p < 0.05$, $^{\#\#}p < 0.01$, $^{\#\#\#}p < 0.001$ (compared to native group).

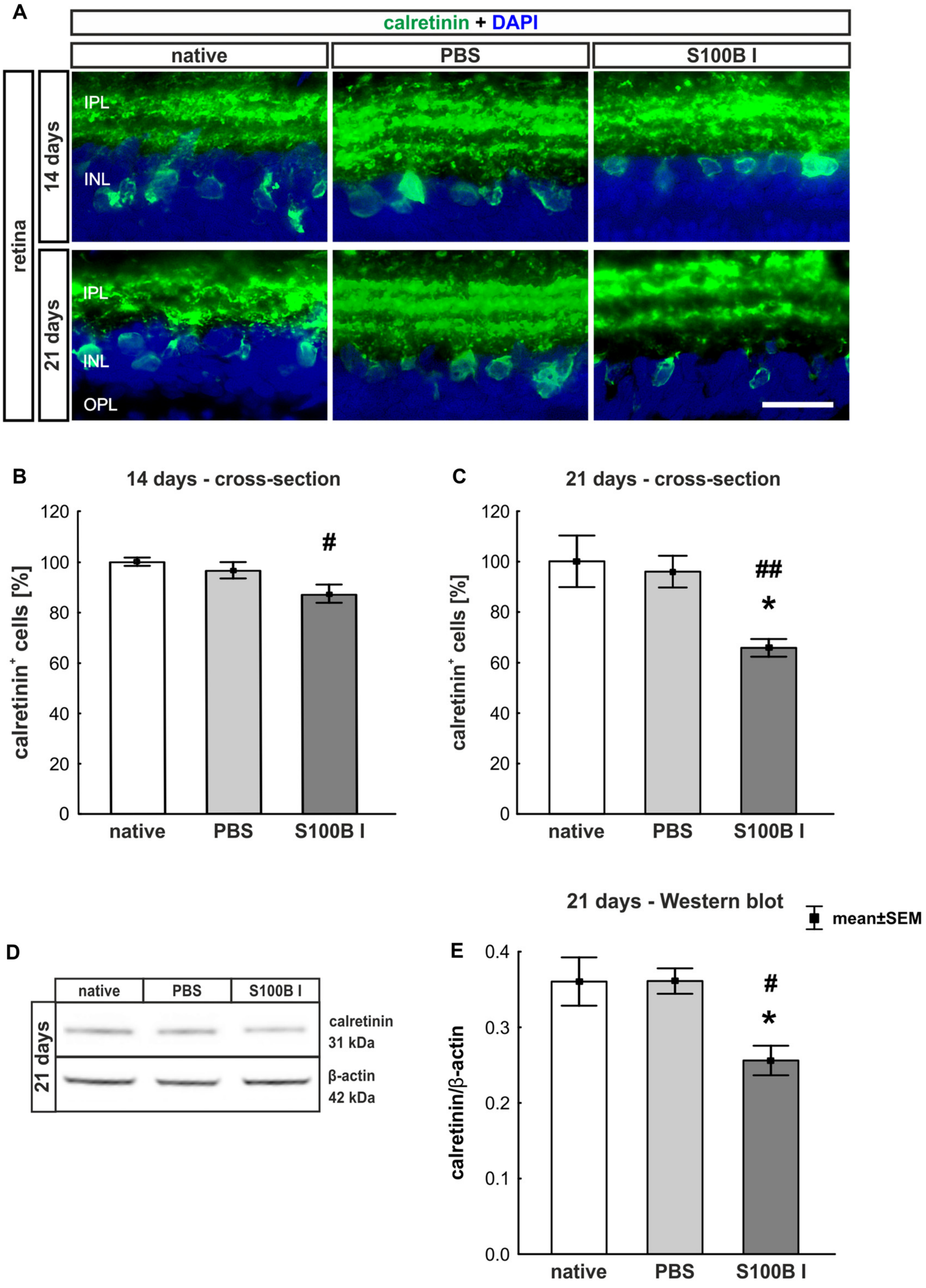

FIGURE 4 | Progressive loss of amacrine cells after intraocular S100B injection. **(A)** We performed immunohistochemical evaluations of amacrine cells (calretinin, green) 14 and 21 days after S100B injection. Cell nuclei were stained with DAPI (blue). **(B)** The examination of calretinin$^+$ cells at 14 days revealed a trend to a loss of cell bodies compared to the PBS ($p = 0.084$) and a lower cell number compared to the native group ($p = 0.015$). **(C)** Whereas, the evaluation after 21 days already showed significantly fewer amacrine cells in the S100B I group compared to the both controls (PBS: $p = 0.014$, native: $p = 0.0098$). **(D)** The protein level of calretinin (31 kDa) was measured with Western blot at day 21 and normalized with β-actin (42 kDa). **(E)** The calretinin protein level decreased at day 21 in comparison to both controls (both: $p = 0.025$). IPL, inner plexiform layer; INL, inner nuclear layer; scale bar = 20 μm, $^*p < 0.05$ (compared to PBS group); $^{\#}p < 0.05$, $^{\#\#}p < 0.01$ (compared to native group).

immune histology using an anti-calretinin antibody, a specific marker for amacrine cells (**Figure 4A**). The count of calretinin$^+$ cells showed a tendency of reduced cell numbers in the S100B I group (87.07 ± 9.58%) compared to the PBS group (96.48 ± 8.58%, p = 0.084) and a lower cell count compared to the native group after 14 days (100.0 ± 1.64%, p = 0.015, **Figure 4B**). This damage extended later on, since we could observe a significant loss of amacrine cells in the S100B I group (65.71 ± 9.26%), compared to both control groups, PBS (95.91 ± 16.64%, p = 0.014) and native retinas (100.0 ± 10.2%, p = 0.0098, **Figure 4C**), after 21 days. This result was confirmed by Western blot analysis (**Figure 4D**). Calretinin signal was significantly reduced in the S100B I group (0.26 ± 0.06 units) compared to the PBS group (0.35 ± 0.043 units, p = 0.025) and to the native group (0.35 ± 0.03 units, p = 0.025; **Figure 4E**) at day 21.

Preserved Integrity of Bipolar Cells

To analyze a possible degeneration of other neurons of the INL, bipolar cells were examined on retina section with an antibody against PKCα, a specific marker for bipolar cells (**Figure 5A**). PKCα$^+$ cell counts did not show any alterations in the S100B I group at 14 (PBS: 100.47 ± 7.2%, S100B I: 86.47 ± 5.54%; p = 0.17, **Figure 5B**) and 21 days (PBS: 95.96 ± 9.32%, S100B I: 83.46 ± 10.21% p = 0.63, **Figure 5C**).

Analysis of Optic Nerve

Tendency of Slow Progressive Degeneration of Myelin Sheaths

We examined longitudinal optic nerve sections 3, 14 and 21 days after the intravitreal application of S100B. We labeled myelin sheaths with LFB (**Figure 6A**) to score the grade of demyelination. Intact myelin sheaths were noted at day 3 in the S100B I (0.37 ± 0.02, $p > 0.9$) and S100B II group (0.36 ± 0.04, $p > 0.9$) compared to the PBS (0.37 ± 0.02) and to the native group (0.34 ± 0.03, **Figure 6B**). Similar results could be seen at day 14. The myelin sheaths of the optic nerves showed no affect for both applied S100B concentrations (S100B I: 0.35 ± 0.16, $p > 0.8$, S100B II: 0.32 ± 0.13, $p > 0.9$, **Figure 6B**) when compared to the PBS group (0.27 ± 0.06) and to the native group (0.27 ± 0.04). After 21 days, a tendency to alteration of the optic nerve sheaths was noted in the S100B I group (0.96 ± 0.11) compared to the PBS group (0.66 ± 0.17, p = 0.22, **Figure 6B**). No differences to the native group were observed (0.64 ± 0.13, p = 0.38).

Progressive Destruction of Optic Nerve Neurofilaments

The labeling of neurofilaments with an antibody to SMI-32 was performed for a more specific evaluation of the optic nerve structure (**Figure 7A**). S100B induced damage to the neurofilaments from day 3 on (S100B I: 0.65 ± 0.09, p = 0.02, S100B II: 0.69 ± 0.06, p = 0.01) compared to the PBS group (0.34 ± 0.02). In comparison to the native group (0.35 ± 0.05) similar results were noticed in the S100B I (p = 0.03) and the S100B II group (p = 0.005, **Figure 7B**). These alterations of the SMI-32 stained structure were progressive. At 14 days, the integrity and structure of the neurofilaments in both S100B groups (S100B I: 0.99 ± 0.04, $p < 0.001$, S100B II: 0.99 ± 0.02, $p < 0.001$) was strongly degenerated in comparison to the PBS group (0.29 ± 0.04, **Figure 7B**). In comparison to the native group (0.24 ± 0.02), the neurofilament damage in both S100B groups was again very prominent (both: $p < 0.001$). We also examined the neurofilaments after 21 days, where the level of destruction remained stable (PBS: 0.42 ± 0.09, S100B I: 0.79 ± 0.06, p = 0.003). Comparison of the S100B I and native group (0.29 ± 0.05) showed a similar result in regard to the level of degeneration ($p < 0.001$, **Figure 7B**).

Furthermore, methylene blue stained optic nerve cross-sections were scored (**Figure 7C**). The structures of the native (1.77 ± 0.14) and the PBS group (1.99 ± 0.09, p = 0.7) were comparable. However, the S100B I injection (2.89 ± 0.26) increased the gliosis signs and the number of swollen axons compared to the PBS (p = 0.007) and native group (p = 0.001, **Figure 7D**). The density of intact axons decreased, especially in the middle part of the S100B I optic nerves.

DISCUSSION

The intravitreal injection of S100B led to an dose independent, but time-dependent degeneration of retina and optic nerve. At day 3, a slight damage of the optic nerve was noted, but the retina was not yet affected. Therefore, we assume the degeneration processes started in the optic nerve. Later, at day 14, RGCs and their axons were damaged via apoptotic mechanisms. However, the myelin fibers remained intact. At the later point in time, further progress of damage was observed. Amacrine cells were affected in the retina from day 21 on and also the optic nerve myeline sheath showed first signs of dissolution. In addition, increased IgG levels in the serum were noted later on.

Impact of S100B on the Retina

It is known that S100B affects neurons in a dose-dependent manner. In a cortical neuronal cell culture or in *in vitro* models, nanomolare doses of S100B protected neurons (Villarreal et al., 2011), while micromolare levels had deleterious effects (Donato, 2001). In our study, S100B was applied in two different doses, 400 nmol and 1 μmol. Both doses showed comparable destroying effects on RGCs in this rodent model. Hence, we did not observe any An dose-dependent effect and only used the lower S100B dose for further investigations.

Time-Dependent Damage of Retinal Ganglion Cells and Optic Nerve

In previous studies, a systemic immunization with S100B first induced a wallerian-like degeneration of the optic nerve (Noristani et al., 2016). Meaning, the axons are initially damaged, while the myelin structure remains intact (Saggu et al., 2010). In this EAG model, the decline of RGC numbers followed later on (Casola et al., 2015; Noristani et al., 2016). A similar degeneration progression was also observed in an ocular hypertension model (Son et al., 2010).

The initial site of damage in this new model is of great interest, since S100B was applied locally to the eye. With our novel

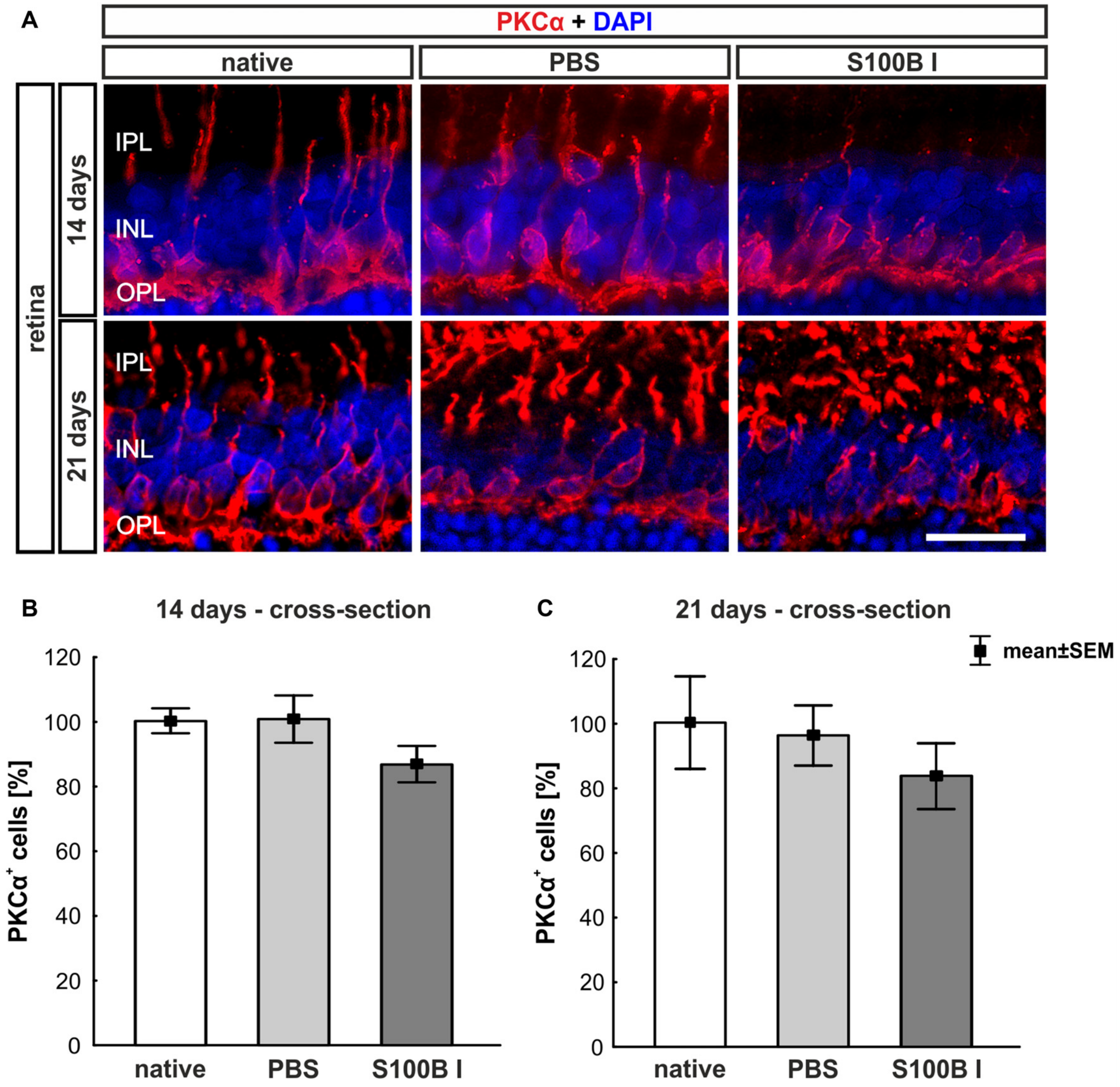

FIGURE 5 | No effect on bipolar cells. **(A)** Exemplary images of retinal cross-sections with bipolar cell (protein kinase Cα, PKCα, red) and cell nuclei (DAPI, blue) staining were shown. **(B)** The PKCα^+ cell count was comparable in all groups at day 14. **(C)** A similar result was seen at day 21. IPL, inner plexiform layer; INL, inner nuclear layer; OPL, outer plexiform layer; scale bar = 20 μm.

approach, we could also observe a wallerian-like degeneration of the optic nerve, which occurred earlier than the RGC loss. Also, other intravitreally applicated substances, like kainic acid, induce a wallerian-like degeneration of the optic nerve (Massoll et al., 2013). The intravitreal injection of TNF-α also led at first to an axon loss with a subsequent retrograde retinal cell body damage at later damage stages (Kitaoka et al., 2006). However, the intravitreal injection of other substances, such as N-methyl-D-aspartate (NMDA; Kuehn et al., 2017) first affected the structures of the retina, while the damage of the optic nerve was a consequence of the cell body loss in the retina.

One explanation for the different site of action for S100B could be that it is mainly expressed by astrocytes (Petrova et al., 2000; Ponath et al., 2007; Brozzi et al., 2009), which have their origin in the optic nerve (Holländer et al., 1991). The receptors or further binding structures for the other intravitreal injected substances are directly situated in the retina. However, both, RGCs and their axons, degenerated earlier in our study than in the EAG model. The intravitreal S100B injection acted directly and did not need to activate an immune response first, which takes more time. The late findings of elevated IgG levels in the serum undermine the conclusion that the intravitreal S100B injection did not trigger a systemic immune response by themself. A possible cause for the late systemic immune response in this new model could be the enhanced damage in retina and optic nerve, which

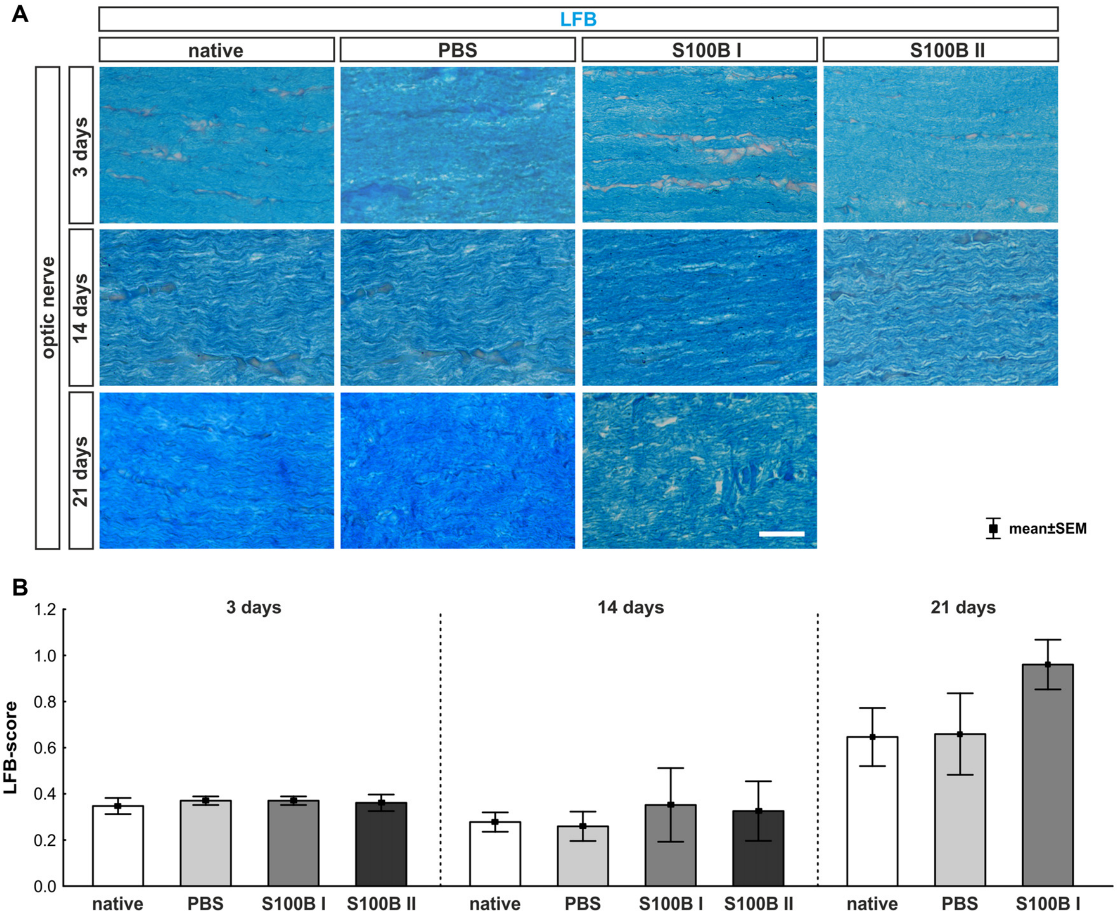

FIGURE 6 | Intact optic nerve myelin sheaths in all groups. **(A)** Luxol fast blue (LFB) was used to stain the optic nerve myelin sheath. **(B)** At day 3, the optic nerves did not show any degeneration. This was also observed at day 14. However, after 21 days, a trend towards an increased LFB score was recorded in the S100B I group when compared to the native group (p = 0.22), but not when compared to the PBS group. Scale bar = 20 μm.

then damaged the blood-retina barrier. A brake-down of this barrier was for example described for a ocular hypertension animal model (Trost et al., 2015). The blood-retina barrier usually controls the immigration of immune cells in the retina (Reichenbach and Bringmann, 2013). One of these cells are B-cells. To produce IgGs B-cells need a priming contact with the antigen and an antigen presenting cell (Janeway, 2002). A porous blood-retina barrier could led to this contact. Previous studys, using the EAG model, could detected alterations of the systemic auto-antibodies patterns (Joachim et al., 2009) and retinal IgG deposits (Joachim et al., 2012). It is postulated that the blood-retina barrier in patients is damaged during glaucoma and therefore auto-antibody pattern alterations were also be detected systemically (Joachim et al., 2005). Furthermore, IgG autoantibody accumulations and B-cells were observed in human retinas (Gramlich et al., 2013). Meaning, a strong retinal damage could trigger an immune response which strengthen the degeneration.

S100B is a protein which regulates the intracellular calcium level (Donaldson et al., 1995; Donato, 2001). Another intravitreally used molecule, which led to an influx of calcium ions in cells, is NMDA. It binds directly to the NMDA receptor, which opens the calcium channels in uncontrolled manner (Urushitani et al., 2001). S100B might bind to the receptor for advanced glycation endproducts (RAGE; Villarreal et al., 2011). In comparison, the degeneration progression through NMDA is faster than through S100B. One day after NMDA injection, RGCs began to degenerate (Manabe and Lipton, 2003) and after 3 days RGCs in the middle and peripheral part of the retina were lost (Kuehn et al., 2017). S100B needs more time for a similar damage pattern. We did not note degeneration signs at 3 days. At day 14, only the RGCs in the middle part of the retina were affected and then at day 21 all regions of the retina showed cell loss.

Only Inner Retinal Layers Were Affected

S100B is a protein, which is more associated with astrocytes than with Müller glia in the retina (Petrova et al., 2000; Brozzi et al., 2009). This could also be confirmed in our study. The astrocytes in this model were mostly located from the nerve

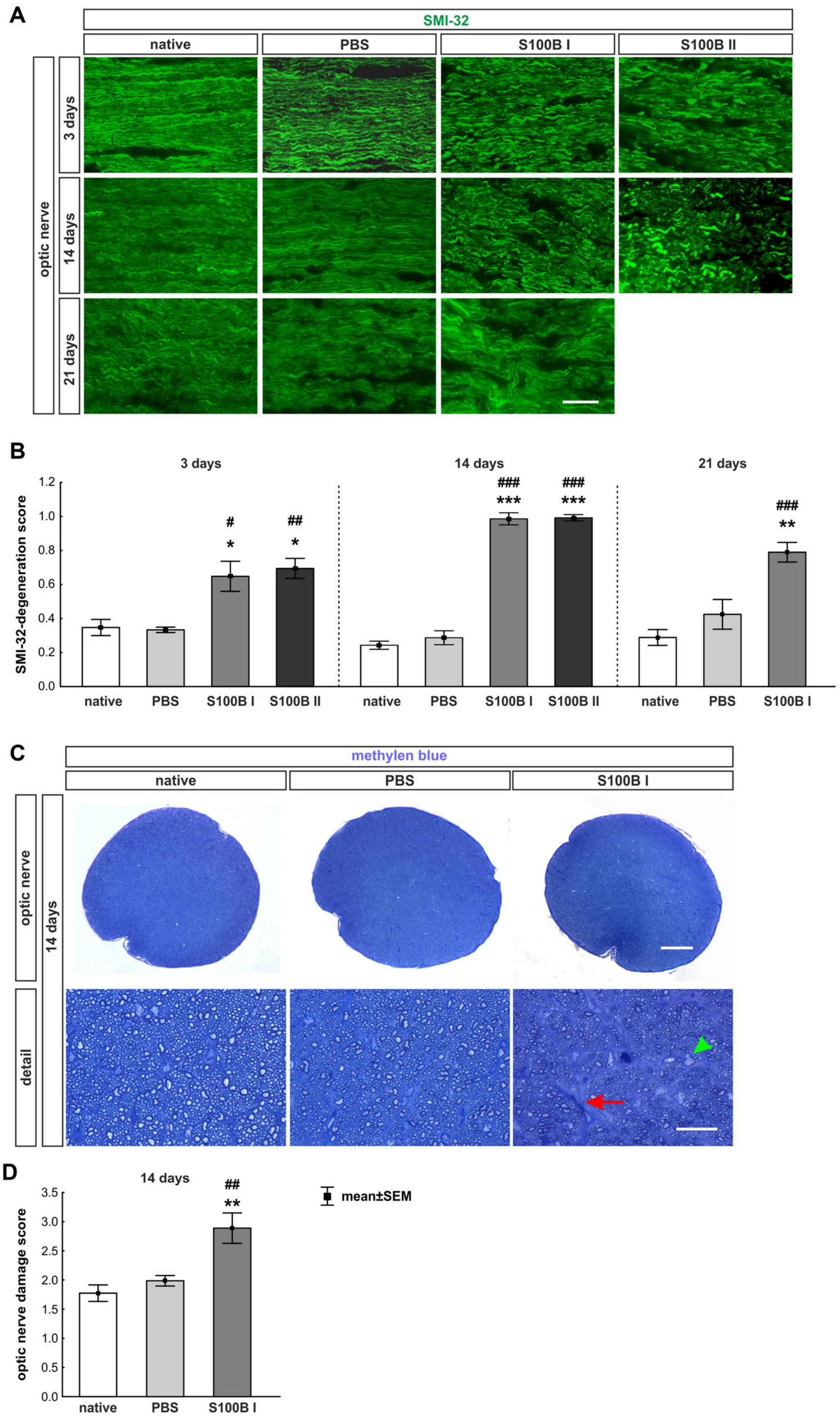

FIGURE 7 | S100B induced progressive degeneration of optic nerve neurofilaments. **(A)** We analyzed neurofilaments of longitudinal optic nerve sections at 3, 14 and 21 days with anti-SMI-32-antibody (green). **(B)** At day 3, the neurofilament showed a low grade of degeneration in the S100B I (PBS: $p = 0.02$, native: $p = 0.03$) and S100B II group (PBS: $p = 0.01$, native: $p = 0.005$). These degeneration signs aggravated after 14 days compared to PBS and native group (both controls: S100B I: $p < 0.001$, S100B II: $p < 0.001$). After 21 days, destruction of neurofilaments was stable in S100B I group in comparison to PBS ($p = 0.003$) and native group ($p < 0.001$). **(C)** In addition, methylene blue stained cross-sections were scored at day 14. **(D)** The S100B I optic nerves showed more gliosis and an increased number of swollen axons compared to the PBS ($p = 0.007$) and native group ($p = 0.001$). Scale bar: **(A)** = 20 μm, **(C)** = 100 μm, **(C)** detail = 20 μm, red arrow: gliosis, green arrow head: swollen axon; $^{*}p < 0.05$; $^{**}p < 0.01$; $^{***}p < 0.001$ (compared to PBS group); $^{\#}p < 0.05$; $^{\#\#}p < 0.01$; $^{\#\#\#}p < 0.001$ (compared to native group).

fiber layer (NFL) to the INL. These layers are the only layers, which were affected in the current study. Not only the RGC but also the amacrine cell number declined, while rod bipolar cell numbers remained stable. Possibly, the astrocytes were triggered in a destroying manner through the S100B application (Villarreal et al., 2014). Then, reactive astrocytes have a extensive molecular repertoire which were involved in all cellular aspects (Sofroniew, 2009). The amacrine cell number decline could also have another cause. Amacrine cells and RGCs are connected via gap junctions and they could transmit the cell death signal (Akopian et al., 2016). The time-cause of the cell loss in this model seems to confirm this assumption, since RGCs were affected from day 14 on and the amacrine cells later, at day 21. However, the functionality of the cells in the INL was alreadey negatively affected at day 14, before cell numbers decreased.

Time-Dependent Apoptotic Mechanisms

Apoptosis is an early hallmark of degeneration in retina damage models (Wang et al., 2005; Noristani et al., 2016). It is known that a high level of S100B can activate the caspase cascade (Donato, 2001). In this study, we noted an increase of cleaved caspase 3, a prominent apoptotic protein, at day 14, which can be induced via intrinsic and extrinsic apoptotic pathways (Nair et al., 2014). At day 21, we detected PARP-1, since this protein will be cleaved by the caspase 3 (D'Amours et al., 2001), which is a late apoptotic mechansism. We could measure a trend for a decline of PARP-1. These results are hints for terminated apoptotic processes at day 21.

CONCLUSION

We could demonstrate, for the first time, that a local, intravitreal injection of S100B leads to glaucoma like damage. Although the application site was the eye, the optic nerve degenerated first, already at day 3. From day 14 on, retinal damage was noted. The RGCs in the middle part of the retina were first affected. At day 21, the damage expanded. RGCs and amacrine cells degenerated in all parts of the retina. Thence, S100B had a direct destroying impact on the axons of the optic nerve, which then led to the damage of the retinal cell bodies.

AUTHOR CONTRIBUTIONS

SK designed the study, carried out experiments, performed statistical analyses, drafted the manuscript and generated graphics. WM carried out experiments, performed statistical analyses and revised the manuscript. PG carried out experiments and generated graphics. CT carried out experiments and revised the manuscript. HD revised the manuscript. SJ designed the study and drafted the manuscript. All authors read and approved the final manuscript.

FUNDING

This project was supported by the Ernst und Berta Grimmke Stiftung.

ACKNOWLEDGMENTS

We thank Mrs. Claudia Grzelak for excellent technical support.

SUPPLEMENTARY MATERIAL

The Supplementary Material for this article can be found online at: https://www.frontiersin.org/articles/10.3389/fncel.2018.00312/full#supplementary-material

FIGURE S1 | RGC density in different flatmount regions. **(A)** At day 3, the RGC numbers in all three regions, peripheral, middle and central of S100B flatmounts were comparable to the PBS and native group. **(B)** At day 14, RGC loss was noted in the middle part of the retina compared to the PBS (S100B I: $p = 0.009$, S100B II: $p = 0.002$) and native group (S100B I: $p = 0.02$, S100B II: $p = 0.002$). $^{**}p < 0.01$ (compared to PBS group), $^{\#}p < 0.05$, $^{\#\#}p < 0.01$ (compared to native group).

REFERENCES

Akopian, A., Kumar, S., Ramakrishnan, H., Viswanathan, S., and Bloomfield, S. A. (2016). Amacrine cells coupled to ganglion cells via gap junctions are highly vulnerable in glaucomatous mouse retinas. *J. Comp. Neurol.* doi: 10.1002/cne.24074 [Epub ahead of print].

Biermann, J., van Oterendorp, C., Stoykow, C., Volz, C., Jehle, T., Boehringer, D., et al. (2012). Evaluation of intraocular pressure elevation in a modified laser-induced glaucoma rat model. *Exp. Eye Res.* 104, 7–14. doi: 10.1016/j.exer.2012.08.011

Brozzi, F., Arcuri, C., Giambanco, I., and Donato, R. (2009). S100B protein regulates astrocyte shape and migration via interaction with Src kinase: implications for astrocyte development, activation, and tumor growth. *J. Biol. Chem.* 284, 8797–8811. doi: 10.1074/jbc.M805897200

Casola, C., Schiwek, J. E., Reinehr, S., Kuehn, S., Grus, F. H., Kramer, M., et al. (2015). S100 alone has the same destructive effect on retinal ganglion cells as in combination with HSP 27 in an autoimmune glaucoma model. *J. Mol. Neurosci.* 56, 228–236. doi: 10.1007/s12031-014-0485-2

D'Amours, D., Sallmann, F. R., Dixit, V. M., and Poirier, G. G. (2001). Gain-of-function of poly(ADP-ribose) polymerase-1 upon cleavage by apoptotic proteases: implications for apoptosis. *J. Cell Sci.* 114, 3771–3778.

Donaldson, C., Barber, K. R., Kay, C. M., and Shaw, G. S. (1995). Human S100b protein: formation of a tetramer from synthetic calcium-binding site peptides. *Protein Sci.* 4, 765–772. doi: 10.1002/pro.5560040416

Donato, R. (2001). S100: a multigenic family of calcium-modulated proteins of the EF-hand type with intracellular and extracellular functional roles. *Int. J. Biochem. Cell Biol.* 33, 637–668. doi: 10.1016/s1357-2725(01)00046-2

Dreyer, E. B., Zurakowski, D., Schumer, R. A., Podos, S. M., and Lipton, S. A. (1996). Elevated glutamate levels in the vitreous body of humans and monkeys with glaucoma. *Arch. Ophthalmol.* 114, 299–305. doi: 10.1001/archopht.1996.01100130295012

EGS. (2017). European glaucoma society terminology and guidelines for glaucoma, 4th edition—chapter 2: classification and terminology supported by the EGS foundation part 1: foreword; introduction; Glossary; Chapter 2 classification and terminology. *Br. J. Ophthalmol.* 101, 73–127. doi: 10.1136/bjophthalmol-2016-egsguideline.002

Goncalves, D. S., Lenz, G., Karl, J., Goncalves, C. A., and Rodnight, R. (2000). Extracellular S100B protein modulates ERK in astrocyte cultures. *Neuroreport* 11, 807–809. doi: 10.1097/00001756-200003200-00030

Gramlich, O. W., Beck, S., von Thun Und Hohenstein-Blaul, N., Boehm, N., Ziegler, A., Vetter, J. M., et al. (2013). Enhanced insight into the autoimmune component of glaucoma: IgG autoantibody accumulation and pro-inflammatory conditions in human glaucomatous retina. *PLoS One* 8:e57557. doi: 10.1371/journal.pone.0057557

Griffin, W. S., Stanley, L. C., Ling, C., White, L., MacLeod, V., Perrot, L. J., et al. (1989). Brain interleukin 1 and S-100 immunoreactivity are elevated in Down syndrome and Alzheimer disease. *Proc. Natl. Acad. Sci. U S A* 86, 7611–7615. doi: 10.1073/pnas.86.19.7611

Grus, F. H., Boehm, N., Beck, S., Schlich, M., Lossbrandt, U., and Pfeiffer, N. (2010). Autoantibody profiles in tear fluid as a diagnostic tool in glaucoma. *Invest. Ophthalmol. Vis. Sci.* 51:6110.

Grus, F. H., Joachim, S. C., Hoffmann, E. M., and Pfeiffer, N. (2004). Complex autoantibody repertoires in patients with glaucoma. *Mol. Vis.* 10, 132–137.

Holländer, H., Makarov, F., Dreher, Z., van Driel, D., Chan-Ling, T. L., and Stone, J. (1991). Structure of the macroglia of the retina: sharing and division of labour between astrocytes and Müller cells. *J. Comp. Neurol.* 313, 587–603. doi: 10.1002/cne.903130405

Horstmann, L., Schmid, H., Heinen, A. P., Kurschus, F. C., Dick, H. B., and Joachim, S. C. (2013). Inflammatory demyelination induces glia alterations and ganglion cell loss in the retina of an experimental autoimmune encephalomyelitis model. *J. Neuroinflammation* 10:120. doi: 10.1186/1742-2094-10-120

Huttunen, H. J., Kuja-Panula, J., Sorci, G., Agneletti, A. L., Donato, R., and Rauvala, H. (2000). Coregulation of neurite outgrowth and cell survival by amphoterin and S100 proteins through receptor for advanced glycation end products (RAGE) activation. *J. Biol. Chem.* 275, 40096–40105. doi: 10.1074/jbc.M006993200

Ikeda, Y., Maruyama, I., Nakazawa, M., and Ohguro, H. (2002). Clinical significance of serum antibody against neuron-specific enolase in glaucoma patients. *Jpn. J. Ophthalmol.* 46, 13–17. doi: 10.1016/s0021-5155(01)00455-5

Janeway, C. A. (Ed.). (2002). *Immunologie.* Heidelberg, Berling: Spektrum Verlag.

Joachim, S. C., Bruns, K., Lackner, K. J., Pfeiffer, N., and Grus, F. H. (2007). Antibodies to α B-crystallin, vimentin and heat shock protein 70 in aqueous humor of patients with normal tension glaucoma and IgG antibody patterns against retinal antigen in aqueous humor. *Curr. Eye Res.* 32, 501–509. doi: 10.1080/02713680701375183

Joachim, S. C., Gramlich, O. W., Laspas, P., Schmid, H., Beck, S., von Pein, H. D., et al. (2012). Retinal ganglion cell loss is accompanied by antibody depositions and increased levels of microglia after immunization with retinal antigens. *PLoS One* 7:e40616. doi: 10.1371/journal.pone.0040616

Joachim, S. C., Grus, F. H., Kraft, D., White-Farrar, K., Barnes, G., Barbeck, M., et al. (2009). Complex antibody profile changes in an experimental autoimmune glaucoma animal model. *Invest. Ophthalmol. Vis. Sci.* 50, 4734–4742. doi: 10.1167/iovs.08-3144

Joachim, S. C., Pfeiffer, N., and Grus, F. H. (2005). Autoantibodies in patients with glaucoma: a comparison of IgG serum antibodies against retinal, optic nerve, and optic nerve head antigens. *Graefes Arch. Clin. Exp. Ophthalmol.* 243, 817–823. doi: 10.1007/s00417-004-1094-5

Kitaoka, Y., Kitaoka, Y., Kwong, J. M., Ross-Cisneros, F. N., Wang, J., Tsai, R. K., et al. (2006). TNF-α-induced optic nerve degeneration and nuclear factor-kappaB p65. *Invest. Ophthalmol. Vis. Sci.* 47, 1448–1457. doi: 10.1167/iovs.05-0299

Krause, M., Brune, M., and Theiss, C. (2016). Preparation of human formalin-fixed brain slices for electron microscopic investigations. *Ann. Anat.* 206, 27–33. doi: 10.1016/j.aanat.2016.04.030

Kremmer, S., Kreuzfelder, E., Klein, R., Bontke, N., Henneberg-Quester, K. B., Steuhl, K. P., et al. (2001). Antiphosphatidylserine antibodies are elevated in normal tension glaucoma. *Clin. Exp. Immunol.* 125, 211–215. doi: 10.1046/j.1365-2249.2001.01578.x

Kuehn, S., Rodust, C., Stute, G., Grotegut, P., Meißner, W., Reinehr, S., et al. (2017). Concentration-dependent inner retina layer damage and optic nerve degeneration in a NMDA model. *J. Mol. Neurosci.* 63, 283–299. doi: 10.1007/s12031-017-0978-x

Luft, J. H. (1961). Improvements in epoxy resin embedding methods. *J. Biophys. Biochem. Cytol.* 9, 409–414. doi: 10.1083/jcb.9.2.409

Manabe, S., and Lipton, S. A. (2003). Divergent NMDA signals leading to proapoptotic and antiapoptotic pathways in the rat retina. *Invest. Ophthalmol. Vis. Sci.* 44, 385–392. doi: 10.1167/iovs.02-0187

Marenholz, I., Lovering, R. C., and Heizmann, C. W. (2006). An update of the S100 nomenclature. *Biochim. Biophys. Acta* 1763, 1282–1283. doi: 10.1016/j.bbamcr.2006.07.013

Maruyama, I., Ohguro, H., and Ikeda, Y. (2000). Retinal ganglion cells recognized by serum autoantibody against γ-enolase found in glaucoma patients. *Invest. Ophthalmol. Vis. Sci.* 41, 1657–1665.

Massoll, C., Mando, W., and Chintala, S. K. (2013). Excitotoxicity upregulates SARM1 protein expression and promotes Wallerian-like degeneration of retinal ganglion cells and their axons. *Invest. Ophthalmol. Vis. Sci.* 54, 2771–2780. doi: 10.1167/iovs.12-10973

Nair, P., Lu, M., Petersen, S., and Ashkenazi, A. (2014). Apoptosis initiation through the cell-extrinsic pathway. *Methods Enzymol.* 544, 99–128. doi: 10.1016/b978-0-12-417158-9.00005-4

Noristani, R., Kuehn, S., Stute, G., Reinehr, S., Stellbogen, M., Dick, H. B., et al. (2016). Retinal and optic nerve damage is associated with early glial responses in an experimental autoimmune glaucoma model. *J. Mol. Neurosci.* 58, 470–482. doi: 10.1007/s12031-015-0707-2

Pang, I. H., and Clark, A. F. (2007). Rodent models for glaucoma retinopathy and optic neuropathy. *J. Glaucoma* 16, 483–505. doi: 10.1097/ijg.0b013e3181405d4f

Petrova, T. V., Hu, J., and Van Eldik, L. J. (2000). Modulation of glial activation by astrocyte-derived protein S100B: differential responses of astrocyte and microglial cultures. *Brain Res.* 853, 74–80. doi: 10.1016/s0006-8993(99)02251-9

Ponath, G., Schettler, C., Kaestner, F., Voigt, B., Wentker, D., Arolt, V., et al. (2007). Autocrine S100B effects on astrocytes are mediated via RAGE. *J. Neuroimmunol.* 184, 214–222. doi: 10.1016/j.jneuroim.2006.12.011

Reichenbach, A., and Bringmann, A. (2013). New functions of Muller cells. *Glia* 61, 651–678. doi: 10.1002/glia.22477

Reinehr, S., Kuehn, S., Casola, C., Koch, D., Stute, G., Grotegut, P., et al. (2018). HSP27 immunization reinforces AII amacrine cell and synapse damage induced by S100 in an autoimmune glaucoma model. *Cell Tissue Res.* 371, 237–249. doi: 10.1007/s00441-017-2710-0

Rothermundt, M., Missler, U., Arolt, V., Peters, M., Leadbeater, J., Wiesmann, M., et al. (2001). Increased S100B blood levels in unmedicated and treated schizophrenic patients are correlated with negative symptomatology. *Mol. Psychiatry* 6, 445–449. doi: 10.1038/sj.mp.4000889

Rothermundt, M., Peters, M., Prehn, J. H., and Arolt, V. (2003). S100B in brain damage and neurodegeneration. *Microsc. Res. Tech.* 60, 614–632. doi: 10.1002/jemt.10303

Saggu, S. K., Chotaliya, H. P., Blumbergs, P. C., and Casson, R. J. (2010). Wallerian-like axonal degeneration in the optic nerve after excitotoxic retinal insult: an ultrastructural study. *BMC Neurosci.* 11:97. doi: 10.1186/1471-2202-11-97

Santamaria-Kisiel, L., Rintala-Dempsey, A. C., and Shaw, G. S. (2006). Calcium-dependent and -independent interactions of the S100 protein family. *Biochem. J.* 396, 201–214. doi: 10.1042/bj20060195

Schmid, H., Renner, M., Dick, H. B., and Joachim, S. C. (2014). Loss of inner retinal neurons after retinal ischemia in rats. *Invest. Ophthalmol. Vis. Sci.* 55, 2777–2787. doi: 10.1167/iovs.13-13372

Sofroniew, M. V. (2009). Molecular dissection of reactive astrogliosis and glial scar formation. *Trends Neurosci.* 32, 638–647. doi: 10.1016/j.tins.2009.08.002

Son, J. L., Soto, I., Oglesby, E., Lopez-Roca, T., Pease, M. E., Quigley, H. A., et al. (2010). Glaucomatous optic nerve injury involves early astrocyte reactivity and late oligodendrocyte loss. *Glia* 58, 780–789. doi: 10.1002/glia.20962

Tezel, G., Seigel, G. M., and Wax, M. B. (1998). Autoantibodies to small heat shock proteins in glaucoma. *Invest. Ophthalmol. Vis. Sci.* 39, 2277–2287.

Tezel, G., Yang, X., Luo, C., Kain, A. D., Powell, D. W., Kuehn, M. H., et al. (2010). Oxidative stress and the regulation of complement activation in human glaucoma. *Invest. Ophthalmol. Vis. Sci.* 51, 5071–5082. doi: 10.1167/iovs.10-5289

Trost, A., Motloch, K., Bruckner, D., Schroedl, F., Bogner, B., Kaser-Eichberger, A., et al. (2015). Time-dependent retinal ganglion cell loss, microglial activation and blood-retina-barrier tightness in an acute model of ocular hypertension. *Exp. Eye Res.* 136, 59–71. doi: 10.1016/j.exer.2015.05.010

Urushitani, M., Nakamizo, T., Inoue, R., Sawada, H., Kihara, T., Honda, K., et al. (2001). N-methyl-D-aspartate receptor-mediated mitochondrial Ca^{2+} overload in acute excitotoxic motor neuron death: a mechanism distinct from chronic neurotoxicity after Ca^{2+} influx. *J. Neurosci. Res.* 63, 377–387. doi: 10.1002/1097-4547(20010301)63:5<377::aid-jnr1032>3.0.co;2-#

Villarreal, A., Aviles Reyes, R. X., Angelo, M. F., Reines, A. G., and Ramos, A. J. (2011). S100B alters neuronal survival and dendrite extension via RAGE-mediated NF-kappaB signaling. *J. Neurochem.* 117, 321–332. doi: 10.1111/j.1471-4159.2011.07207.x

Villarreal, A., Seoane, R., González Torres, A., Rosciszewski, G., Angelo, M. F., Rossi, A., et al. (2014). S100B protein activates a RAGE-dependent autocrine loop in astrocytes: implications for its role in the propagation of reactive gliosis. *J. Neurochem.* 131, 190–205. doi: 10.1111/jnc.12790

Wang, X., Ng, Y. K., and Tay, S. S. (2005). Factors contributing to neuronal degeneration in retinas of experimental glaucomatous rats. *J. Neurosci. Res.* 82, 674–689. doi: 10.1002/jnr.20679

Yang, J., Tezel, G., Patil, R. V., Romano, C., and Wax, M. B. (2001). Serum autoantibody against glutathione S-transferase in patients with glaucoma. *Invest. Ophthalmol. Vis. Sci.* 42, 1273–1276.

Yu, S. W., Andrabi, S. A., Wang, H., Kim, N. S., Poirier, G. G., Dawson, T. M., et al. (2006). Apoptosis-inducing factor mediates poly(ADP-ribose) (PAR) polymer-induced cell death. *Proc. Natl. Acad. Sci. U S A* 103, 18314–18319. doi: 10.1073/pnas.0606528103

Conflict of Interest Statement: The authors declare that the research was conducted in the absence of any commercial or financial relationships that could be construed as a potential conflict of interest.

The reviewer TA and the handling Editor declared their shared affiliation, at the time of the review.

frontiers
in Cellular Neuroscience

ORIGINAL RESEARCH
published: 26 March 2019
doi: 10.3389/fncel.2019.00036

A Space-Variant Visual Pathway Model for Data Efficient Deep Learning

*Piotr Ozimek, Nina Hristozova, Lorinc Balog and Jan Paul Siebert**

Computer Vision for Autonomous Systems Group, School of Computing Science, University of Glasgow, Glasgow, United Kingdom

We present an investigation into adopting a model of the retino-cortical mapping, found in biological visual systems, to improve the efficiency of image analysis using Deep Convolutional Neural Nets (DCNNs) in the context of robot vision and egocentric perception systems. This work has now enabled DCNNs to process input images approaching *one million pixels* in size, *in real time*, using only consumer grade graphics processor (GPU) hardware *in a single pass of the DCNN*.

Keywords: data efficiency, deep learning, retina, foveated vision, biological vision, egocentric perception, robot vision, visual cortex

Edited by:
Bela Volgyi,
University of Pécs, Hungary

Reviewed by:
Garrett T. Kenyon,
Los Alamos National Laboratory (DOE), United States
Zsolt Kisander,
University of Pécs, Hungary

****Correspondence:***
Jan Paul Siebert
paul.siebert@glasgow.ac.uk

Received: *29 September 2018*
Accepted: *23 January 2019*
Published: *26 March 2019*

Citation:
Ozimek P, Hristozova N, Balog L and Siebert JP (2019) A Space-Variant Visual Pathway Model for Data Efficient Deep Learning. Front. Cell. Neurosci. 13:36. doi: 10.3389/fncel.2019.00036

1. INTRODUCTION

Deep Learning methods have revolutionised signal and image analysis, and indeed end-to-end approaches to training these networks can achieve the state-of-the-art in vision-based control (Viereck et al., 2017; Morrison et al., 2018) and recognition for robotics. However, a real obstacle to the practical adoption of DCNNs is their requirement for very large training data sets and their inability to scale to process image matrices of greater than approximately 300 × 300 px in a single pass. We address this issue directly by adopting a computational model of the space-variant, i.e., *foveated,* visual processing architecture found in the mammalian vision system (Schwartz, 1977). Our 50K node retina-preprocessor enables current DCNN networks to process input images of 930×930px in size, using only consumer grade graphics processor (GPU) hardware, *in a single pass of the DCNN* and this retina pre-processing approach has the potential to scale to accommodate larger input image sizes. In addition, this pre-processor mapping confers a degree of scale and rotation invariance to the transformed images facilitating a number of perception tasks, reducing the parameter size and computation required to train a DCNN.

The above visual processing limitations of current DCNN implementations appear to have been addressed effectively in biological vision systems. The visual pathway from the retina to V1 itself implements space variant sampling in the retina to afford a very substantial data reduction and also a key spatial transformation, the retino-cortical mapping (Schwartz, 1980). This transformation affords a number of additional signal simplifications, including a degree of scale and rotation invariance.

In this paper we present a retina-DCNN pipeline that confirms our hypothesis that DCNNs are capable of learning in *cortical-space* and undertaking inferences in a single pass of this space. We detail the results of experiments that confirm it is possible to harness simple functional computational models of the space-variant retino-cortical mapping to improve the efficiency of DCNNs and demonstrate combining our latest functional retina models with this mapping. Accordingly, by applying a model of the retino-cortical transform, as a pre-processing step, to produce a much smaller *cortical image*, current DCNNS are capable of processing, in a single pass, cortical images generated from retina input images of the order of one million pixels. The above efficiency improvement, and those predicted for the other known processing transformations in the visual pathway, appear to have the potential to solve many of the data efficiency issues in adopting DCNNs in practice.

Within the retina itself, opponent ganglion cells compute a colour space potentially capable of simplifying tasks such as texture perception and contour detection. Motivated by this signal simplification property, we present a GPU accelerated high resolution software retina implementation that incorporates basic models of opponent colour and intensity P-pathway ganglion cells.

In addition to the above contributions, we outline a number of practical examples of the utility of the retina-DCNN combination: an egocentric perception system based on human eye-tracking to provide retina gaze control for training and object recognition, pan-tilt control of a robot wrist-mounted camera, retina enabled camera interfaces and retina data management tools.

We now overview the relevant properties of early mammalian visual pathway and the retino-cortical mapping that are relevant to supporting efficient visual computations, in the next section.

2. PRIOR RESEARCH IN RETINO-CORTICAL MAPPING MODELS OF THE VISUAL PATHWAY

2.1. The Mammalian Vision System

Any perceived light entering the eye-ball stimulates a hemispherical layer of photoreceptor cells. These cells are densely packed in the central *foveal* region of the retina and are more sparsely distributed in its peripheries (Curcio et al., 1990). Of the two types of photoreceptor cells, rods & cones, we have only considered the cones which facilitate *photopic* colour vision and discern fine detail. Since the rods are not present in the fovea, we have not investigated the rod pathway within the scope of this work which focuses on robot vision systems.

The signals produced by the photoreceptor cells are sequentially pre-processed through up to four different neuron types before exiting the retina and reaching the brain. It is important to note that the typologies of these intermediate retinal neurons coarsely follow the foveated topology of photoreceptor cells, i.e., are held in retinotopic registration, and that it is these topologies combined with visual attention mechanisms that enable the retina to control the rate of visual information passed onto the brain, Curcio and Allen (1990). It has been estimated (Schwartz, 1993), that if our eyes sampled our whole field of view at the foveal resolution, our visual cortex would have to be larger by several orders of magnitude to accommodate this computational load.

An important feature of the retina's neural architecture is the concept of *receptive fields*. The final intermediate retinal neurons that relay the visual signal to the brain are called retinal ganglion cells (RGCs), and most of them receive information from multiple neighboring photoreceptor cells through intra-retinal pathways. Those local clusters of photoreceptor cells comprise the RGC's receptive field. The sizes of these receptive fields increase with the distance (*eccentricity*) from the fovea, with the foveal RGCs only relaying information from individual photoreceptor cells (Hubel et al., 1995). Different RGCs have receptive fields of different response profiles depending on their specific function, which can range from discerning detail to computing the magnitude of differential motion (Ölveczky et al., 2003, 2007). Our basic retino-cortical mapping work is presented in the next section and more detailed RGC models are also presented in section 6.1.

2.2. The Retino-Cortical Transform

The RGCs pass the visual signal from the retina to the primary visual cortex (*V1*). The signal from each eyeball is split into two halves and each half is projected separately via a structure known as the Lateral Geniculate Nucleus (LGN) onto each hemisphere in V1, where it is can be observed as a form of spatial complex logarithmic mapping, similar to that in **Figure 1**, Left. This mapping appears to be the format in which our brains process vision and it could potentially be one of the mechanisms that facilitate scale invariance in biological vision systems (Schwartz, 1977).

The key phenomenon that Schwartz models in **Figure 1**, Left above is *cortical magnification*. The densely sampled fovea achieves the effect of appearing to be magnified in the cortex when compared the retina periphery, which appears to be progressively compressed as a function of retinal eccentricity. This of course reflects the photoreceptor sampling density within the retina beyond the fovea, which decreases exponentially.

The above also gives rise to the data-reduction property of the retino-cortical mapping and hence its resultant data efficiency. In *O* notation used to specify computational complexity, i.e., *order of*, a uniform areal sampling of the retina would require $O(r^2)$ receptive fields while a log-polar mapping reduces this to $O(r)$, (Wilson and Hodgson, 1992). Indeed if we consider the number of receptive fields required to sample a *contour* this becomes *constant* (Wilson, 1983, 1985). As a consequence, the space-variant structure of the retina provides foveal full resolution and the ability for a human to "thread a needle", while simultaneously monitoring ~180° (combined binocular vision) of the environment. In effect nature has equipped us with a static "zoom lens".

Schwartz (1980), proposed that the retinal samples are mapped to the cortex via a form of log-polar mapping. A number of further perceptual gains arise from the above architecture: a *pure* log-polar mapping, Equations 1, 2, results in a local edge contour segment translating along the θ axis under input rotation about a fixation point, while scale change centred on the fixation point causes a local contour segment to translate along the ρ cortical axis. In addition, peripheral objects located on a common ground plane (with respect to an observer) also retain their local shape appearance, i.e., exhibit projective invariance in the cortex. These three invariance properties are illustrated in **Figure 1**, Right (for a log (z+1) cortical mapping) and are referred to as *edge invariance*, since the *conformal* log-polar mapping only preserves

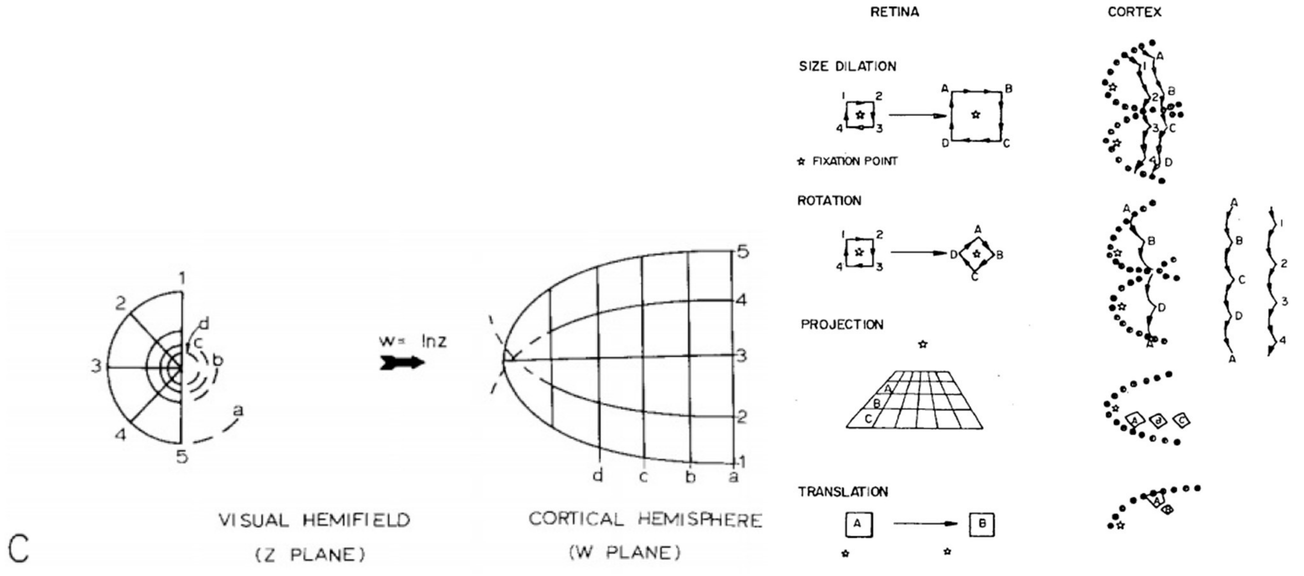

FIGURE 1 | Left: Global retinotopic mapping (Schwartz, 1977); **Right**: Scale rotation and projection invariance for a log(z+1) cortical mapping, taken from Schwartz (1980).

local angles, and the local shape of the contour, but not its global shape. However, this architectural organisation is clearly of significance in terms of scale, rotation and projective invariance for feature descriptors operating over the whole cortical field (Wilson and Hodgson, 1992), and likewise offers potential utility for the interpretation of stereopsis and texture perception in the striate cortex (Schwartz, 1981).

Unfortunately, a pure log-polar transform gives rise to a non-uniform fovea and a sampling density singularity at the centre of the fovea. In order to avert this topological crisis, Schwartz proposed that a small constant, α, be introduced to the horizontal mapping axis, Equations 4–7. When α is small compared to the horizontal Field of View (FoV), the fovea then becomes approximately linear (i.e., shift invariant) in sampling and the periphery approximates a log-polar mapping. This mechanism also gives rise naturally to the split in the retinal vertical meridian observed in the mammalian eye-brain mapping, as described in Equations (6, 7), and illustrated in **Figure 5**. While the mapping no longer produces a purely orthogonal output map in response to scale input transformations, the effect of such input changes is to produce a smoothly continuous warp of input contours along streamlines in cortical space. Accordingly, the continuity of these transformations still reduces the size of the cortical pattern space that any subsequent perceptual system must learn to accommodate invariance to input scale and rotation changes.

Further implications can be found for interpreting egocentric optical flow fields, where time-to-impact can be read directly from the ρ axis on the cortex and deviation from a horizontal flow field can be interpreted as being due to the presence of non-stationary objects in the FoV (Rojer and Schwartz, 1990).

Schwartz (1980) also demonstrates how his complex-log mapping can be used to explain the cortical magnifications observed in a number of mammalian species. Johnson (1986, 1989) extends Schwartz's analysis by demonstrating that the 3D nature of retina and cortex that should be taken into account in order to explain fully the mapping and confirms this hypothesis with biological data. However, Johnson's extended mapping is beyond the scope of this paper.

The foveated nature of the mammalian visual architecture also impacts visual search, affording an "attentional spotlight" that suppresses extraneous details while retaining pertinent diagnostic image features, e.g., one recognises an individual from the gross structural features of their face, as opposed the detailed arrangement of their skin pores or strands of their hair. Hence, full visual acuity is directed by the visual system to interrogate the scene where required, while gross structural features provide both context and the necessary diagnostic information for visual interpretation of the scene, and specific items, or regions, within it. In an earlier implementation of the retina described here based on the use of SIFT (Scale Invariant Feature Transform) (Lowe, 2004), visual descriptors for image matching, we found that the retina actually improved recognition rates over the use of SIFT processing at full-resolution. We attribute this result to the retina smoothing out irrelevant detail, when it is directed to classify diagnostic locations (Ram and Siebert, 2011).

2.3. Functional Retina Models

Commencing with the pioneering work by Schwartz and his contemporaries, many implementations of vision systems have been reported which adopt log-polar mappings (for example: Weiman, 1988; Bolduc and Levine, 1997; Gomes, 2002; Balasuriya and Siebert, 2006). A relatively recent example of a space-variant vision system was proposed by Pamplona and Bernardino (2009) who devised a method of generating foveated images using overlapping Gaussian receptive fields and a technique for performing conventional image processing functions on such images using matrix operations. This work makes a strong case for using Gaussian receptive fields rather than superpixels as an accurate and computationally efficient way of performing retinal sampling, although the resultant images produced by their method suffer from a number of artefacts.

We have based our work on an earlier retina model developed by Balasuriya (2006) which also employs Gaussian receptive fields. Balasuriya reports a complete vision system based on a self-organised software retina that combines mechanisms for retina tessellation generation, retina sampling, feature extraction and gaze control, Balasuriya and Siebert (2003, 2006). The output from this retina was originally processed using SIFT-like descriptors and directed by means of a SIFT keypoint based gaze control system and is now processed using DCNNs in the work reported here.

2.3.1. Balasuriya's Retina

A central issue is how to generate a retina tessellation in such a way that no local discontinuities, distortions or other artefacts are produced when making a transition between the retina's quasi-uniform fovea and its log-polar periphery. To solve this problem Balasuriya employs a self-similar neural network (Clippingdale and Wilson, 1996). This method relies on a network of N units jointly undergoing random translations to produce a tessellation with a near-uniform dense foveal region that seamlessly transitions into a sparse periphery, **Figure 2**, Left. Each node in the resultant tessellation defines the location of a receptive field's centre. The receptive fields somewhat follow the biological retina's architecture; they all have a Gaussian response profile the standard deviation of which scales linearly as a function of local node density, which in turn scales statistically with eccentricity, **Figure 2**, Right, due to the stochastic nature of the tessellation. This scaling balances between introducing aliasing at the sparsely sampled peripheries and super-Nyquist sampling at the densely sampled foveal region. Since the receptor scaling varies locally with node density it is possible to have receptive fields at the same eccentricity with slightly different field diameters, as found in nature, to avoid "holes" in the receptor layout.

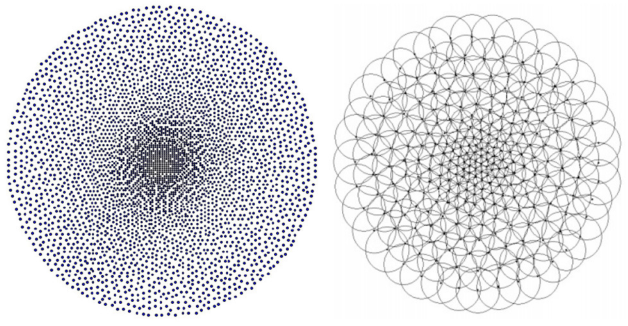

FIGURE 2 | Left: The 4196 node tessellation used in this paper. **Right:** Gaussian receptive fields on top of a retina tessellation, taken from Balasuriya (2006).

The values sampled by the receptive fields are stored in an *imagevector*, which is essentially a one-dimensional array of intensity values. After defining the retina in Balasuriya (2006), a scale-space retina pyramid is presented which is used to extract corner-based saliency information that drives the gaze control mechanism. The saliency information is extracted from the receptive fields, stored in imagevector format, and then back-projected onto the saliency map which is then normalised based on the Gaussian field intensity. An inhibition-of-return map employing a similar mechanism has been adopted to prevent the retina from continuously fixating upon the same location. Having computed the saliency map, the retina saccades to the location with the highest value of the difference between the saliency map and the inhibition-of-return map and the whole process is repeated for each retina fixation that follows. The work presented here is based on an improved version of Balasuriya's retina implementation and conceptual aspects of his gaze control mechanism.

2.4. A 4196 Node Retina Implementation

Our first attempt at coupling the software retina described in section 2.3.1 to a DCNN utilised a tessellation comprising $N = 4,196$ nodes, for $r_{fov} = 0.1$, and required $N_{iter} = 20,000$ iterations to stabilise, **Figure 2**, Left and is defined by the following tessellation parameters:

- N - number of nodes in the retina tessellation
- r_{fov} - the fovea's radius as a fraction of the tessellation's radius.
- N_{iter} - number of iterations for self-organisation of the self-similar neural network, used in generating the retina tessellation.

Receptive field parameters:

- $dist_5$ - the mean pixel distance of the 5 central foveal nodes to their 5 closest neighbors
- σ_{base} - base standard deviation of the Gaussian receptive fields
- σ_{ratio} - the eccentricity scaling factor of the Gaussian receptive fields' standard deviation

While the generated tessellation does not exhibit obvious classical log-polar spirals, due to the stochastic nature of its production, In **Figure 2**, Left, we can observe that, at least subjectively, the annealed retinal tessellation appears similar to the spatial distribution of cone receptors in the human retina itself (Sawides et al., 2016). Regarding the locally random nature of the retina tessellation, has been reported that the stochastic, non-uniform placement of retina photoreceptors appears to contribute to the image sampling process by transforming aliasing artefacts to appear more similar to a noise component which in turn can be more readily accommodated in subsequent neural processing (Yellott, 1983).

The $dist_5$ variable essentially defines the pixel distance between the two closest nodes in the tessellation by globally scaling the tessellation. The σ_{base} variable defines the base size and standard deviation of the Gaussian receptive fields: increasing it results in blurrier images, while overly decreasing it results in aliasing (jaggy) artefacts as visible in the top right image in **Figure 3**. The aliasing artefacts are especially apparent at the peripheries of the

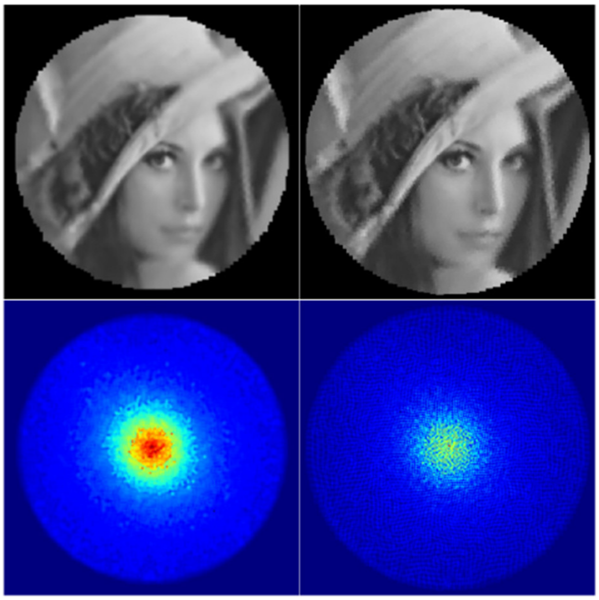

FIGURE 3 | Backprojected retinal images and their retinas' Gaussian heatmaps. **Left:** a well-parametrised retina. **Right:** a badly parametrised retina.

image. Finally, σ_{ratio} defines the difference between the receptive field sizes in the fovea and the peripheries of the retina.

The information captured by the retina can be visualised directly by generating a *backprojected retina image* (**Figure 3**, top row). It allows one to check visually whether the retinal subsampling appears sharp and free of aliasing artefacts. In order to obtain the backprojected image, every Gaussian receptive field kernel is projected onto an image-plane and scaled by its corresponding imagevector value. This image is then normalised by the *Gaussian heatmap image* (**Figure 3**, bottom row), which by itself is a useful visualisation of the spatial distribution of retina's receptive fields. The heatmap image can be obtained by simply projecting the receptive field Gaussians without scaling them by imagevector values. Aliasing artefacts in backprojected images can be produced by gaps between receptive fields in the retina's Gaussian heatmap image and can be suppressed by increasing the standard deviation of the projected Gaussian field. However, this comes at the expense of increasing the degree of blur the reconstructed image.

The receptive field parameters used were chosen manually by visually examining the Gaussian heatmaps and backprojected images for various parameter combinations. The objective being to produce heatmaps which are both free from "holes" mentioned above and also not significantly blurred. The chosen receptive field parameters are: $dist_5 = 1.0$, $\sigma_{base} = 0.4$ and $\sigma_{ratio} = 0.26$ to produce a retina of 168 × 168 px in size.

3. EXPLOITING THE RETINO-CORTICAL MAPPING WITHIN DEEP LEARNING

As described above, the basic retina samples an input image and produces an image vector as output, in a manner somewhat analogous to the optic nerve. However, this form of output is not compatible with current DCNN software environments as these have been designed to process regular image matrices as input. We have solved this compatibility issue by generating a *cortical image*. Even though our initial retina implementations did not fully exploit the potential data reduction efficiency of the retina image sampling approach, they did provide a straightforward and viable means to coupling the retina to any conventional DCNN architecture. The cortical image efficiency issue has now been substantially addressed in subsequent implementations (Shaikh, 2018) section 6.

3.1. Cortical Image Generation

3.1.1. Requirements and Approach

We generate cortical images using Gaussian interpolated forward projection, a technique frequently employed in computer graphics. The receptive field centres used for retina sampling are first mapped into *cortical space* and then each imagevector intensity value is used to scale a small Gaussian kernel which is accumulated into the cortical image, centred on the appropriate cortical location. An alternative approach would be to map the back-projected retinal image pixel-by-pixel onto a new space; this however would be more computationally intensive and would not take advantage of the compression achieved by the imagevector. Additionally, the pixel-by-pixel approach would be much less flexible due to fewer parameters defining the behaviour of the process. It would also result in significant holes in the foveal region of resultant cortical images, similar to those reported in the work of Pamplona and Bernardino (2009). The approach taken eliminates the possibility of holes in the mapping as the size of the Gaussian kernel projected into the cortical image can be increased to provide the required degree of overlap and also suppress aliasing.

The cortical images should ideally preserve local angles, maintain a fairly uniform receptive field density and preserve all local information captured by the retina without introducing any noise. These requirements are laid out in order to enable the convolution kernels of CNNs to extract features from the resultant cortical image. The literature reviewed points toward a form of log-polar space as being the most appropriate approach since it has been shown to model with reasonable fidelity the mapping observed in the primate visual cortex (Schwartz, 1977). Mathematically, this mapping provides a plausible model, affording the key geometric features of observed cortical magnification of the fovea and compression of the peripheral visual field accordingly; it is also a conformal mapping, meaning that it preserves local angles.

3.1.2. The Cortical Mapping

Retinal log-polar coordinates consist of θ, which is the angle about the origin (the centre-most point of the fovea), and ρ, which is the log of the distance from the origin. The x and y variables below represent retinal space Cartesian coordinates relative to the origin.

$$\rho = log\sqrt{x^2 + y^2} \tag{1}$$

$$\theta = atan2(y/x) \tag{2}$$

As evident in the left side of **Figure 4** the log-polar space suffers from severe sparsity in the foveal region and excessive density at the peripheries. This has been mitigated by deviating from the approach proposed in the literature, removing the log operator from Equation (1) and switching to the "linear" polar space:

$$r = \sqrt{x^2 + y^2} \tag{3}$$

The right side of **Figure 4** demonstrates the drastic improvement in node uniformity by switching to the polar space, although the foveal region is still undesirably sparse and the extreme peripheries are packed in tight rows. The uniformity of the polar mapping also suffers at $r = 30$ where the node density is too high compared to other regions. These issues have been resolved by adopting the approach from the work of Schwartz (1980) and adjusting the mapping with an α parameter while also splitting the retina tessellation vertically into two halves and mapping each half separately. This solves the singularity issue at the fovea and brings the mapping closer to the experimental data of activations in the visual cortices of different primates. The resultant coordinate equations for the cortical mappings are:

$$Y_{cort} = \sqrt{(x+\alpha)^2 + y^2} \tag{4}$$

$$X_{cort} = atan2(y/(x+\alpha)) \tag{5}$$

As seen in **Figure 5** the α parameter is added to the x coordinate to shift the tessellation's nodes away from the origin horizontally. In polar space this manifests itself by translating the nodes closer to $X = 0$, with the effect increasing logarithmically toward the foveal nodes at $Y = 0$. As the α parameter increases, the peripheral nodes (red and dark blue in **Figure 5**, Left) protrude proportionately; this is desirable as it addresses the issue of tightly packed rows of nodes from **Figure 4**. Accordingly, α sets the field of view of the quasi-linear region of the retino-cortical mapping. Note that in order for the left half of the retina to mirror the right one in **Figure 5**, Left its coordinates have been adjusted as follows:

$$X_{left} = -\sqrt{(x-\alpha)^2 + y^2} \tag{6}$$

$$Y_{left} = atan2(y/x-\alpha) - sign(atan2(y/x-\alpha)) * \pi \tag{7}$$

It was decided that a value of $\alpha = 10$ will be used as upon visual inspection it appeared the most uniform. Lower α values lead to an overly sparse foveal region, while higher values produced an overly dense region at $Y \approx \pm 70$, $X \approx 0$. In order to define the aspect ratio of cortical images the mean node distances along the x and y axes were equated.

Cortical images were produced by projecting Gaussians scaled by the associated imagevector value onto the appropriate nodes' locations with a sub-pixel accuracy of 1 decimal place. The resultant image was then normalised by pixel-wise division with the cortical Gaussian heatmap image, in a similar process to that used to generate retinal backprojected images in section 2.4. The cortical Gaussians were parameterised with $\sigma = 1.2$ and clipped at 7 pixels width. The two halves of the cortical image are also realigned to facilitate visual inspection.

The resultant cortical images, an example of which can be seen in **Figure 5**, Right, satisfy all the criteria for an acceptable input to a CNN: local angles are preserved, receptive fields are projected at a sufficiently uniform density and most of the local information captured by the retina is preserved without introducing any noise or artefacts. The cortical images have a

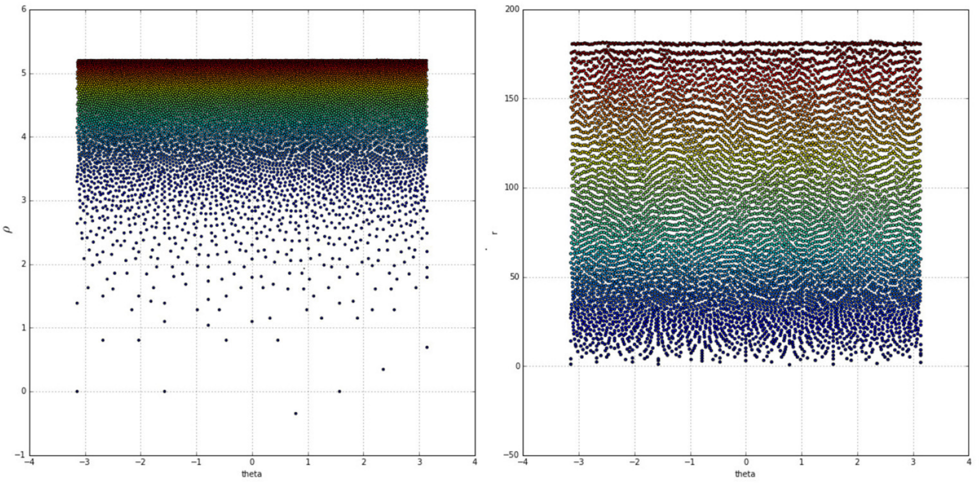

FIGURE 4 | Colour coded receptive field centres mapped onto the log-polar **(Left)** and linear-polar **(Right)** spaces. Warmer colours indicate receptive fields closer to the peripheries, whereas colder colours indicate points closer to the fovea.

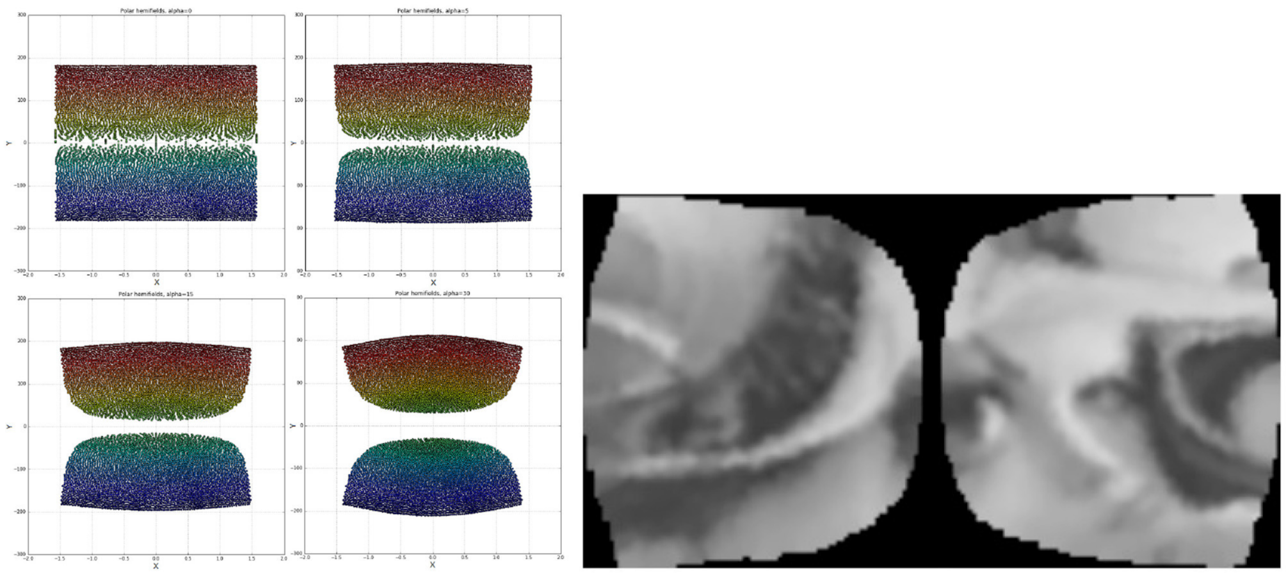

FIGURE 5 | Left: Two hemifields of receptive field centres mapped onto a polar space. Going from top left to bottom right the α values are: 0, 5, 15, 30. The points are colour-coded based on the value of $sign(x) * r$. **Right:** A cortical image of the standard Lena image, equivalent to the optimal retinal backprojection from the left side of **Figure 3**.

resolution of 179 × 96 px, while a square that best fits the retina's resolution is 168 × 168 px large.

The cortical parameters were selected with a focus on reconstructing the foveal region of the image to ensure that the high-frequency content captured by the retina reaches the CNN. As a result the cortical images for this parameterisation display aliasing artefacts which are especially visible on images of synthetic objects with straight edges (Lena's hat in **Figure 5**, Right). Subsequent mappings, described in section 4, now address this issue.

While the visual data reduction achieved by this retina is approximately ×7, the compression ratio of the cortical transform is 1.64 : 1, due to the pixel interpolation required to generate a hole-free cortical image. However, our ongoing research has demonstrated that it is now possible to achieve the full data reduction potential for the approach section 6.

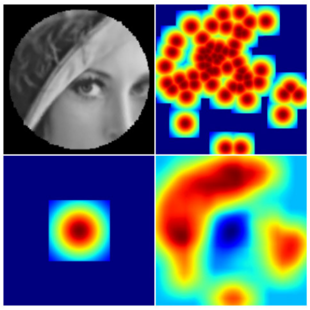

FIGURE 6 | Going left-to-right, top-to-bottom: a retinal backprojection image; the equivalent region of the initial saliency map denoting SIFT feature locations; the equivalent region of the inhibition map resulting from the singular fixation; the final saliency map.

3.1.3. Fovea Size and Hemifield Overlap

As we are inputting image files to the retina, as opposed to characterising a camera as input with specific FoV characteristics as determined by a lens etc., the concept of FoV in terms of visual angle does not apply to this retina as such, but in terms of *pixels*, 168px as described above. Specified as a fraction of the radial FOV, the retina parameterisation above has been chosen to generates a fovea of ~10%.

Due to the disjoint nature of the cortical mapping at the interface between the projected cortical hemifields, there is a loss of neighborhood information along the retina's vertical meridian, which is the 'U' shaped border region in the cortical mapping as evident in **Figure 5**, Right. In future versions this could be resolved by having the two halves of the cortical mapping duplicate a set of nodes on the meridian, as found in the mammalian visual system which shares of the order of 1° of visual overlap along the vertical meridian in the retina, between each cortical hemifield in human vision. As both cortical hemifields are processed by a single DCNN in the implementation reported here, we believe that any information loss is likely to be minimal.

3.2. Gaze Control

The implemented system follows Balasuriya (2006) by maintaining a saliency map of the input image, as well as an inhibition-of-return (IOR) map describing past fixations **Figure 6**. Initially the retina is fixated upon the centre of the image. To populate the saliency map the retinal backprojected image is scanned for SIFT features. A Gaussian is then projected at each feature's corresponding location in the saliency map, with the caveat that the projections do not sum with the saliency map's prior value, but override it if they are larger.

The location of each fixation is represented in the IOR map as an amplified Gaussian spanning the retina's foveal region. In order to determine the coordinates of the next fixation, the IOR map is subtracted from the saliency map, the result is blurred with a 37 × 37 averaging convolution kernel. The coordinates of the maximum value on the final saliency map determine the next fixation point. The result is satisfactory - the retina focuses on areas of the input image with the most corners present, and does not re-fixate upon the same location.

3.3. Validating the 4196 Node Retina

A dataset suitable for training and evaluating retina-integrated DCNNs (RI-CNNs) has to meet a set of requirements: the object of interest has to occupy most of the image in order to maximise the likelihood of the gaze control algorithm producing good fixations. Ideally, said object would be either segmented or cropped out from the background. The images have to be large enough to take advantage of the retina, but not too large so that a single fixation of the retina captures a reasonable proportion of the object of interest. In order to prevent the classification task from being trivial, each object class in the dataset should share a subset of its visual features with at least one other class, meaning that the classes should be somewhat similar to each other.

In order to fulfill the above requirements, a new dataset was created by selecting and pre-processing the appropriate classes from ImageNet (Deng et al., 2009). This dataset consists of three subsets: subset A is made up of cortical images (**Figure 7**, left), subset B is retinal backprojected images (**Figure 7**, centre) and subset C consists of the conventional images of each fixation, masked with the retinal lens (**Figure 7**, right).

The object categories selected for the classification task are *Basketball Hoop*, *Brown Bear*, *Keyboard* and *Racoon*. The similarities between *Brown Bear* and *Racoon* (furry animal), *Basketball Hoop* and *Keyboard* (synthetic object with a grid-like key feature) helped ensure that the classification task is not trivial. The class objects were cropped out from their original images using the bounding boxes provided in ImageNet. The resultant images passed automatic selection that ensured the images were not too small ($width, height > 75, 75$) or too long ($1/3 < width/height < 3$), and were then processed by appropriate parts of the retina pipeline to produce the three subsets. In order to correct a large imbalance between the class frequencies, the number of retina fixations was varied per class. After the subsets were produced, they were manually edited to remove exceptionally bad fixations and false positives resulting from incorrect labels assigned in ImageNet. The final image counts in the dataset can be seen in **Table 1**, Left.

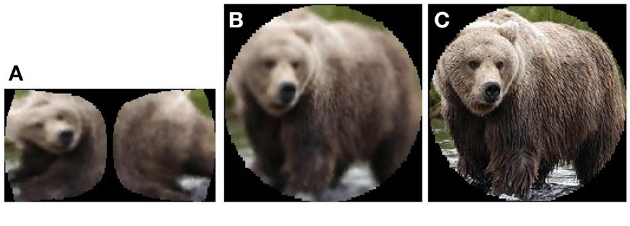

FIGURE 7 | An example *Brown Bear* image from each of the three subsets **(A–C)**.

3.4. 4196 Node Retina Results and Discussion

In order to evaluate the performance of the retinal subsampling mechanism and the cortical image representation in isolation, three DCNNs were trained, each with the same architecture but each using a different subset of the dataset built in the previous section. The DCNN architecture used, **Table 1**, Right, was chosen by trialing various architectures to maximise their performance over the cortical image dataset. The Keras 2.0.2. library was chosen as the Deep Learning platform used in this work. A relatively simple DCNN architecture was chosen in this pilot study, as our priority was to achieve benchmark classification performance testing, as opposed to optimisation of the recognition network.

We employed the Adam Kingma and Ba (2014) optimiser and a *categorical cross-entropy* loss function when training the DCNN. Improvements in validation accuracy were monitored and training was terminated automatically when this was no longer productive. L2 regularisation of strength $\lambda = 0.02$ was applied to the internal fully connected layers to prevent overfitting, however that value could most likely have been increased as the model continued to display signs of overfitting. The key figures from the training process are:

- **Network EVAL-A**, using (96 × 179) cortical images, reached its peak performance **(validation loss = 0.605, validation accuracy = 82.26%)** after **16 epochs**.
- **Network EVAL-B**, using (168× 168) retinal backprojected images, reached its peak performance **(validation loss = 0.493, validation accuracy = 86.14%)** after **21 epochs** of training.
- **Network EVAL-C**, using (168× 168) conventional images, reached its peak performance **(validation loss = 0.488, validation accuracy = 87.51%)** after **25 epochs** of training.

The results from evaluating the networks against the test set (**Figure 8**) show that both applying the full retino-cortical transform and the retinal subsampling lead to a modest decrease in the DCNNs' performance. The network trained on conventional images performed the best, with an average F1 score of 0.86; the network trained on retinal images landed an F1 score of 0.84 while the cortical images network had an F1 score of 0.80 showing that remapping the image from the retinal to the cortical space was the most damaging aspect of the retino-cortical transform. As seen in the matrices in **Figure 8**, the majority of the networks' confusion is between the classes sharing similar key features.

Although the retina has reduced classification performance, the gap between the different networks' performances is not excessive and the network EVAL-A has successfully demonstrated the learning capacity of convolutional neural networks for images in the cortical view while achieving a 7-fold visual data reduction and a 1.64 DCNN input compression ratio, fulfilling the main objective of this pilot study.

When interpreting the above pilot results, it should be kept in mind that it is possible that manually editing the dataset may not have removed all false positive and bad fixation images. The dataset is also not optimally large, and the input images are often small resulting in a number of fixation images being mostly empty, i.e., lacking visual input by fixating on the black border surrounding the image region sampled by the retina.

4. A HIGH RESOLUTION 50,000 NODE REAL-TIME RETINA IMPLEMENTATION

In the light of the above experiment it was decided to develop a a high-resolution 50K node retina (∼10% fovea size by radius) to achieve a visual data-rate reduction of approximately ×16.7. While initial implementations achieved compression ratios of the order of ×3, even this level of data reduction allows current DCNN implementations to process images approaching megapixel resolution *in a single pass*, described in section 5. A compression ratio of ×11.5 has now been achieved for this retina, section 6. Accordingly, the need to apply a DCNN window that is scanned over an image pyramid is no longer required and this greatly improves the overall efficiency of the DCNN Ozimek and Siebert (2017), Ozimek et al. (2017), and Hristozova et al. (2018). This retina implementation has been optimised in terms of reducing aliasing artefacts resulting from retinal sampling and cortical image production. Examples of cortical and back-projected retina images are shown in **Figure 10**.

TABLE 1 | Left: Per class and per split fixation image counts. The numbers are consistent across all 3 subsets of the dataset. **Right:** DCNN architecture for 4,196 node retina.

	Training	Evaluation	Test	TOTAL
Basketball Hoop	2,560	727	372	3,659
Brown Bear	2,422	693	350	3,465
Keyboard	2,490	711	360	3,561
Racoon	2,492	704	339	3,535
TOTAL	9,964	2,835	1,421	14,220

Input Image
A: (96 × 179 × 3)
B&C: (168 × 168 × 3)
1st Convolutional Layer
Conv2D: 32, (5 × 5), *ReLU*
MaxPooling2D: (2 × 2)
2nd, 3rd & 4th Convolutional Layer
Conv2D: 64, (3 × 3), *ReLU*
MaxPooling2D: (2 × 2)
Flatten
1st & 2nd Fully Connected Layer
Dense: 512, *ReLU*
Dropout: 30%
Output Layer
Dense: 4
Activation: *Softmax*

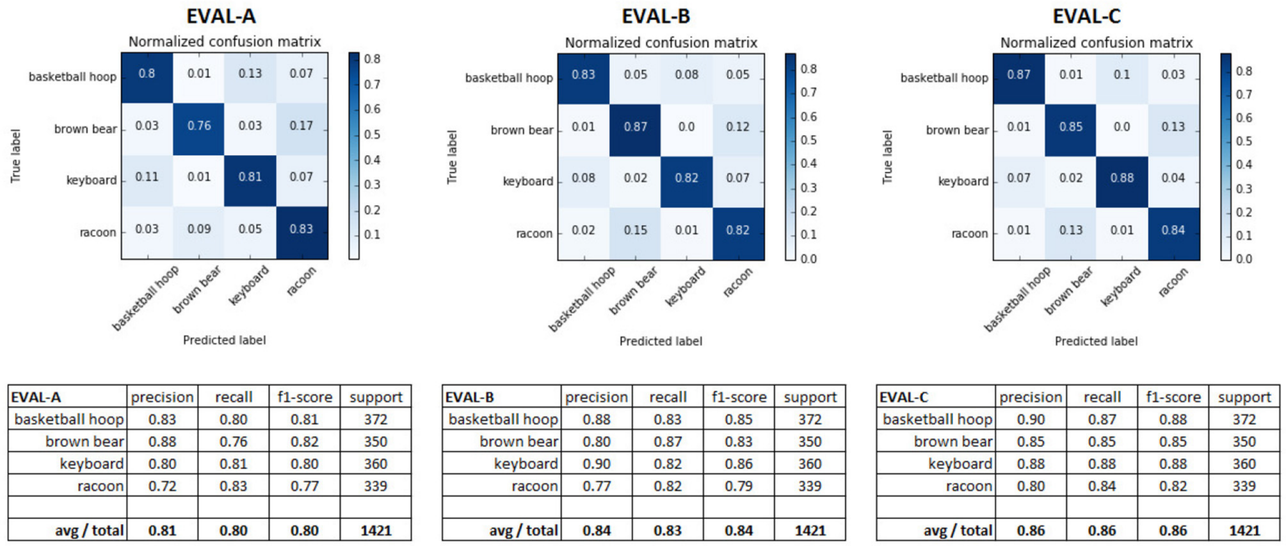

EVAL-A	basketball hoop	brown bear	keyboard	racoon
basketball hoop	0.8	0.01	0.13	0.07
brown bear	0.03	0.76	0.03	0.17
keyboard	0.11	0.01	0.81	0.07
racoon	0.03	0.09	0.05	0.83

EVAL-B	basketball hoop	brown bear	keyboard	racoon
basketball hoop	0.83	0.05	0.08	0.05
brown bear	0.01	0.87	0.0	0.12
keyboard	0.08	0.02	0.82	0.07
racoon	0.02	0.15	0.01	0.82

EVAL-C	basketball hoop	brown bear	keyboard	racoon
basketball hoop	0.87	0.01	0.1	0.03
brown bear	0.01	0.85	0.0	0.13
keyboard	0.07	0.02	0.88	0.04
racoon	0.01	0.13	0.01	0.84

EVAL-A	precision	recall	f1-score	support
basketball hoop	0.83	0.80	0.81	372
brown bear	0.88	0.76	0.82	350
keyboard	0.80	0.81	0.80	360
racoon	0.72	0.83	0.77	339
avg / total	**0.81**	**0.80**	**0.80**	**1421**

EVAL-B	precision	recall	f1-score	support
basketball hoop	0.88	0.83	0.85	372
brown bear	0.80	0.87	0.83	350
keyboard	0.90	0.82	0.86	360
racoon	0.77	0.82	0.79	339
avg / total	**0.84**	**0.83**	**0.84**	**1421**

EVAL-C	precision	recall	f1-score	support
basketball hoop	0.90	0.87	0.88	372
brown bear	0.85	0.85	0.85	350
keyboard	0.88	0.88	0.88	360
racoon	0.80	0.84	0.82	339
avg / total	**0.86**	**0.86**	**0.86**	**1421**

FIGURE 8 | Confusion matrices and different performance metrics of the three DCNNs evaluated against the appropriate test sets.

Given the level of computation required to execute the new 50K node retina and the need to support subsequent retina developments and real-time applications based on retina sampling, we decided to implement a hardware accelerated retina. This implementation has been written in CUDA C to execute on the NVIDIA series of Graphics Processor Units (GPUs) and is capable of sampling an RGB image to produce a triple of RGB image vectors in 39.1 ms, executing on an NVIDIA GTX 1080 Ti GPU (Balog, 2017).

5. HUMAN EYE-TRACKING BASED EGOCENTRIC PERCEPTION

We have undertaken an experiment (Hristozova, 2018), to combine the high-resolution 50K node software retina (Balasuriya, 2006; Ozimek and Siebert, 2017; Ozimek et al., 2017) with a custom designed DCNN architecture [based on DeepFix (Kruthiventi et al., 2017)] coupled to an image stream collected by Tobii Pro 2 eye-tracking glasses (AB, 2017) (**Figure 9**) worn by a human observer. Our objective is to demonstrate that we can achieve state-of-the-art recognition performance using our high-resolution retina implementation while also achieving efficiency gains. In addition, we wanted to investigate the potential to adopt a human observer for directing our software retina's gaze to thereby construct a truly egocentric perception system suitable for both humans and robots. Our final objective for this experiment is to demonstrate that it is possible for a human operator to collect appropriate training data for a software retina-based egocentric perception (Siebert et al., 2016; Ozimek et al., 2017) system simply by looking at objects. These objects may then be recognised in images collected by a human observer using eye tracking glasses, or a machine observer equipped with a saliency model to direct visual gaze.

5.1. Eye Tracking Pipeline

Our processing pipeline comprises four stages: image capture, fixation cluster extraction, retina transformation and DCNN processing. Following image collection using the Tobii glasses, described below, the images for the observations of each object are composited, in order to allow the individual fixations associated with each observation (fixation) to be overlaid on a single reference image. This approximate alignment was initially achieved by means of SIFT descriptor matching and extraction of the inter-image homographies, however, we discovered that simple head stabilisation was sufficient to achieve the required image registration. *K*-means clustering is then applied to these co-referenced fixation locations, where *K* has been set to 1% of the number of fixations in the observations for the current object class. This both reduces the number of fixated training images to manageable numbers and also selects locally coherent clusters of fixations, whose convex hulls are used to locate the software retina within the input image, as shown in **Figure 9**. The smaller cortical images produced by the retina are then input to the DCNN for both training and inference purposes.

5.2. Eye Tracking Data Collection

A custom interface was developed to allow an operator to control the acquisition of images using the Tobii Pro 2 eye tracking glasses. The two observers who participated in this experiment were instructed to look at locations on the surface of each object which seem particularly salient, or diagnostic of each object's identity, when collecting images. As mentioned above, it was necessary to stabilise observer's head by resting their chin on a desk surface while observing each object using the Tobii glasses and also by their consciously minimising any head movement. A data set of over 26,000 images was collected using the Tobii glasses, split into three categories: Training, Validation and Test. Each of these categories contains 9 object classes: Eggs, Gnocchi, Juice, Ling, Milk, Rice, Strep, VitC and Yogurt. Each of the data categories comprises the following proportion of the total data: Training 80%, Validation 18% and Test 2%.

5.3. Building a DCNN for Classifying Eye Tracking Image Data

Inspired by Kruthiventi's DeepFix Kruthiventi et al. (2017) network we developed a hand-optimised DCNN architecture comprising seven *convolutional layers(CLs)*, as summarised in **Table 2**. The first two CLs have been configured with 32 convolution filters, the second two CLs with 64 convolution filters, the fifth CL comprises 128 filters while the final two CLs comprise 256 filters. In all seven convolution layers the filters are 3 × 3 in size and each of these layers is coupled by a 2 × 2 ReLU max pooling function. Thereafter, the output of the last pooling layer has been flattened prior to being coupled to three *fully connected (FC)* layers, each comprising 132 nodes and a final fully connected layer configured with nodes corresponding to the number of output classes, in this case 9. Each FC layer

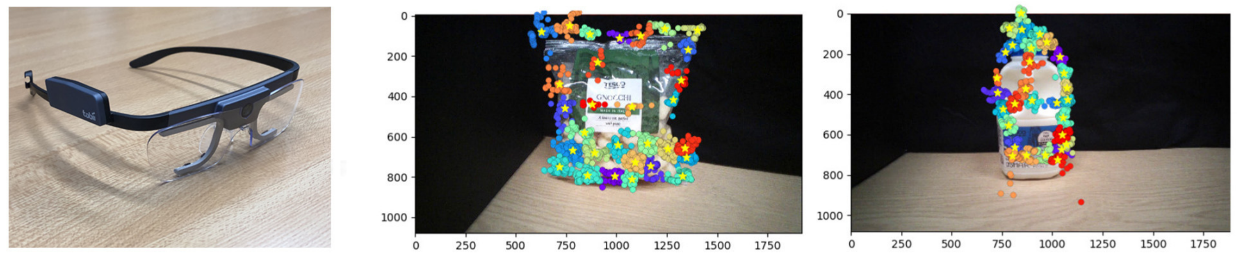

FIGURE 9 | Left: Tobii Pro2 Eye Tracker Glasses; **Right:** Fixation clustering following homography alignment.

TABLE 2 | DCNN architecture for Cortical and Fixation Crop image classification using the 50K node retina.

Input Image
Cortical Image: (399 × 752 × 3)
Fixation Crop Image: (926 × 926 × 3)
1st & 2nd Convolutional Layer
Conv2D: 32, (3 × 3), *ReLU*
MaxPooling2D: (2 × 2)
3rd & 4th Convolutional Layer
Conv2D: 64, (3 × 3), *ReLU*
MaxPooling2D: (2 × 2)
5th Convolutional Layer
Conv2D: 128, (3 × 3), *ReLU*
MaxPooling2D: (2 × 2)
6th & 7th Convolutional Layer
Conv2D: 256, (3 × 3), *ReLU*
MaxPooling2D: (2 × 2)
Flatten
1st Fully Connected Layer
Dense: 132, *ReLU*
Dropout: 50%
2nd Fully Connected Layer
Dense: 132, *ReLU*
Dropout: 0%
3rd Fully Connected Layer
Dense: 132, *ReLU*
Dropout 0%
Output Layer
Dense: 9
Activation: *Softmax*

had a rectifier activation function. While the activation function of the output layer was set to *softmax*, to provide classification values ranging from 0 to 1. The classifier was optimised using *stochastic gradient descent* and *categorical cross entropy* was used to compute the loss function. Drop-out was set to 50% and applied only once, after the first fully connected layer.

5.4. Cortical and Fixation Crop Image DCNN Validation

In order to compare the performance obtained when pre-processing images using the software retina, as opposed to classifying standard images, two DCNN models were trained: the first with fixation crop images of size 926 × 926 px and the second with the cortical images of size 399 × 752 px. Examples of fixation crop and cortical images are given **Figure 10**. These images were also normalised prior to being input to the DCNN.

5.4.1. Cortical Image DCNN Validation

The cortical image classification DCNN model was trained using 270 steps per epoch (total number of images/batch size), where the batch size was set to 64 and the training and validation data sets comprised 21,310 and 4,800 images respectively. This model required 55 min processing time to execute 18 epochs and produced 98% validation accuracy. **Figure 11** shows the accuracy and loss respectively. 6 s of processing time were required for this model to classify the data in its test set, resulting in an average accuracy of 98.2%.

5.4.2. Fixation Crop Image DCNN Validation

As illustrated in **Figure 10**, the fixation crop of an original image contains the retina's field of view, but retains the full image resolution. In order to benchmark the performance of the cortical image DCNN classifier, a DCNN model was trained using the full-resolution fixation crop images. In this case 1217 steps per epoch were used (again total number of images/ batch size) where the batch size is set to 16 and the training and validation data sets comprised 19,485 and 4,390 images respectively. The batch size had to be reduced to 16 from 64 used for the cortical image DCNN, because the increased numbers of pixels in the fixation crop images invoked a TensorFlow memory exhaustion error at any larger batch size. The resulting accuracy and loss are shown on **Figure 11**. This model required 2 h and 30 min to execute 18 epochs and produced 99% validation accuracy. 12 s of processing time were required for this model to classify the data in its test set, resulting in an average accuracy of 99.5%.

5.5. Eye Tracking Based Retina Validation Discussion

From the above results, use of retina pre-processing has reduced the training time for the DCNN from 150 min (using full-resolution input images) to 55 min using cortical input images. Since the full-resolution images are ×3 larger than the cortical images, the training batch size had to be reduced to 16 images for training with full-resolution images, as compared to a batch size of 64 images when training with cortical images. This improvement in data efficiency came at the expense of an average classification performance reduction of 1.3%. Even this modest reduction in performance has now been removed in subsequent work that uses a more efficient cortical image generation process, Section 6.

In both the cortical image and fixation crop classification experiments, the validation accuracy obtained for each classifier is close to the corresponding training accuracy result. Given the limited range of observations when the observer's head is constrained to be stationary, the captured images will be correspondingly similar. However, due to the non-linear nature of the retina transformation, the cortical images continue to exhibit significant variation in appearance when undertaking small saccades when exploring an object. Since small translations in retina space result in rotations in the cortex, this appears to afford a degree of *implicit data augmentation* when training the DCNN in cortical space, i.e., the rotated versions of patterns in the cortex provide a wider range of training data in terms of pattern-space than the corresponding retinal observations would otherwise.

6. RETINA DEVELOPMENTS

Our primary technological objective is to realise fully the potential gains of the combined retina-DCNN approach, its integration within mainstream robot visual processing DCNNs

FIGURE 10 | Left-Right: Fixation Crop Image, Corresponding Cortical Image (up-scaled), Example Cortical Images of the 9 Object Classes Captured.

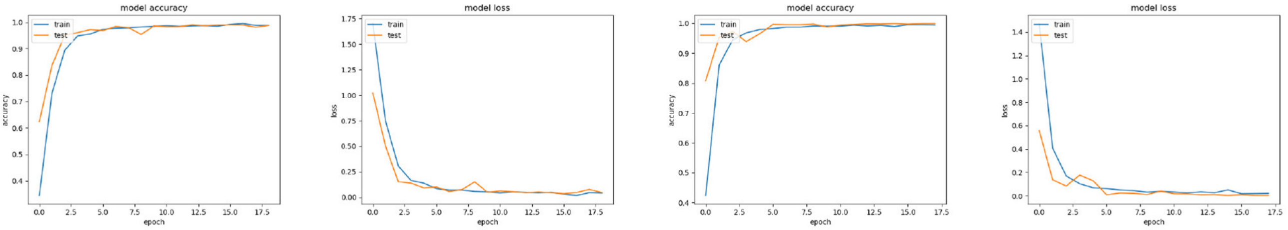

FIGURE 11 | Left-Right: Cortical image accuracy, Cortical image loss, Fixation Crop image accuracy, Fixation Crop image loss, each versus training epoch.

and underpin practical low-cost visual sensors for autonomous systems. However, any new image format must be adequately supported to be of any practical utility. Accordingly, the following section outlines recent work to advance the development of the retina and to support applications based on the retina image format.

6.1. Retina Filter Models

In order to further investigate the utility of mimicking the human visual system we extended the software retina to incorporate a functional model of single and double-opponent retina cells that has potential to improve data efficiency through sparsification, partial figure-ground separation, texture description and contour isolation **Figure 13**.

Retina cell models for computer vision purposes typically comprise basic implementations of the Marr-Hildreth difference of Gaussians operator (Marr and Hildreth, 1980), perhaps incorporating a filter-bank operating at a number of different spatial scales. An example of a more complex retina model is reported by Gobron et al. (2007) who implement the coarse functional properties of the retina using cellular automata and accelerate their model using GPU programming in the OpenGL environment. The general function of the 5 different retinal neuron types has been expressed, while other architectural features of the retina, such as the foveated topography of its neurons and their receptive field response profiles, are not represented in this model. The output from this retina is a depth-like contrast image that is sensitive to motion. While this model might prove valuable in a retina inspired edge detection task, it is incompatible with the space-variant retina architecture adopted here.

Given the limitations of the above retina models based on uniform sampling, we have developed our own model that incorporates a basic functional implementation of single and double opponent retinal ganglion cells which vary in their receptive field size as a function of eccentricity. This model utilises a high resolution (50K node), GPU accelerated retina and is based on the work of Gao et al. (2013). The single and double colour opponent ganglion cells compute a colour space potentially capable of simplifying texture perception, colour constancy and ground-figure segmentation owing to the combination of both colour and texture features in a single mapping (Saarela and Landy, 2012).

Our model implements single and double opponent receptive fields using difference-of-Gaussians kernels, with the surround receptive field Gaussian having the *sigma* parameter three timer larger than the centre receptive field Gaussian, based on physiological findings regarding the structure of cat retinal ganglion cells (Rodieck, 1965). The model supplements the RGB colour space with a yellow channel ($(r + g) / 2$) in order to simulate four Type-2 single opponent cell species: centre opponent r-g and b-y, and surround opponent g-r and y-b.

A single opponent cell is simulated by applying retinal sampling twice: once using the standard retina (to sample the centre fields) and then a second time using a retina with Gaussian receptive fields with a *sigma* scaled by a factor of three (to sample the surround fields). Single opponent cells of any species can then be implemented efficiently by simply subtracting the appropriate centre and surround image vector responses. The differential image vector responses simulating single opponent cells are then added together in a spatially opponent manner in order to produce colour channels that model the double opponent cells.

In order to remain faithful to cortical physiology the summation of the type 2 single opponent cells is *leaky*, meaning that the centre receptive field is not perfectly balanced with the surround receptive field (Shapley and Hawken, 2011). To realise this the surround receptive field has been scaled by $k = 0.9$ (Gao et al., 2013). Such leaky fields imply that absolute intensity or colour stimuli will generate a response and therefore be encoded along with the differential response of the antagonistic fields.

For visualisation purposes the outputs of the double opponent cells were backprojected (section 2.4) onto the image plane using the centre receptive fields. **Figure 12** shows the resultant images and demonstrates the improved figure-ground differentiation using colour blindness tests. Since negative-valued signals are processed in the brain using separate pathways to positive-valued signals, the outputs of the double opponent cells should be split into their negative and positive components using a threshold before further processing. (To enhance visualisation of the filter outputs, this step was omitted when generating the images in **Figure 12** and diverging colour maps were employed instead).

6.2. Real-Time Tracking Retina

The GPU accelerated implementation of the 50K node retina has been used to demonstrate real-time gaze control in a target tracking task (Boyd, 2018). In this experiment we trained a retina pre-processed DCNN pipeline with example tracking data based on a centroid colour tracker following an orange coloured target set against a dark background. The DCNN system learned to drive the Baxter Research Robot's wrist camera using pan-tilt signals learned from the cortical images input to a custom DCNN we designed. Accordingly our DCNN was able to regress, directly in real time, from cortical space, the appropriate pan-tilt activation to allow the robot's wrist camera to track the coloured target.

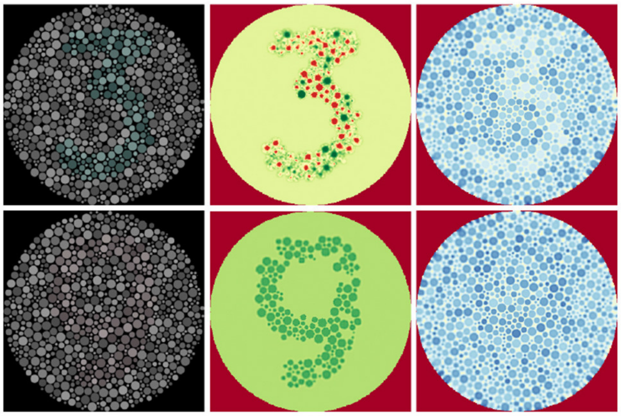

FIGURE 12 | Low contrast colour-blindness tests processed using our double-opponency model. Reproduced by permission of EnChroma Inc., from enchroma.com. **Left:** Original images. **Centre:** Retinal backprojections of the *red-green* double opponent cells, coloured using a divergent colour map. Red indicates negative values, yellow indicates values near zero, and green stands for positive values. **Right:** retinal backprojections of the *blue-yellow* double opponent cells, coloured using a divergent colour map. Red indicates negative values, yellow indicates values near zero, and blue stands for positive values.

6.3. Retina Efficiency

We have made an initial attempt to tackle the fundamental issue of how best to couple the retina directly to the DCNN to obtain the maximum data efficiency. Shaikh (2018) discovered that simply subsampling the cortical image a network input data reduction of ×11.5 can be achieved, without compromising performance when undertaking the eye tracking based classification task described in section 5. Furthermore, by adopting a scattered datapoint gridding algorithm, developed for astronomy data processing purposes (Winkel et al., 2016), he was able to produce cortical images that yield both a network input data reduction of ×10.8, and also a modest increase in classification accuracy.

Generating an optimal cortical image offers two strong advantages: Firstly, the retina pre-processor remains fully compatible with existing DCNN processing architectures developed for visual processing. Secondly, by retaining the continuity of retinotopic map explicitly within a cortical image, it simplifies the task of interpreting and devising and debugging new "retinised" visual processing DL networks and allows efficient shared convolutions to be applied to the CNN layers which process the input cortical image.

6.4. Retina Sensors for Robotics and Egocentric Perception

In order to develop self-contained smartphone-based retina sensors for robotics and egocentric perception applications and a convenient method for capturing training data by non-expert users, we have implemented the 4196 node retina on an Apple iPhone (Wong, 2017). This comparatively small retina samples a patch in an image captured by the iPhone's camera and SIFT, descriptors are extracted from the cortical image to direct the next retinal fixation location of the next in conjunction with a simple inhibition of return algorithm. The concept has been extended to port the 50K node retina to both iPhone (Vinickis, 2018), and Android (Yang, 2018), smartphone platforms. In the Android implementation no gaze-control has been implemented, instead relying on the user to direct the cameras to record compact image vectors, which can then be stored on the cloud.

A fundamental characteristic of any vision system based on a space variant retina architecture is that it must be directed appropriately to sample the scene. Commercial high-resolution pan-tilt security cameras have the potential to serve as low-cost imaging sensors that can be steered under computer control. We have constructed a software interface to a standard networked pan-tilt security camera controller (Zhou, 2018), to allow this to serve within an active autonomous vision system using retina processing and cortex-based gaze control algorithms.

Finally, to manage the data generated by retina-supported camera systems, we have developed a prototype software tool to allow editing and formatting prior to training DCNN systems (Fulton, 2018).

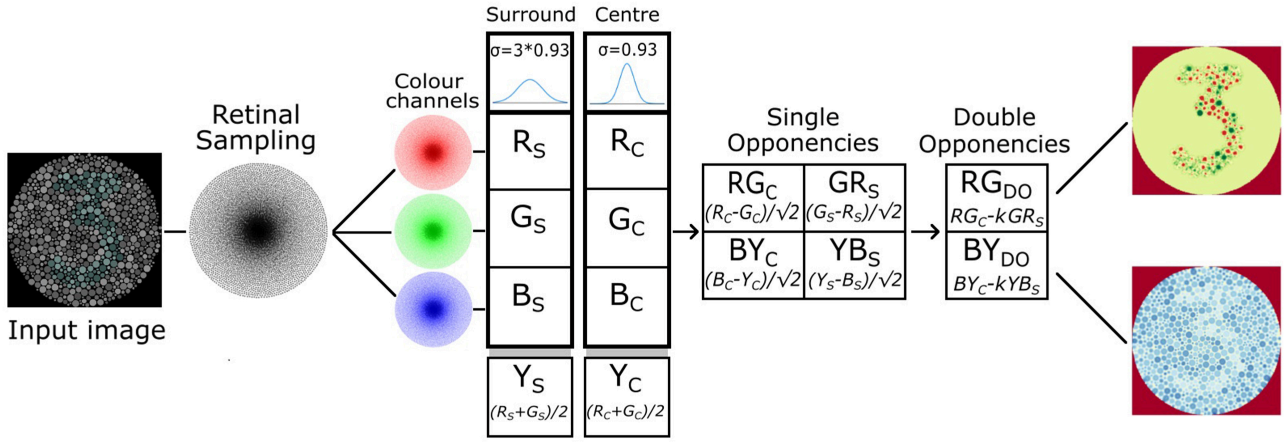

FIGURE 13 | Single and double opponent retina cell model implemented for our 50K node retina, based on the work of Gao et al. (2013).

7. CONCLUSIONS AND ONGOING WORK

We have confirmed the utility of the functional architecture of the human visual pathway, as predicted by Schwartz and others, by investigating retino-cortical mapping models within implementations of computer vision systems based on Deep Learning. Our primary experiment has shown that it is possible to make substantial data efficiency gains in terms of training computation, DCNN sizes, and inference rates by pre-processing images using our biologically inspired retina-cortex mapping that affords both visual data reduction and also a degree of scale and rotation invariance. It should be noted that we have not yet measured directly any scale and rotation invariance afforded by our retino-cortical mappings in the DCNNs we have trained to date, but plan to in future investigations.

While our initial attempt at demonstrating the concept, based on a 4,196 node retina, achieved only modest data reduction gains, our 50K node retina is now able to achieve a ~ ×16.7 visual data reduction and network input reduction of ~ ×11.5, while maintaining state-of-the-art performance in a classification task. We also demonstrated the viability of using human fixations to provide gaze-control for this 50K node software retina, which generated cortical images that were processed by means of our own DCNN model to obtain excellent classification performance on a database of 9 object classes. This approach has also demonstrated substantial reductions in DCNN training times and critically has provided the means for a DCNN to process an image of 930×930 px image for training or prediction *in a single pass*, while executing on a standard consumer-grade GPU.

Given that the initial experiments we report here have utilised the most basic of DCNN architectures, our current research is focussed on building improved DCNN models to process the cortical images generated by the retina. Inspired by predictive encoding brain theory, deep predictive coding networks Wen et al. (2018) which adopt feedforward, feedback and recurrent connections and have been reported to consistently outperform feedforward only DCNNs when undertaking object recognition and would therefore appear to be a promising architecture to investigate coupling to the retina.

The combined retina-DCNN approach is currently being investigated in a number of contexts for visual processing required by robotics systems for tracking and grasping and in the perception of egocentric imagery. Accordingly, our laboratory is developing the necessary infrastructure in terms of camera interfaces and data management tools to support DL-based visual processing based on the software retina. Furthermore, the software retina mapping also has potential for use in visual models developed to interpret human fMRI imagery for visual cortex modelling purposes.

Given both the visual data reduction potential of the retino-cortical mapping and the consequent implications for low-cost robotics and egocentric visual processing systems, especially mobile systems using smartphone or embedded processing hardware, the authors believe that this approach will underpin both a new wave of biologically motivated computer vision research and make possible vision-based products requiring high-resolution imaging that would otherwise be impractical to achieve using currently available hardware technology.

In conclusion, researchers have been attempting to harness log-polar visual mappings for over four decades and the authors believe that work we have presented is the first viable demonstration of using the retino-cortical mapping within a general purpose visual processing methodology.

DATA AVAILABILITY

The datasets analysed for this study can be found in doi: 10.5525/gla.researchdata.744.

AUTHOR CONTRIBUTIONS

PO implemented the retina codes, contributed associated text and undertook the 4K retina study. NH undertook the Eye tracking study, contributed associated text. LB implemented the GPU accelerated retina. JS proposed the retina-DCNN approach, lead preparation of manuscript, supervised the research presented.

FUNDING

The research reported here has been supported by the Innovate UK funded iSee project by the Engineering and Physical Sciences Research Council (EPSRC) [Ep/R0056505/1] and also by an EPSRC Doctoral Training Award [Ep/N509668/1]. It has also been supported by the project entitled Introducing retinal model into a deep convolutional neuronal network model for more realistic modelling of early visual cortex, as an extension of the ERC project Brain reading of contextual feedback and predictions [ERC StG 2012_311751-BrainReadFBPredCode].

ACKNOWLEDGMENTS

We would like to acknowledge those who have contributed to the software retina research reported here, including: Sumitha Balasuriya, Indradeo Ram, Tom Esparon, Lewis Boyd, Ryan Wong, Marius Vinickis, Yi Yang, Connor Fulton, Hashim Asgar Shaikh, Jianwen Zhou, Promboon Jirawattanakitja and Gerardo Aragon-Camarasa. We would also like to thank Béla Volgyi for his useful discussions, guidance and encouragement regarding the production of this paper and the research it describes. The authors would like to thank Prof. Lars Muckli for his collaboration and support for the retina work reported here.

REFERENCES

AB, T. (2017). *Tobii Pro Glasses 2: User's Manual*.

Balasuriya, L., and Siebert, J. (2003). "An artificial retina with a self-organised retinal receptive field tessellation," in *Proceedings of the AISB 2003 Symposium: Biologically Inspired Machine Vision, Theory and Applications* (Aberystwyth, UK), 7–11.

Balasuriya, L. S., and Siebert, J. P. (2006). Hierarchical feature extraction using a self-organised retinal receptive field sampling tessellation. *Neural Inform. Proc. Lett. Rev.* 10, 83–95. Available online at: http://bsrc.kaist.ac.kr/nip-lr/V10N04-06/V10N04P2-83-95.pdf

Balasuriya, S. (2006). *A Computational Model of Space-Variant Vision Based on a Self-Organized Artifical Retina Tessellation*. Ph.D. thesis, Department of Computing Science, University of Glasgow.

Balog, L. (2017). *A GPU Accelerated Software Retina*. Master's thesis, School of Computing Science, University of Glasgow (Glasgow).

Bolduc, M., and Levine, M. D. (1997). A real-time foveated sensor with Overlapping receptive fields. *Real Time Imaging* 3, 195–212. doi: 10.1006/rtim.1996.0056

Boyd, L. (2018). *A Retina-Based Vision System for Motion Control of the Baxter Robot*. Bachelor's thesis, Department of Computing Science, University of Glasgow (Glasgow).

Clippingdale, S., and Wilson, R. (1996). Self-similar neural networks based on a kohonen learning rule. *Neural Netw*. 9, 747–763.

Curcio, C. A., and Allen, K. A. (1990). Topography of ganglion cells in human retina. *J. Comp. Neurol.* 300, 5–25.

Curcio, C. A., Sloan, K. R., Kalina, R. E., and Hendrickson, A. E. (1990). Human photoreceptor topography. *J. Comp. Neurol.* 292, 497–523.

Deng, J., Dong, W., Socher, R., Li, L.-J., Li, K., and Fei-Fei, L. (2009). "Imagenet: a large-scale hierarchical image database," in *Computer Vision and Pattern Recognition, 2009. CVPR 2009. IEEE Conference on* (Fontainebleau, Miami Beach, FL: IEEE), 248–255.

Fulton, C. (2018). *Data Management Tools for Retina-Based Vision Systems*. Master's thesis, School of Computing Science, University of Glasgow, (Glasgow).

Gao, S., Yang, K., Li, C., and Li, Y. (2013). "A color constancy model with double-opponency mechanisms," in *The IEEE International Conference on Computer Vision (ICCV)* (Sydney, NSW).

Gobron, S., Devillard, F., and Heit, B. (2007). Retina simulation using cellular automata and gpu programming. *Mach. Vis. Appl.* 18, 331–342. doi: 10.1007/s00138-006-0065-8

Gomes, H. (2002). *Model Learning in Iconic Vision*. Ph.D. thesis, University of Edinburgh, School of Informatics, (Edinburgh).

Hristozova, N. (2018). *Dissertation Using Eye-Tracking Glasses for Training Dcnns*. Bachelor's thesis, Department of Computing Science, University of Glasgow (Glasgow).

Hristozova, N., Ozimek, P., and Siebert, J. P. (2018). "Efficient egocentric visual perception combining eye-Tracking, a software retina and deep learning," in *Submitted to the ECCV 2018 Workshop on Egocentric Perception, Interaction and Computing* (Munich).

Hubel, D. H., Wensveen, J., and Wick, B. (1995). *Eye, Brain, and Vision*. New York, NY: Scientific American Library.

Johnson, A. (1986). A spatial property of the retino-cortical mapping. *Spatial Vis.* 1, 319–331. doi: 10.1163/156856886X00115

Johnson, A. (1989). The geometry of the topographic map in the striate cortex. *Vis. Res.* 29, 1493–1500. doi: 10.1016/0042-6989(89)90133-8

Kingma, D., and Ba, J. (2014). Adam: A method for stochastic optimization. *arXiv [preprint]. arXiv:1412.6980*. Available online at: http://arxiv.org/abs/1412.6980

Kruthiventi, S. S. S., Ayush, K., and Babu, R. V. (2017). Deepfix: A fully convolutional neural network for predicting human eye fixations. *IEEE Trans. Image Proc.* 26, 4446–4456. doi: 10.1109/TIP.2017.2710620

Lowe, D. G. (2004). Distinctive image features from scale-invariant keypoints. *Int. J. Comput. Vis.* 60, 91–110. doi: 10.1023/B:VISI.0000029664.99615.94

Marr, D., and Hildreth, E. (1980). Theory of edge detection. *Proc. R. Soc. Lond. B* 207, 187–217. doi: 10.1098/rspb.1980.0020

Morrison, D., Corke, P., and Leitner, J. (2018). Closing the loop for robotic grasping: a real-time, generative grasp synthesis approach. *arXiv [preprint]. arXiv:1804.05172*.

Ölveczky, B. P., Baccus, S. A., and Meister, M. (2003). Segregation of object and background motion in the retina. *Nature* 423, 401–408. doi: 10.1038/nature01652

Ölveczky, B. P., Baccus, S. A., and Meister, M. (2007). Retinal adaptation to object motion. *Neuron* 56, 689–700. doi: 10.1016/j.neuron.2007.09.030

Ozimek, P., Balog, L., Wong, R., Esparon, T., and Siebert, J. P. (2017). "Egocentric perception using a biologically inspired software retina integrated with a deep CNN," in *ICCV 2017 Workshop on Egocentric Perception, Interaction and Computing*.

Ozimek, P., and Siebert, J. (2017). "Integrating a Non-Uniformly Sampled Software Retina with a Deep CNN Model," in *BMVC 2017 Workshop on Deep Learning On Irregular Domains* (London).

Pamplona, D., and Bernardino, A. (2009). "Smooth foveal vision with gaussian receptive fields," in *Humanoid Robots, 2009. Humanoids 2009. 9th IEEE-RAS International Conference on* (Nashville, TN), 223–229.

Ram, I., and Siebert, J. P. (2011). "Point-based matching applied to images generated by log(z) and log(z+alpha) forms of artificial retina," in *2011 Third World Congress on Nature and Biologically Inspired Computing* (Salamanca), 451–458.

Rodieck, R. W. (1965). Quantitative analysis of cat retinal ganglion cell response to visual stimuli. *Vis. Res.* 5, 583–601. doi: 10.1016/0042-6989(65)90033-7

Rojer, A. S., and Schwartz, E. L. (1990). "Design considerations for a space-variant visual sensor with complex-logarithmic geometry," in *[1990] Proceedings. 10th International Conference on Pattern Recognition* (Atlantic City, NJ), Vol. ii, 278–285.

Saarela, T. P., and Landy, M. S. (2012). Combination of texture and color cues in visual segmentation. *Vis. Res.* 58, 59–67. doi: 10.1016/j.visres.2012.01.019

Sawides, L., de Castro, A., and Burns, S. (2016). The organization of the cone photoreceptor mosaic measured in the living human retina. *Vis. Res.* 132, 34–44. doi: 10.1016/j.visres.2016.06.006

Schwartz, E. L. (1977). Spatial mapping in the primate sensory projection: analytic structure and relevance to perception. *Biol. Cybern.* 25, 181–194. doi: 10.1007/BF01885636

Schwartz, E. L. (1980). Computational anatomy and functional architecture of striate cortex: a spatial mapping approach to perceptual coding. *Vis. Res.* 20, 645–669. doi: 10.1016/0042-6989(80)90090-5

Schwartz, E. L. (1981). Cortical anatomy, size invariance, and spatial frequency analysis. *Perception* 10, 455–468. doi: 10.1068/p100455

Schwartz, E. L. (1993). "Topographic mapping in primate visual cortex: History, anatomy, and computation," in *Visual Science and Engineering: Models and Applications*, eds D. H. Kelly, New York & London: Taylor and Francis, 293–360.

Shaikh, H. A. (2018). *A Data Efficient Retino-Cortical Image Transformation Mapping* . Master's thesis, School of Computing Science, University of Glasgow, (Glasgow).

Shapley, R., and Hawken, M. J. (2011). Color in the cortex: single-and double-opponent cells. *Vis. Res.* 51, 701–717. doi: 10.1016/j.visres.2011.02.012

Siebert, J., Schmidt, A., Aragon-Camarasa, G., Hockings, N., Wang, X., and Cockshott, W. P. (2016). "A software retina for egocentric & robotic vision applications on mobile platforms," in *ECCV 2016 Workshop on Egocentric Perception, Interaction and Computing* (Amsterdam).

Viereck, U., Pas, A., Saenko, K., and Platt, R. (2017). "Learning a visuomotor controller for real world robotic grasping using simulated depth images," in *Proceedings of the 1st Annual Conference on Robot Learning*, eds S. Levine, V. Vanhoucke, and K. Goldberg, Vol. 78, *Proceedings of Machine Learning Research* (Mountain View, CA: PMLR), 291–300.

Vinickis, M. (2018). *A Software Retina Based Vision System on an Iphone.* (Glasgow).

Weiman, C. F. R. (1988). "Exponential sensor array geometry and simulation," in *Proceedings Volume 0938, Digital and Optical Shape Representation and Pattern Recognition* (Orlando, FL).

Wen, H., Han, K., Shi, J., Zhang, Y., Culurciello, E., and Liu, Z. (2018). Deep predictive coding network for object recognition. *CoRR* abs/1802.04762.

Wilson, J., and Hodgson, R. (1992). "Log polar mapping applied to pattern representation and recognition," in *Computer Vision and Image Processing* (IGI Global), 245–277.

Wilson, S. W. (1983). On the retino-cortical mapping. *Int. J. Man Mach. Stud.* 18, 361–389.

Wilson, S. W. (1985). "Adaptive 'cortical' pattern recognition," in *Proceedings of the 1st International Conference on Genetic Algorithms* (Hillsdale, NJ: L. Erlbaum Associates Inc.), 188–196.

Winkel, B., Lenz, D., and Flöer, L. (2016). Cygrid: a fast cython-powered convolution-based gridding module for python. *A&A* 591:A12. doi: 10.1051/0004-6361/201628475

Wong, R. (2017). *A Smartphone Software Retina*. Master's thesis, School of Computing Science, University of Glasgow, (Glasgow).

Yang, Y. (2018). *A Software Retina on an Android Smartphone*. Master's thesis, School of Computing Science, University of Glasgow, (Glasgow).

Yellott, J. (1983). Spectral consequences of photoreceptor sampling in the rhesus retina. *Science* 221, 382–385.

Zhou, J. (2018). *Data Management Tools for Retina-Based Vision Systems*. Master's thesis, School of Computing Science, University of Glasgow, (Glasgow).

Conflict of Interest Statement: The authors declare that the research was conducted in the absence of any commercial or financial relationships that could be construed as a potential conflict of interest.

Advantages of publishing in Frontiers

OPEN ACCESS
Articles are free to read
for greatest visibility
and readership

FAST PUBLICATION
Around 90 days
from submission
to decision

HIGH QUALITY PEER-REVIEW
Rigorous, collaborative,
and constructive
peer-review

TRANSPARENT PEER-REVIEW
Editors and reviewers
acknowledged by name
on published articles

Frontiers
Avenue du Tribunal-Fédéral 34
1005 Lausanne | Switzerland

Visit us: www.frontiersin.org
Contact us: info@frontiersin.org | +41 21 510 17 00

REPRODUCIBILITY OF RESEARCH
Support open data
and methods to enhance
research reproducibility

DIGITAL PUBLISHING
Articles designed
for optimal readership
across devices

FOLLOW US
@frontiersin

IMPACT METRICS
Advanced article metrics
track visibility across
digital media

EXTENSIVE PROMOTION
Marketing
and promotion
of impactful research

LOOP RESEARCH NETWORK
Our network
increases your
article's readership